NONLINEAR SEISMIC BEHAVIOUR OF STEEL PLANAR MOMENT-RESISTING FRAMES

Thesis by

Venkata Ramana Murty Challa

In Partial Fulfillment of the Requirements

for the Degree of

Doctor of Philosophy

California Institute of Technology

Pasadena, California

1992

(Submitted 10 April 1992)

To my parents . . .

ACKNOWLEDGEMENTS

I express my sincere gratitude to my advisor Professor John F. Hall for his enthusiastic guidance, continued support and encouragement throughout the course of the dissertation. His open doors and many a fruitful discussion are greatly appreciated. I have learnt many things from him, both academic and non-academic, which I will try to reflect in my career.

I thank the members of the doctoral committee Professors James L. Beck and Ronald F. Scott for their valuable suggestions during the course of the research. I would also like to thank Professor James K. Knowles and Dr. Thomas H. Heaton, Faculty Associate and Scientist-in-charge of U.S. Geological Survey Pasadena Office, for readily agreeing to be members of the thesis defense committee. I am grateful to the California Institute of Technology for the excellent education and the generous financial support it provided throughout my graduate studies.

I am deeply indebted to my *parents* for their love and affection. Their numerous sacrifices which made it possible for me to pursue my educational goals. I dedicate this thesis to both of them . . .

My deepest thanks go to my wife, Anuradha, for her warm support and for helping me in the preparation of this manuscript, and to my siblings and their spouses for their unparalled affection. My personal respects are due to Professor V.S.Raju and his family for their warm support and care.

I thank Cecelia Lin for her expert help in preparing the illustrations. I also thank sri.A.K.Gupta, sri.R.D.Koilpillai, sri.T.Ravishanker, sri.K.T.Venkateswara Rao, sri. S. Shashi Kumar, sri. B. Venkateswara Rao, sri. N.L. Murari, sri. M.A.M. Sudhir Gowda, sri. S. Siddarth, sri. V.K. Gupta, sri. A.D.Lewis, sri. B.V. Ratna Kumar, sri. M. Srinivasa Rao, sri. G. Subhash, sri. A. Bhattacharrya, sri. G.J. Pendse, and their families for their warm friendship.

ABSTRACT

The nonlinear response of steel planar moment-resisting frames during strong earthquakes poses a strong need for accurately modelling inelastic behaviour and large displacements. This thesis attempts to provide realistic and efficient analytical tools to aid this study.

Two *large-displacement small-strain* beam-column models are employed to include material and geometric nonlinearities. The first model assumes lumped plasticity, and discretises an element into segments. Axial force-Bending Moment strength interaction and flexural bowing are considered. Ten characteristic segment states are identified. An efficient numerical scheme is suggested to solve the nonlinear governing equations. This model only approximately represents the strength and stiffness of beam-columns.

A comprehensive finite element beam-column model is developed to more accurately model the strength and stiffness. A beam-column is discretised into segments, and further, each segment into one-dimensional fibres. A uniaxial cyclic constitutive law valid under arbitrary transient loading is proposed for structural steel. This physically motivated law incorporates the initial yield plateau, and provides explicit expressions for stress in terms of strain throughout the hysteretic path. This law is used to control the hysteretic loading of fibres.

A simple semi-empirical model is employed to analytically describe the highly nonlinear hysteretic behaviour of flexible joint panel zones in steel planar frames. Some modelling assumptions that may be made in frame analyses are evaluated. Numerical study of a building frame with flexible joints indicates that its collapse is sensitive to the joint panel zone design in addition to the ground motion.

...

TABLE OF CONTENTS

...

LIST OF TABLES

...

LIST OF FIGURES

...

LIST OF SYMBOLS

Sym. Description

$\underline{a}$ Vector of end-displacments of a beam-column segment in member coordinates

A Area of cross-section of the beam-column segment

A_* Area of cross-section of the beam-column segment effective in resisting shear

b_1, b_2 Bowing functions of a beam-column segment in the Plastic Hinge Model

b_1', b_2' Derivatives with respect to the normalised axial load, p, of the bowing functions of a beam-column segment in the Plastic Hinge Model

$\mathbf{B}$ Strain displacement matrix relating the end-displacements of a beam-column segment in member and local coordinates

c_b Coefficient of bowing of a beam-column segment in the Plastic Hinge Model

c_1, c_2 Stability functions of a beam-column segment in the Plastic Hinge Model

c_1', c_2' Derivatives with respect to the normalised axial load, p, of the stability functions of a beam-column segment in the Plastic Hinge Model

$\mathbf{C}$ Damping matrix of the MRF

$\underline{d}$ Vector of end-displacments of a beam-column segment in local coordinates

E Modulus of Elasticity of steel

$\underline{f}$ Vector of end-forces of a beam-column segment in global coordinates

$\underline{f}(t)$ Vector of external forces on the MRF at time, t

$\underline{f}$ Vector of end-forces of a beam-column segment in global coordinates

$\underline{f}^m$ Vector of end-forces of a member (beam-column or joint)

$\underline{f}^{cm}$ Vector of nodal residual forces of a multi-segment beam-column

$\underline{g}$ Vector of end-displacements of a fibre of a beam-column segment in global coordinates in the Fibre Model

G Shear Modulus of steel

$\mathbf{G}_c$ Geometric stiffness matrix of a beam-column segment corresponding to the chord rotation in local coordinates

$\mathbf{G}_{rc}$ Tangent stiffness matrix of a beam-column segment in local coordinates which includes the elastic stiffness and the geometric stiffness corresponding to the displacements relative to the chord

$\underline{h}$ Vector of end-forces of a fibre of a beam-column segment in global coordinates in the Fibre Model

I Moment of inertia about the axis of bending of the beam-column segment

$\mathbf{K}$ Stiffness matrix of the MRF

$\mathbf{K}_t$ Tangent stiffness matrix of the MRF

$\mathbf{K}_t^m$ Tangent stiffness matrix of a beam-column segment in member coordinates

$\mathbf{K}_t^l$ Tangent stiffness matrix of a beam-column segment in local coordinates

$\mathbf{K}_t^*$ Popularly used approximate tangent stiffness matrix of a beam-column segment in local coordinates

$\mathbf{K}_e^*$ Elastic stiffness matrix of a beam-column segment in local coordinates

$\mathbf{K}_g^*$ Popularly used approximate geometric stiffness matrix of a beam-column segment in local coordinates

${}^f\mathbf{K}_t$ Tangent stiffness matrix of a fibre of a beam-column segment in global coordinates in the Fibre Model

${}^{ab}\mathbf{K}_t$ Tangent stiffness matrix corresponding to the axial and bending effects of a beam-column segment in global coordinates in the Fibre Model

${}^{sh}\mathbf{K}_t$ Tangent stiffness matrix corresponding to the shear effects of a beam-column segment in global coordinates in the Fibre Model

${}^{sh}\mathbf{K}_t^l$ Tangent stiffness matrix corresponding to the shear effects of a beam-column

segment in local coordinates in the Fibre Model

${}^f\mathbf{K}_t^{GS}$ Geometric stiffness matrix of a fibre of a beam-column segment in global coordinates in the Fibre Model

${}^f\mathbf{K}_t^{TS}$ Truss stiffness matrix of a fibre of a beam-column segment in global coordinates in the Fibre Model

$\mathbf{K}_t^s$ Tangent stiffness matrix of a beam-column segment in global coordinates

$\mathbf{K}_t^{BC}$ Tangent stiffness matrix of a beam-column

$\mathbf{K}_t^J$ Tangent stiffness matrix of a joint

L Undeformed length of the member

L_s Undeformed length of the beam-column segment

$\underline{m}$ Moment vector of a joint

$\mathbf{M}$ Mass matrix of the MRF

M_p Plastic bending moment capacity of a beam-column cross-section

M_{pr} Reduced plastic moment capacity of a beam-column cross-section accounting for the presence of axial load

M_y Yield Moment of a joint

M_1, M_2 End-moments on a beam-column segment

$\underline{p}(t)$ Vector of stiffness forces in the MRF at time, t

p Axial load in the beam-column segment normalised with its first Euler load

$\underline{p}$ Vector of end-forces of a beam-column segment in local coordinates

P Axial load in the beam-column segment

P_e First Euler load of the beam-column

P_e^s First Euler load of the beam-column segment

P_y Yield axial load capacity of a beam-column cross-section

Q Equilibrium shear force on the beam-column segment

$\underline{s}$ Vector of end-forces of a beam-column segment in member coordinates

$\mathbf{R}$ Matrix relating the end-displacements and end-forces of a fibre to those of a segment of a beam-column in global coordinates in the Fibre Model

$\mathbf{T}$ Matrix relating the displacements and forces in local and global coordinates

$\underline{u}^m$ Vector of end-displacments of a member (beam-column or joint)

$\underline{u}$ Vector of end-displacments of a beam-column segment

$\underline{u}^{cm}$ Vector of nodal displacements of all the degrees of freedom of a multi-segment beam-column

$\underline{x}$ Vector of nodal displacements of the MRF

w Tranverse displacement of a beam-column segment normal to its chord

$\dot{\underline{x}}$ Vector of nodal velocities of the MRF

$\ddot{\underline{x}}$ Vector of nodal accelerations of the MRF

z Coordinate along the segment chord of a beam-column

γ_y Yield strain of a joint

κ Plastic rotations of the plastic moment hinges at the ends of a beam-column segment in the Plastic Hinge Model.

μ Beam rotation at a joint

μ Column rotation at a joint

ω Axial load parameter given by $\pi\sqrt{|p|}$

ϕ_1, ϕ_2 Elastic end-rotations of a beam-column segment within the plastic moment hinges, if any, in the Plastic Hinge Model.

θ_1, θ_2 Total end-rotations of a beam-column segment

...

Chapter 1

INTRODUCTION

1.1 General

Most engineering structures, *e.g.,* buildings and bridges, are composed of a number of straight members joined together. A structure formed with straight members is commonly called a *frame.* A frame member may be categorised into a beam, if bending moment predominates; a column, if axial force predominates; and a beam-column, if both bending moment and axial force are significant. Further, a frame which resists lateral loads only through the bending of the members without any braces, is called a *moment-resisting frame* (MRF).

All structures deform under loading. In general, the effect of this deformation upon the overall geometry can be ignored in beams. However, in columns as well as beam-columns, these deformations may cause significant additional axial force and bending moment. Therefore, their equilibrium equations must include the effect of change in geometry. This *geometric nonlinearity* makes their response nonlinear even for a purely linear elastic material. And, for a material with nonlinear stress-strain relation, the *material nonlinearity* further complicates the solution. Under the combined effects of geometric and material nonlinearities, the solution of the governing equations is often intractable, and recourse to numerical methods is essential.

The second most important component of a frame is the finite-sized junction of the beams and the columns, known as the *joint.* The response of a joint is highly nonlinear due to the various adjoining structural elements that contribute to its

strength and stiffness, and hence its analytical modelling is involved. In order to better understand the inelastic response of MRFs under strong seismic forces, the nonlinear behaviour of both the beam-columns and the joints must be assessed as close to reality as possible.

1.2 Review of Literature

The significant contributions to the analytical modelling of beam-columns and joints are summarised in this section. Also, the relevant terminology frequently used in this thesis is introduced. Hereinafter, the term *beam-column* refers to a general member of a MRF, and not necessarily the one in which both axial force and bending moment are significant.

1.2.1 Beam-Columns

For three decades now, nonlinear behaviour of steel planar beam-columns has been a subject of considerable research. Most of the research is devoted to prismatic members. Early research on this subject focussed only on the elastic stability of beam-columns, a topic which was studied using the results from long-hand computations of the closed-form solutions. The beam-column models were based on the linear theory of structures assuming geometric and material linearity, *i.e.,* linear strain-displacement and stress-strain relations, respectively. The governing equations were derived in the initial undeformed geometry assuming *small-displacements and small-strains.* However, the use of these models is limited to the service load conditions.

In as early as 1956, the ability of frames to dissipate energy through inelastic cyclic deformations was demonstrated [1]. The second generation of models extended the range of applicability up to the ultimate state by including material nonlinearity. Initially, the inelastic responses of beam-columns with elastic-perfectly plastic force-deformation relationship were studied [2,3]. Gradually, bilinear with strain-hardening and nonlinear force-deformation relationships were intro-

duced [4,5]. Several researchers included effects due to geometric nonlinearities also through large deformation, P-Δ effect, effect of axial load on the flexural stiffness and effect of bending moments on axial strain. Equilibrium of the beam-column was sought in the deformed configuration allowing *large-displacements and small-strains*. However, these models are valid only for monotonic loading and not for inelastic cyclic loading.

Nonlinear response analysis of beam-columns is a mathematically difficult problem. There are only a few extremely simple cases with exact closed-form solutions. And, even these cases do not consider material nonlinearities. But, in the late 1950's, when the digital computers became available to a larger domain of researchers, numerical techniques were explored to solve the exact nonlinear governing equations. Two approaches, namely the *Finite Element Approach* and the *Beam-Column Approach*, evolved from them. Consequently, quite a few analytical models were proposed. The simple models are used in engineering practice, while the comprehensive ones are primarily research oriented.

In the Finite Element Approach, each member is discretised into an assemblage of smaller elements. The continuum problem is replaced by a set of unknowns identified at each of the nodes of discretisation. The response of the beam-column is examined by continuously monitoring these control sections each of which is analysed by a linear or a simple nonlinear technique. Incremental equilibrium equations are derived based on an assumed displacement model and solved iteratively until convergence. The displacement-based formulation provides an upper bound to the true stiffness and the total potential energy, and converges to the exact solution from below [6]. This convergence is rigorously assured through the inter-element *compatibility* or *conforming* condition. The displacement functions are chosen to satisfy the *completeness* criterion, which requires that all the uniform strain states and the rigid body displacements of the element be included.

However, in the Beam-Column Approach, each member represented by its cen-

troidal axis is analysed as a single unit by a simplified method eliminating its further sub-division. This approach takes the standpoint of the methods of strength of materials. Instead of taking an elementary material point for investigating internal stresses and strains, the entire cross-section is considered. The cross-section is subjected to *generalised stresses*, namely axial force and bending moments, under the corresponding *generalised strains*, namely axial strain and curvatures. As in the classical theories of elasticity and plasticity, the solution satisfies the equations of equilibrium in the generalised space, the conditions of geometry or compatibility, and the generalised stress-strain relation. The equilibrium equation and the compatibility conditions are straightforward. The important issue is the derivation of relations between generalised stresses and generalised strains for which a number of simplifying but powerful kinematic and geometric assumptions are made.

Plasticity is a common phenomenon under inelastic conditions. The extent of plastification is varied along the length and across the cross-section of the beam-column. Owing to the discrete nature of plastification, the finite element models capture this effect and are called as *Distributed Plasticity* models. These models are quite realistic and are particularly used while taking a microscopic look at the beam-columns. On the other hand, the models based on this Beam-Column Approach, are *Lumped Plasticity* and do not consider this effect. They are less realistic, but simple and very popular in modelling the inelastic behaviour of beam-columns.

The parallel between the six stress components at a material point and the six generalised stress components at a member cross-section motivated some researchers using the Beam-Column Approach to extend the Classical Stress Space Plasticity Theory to the generalised stress space. However, the validity of such an extension has not been justified yet [7]. Hence, the Generalised Continuum Plasticity Theory applied to models based on Beam-Column Approach has not gained much attention.

On the computational front, when the Linearised Incremental Method showed a lack of convergence, the Method of Successive Substitution and the Newton-

Raphson Method were developed. A modified version of the Newton-Raphson Method has been the most popular choice for the nonlinear analysis of beam-columns. This method encouraged researchers to formulate and solve incremental equilibrium equations. Thus, tangent stiffness matrices were derived in the Updated Lagrangian coordinates using conventional beam-column theory assuming *large-displacements and small-strains.*

The cyclic loading of beam-columns was addressed in 1970 [8]. Experiments [9] showed that dynamic axial loads in building frame columns could be as large as 3.5 times the corresponding gravity axial loads. These inelastic strain reversal effects were not incorporated in the earlier models for the dynamic response of beam-columns [10]. Effects of partial plastification of the beam-column and inelastic unloading of the cross-section were included [11] to more accurately capture the variation in the axial and flexural strength and stiffness during cyclic response.

Insofar as present structural design is concerned, the development of the *Limit State Approach to Design* has focussed particular attention on the use of ultimate loads and on the behaviour of the structures at these loads [12]. Thus, accurate information on the ultimate strength and nonlinear load-deformation behaviour through the entire range of loading is very essential. Two significant beam-column models [13,10] based on the Beam-Column Approach include most of the features discussed above. The first model uses a generalised plasticity theory and includes approximate geometric stiffness. The second model includes the exact geometric stiffness but is valid only for monotonic loading.

1.2.2 Joint Panel Zones

In the earlier methods of frame analysis, the joints were idealised as mere points with zero dimensions. Later, the finite-sized joints were modelled as rigid elements in frame analysis. In the early 1970's, detailed experimental [14] and numerical [15] studies revealed that the joints possess highly nonlinear characteristics in the

form of large ductilities and good hysteretic properties. Since then, the joints were represented as explicit flexible elements in the nonlinear modelling of frames.

The joints are observed to be stiff axially and flexurally, but flexible in in-plane shear. In spite of this, the analytical modelling of the joints is burdened by their complex construction. The joint panel plate, the flanges of the beams and the columns, the doubler plates and the stiffeners enter the load-deformation characteristics together. A clear distinction of the contribution due to each of these is not possible due to their inter-dependence. In spite of these difficulties, some researchers have proposed simplified models accounting for one or more of these contributions to analytically describe the hysteretic strength and stiffness of the joint. Very few of them [16,17,18] are valid under *cyclic* loads.

1.3 Object and Scope of Present Study

The study described in this thesis attempts to extend the current knowledge on the hysteretic behaviour of steel planar MRFs. A brief outline of the specifics within this objective is as follows :

(i) Review existing cyclic constitutive law models for structural steel. Propose a simple cyclic constitutive law for the axial stress-strain behaviour of structural steel for inclusion in displacement-based finite element formulations based on experimental hysteretic data.

(ii) Review existing formulations of the beam-column models. Propose two analytical beam-column models, one simple and another comprehensive, to capture the hysteretic response.

(iii) Review existing formulations of flexible joint panel zones. Propose a joint element to analytically describe its cyclic behaviour.

(iv) Develop a computer program for the nonlinear dynamic analysis of planar MRFs using the proposed beam-column and joint elements. Analyse the realistic MRF of a tall building and study its collapse states under big earthquakes.

This thesis deals with the in-plane behaviour and analysis of MRFs. The material covered herein is structural *steel.* Though frequent reference is made to seismic loads, the proposed models are valid under any static and dynamic loading history.

The present study of beam-columns is confined to prismatic and partially prismatic members subjected to configuration-independent concentrated loads applied at the nodes or within the beam-column members. Two beam-column models, are developed assuming *large-displacements and small-strains* using the conventional beam-column theory. The first model is a Lumped Plasticity model while the second is a Distributed Plasticity model. Both models include material and geometric nonlinearities, and cyclic loading of the cross-sections.

The inelastic deformations considered, *i.e.,* the permanent deformations on the release of the load, are independent of time. The stability of beam-columns which sustain dynamic loads in excess of those under static conditions, is within the purview of this study. Inelastic effects on axial and bending stiffness, partial plastification of the cross-section, spread of plastification along the member length, and inelastic strain reversals and their effect on the stress-strain relationship, are included. Hence, the transition between fully elastic and fully plastic states of the cross-section are treated. Further, residual stresses can also be included.

Two cases of plane frame idealisation, namely frames *without* and *with* joint elements, are considered. In the frames with joint elements, the joints have the capability of being assigned desired magnitudes of strength and stiffness. Thus, the entire range of joints *from weak to strong* and *from flexible to rigid* can be included in the plane frame analysis. The analytical model for the flexible joint panel zone behaviour considers only its in-plane shear deformations, and neglects the effects of axial load and bending moments in it.

1.4 Organization of the Thesis

The thesis is organised into eight relatively independent chapters. Chapter 1 introduces the subject matter of this research and reviews the associated literature. The purpose and scope of this research are clearly outlined. The role of the beam-column and joint models in a general formulation of inelastic plane frame analysis is described in Chapter 2.

A detailed account of the Lumped Plasticity beam-column element, namely the Plastic Hinge Model, is presented in Chapter 3. The governing equations are derived, and the elastic and inelastic behaviour of beam-columns are discussed. Numerical implementation of the model is detailed. Numerical studies on single members are carried out to emphasise the highlights of the model. Similarly, a graphic picture of the Distributed Plasticity beam-column element, namely the Fibre Model, is presented in Chapter 4. A one-dimensional cyclic constitutive law for axial stress-strain behaviour of structural steel is proposed. The tangent stiffness matrices are derived. Results from single member numerical studies using this model are discussed.

The effect of flexible joint elements on the behaviour of planar MRFs is enunciated in Chapter 5. The proposed Joint Hysteresis Model is described. Comparisons of the model responses and the experimental data are shown.

Some modelling assumptions that may be made during the analysis of planar MRFs to reduce the computational effort are evaluated in Chapter 6. The realistic analyses of a planar building frame under strong seismic excitation is presented in Chapter 7 by including the joint elements in the frame discretisation. Issues regarding the design of steel planar MRFs are raised in light of this numerical study.

Finally, the summary and conclusions of this research are listed in Chapter 8. Specific recommendations are made for future work in this area.

1.5 Sign Convention, Notation and Units

This thesis adopts a consistent sign convention in all the derivations and numerical examples. Tensile displacements and tensile axial loads are considered positive. Rotational deformations follow the structural analysis convention. Anti-clockwise rotations and anti-clockwise bending moments are positive.

Scalars are indicated by their variable names, *e.g.*, a. The variable names of one-dimensional arrays, or *vectors*, are underlined in script, *e.g.*, $\underline{u}$. The variable names of two-dimensional arrays, or *matrices*, are cast in capital bold type face script, *e.g.*, $\mathbf{M}$. The *increment* in a scalar, a vector or a matrix between two distinctly different states is written with a dot over their variable names, *e.g.*, $\dot{h}$, $\dot{\underline{g}}$ and $\dot{\mathbf{B}}$. Superscript T denotes the transpose of the vector or the matrix, *e.g.*, $\underline{p}^T$ and $\mathbf{T}^T$.

Dimensional quantities are referred in *SI units*. A *millimeter (mm)* is the unit of linear dimension. A *Newton (N)* is the unit of force. A *second (sec)* is the unit of time.

...

Chapter 2

NONLINEAR DYNAMIC PLANE FRAME ANALYSIS

2.1 Introduction

A well-designed and constructed steel MRF is expected to behave inelastically under strong seismic forces, and dissipate the seismic energy without collapse. The inelastic behaviour of the MRF can arise either individually from beams, columns or joints; or together from the inelastic and geometric effects of the frame as a whole. The true behaviour of the MRF under severe seismic forces can be studied only through a nonlinear dynamic analysis. And while doing so, all the nonlinearities in the frame that appear in reality, must be included.

2.2 Sources of Nonlinear Frame Behaviour

The major sources of nonlinearity in a MRF are :

(1) Material Nonlinearity - It arises from nonlinear material constitutive laws. It is reflected in the load-deformation relationships of the structural elements.

(2) Geometric Nonlinearity - It stems from nonlinear member strain-deformation relationships, and from the formulation of frame equilibrium equations in its deformed configuration. Sometimes, a MRF may laterally support other non-MRFs. Then, the lateral forces applied on the MRF by the non-MRFs are a function of the deformation of the MRF itself. These forces also classify under the effects of geometric nonlinearity.

(3) Nonlinearity of Other Energy Dissipation Sources - It originates from the in-

ternal damping forces of the frame which get activated during the course of the response. Cracks in the partition walls, infill brickwork and reinforced concrete structural elements, and loose bolt friction are some examples.

In general, material nonlinearity is important in the inelastic frame behaviour. Geometric nonlinearity becomes significant in slender members. The P-Δ effect plays a critical role when the nodal loads on the frame are large or when its lateral drift is large. The other energy dissipation sources may be very important under strong shaking, but these nonlinearities are very difficult to quantify. The nonlinear frame analysis discussed in this chapter includes only the first two types of nonlinearities.

2.3 Basic Modelling Considerations

The nonlinear dynamic frame analysis described in this chapter makes use of certain basic modelling considerations. A frame is discretised into a finite number *beam-columns* inter-connected through the *joints*. Two cases of plane frame idealisation are studied, namely frames *with* and *without* joint elements. In frames without joint elements, the joints are idealised as points and centerline dimensions are used for the beam-columns connecting them. However, in frames with joint elements, the finite dimensions of the joints are considered and clear spans are used for the beam-columns instead. The external concentrated loads may be applied at the joints or at locations interior to the beam-column members.

The other basic modelling considerations are :

(1) The out-of-plane motions and forces of the plane frame are not considered.

(2) The mass of the frame is lumped at the nodes at the floor level. The beam-column members are massless. The rotary inertia of the nodal masses is neglected. The mass of the frame is constant throughout its response.

(3) Damping other than that due to plastic behaviour of the steel members in the frame is assumed to be viscous and constant throughout its response.

(4) The vertical and rotational components in the ground motion are neglected. The lateral ground motion is assumed to be uniform.

(5) The soil-structure interaction is neglected.

(6) The analyses of MRFs correspond to those of the bare steel frames neglecting the stiffening effects of the concrete floors and the in-fill walls.

2.4 Degrees of Freedom

At each node of the natural global discretisation, *i.e.,* at the junctions of the beams and the columns, a plane frame with joint elements has four degrees of freedom, namely two in-plane translations, beam rotation and column rotation. But, in a plane frame without joint elements, the beam rotation and the column rotation are equal. Thus, the nodal degrees of freedom reduce to three, namely two in-plane translations and joint rotation. Fig.2.1 shows the same.

Irrespective of whether the plane frame is discretised with or without joint elements, a beam-column has six exterior degrees of freedom, as shown in Fig.2.2a. If $\underline{u}$ is the end-displacement vector and $\underline{f}$ is the end-force vector of a beam-column, then its linearised incremental equilibrium equation is written as

$$\mathbf{K}_t^{BC}\,\underline{\dot{u}} = \underline{\dot{f}}\,, \tag{2.1}$$

where

$$\underline{\dot{u}}^T = \langle\, \dot{u}_1 \quad \dot{v}_1 \quad \dot{\theta}_1 \quad \dot{u}_2 \quad \dot{v}_2 \quad \dot{\theta}_2 \,\rangle$$

and $$\underline{\dot{f}}^T = \langle\, \dot{f}_1 \quad \dot{f}_2 \quad \dot{f}_3 \quad \dot{f}_4 \quad \dot{f}_5 \quad \dot{f}_6 \,\rangle\,.$$

In Eq.(2.1), $\mathbf{K}_t^{BC}$ is the tangent stiffness matrix of the beam-column. When a beam-column member is composed of multiple segments, the interior nodes have three degrees of freedom, namely two in-plane translations and joint rotation. These degrees of freedom are not included in the global matrix of unknowns, since the interior nodes are assumed to have no mass and damping.

When a plane frame is discretised with explicit joint elements, each joint has two degrees of freedom, namely beam rotation, μ, and column rotation, ν, as shown

in Fig.2.2b. If $\underline{\mu}$ is the joint rotation vector and $\underline{m}$ is the joint moment vector, then the linearised incremental equation of the joint panel is written as

$$\mathbf{K}_t^J \, \underline{\dot{\mu}} = \underline{\dot{m}}, \tag{2.2}$$

where

$$\underline{\dot{\mu}}^T = \langle \, \dot{\mu} \quad \dot{\nu} \, \rangle \, ,$$

$$\underline{\dot{m}}^T = \langle \, \dot{M}_\mu \quad \dot{M}_\nu \, \rangle \, ,$$

$$\dot{M}_\mu = \dot{M}_l + \dot{M}_r$$

$$\text{and} \quad \dot{M}_\nu = \dot{M}_t + \dot{M}_b \, .$$

In Eq.(2.2), $\mathbf{K}_t^J$ is the tangent stiffness matrix of the joint. $\dot{M}_l, \dot{M}_r, \dot{M}_t, \dot{M}_b$ are the increments in the two beam moments and the two column moments, respectively, that appear on the joint as shown in Fig.2.2.

2.5 Numerical Implementation

The numerical procedure of the nonlinear dynamic analysis of MRFs is straightforward. This section presents only the salient computational features with specific reference to flexible joint frames.

2.5.1 Mass Matrix

For straight structural elements like beam-columns, the refinement obtained in the solution by employing the consistent mass matrix is marginal. Hence, the mass of the frame is assumed to be lumped at the global nodes at the floor level, and rendering its mass matrix, M, diagonal. Since, the rotary inertia of the lumped nodal masses is neglected, the only non-zero terms of the mass matrix, M, are those diagonal terms corresponding to the two in-plane translational degrees of freedom.

In the dynamic analysis of frames under specified ground motions, considering the entire design live load to be effective may be very conservative. On the other hand, it may be unconservative to completely ignore it. In fact, due to the lack of a rigid connection between the live load and the frame, the UBC 1991 [19] and the

SEAOC provisions [20] recommend that only a part of it be included in estimating the seismic weight or mass of the frame. In the current study, 20% of the design live load is considered to be effective.

The mass of the laterally supported non MRFs, if any, is also effective for computing the lateral inertia of the MRF. Consequently, at node i, the masses associated with the translational degrees of freedom, M_{xi} and M_{yi} respectively, are not equal. M_{xi} accounts for the dead load plus 20% design live load of both the MRF and the non-MRFs. M_{yi} accounts for the dead load plus 20% live load of the MRF only. Thus, the mass matrix, $\mathbf{M}$, of the plane frame with joint elements is of the form

$$\mathbf{M} = \begin{bmatrix} \ddots & & & & & & \\ & M_{xi} & & & & & \\ & & M_{yi} & & & & \\ & & & 0 & & & \\ & & & & 0 & & \\ & & & & & \ddots & \end{bmatrix}, \tag{2.3}$$

where the masses corresponding to the four degrees of freedom of a typical node, i, are indicated explicitly. The mass matrix, $\mathbf{M}$, of a plane frame without joint elements has only three entries associated with each node.

2.5.2 Damping Matrix

Even though it is an important dynamic characteristic of a frame, damping is yet to be thoroughly understood. A significant amount of literature is available on the damping of a building under elastic vibrations. But, little is known about damping of frames during strong vibrations. The damping coefficient in a building, which is constant under elastic vibrations, is found to vary with time [21] under inelastic vibrations.

Hysteretic Damping and Viscous Damping are two popular models proposed to mathematically quantify the damping in a frame. Though the former is found more appropriate, often the latter is used owing to its mathematical convenience. The

Caughey Series [22] is one representation of viscous damping. Rayleigh Damping, which constitutes the first two terms of the Caughey Series, is used in the present nonlinear frame analysis to estimate damping other than that due to the plastic behaviour of the steel members. If $\mathbf{M}$ and $\mathbf{K}$ are the mass and stiffness matrices of the frame, respectively, then the viscous damping matrix, $\mathbf{C}$, is given by

$$\mathbf{C} = a_0\mathbf{M} + a_1\mathbf{K}\,, \tag{2.4}$$

where the coefficients a_0 and a_1 are determined based on the desired level of damping. Since $\mathbf{M}$ is diagonal and $\mathbf{K}$ is symmetric and banded, $\mathbf{C}$ is symmetric and banded. The modal representation of Eq.(2.4) is

$$\zeta = \frac{1}{2\omega}\left\{a_0 + a_1\omega^2\right\}\,, \tag{2.5}$$

where ζ is the damping ratio and ω is the frequency in radians/sec. The Rayleigh Damping so estimated is frequency dependent as shown in Fig.2.3. If the same damping ratio, ζ_0, is desired at two frequencies ω_1 and ω_2, then

$$\begin{aligned} a_0 &= \zeta_0\,\frac{2\omega_1\omega_2}{\omega_1+\omega_2} \\ \text{and} \qquad a_1 &= \zeta_0\,\frac{2}{\omega_1+\omega_2}\,. \end{aligned} \tag{2.6}$$

2.5.3 Incremental Equation of Motion

The matrix equation of dynamic equilibrium of the frame at time, t, is

$$\underline{p}(\underline{x},t) + \mathbf{C}\,\dot{\underline{x}}(t) + \mathbf{M}\,\ddot{\underline{x}}(t) = \underline{f}(t)\,, \tag{2.7}$$

where $\underline{x}(t)$, $\dot{\underline{x}}(t)$ and $\ddot{\underline{x}}(t)$ are respectively its displacement, velocity and acceleration responses relative to the ground at time, t. $\underline{p}(\underline{x},t)$ represents the stiffness forces produced in the frame under the application of external forces, $\underline{f}(t)$, comprising the constant gravity loads, $\underline{f}_0$, and the inertial forces, $\underline{f}_g(t)$. Hence,

$$\underline{f}(t) = \underline{f}_0 + \underline{f}_g(t)\,, \tag{2.8}$$

where

$$\underline{f}_g(t) = -\mathbf{M}\,\underline{\ddot{x}}_g(t)\,.$$

The non-zero terms of $\underline{\ddot{x}}_g(t)$ at time, t, are the input ground acceleration, a_g, associated with the lateral degrees of freedom. The nonlinear response quantities $\underline{x}$, $\underline{\dot{x}}$ and $\underline{\ddot{x}}$ at time, t, are obtained by the direct integration of Eq.(2.7) in the time domain.

Consider the load step from time, t, to time, $(t+\Delta t)$. The equation of equilibrium at time, $(t+\Delta t)$, is

$$\underline{p}(\underline{x},(t+\Delta t)) + \mathbf{C}\,\underline{\dot{x}}(t+\Delta t) + \mathbf{M}\,\underline{\ddot{x}}(t+\Delta t) = \underline{f}(t+\Delta t)\,. \tag{2.9}$$

For the k^{th} iteration, the incremental equilibrium matrix equation is obtained from Eq.(2.9) as shown below :

(1) Substitute for $\underline{\dot{x}}(t+\Delta t)$ and $\underline{\ddot{x}}(t+\Delta t)$ in Eq.(2.9) in terms of $\underline{x}(t)$, $\underline{\dot{x}}(t)$, $\underline{\ddot{x}}(t)$ and $\underline{x}(t+\Delta t)$ using the Newmark's difference scheme recipes given below :

$$\begin{aligned} &\underline{\dot{x}}(t+\Delta t) = \underline{\dot{x}}(t) + \{(1-\gamma)\underline{\ddot{x}}(t) + \gamma\underline{\ddot{x}}(t+\Delta t)\}\,(\Delta t) \\ \text{and}\quad &\underline{x}(t+\Delta t) = \underline{x}(t) + \underline{\dot{x}}(t)\Delta t + \left\{(\frac{1}{2}-\beta)\underline{\ddot{x}}(t) + \beta\underline{\ddot{x}}(t+\Delta t)\right\}(\Delta t)^2, \end{aligned} \tag{2.10}$$

where β and γ are called Newmark's parameters.

(2) Replace $\underline{x}(t+\Delta t)$ by $\underline{x}^{k+1}(t+\Delta t)$.

(3) Express $\underline{x}^{k+1}(t+\Delta t) = \underline{x}^{k}(t+\Delta t) + \Delta\underline{x}^{k}$. (2.11)

(4) Replace $\underline{p}(t+\Delta t)$ by $\underline{p}^{k+1}(t+\Delta t)$.

(5) Express $\underline{p}^{k+1}(t+\Delta t) = \underline{p}^{k}(t+\Delta t) + \mathbf{K}_t^k\ \Delta\underline{x}^{k}$. (2.12)

The matrix $\mathbf{K}_t^k$ in Eq.(2.12) is the tangent stiffness matrix of the frame evaluated at the start of the k^{th} iteration. After making the above substitutions and

re-arranging the terms, Eq.(2.9) reduces to

$$\begin{aligned}
&\left[\beta \mathbf{K}_t^k + \frac{\gamma}{\Delta t}\mathbf{C} + \frac{1}{(\Delta t)^2}\mathbf{M}\right] \Delta \underline{x}^k \\
&= \beta \underline{f}(t+\Delta t) - \beta \underline{p}^k(t+\Delta t) \\
&- \left[\frac{\gamma}{\Delta t}\mathbf{C} + \frac{1}{(\Delta t)^2}\mathbf{M}\right] \underline{x}^k(t+\Delta t) + \left[\frac{\gamma}{\Delta t}\mathbf{C} + \frac{1}{(\Delta t)^2}\mathbf{M}\right] \underline{x}(t) \\
&+ \left[(\gamma-\beta)\mathbf{C} + \frac{1}{\Delta t}\mathbf{M}\right] \dot{\underline{x}}(t) + \left[(\gamma-2\beta)\frac{\Delta t}{2}\mathbf{C} + (\frac{1}{2}-\beta)\mathbf{M}\right] \ddot{\underline{x}}(t).
\end{aligned} \tag{2.13}$$

Eq.(2.13) is the incremental equilibrium equation to be solved iteratively.

2.5.4 Solution of the Incremental Equation of Motion

The right hand side of the system of algebraic equations, Eq.(2.13), is called the residual load on the frame. The left hand side of Eq.(2.13) requires the frame tangent stiffness matrix, $\mathbf{K}_t^k$. Since nonlinearities develop within the time step, the matrix on the left hand side needs to be recast at each global iteration within the load step. This iteration scheme using the tangent stiffness, known as the Newton-Raphson Method, is often computationally very intensive. Instead, the Modified Newton-Raphson Method, may be used, wherein in Eq.(2.13), $\mathbf{K}_t^k$ is replaced by the initial elastic stiffness matrix, $\mathbf{K}_e$. Hence, Eq.(2.13) is modified as

$$\begin{aligned}
&\left[\beta \mathbf{K}_e + \frac{\gamma}{\Delta t}\mathbf{C} + \frac{1}{(\Delta t)^2}\mathbf{M}\right] \Delta \underline{x}^k \\
&= \beta \underline{f}(t+\Delta t) - \beta \underline{p}^k(t+\Delta t) \\
&- \left[\frac{\gamma}{\Delta t}\mathbf{C} + \frac{1}{(\Delta t)^2}\mathbf{M}\right] \underline{x}^k(t+\Delta t) + \left[\frac{\gamma}{\Delta t}\mathbf{C} + \frac{1}{(\Delta t)^2}\mathbf{M}\right] \underline{x}(t) \\
&+ \left[(\gamma-\beta)\mathbf{C} + \frac{1}{\Delta t}\mathbf{M}\right] \dot{\underline{x}}(t) + \left[(\gamma-2\beta)\frac{\Delta t}{2}\mathbf{C} + (\frac{1}{2}-\beta)\mathbf{M}\right] \ddot{\underline{x}}(t).
\end{aligned} \tag{2.14}$$

The iterating stiffness matrix within the square brackets on the left hand side of Eq.(2.14) is constant, and independent of the loading history and the response of the frame. While solving Eq.(2.14) by the Gauss Elimination Procedure, it is advantageous to prefactor this iterating stiffness matrix by forward reduction. Though this modified scheme consumes a larger number of global iterations, the

cost per iteration is less, and is less likely to get lost during unloading when the structure stiffens.

At the start of the first iteration in the load step from time, t, to time, $(t+\Delta t)$, the initial estimates for $\underline{x}^k(t+\Delta t)$ and $\underline{p}^k(t+\Delta t)$ are taken as $\underline{x}(t)$ and $\underline{p}(t)$, respectively. In the k^{th} iteration, Eq.(2.14) is solved by back substitution in the Gauss Elimination Procedure to obtain $\Delta\underline{x}^k$. Then, using Eq.(2.11), $\underline{x}^{k+1}(t+\Delta t)$ is updated. Using this updated incremental displacement vector, the state of all the members and joints is updated. The updated member-end forces and joint forces are assembled to form the revised $\underline{p}^{k+1}(t+\Delta t)$ vector. The iterations are continued until the residual force vector is within the tolerance.

For unconditional stability of the numerical scheme in linear problems, the Newmark's Method requires $\gamma \geq 0.5$ and $\beta \geq 0.25(0.5+\gamma)^2$. The proposed frame analysis uses the values $\beta = 0.25$ and $\gamma = 0.5$. This choice of the Newmark's parameters, β and γ, called the *Constant Average Acceleration Method* or the *Trapezoidal Method*, has an advantage in that it introduces no artificial damping through the numerical scheme.

2.5.5 Obtaining the $\underline{p}^{k+1}(t+\Delta t)$ Vector

While deriving the global incremental equation of motion, Eq.(2.12) is used to express $\underline{p}^{k+1}(t+\Delta t)$ in terms of $\underline{p}^k(t+\Delta t)$ and $\mathbf{K}_t^k$. However, the updated $\underline{p}^{k+1}(t+\Delta t)$ vector is not obtained using this linearised equation. Instead, it is obtained directly by assembling the load vectors of the beam-column and joint elements updated at the end of each global iteration.

For a frame without flexible joint elements, the updated global nodal incremental displacement vector, $\Delta\underline{x}$, is decomposed to form individual global incremental end-displacement vector, $\underline{u}^m$, of member, m, whether a beam-column or a joint. Mathematically, if $\prod^m$ is the decomposition operator which depends on the degrees

of freedom at the ends of member, m, then

$$\underline{\dot{u}}^m = \prod^m \{\Delta \underline{x}\} \ . \tag{2.15}$$

However, in a frame with flexible joint elements, the following simple calculation gives the global incremental end-displacement vectors, $\underline{\dot{u}}^m$, of the beam-columns. With reference to Fig.2.2b, if O is the centre of the joint panel zone, then the coordinates of the member-end locations, A and B of the beam and the column respectively, are given by

$$\begin{aligned} x_A &= x_O + \frac{d_c}{2}\cos\nu \,, \\ y_A &= y_O + \frac{d_c}{2}\sin\nu \,, \\ x_B &= x_O - \frac{d_b}{2}\sin\mu \\ \text{and} \quad y_B &= y_O + \frac{d_b}{2}\cos\mu \,. \end{aligned} \tag{2.16}$$

Using Eq.(2.16), the member-end displacement increments are expressed as

$$\begin{aligned} \dot{u}_A &= \dot{u}_O + \frac{d_c}{2}(\cos\nu - \cos\nu_t) \,, \\ \dot{v}_A &= \dot{v}_O + \frac{d_c}{2}(\sin\nu - \sin\nu_t) \,, \\ \dot{u}_B &= \dot{u}_O - \frac{d_b}{2}(\sin\mu - \sin\mu_t) \\ \text{and} \quad \dot{v}_B &= \dot{v}_O + \frac{d_b}{2}(\cos\mu - \cos\mu_t) \,, \end{aligned} \tag{2.17}$$

where μ_t and ν_t are the beam and column rotations at the start of the load step, respectively. μ and ν are the updated beam and column rotations within the load step, respectively.

The global incremental end-displacement, $\underline{\dot{u}}^m$, is applied to the state of member, m, at the start of the time step, and the coordinates of its end-nodes are updated. The updated global end-force vector, $\underline{f}^m$, of member, m, is obtained using its constitutive relations. Chapters 3, 4 and 5 describe in detail how to obtain

$\underline{f}^m$ using $\underline{\dot{u}}^m$. These global member end-force vectors are assembled to form the updated $\underline{p}^{k+1}(t+\Delta t)$ vector. If $\sum$ is the assembly operator, then

$$\underline{p}^{k+1}(t+\Delta t) = \sum_{m=1}^{N} \{\underline{f}^m\} \tag{2.18}$$

where N is the total number of beam-columns and joints in the frame.

2.5.6 Artificial Unloading during Global Iterations

While iteratively solving for the global nodal unknowns, $\Delta\underline{x}$, of the frame using Eq.(2.14), if the unloading stiffness is different from the loading stiffness, *artificial unloading* may occur due to the numerical scheme, as shown in Fig.2.4.

With reference to Fig.2.4, let δ_1 and δ_2 be the displacement sub-increments from global iterations 1 and 2, such that $\delta_1 > 0$ and $\delta_2 < 0$. Let $\delta > 0$ be the cumulative total of δ_1 and δ_2. Let 'T' be the state of the frame at time, t. Let 'A' be the updated state of the frame at the end of global iteration 1. Now, if the displacement sub-increment, δ_2, is applied to state 'A' of the frame, owing to unloading the resulting updated state at the end of global iteration 2 becomes 'B_*'. Instead, if δ, the cumulative total of the displacement sub-increments, is applied to the state 'T' of the frame, the updated state at the end of global iteration 2 is only 'B'. Clearly, state 'B_*' is erroneous, as the response of the frame can only be monotonic within the load step from time, t, to time, $(t+\Delta t)$. Thus, artificial unloading occurs when the new state of the frame is obtained by sequentially applying each displacement sub-increment from the most recent global iteration to the updated frame state at the end of the previous global iteration.

To avoid this, the cumulative total of the displacement sub-increments from all the global iterations within the load step is applied to the state of the frame at the start of the load step. Hence, the term $\Delta\underline{x}$ in Eq.(2.15) is defined as

$$\Delta\underline{x} = \underline{x}^{k+1}(t+\Delta t) - \underline{x}(t)\,. \tag{2.19}$$

2.6 NDA2 Computer Program

Based on the formulation discussed in this chapter, a computer program **NDA2** is developed for the nonlinear dynamic analysis of steel planar moment-resisting frames. The beam-columns are modelled using the Plastic Hinge Model and the Fibre Model elements described in Chapters 3 and 4, respectively. The joint panel zones are modelled using the Joint Hysteresis Model described in Chapter 5.

2.7 Choice of Ground Motion

To study the response of planar MRFs of tall buildings at their collapse states under very strong shaking, the nonlinear dynamic analysis must include appropriate and realistic ground motion time histories, in addition to all the nonlinearities in the load-deformation characteristics of the structures.

2.7.1 Long-Period Acceleration Content

Big earthquakes occur when significant slip takes place along the faults. The high frequency acceleration content of the ground motion decays rapidly with distance away from the fault. Even otherwise, the high frequency acceleration content is not important for tall buildings. To be critical regarding collapse of tall buildings, the ground acceleration must contain a significant amount of low frequency or long-period motion close to the period of the building. Such a ground motion causes resonance in the building, which may even lead to its collapse.

Amongst the available records in digitised form [23], the Holiday Inn S90W record collected at 8244 Orion Blvd. (Ground Floor), Los Angeles, California, on 9th February 1971, has a significant long-period acceleration content, as seen in Fig.2.5. The elastic pseudo-acceleration response spectrum of the Holiday Inn record scaled to 0.5g(peak) for 2% damping is shown in Fig.2.7. In the numerical studies discussed in Chapters 6 and 7, this record is considered appropriate for the moment-resisting frame chosen.

2.7.2 Large Pulses

There is yet another type of ground motion caused by big earthquakes that may be detrimental to tall buildings. The ground motion close to the fault is characterised by a large pulse. Such a pronounced pulse can cause high strains in the buildings which lie over or in the proximity of the faults. Consequently, they may undergo severe inelastic excursions resulting in their collapse. Recent studies [24,25] show that the nature of the large pulses in the ground motions depends on direction with respect to the fault, *viz.,* parallel or normal. The fault-parallel motions have displacement offsets, while the fault-normal motions have displacements pulses. The schematics of these pulses are shown in Figs.2.8 and 2.9, respectively.

Again, amongst the available records in the digitised form [23], the Pacoima Dam S16E record measured at the abutment of the Pacoima Dam, California, on 9th February 1971, is found to have a large velocity pulse, as shown in Fig.2.6. The elastic pseudo-acceleration response spectrum of this ground motion for 2% damping is also shown in Fig.2.7.

Two types of synthetic acceleration ground motions (see Figs.2.8 and 2.9) with a single large pulse of duration, T, are designed in light of the MRFs studied in Chapters 6 and 7. The duration of the pulse, T, the peak ground acceleration, a_0, the peak ground velocity, v_0, and the peak ground displacement, d_0, of these synthetic ground motions, are listed in Table 2.1. The response of the MRF is recorded for 20 *seconds* in total.

In comparison, the two types of synthetic ground motion pulses have the same duration and peak velocity. However, the peak accelerations of the fault-normal pulses are twice those of the corresponding fault-parallel pulses, and their peak displacements are about half as much as the corresponding values for the fault-parallel pulses. The pseudo-acceleration response spectra of these ground motions for 2% damping are shown in Fig.2.10.

2.7.2 Comment on Response Spectra

The pseudo-acceleration spectra shown in Figs.2.7 and 2.10 are based on the elastic damped single degree of freedom system. The frames discussed in Chapters 6 and 7 undergo considerable inelasticities. The natural periods of the nonlinear frames will therefore be larger than the corresponding estimates for elastic frames. This aspect must be remembered while interpreting the nonlinear responses of the frames using the elastic reponse spectra.

2.8 Numerical Results

In Chapters 6 and 7, the frame analysis program **NDA2** is used to study a realistic building frame [26] under specified ground motions. One important numerical aspect associated with frame analysis is discussed here.

2.8.1 Control on Tolerances

In displacement-based formulations, when iterations are required to solve implicit nonlinear equations, the convergence of these iterations is assessed based on the magnitude of the residual load vector. For practical reasons of finite precision, the iterations may be declared to have converged, if every residual load quantity is less than some specified *tolerance*. Since the residual force vector contains both force and moment quantities, rational and separate limits are set for the tolerance associated with each of them.

The direct stiffness approach of nonlinear frame analysis discussed above has three levels of iterations - global iterations, local iterations and segment iterations. *Global iterations* refer to the Modified Newton-Raphson iterations at the frame level, wherein displacement unknowns at each global degree of freedom are sought in each load step. *Local iterations* refer to the Newton-Raphson iterations at each beam-column level, wherein displacement unknowns at each interior degree of freedom in the member are sought within each global iteration in each load step. *Segment*

iterations are relevant only to the Plastic Hinge Model beam-column elements. Newton type iterations are conducted to compute the segment axial load for each assumed characteristic final state at each local iteration within each global iteration in each time step. Here, convergence is achieved, when the incremental axial force during any segment iteration becomes smaller than the tolerance.

Clearly, the convergence of the local iterations is essential before the convergence of the global iterations. And in case of the Plastic Hinge Model element beam-columns, the convergence of the segment iterations is essential before that of the local iterations. The tolerance limits given below are adopted in all numerical studies discussed in this thesis :

Global Tolerances	:	residual force	$= 10\,N$
		residual moment	$= 10000\,N-mm$,
Local Tolerances	:	residual force	$= 10\,N$
		residual moment	$= 10000\,N-mm$,
Segment Tolerance	:	incremental axial force	$= 0.5\,N$

which provided sufficient accuracy and good convergence results.

...

Chapter 3

THE PLASTIC HINGE MODEL

3.1 Introduction

A beam-column member under increasing magnitudes of end-rotations reaches its yield moment capacity when the outermost fibres at the end cross-section just reach the yield stress. On further increase of the end-rotation, the yielding spreads to the inner fibres across the cross-section and to the neighbouring cross-sections along the length. And, when the entire cross-section is yielded, the member is said to have formed a flexural moment hinge, or a *plastic hinge*, at that cross-section and the corresponding bending moment is called as the *plastic moment.* In the *Lumped Plasticity Approach* of modelling beam-columns, the inelastic action is defined for the whole cross-section area and not for individual fibres in it. Yield is assumed to take place only at discrete locations, called *plastic hinges*, instead of being spread along the length of the member. Further, the member is assumed to remain elastic between the plastic hinges.

The Beam-Column Approach, which idealises the member by its geometric centroidal axis, adopts the concept of *Lumped Plasticity*, to model the nonlinear and inelastic behaviour of beam-columns. These beam-column elements are capable of forming plastic hinges at their ends. The concept of zero-length plastic hinge or for that matter the theory of lumped plasticity itself, is a mathematical abstraction, because it implies infinite curvatures. Nevertheless, the concept is computationally convenient, and is sufficiently accurate for many practical beam-column applications, where the plastic action is confined to small regions at the ends.

A number of two-dimensional beam-column elements based on plastic hinge concepts have been described in the literature. These models are generally of either the parallel type [27,28] or the series type [13,29,30], as described in Fig.3.1. The series model spatially separates the zones of inelasticities or nonlinearities in a sequential order. Thus, the element is composed of a set of sub-elements with distinct load-deformation characteristics. On the other hand, the parallel model considers the inelastic actions to be distributed over the entire length of the member. In the case of beam-columns subjected to strong seismic excitation, the inelastic regions are concentrated at the ends. Hence, to model such members, the series model is distinctly superior to the parallel model owing to its realistic representation of the actual behaviour. The available theory behind the hinge sub-element in a series model [31] ignores strain rate dependence and stiffness degradation.

Two recent independent research efforts in the modelling of nonlinear and inelastic response of beam-columns, are significant. One of them [10], is based on the Beam-Column Approach with the capability of forming plastic hinges at the ends. It employs exact closed form expressions for the geometric stiffness of the beam-columns. But, it does not incorporate cyclic loading of the plastic hinges. The second model [31] uses a specially developed Generalised Plasticity Theory for Beam-Columns and includes the cyclic loading of the moment hinges. Only approximate expressions for geometric stiffness are used therein. Further, the applicability of the Generalised Plasticity Theory for Beam-Columns is yet to be justified.

This chapter describes a beam-column element, which for the first time includes both the exact geometric stiffness and the cyclic loading of the plastic hinges. This proposed beam-column element is henceforth called as the *Plastic Hinge Model*, with the capital letters. The Plastic Hinge Model element is developed using the simplistic Beam-Column Approach of the series type and the Finite Element Approach combined. The effect of axial load on bending stiffness and the effect of bending moments on axial stiffness [32] are included. However, the effects of shear deformations are not included. Also, this model does not include strain-hardening,

and partial plastic yielding and unloading of the cross-section.

3.2 Model Description

A Plastic Hinge Model beam-column element, as shown in Fig.3.2, comprises one or more sub-elements, called *segments* unlike the conventional model elements based on the Beam-Column Approach, which consist of just one segment. All nodes, interior and exterior, have three degrees of freedom corresponding to the two translations and the in-plane rotation. Since the interior nodes have no mass and damping, these degrees of freedom do not enter the global matrix of unknowns.

While modelling beam-columns, the feature of mutiple segments helps in bringing out the true large deformational characteristics, accurately estimating the elastic post-buckling strength important for slender members, and capturing the formation of plastic hinges at locations other than at the ends. In addition, the external transverse loads applied at locations other than the end nodes are included in the analysis using the interior nodes, without introducing additional global degrees of freedom. Thus, the natural global discretisation of single members between junctions of beams and columns is retained. In contrast to the finite element models which discretise a member into a large number of segments along its length, usually at least 10, this model requires only a couple of segments, at best. Usually, a maximum of four sub-elements is found adequate to provide sufficient accuracy.

The basis of this model is the assumption that a beam-column segment behaves elastically within the plastic hinges formed at its ends. Hence, even under inelastic conditions, the deformation of the segment within the hinges is completely defined by the elastic equilibrium equations. Two additional degrees of freedom different from the applied end-rotations, corresponding to the two elastic end-rotations within the plastic hinges are introduced to include the inelastic cyclic load reversals. A typical segment of the Plastic Hinge Model is shown in Fig.3.3. At each end, it has three external degrees of freedom - two translations and a rotation; and one

internal degree of freedom - the elastic rotation within the plastic hinge. The plastic hinge is activated only when the bending moment reaches its capacity. However, the equilibrium shear is completely transferred by the hinge to the joint irrespective of the formation of plastic hinges.

This model combines the merits of the beam-column approach, namely, simplicity, computational convenience and sufficient accuracy, with those of the finite element approach, namely, refined modelling, realistic behaviour patterns, general possibilities of loading and guaranteed convergence.

3.3 Equilibrium Equation

In structural mechanics too as is customary in solid mechanics, the fundamental field equations, the governing constitutive law, and the initial and boundary conditions must be solved for the dynamic state of a structure. For the beam-column segment, the field equations or the equilibrium equations, are written in terms of the generalised stresses, namely axial force and end-moments, and the generalised strains, namely axial displacement and end-rotations. Since equilibrium must be satisfied under dynamic and inelastic conditions, the incremental equilibrium equation is more relevant for general application than the total equilibrium equation.

The Updated Lagrangian formulation, where the geometry of the element is revised during the loading, is found most suitable to derive the incremental equilibrium equations. The Euler-Bernoulli kinematic assumption is made, and hence *plane sections normal to the centroidal axis before bending, remain plane and normal to it even after bending.* Further, the strains and the displacements relative to the chord are assumed to be small, which imply that the bowing in the member is small. The segment chord is shown in Fig.3.4a.

3.3.1 Total Equilibrium Equation of a Segment

Deriving total equilibrium matrix equation is the first step toward obtaining the

incremental equilibrium matrix equation. Consider a typical beam-column segment of length, L, cross-sectional area, A, and moment of inertia, I, in its deflected configuration. Let E be the Modulus of Elasticity of the material. Let the net axial displacement, u, and the two end-rotations, ϕ_1, ϕ_2, produce in the segment an axial load, P, and end-moments, M_1, M_2, as shown in Fig.3.4b in the member coordinate frame, *i.e.*, coordinate frame relative to the chord.

Stability Functions -

With reference to the free-body diagram shown in Fig.3.4c, the transverse displacement, $w(z)$, of the prismatic segment normal to its undeformed chord is related to the applied loads, namely the axial load, P, the end-moments, M_1, M_2, and the equilibrium shear force, Q, through the governing differential equation

$$EI\,\frac{\mathrm{d}^2 w}{\mathrm{d}z^2} = -M_2 + Qz + Pw\,, \tag{3.1}$$

where

$$Q = \frac{M_1 + M_2}{L}\,. \tag{3.2}$$

Hence, Eq.(3.1) becomes

$$\frac{\mathrm{d}^2 w}{\mathrm{d}z^2} - \frac{P}{EI}w = \frac{1}{EI}\left\{-M_2 + \frac{M_1 + M_2}{L}z\right\}\,. \tag{3.3}$$

Since the frame of reference is relative to the chord, the boundary conditions are

$$w(0) = w(L) = 0\,. \tag{3.4}$$

Solving Eq.(3.3) subject to the boundary conditions in Eq.(3.4),

$$\begin{aligned} w(z) &= \frac{M_1}{|P|}\left\{\frac{z}{L} - \frac{\sin\beta z}{\sin\beta L}\right\} + \frac{M_2}{|P|}\left\{\frac{-(L-z)}{L} + \frac{\sin\beta(L-z)}{\sin\beta L}\right\} && P<0 \\ &= \frac{M_1 L}{6EI}\,z\left\{\frac{z^2}{L^2} - 1\right\} - \frac{M_2 L}{6EI}(L-z)\left\{\frac{(L-z)^2}{L^2} - 1\right\} && P=0 \\ &= \frac{M_1}{P}\left\{\frac{z}{L} - \frac{\sinh\beta z}{\sinh\beta L}\right\} + \frac{M_2}{P}\left\{\frac{-(L-z)}{L} + \frac{\sinh\beta(L-z)}{\sinh\beta L}\right\} && P>0 \end{aligned} \tag{3.5}$$

where

$$\beta = \sqrt{\frac{|P|}{EI}}\,.$$

The end-rotations, ϕ_1, ϕ_2, are given by

$$\phi_1 = \left.\frac{\mathrm{d}w}{\mathrm{d}z}\right|_{z=L} \quad \text{and} \quad \phi_2 = \left.\frac{\mathrm{d}w}{\mathrm{d}z}\right|_{z=0} . \tag{3.6}$$

Substituting for $w(z)$ from Eq.(3.5) in Eq.(3.6),

$$\begin{Bmatrix} M_1 \\ M_2 \end{Bmatrix} = \frac{EI}{L} \begin{bmatrix} c_1 & c_2 \\ c_2 & c_1 \end{bmatrix} \begin{Bmatrix} \phi_1 \\ \phi_2 \end{Bmatrix} \tag{3.7}$$

where

$$c_1 = \begin{cases} \omega(\sin\omega - \omega\cos\omega)/(2 - 2\cos\omega - \omega\sin\omega) & P < 0 \\ 4 & P = 0 \\ \omega(\omega\cosh\omega - \sinh\omega)/(2 - 2\cosh\omega + \omega\sinh\omega) & P > 0 \end{cases} ,$$

$$c_2 = \begin{cases} \omega(\sin\omega - \omega)/(2 - 2\cos\omega - \omega\sin\omega) & P < 0 \\ 2 & P = 0 \\ \omega(\sinh\omega - \omega)/(2 - 2\cosh\omega + \omega\sinh\omega) & P > 0 \end{cases} ,$$

and $\quad \omega = \sqrt{\dfrac{|P|}{EI}}\, L .$

Eq.(3.7) is the flexural load-deformation equation in the member coordinate frame. Parameters c_1, c_2 are called *Stability Functions*. These functions reflect the effect of axial load on the flexural stiffness of the segment as shown in Fig.3.5a. In particular, if $P = 0$, then Eq.(3.7) reduces to the linear relation

$$\begin{Bmatrix} M_1 \\ M_2 \end{Bmatrix} = \frac{EI}{L} \begin{bmatrix} 4 & 2 \\ 2 & 4 \end{bmatrix} \begin{Bmatrix} \phi_1 \\ \phi_2 \end{Bmatrix} . \tag{3.8}$$

In Eq.(3.7), ω can be expressed in terms of p, the segment axial load normalised with the first Euler load of the segment, P_e, as

$$\omega^2 = \pi^2 \frac{|P|}{P_e} = \pi^2 |p| , \tag{3.9}$$

where

$$P_e = \frac{\pi^2 EI}{L^2} . \tag{3.10}$$

Bowing Functions -

With reference to Fig.3.4b, an end-moment causes a transverse deformation in the segment, called *flexural bowing*, resulting in an increase in its length. Thus, if

c_b is the coefficient of bowing, then the increase in length due to bowing is c_bL. If u is the axial displacement along the chord, then the axial force is

$$P = EA\left(\frac{u}{L} + c_b\right) . \tag{3.11}$$

Commensurate with the assumption of small-strain and small-displacements relative to the chord, no distinction is made between the undeformed and deformed chord lengths, L and $(L+u+c_bL)$, respectively. Thus, in the following derivation, the segment length always remains L. Consider a differential element of arc length, ds, whose projection along the chord is dz, where the coordinate, s, is measured along the deformed arc as shown in Fig.3.4b. The increase in length due to bowing, is

$$c_bL = L_{\text{arc}} - L_{\text{chord}} = \int_0^L (ds - dz) = \int_0^L \left(\sqrt{1+\left(\frac{dw}{dz}\right)^2} - 1\right) dz .$$

Neglecting terms of order four and higher in the Taylor expansion,

$$c_bL \doteq \frac{1}{2}\int_0^L \left(\frac{dw}{dz}\right)^2 dz . \tag{3.12}$$

Substituting Eq.(3.5) in Eq.(3.12),

$$c_b = b_1(\phi_1+\phi_2)^2 + b_2(\phi_1-\phi_2)^2 \tag{3.13}$$

where

$$b_1 = \begin{cases} (c_1+c_2)(c_2-2)/8\omega^2 & P<0 \\ 1/40 & P=0 \\ -(c_1+c_2)(c_2-2)/8\omega^2 & P>0 \end{cases} ,$$

$$b_2 = \begin{cases} c_2/8(c_1+c_2) & P>0 \\ 1/24 & P=0 \\ c_2/8(c_1+c_2) & P<0 \end{cases}$$

and $\omega^2 = \pi^2|p| .$

Substituting Eq.(3.13) in Eq.(3.11),

$$P = EA\left(\frac{u}{L} + b_1(\phi_1+\phi_2)^2 + b_2(\phi_1-\phi_2)^2\right) , \tag{3.14}$$

which is the axial load-deformation equation in member coordinates. Parameters b_1, b_2 are called *Bowing Functions.* These functions reflect the effect of axial load on the axial stiffness of the segment as shown in Fig.3.6a. In the absence of bowing, *i.e.,* in the absence of bending moments, Eq.(3.14) reduces to the linear relation

$$P = \frac{EA}{L}\, u\,. \tag{3.15}$$

Derivatives -

The need for the derivatives of Stability Functions and Bowing Functions with respect to the normalised axial load, p, arises while deriving the incremental equilibrium equations in Sec.3.3.2. The direct differentiation of these functions defined in Eqs.(3.7) and (3.13), with respect to p yields

$$\begin{aligned} c_1' &= 2\pi^2(b_1+b_2)\,, \\ c_2' &= 2\pi^2(b_1-b_2)\,, \\ b_1' &= -\frac{\pi^2}{4\omega^2}\left((b_1-b_2)(c_1+c_2)+2b_1c_2\right) \\ \text{and} \qquad b_2' &= -\pi^2\left(\frac{16b_1b_2-b_1+b_2}{4(c_1+c_2)}\right)\,, \end{aligned} \tag{3.16}$$

where

$$\omega^2 = \pi^2|p|\,.$$

Figs.3.5b and 3.6b show the dependance of these derivatives on p.

Taylor Series Expansions about $p = 0$ -

The Taylor Series expansions about $p=0$ of the Stability Functions, Bowing Functions and their derivatives, are necessary because some of these closed-form expressions become indeterminate at $p=0$, the transition point of the expressions for tensile and compressive axial load. In the neighbourhood of $p=0$, the closed form expressions yield inaccurate results owing to the nearness to indeterminacy. To overcome these computational difficulties, the truncated Taylor Series expansions

noted below are successfully employed in the range $-0.1 < p < +0.1$:

$$
\begin{aligned}
c_1 &= 4 + \frac{2}{15}\pi^2 p - \frac{11}{6300}\pi^4 p^2 + \frac{1}{27000}\pi^6 p^3 \ , \\
c_2 &= 2 - \frac{1}{30}\pi^2 p + \frac{13}{12600}\pi^4 p^2 - \frac{11}{378000}\pi^6 p^3 \ , \\
b_1 &= \frac{1}{40} - \frac{1}{2800}\pi^2 p + \frac{1}{168000}\pi^4 p^2 - \frac{37}{388080000}\pi^6 p^3 \ , \\
b_2 &= \frac{1}{24} - \frac{1}{720}\pi^2 p + \frac{1}{20160}\pi^4 p^2 - \frac{1}{604800}\pi^6 p^3 \ , \\
c_1' &= \pi^2 \left\{ \frac{2}{15} - \frac{11}{3150}\pi^2 p + \frac{1}{9000}\pi^4 p^2 \right\} , \\
c_2' &= \pi^2 \left\{ -\frac{1}{30} + \frac{13}{6300}\pi^2 p - \frac{11}{126000}\pi^4 p^2 \right\} , \\
b_1' &= \pi^2 \left\{ -\frac{1}{2800} + \frac{1}{84000}\pi^2 p - \frac{37}{129360000}\pi^4 p^2 \right\} \\
\text{and} \qquad b_2' &= \pi^2 \left\{ -\frac{1}{720} + \frac{1}{10080}\pi^2 p - \frac{1}{201600}\pi^4 p^2 \right\} .
\end{aligned}
\tag{3.17}
$$

These series expansions are also shown in Figs.3.5 and 3.6.

3.3.2 Incremental Equilibrium Equation of a Segment

The elastic total equilibrium equations derived in Sec.3.3.1 are not valid in the inelastic range. Only incremental equations are meaningful. And, even within the elastic range, explicit closed form solutions of these implicit equations cannot be obtained. Thus, recourse to numerical solution methods is essential. The most popular one is the Newton-Raphson Method, which employs tangent expressions of these nonlinear equations. Thus, a need arises to develop equations relating the incremental load vector to the incremental displacement vector through the *Segment Tangent Stiffness Matrix.*

Member Coordinates -

The total equilibrium equations of the segment from Eqs.(3.7) and (3.14) are

$$
\begin{aligned}
P &= EA\left(\frac{u}{L} + b_1(\phi_1+\phi_2)^2 + b_2(\phi_1-\phi_2)^2\right) , \\
M_1 &= \frac{EI}{L}(c_1\phi_1 + c_2\phi_2) \\
\text{and} \qquad M_2 &= \frac{EI}{L}(c_2\phi_1 + c_1\phi_2) .
\end{aligned}
\tag{3.18}
$$

Differentiating each of these equations with respect to each of the displacement quantities u, ϕ_1, ϕ_2, yields the components of the tangent stiffness matrix. Since c_1, c_2, b_1, b_2 are functions of the axial load, P, which in turn is a function of u, ϕ_1, ϕ_2, the chain rule of differentiation is applied. Denote $\dot{\underline{a}}$ as the incremental displacement vector, $\dot{\underline{s}}$ as the incremental load vector and $\mathbf{K}_t^m$ as the segment tangent stiffness matrix in the member coordinates. If P_e is given by Eq.(3.10), then the incremental equilibrium equation in member coordinates is

$$\mathbf{K}_t^m \ \dot{\underline{a}} = \dot{\underline{s}} \tag{3.19}$$

where

$$\mathbf{K}_t^m = \frac{EI}{L} \begin{bmatrix} \frac{\pi^2}{HL^2} & \frac{G_1}{HL} & \frac{G_2}{HL} \\ \frac{G_1}{HL} & c_1 + \frac{G_1^2}{H\pi^2} & c_2 + \frac{G_1 G_2}{H\pi^2} \\ \frac{G_2}{HL} & c_2 + \frac{G_1 G_2}{H\pi^2} & c_1 + \frac{G_2^2}{H\pi^2} \end{bmatrix} ,$$

$$G_1 = c_1' \phi_1 + c_2' \phi_2 \ ,$$

$$G_2 = c_2' \phi_1 + c_1' \phi_2 \ ,$$

$$H = \frac{P_e}{EA} - b_1'(\phi_1 + \phi_2)^2 - b_2'(\phi_1 - \phi_2)^2 \ ,$$

$$\dot{\underline{a}}^T = \langle \ \dot{u} \quad \dot{\phi}_1 \quad \dot{\phi}_2 \ \rangle$$

and $$\dot{\underline{s}}^T = \langle \ \dot{P} \quad \dot{M}_1 \quad \dot{M}_2 \ \rangle \ .$$

Local Coordinates -

Consider the geometry of the segment chord shown in Fig.3.8. The local displacement quantities are related to the member displacement quantitites as

$$\begin{aligned} u &= (d_1 - d_4) + \frac{(d_2 - d_5)^2}{2L} + \cdots \ , \\ \phi_1 &= \theta_1 - \frac{(d_2 - d_5)}{L} + \frac{(d_1 - d_4)(d_2 - d_5)}{L^2} + \cdots \\ \text{and} \quad \phi_2 &= \theta_2 - \frac{(d_2 - d_5)}{L} + \frac{(d_1 - d_4)(d_2 - d_5)}{L^2} + \cdots \ . \end{aligned} \tag{3.20}$$

The incremental form of Eq.(3.18) is

$$\begin{aligned} \dot{u} &= (\dot{d}_1 - \dot{d}_4) + \frac{(\dot{d}_2 - \dot{d}_5)(\dot{d}_2 - \dot{d}_5)}{L} + \cdots \ , \\ \dot{\phi}_1 &= \theta_1 - \frac{(\dot{d}_2 - \dot{d}_5)}{L} + \frac{(\dot{d}_1 - \dot{d}_4)(d_2 - d_5)}{L^2} + \frac{(d_1 - d_4)(\dot{d}_2 - \dot{d}_5)}{L^2} + \cdots \\ \text{and} \quad \dot{\phi}_2 &= \theta_2 - \frac{(\dot{d}_2 - \dot{d}_5)}{L} + \frac{(\dot{d}_1 - \dot{d}_4)(d_2 - d_5)}{L^2} + \frac{(d_1 - d_4)(\dot{d}_2 - \dot{d}_5)}{L^2} + \cdots \ . \end{aligned} \tag{3.21}$$

To obtain the instantaneous incremental end-displacement vector in member coordinates, $\dot{\underline{a}}$, in terms of the instantaneous incremental end-displacement vector in local coordinates, $\dot{\underline{d}}$, the end-displacement vector in local coordinates, $\underline{d}$, is set to zero, *i.e.*, $\underline{d} \equiv 0$. Hence, the incremental relation in Eq.(3.21) reduces to

$$\dot{\underline{a}} = \mathbf{B}\, \dot{\underline{d}}, \tag{3.22}$$

where

$$\mathbf{B} = \begin{bmatrix} 1 & 0 & 0 & -1 & 0 & 0 \\ 0 & -\frac{1}{L} & 1 & 0 & \frac{1}{L} & 0 \\ 0 & -\frac{1}{L} & 0 & 0 & \frac{1}{L} & 1 \end{bmatrix},$$

$$\dot{\underline{d}}^T = \langle\, \dot{d}_1 \quad \dot{d}_2 \quad \dot{d}_3 \quad \dot{d}_4 \quad \dot{d}_5 \quad \dot{d}_6 \,\rangle$$

and $\quad \dot{\underline{a}}^T = \langle\, \dot{u} \quad \dot{\phi}_1 \quad \dot{\phi}_2 \,\rangle\,.$

Again, from Fig.3.8, the segment end-forces in local coordinates can be written in terms of the corresponding quantities in the member coordinates as

$$\begin{aligned} p_1 &= P\,\cos\theta + Q\,\sin\theta\,, \\ q_1 &= P\,\sin\theta - Q\,\cos\theta \\ \text{and} \qquad m_1 &= M_1\,, \end{aligned} \tag{3.23}$$

where

$$\begin{aligned} \cos\theta &= \frac{L+(d_1-d_4)}{L+u}\,, \\ \sin\theta &= \frac{(d_2-d_5)}{L+u} \\ \text{and} \qquad Q &= \frac{(M_1+M_2)}{L+u}\,. \end{aligned}$$

Substituting Eq.(3.20) in Eq.(3.23) yields

$$\begin{aligned} p_1 &= P\left\{1-\frac{(d_2-d_5)^2}{2L^2}\right\} \\ &\quad + \frac{(M_1+M_2)}{L}\left\{\frac{(d_2-d_5)}{L} - \frac{2(d_1-d_4)(d_2-d_5)}{L^2}\right\} + \cdots\,, \\ q_1 &= P\left\{\frac{(d_2-d_5)}{L} - \frac{(d_1-d_4)(d_2-d_5)}{L^2}\right\} \\ &\quad - \frac{(M_1+M_2)}{L}\left\{1-\frac{(d_1-d_4)}{L} + \frac{(d_1-d_4)^2}{L^2} - \frac{(d_2-d_5)}{L^2}\right\} + \cdots \\ \text{and} \qquad m_1 &= M_1\,. \end{aligned} \tag{3.24}$$

Again, the incremental form of Eq.(3.24) is

$$
\begin{aligned}
\dot{p}_1 &= \dot{P}\left\{1-\frac{(d_2-d_5)^2}{2L^2}\right\} + P\left\{-\frac{(d_2-d_5)(\dot{d}_2-\dot{d}_5)}{L^2}\right\} \\
&\quad + \frac{(\dot{M}_1+\dot{M}_2)}{L}\left\{\frac{(d_2-d_5)}{L} - \frac{2(d_1-d_4)(d_2-d_5)}{L^2}\right\} \\
&\quad + \frac{(M_1+M_2)}{L}\left\{\frac{(\dot{d}_2-\dot{d}_5)}{L} - \frac{2(\dot{d}_1-\dot{d}_4)(d_2-d_5)}{L^2} - \frac{2(d_1-d_4)(\dot{d}_2-\dot{d}_5)}{L^2}\right\} \\
&\quad + \cdots , \\
\dot{q}_1 &= \dot{P}\left\{\frac{(d_2-d_5)}{L} - \frac{(d_1-d_4)(d_2-d_5)}{L^2}\right\} \\
&\quad + P\left\{\frac{(\dot{d}_2-\dot{d}_5)}{L} - \frac{(\dot{d}_1-\dot{d}_4)(d_2-d_5)}{L^2} - \frac{(d_1-d_4)(\dot{d}_2-\dot{d}_5)}{L^2}\right\} \\
&\quad - \frac{(\dot{M}_1+\dot{M}_2)}{L}\left\{1-\frac{(d_1-d_4)}{L} + \frac{(d_1-d_4)^2}{L^2} - \frac{(d_2-d_5)}{L^2}\right\} \\
&\quad - \frac{(M_1+M_2)}{L}\left\{-\frac{(\dot{d}_1-\dot{d}_4)}{L} + \frac{2(d_1-d_4)(\dot{d}_1-\dot{d}_4)}{L^2} - \frac{2(d_2-d_5)(\dot{d}_2-\dot{d}_5)}{L^2}\right\} \\
&\quad + \cdots
\end{aligned}
$$

$$
\text{and} \qquad \dot{m}_1 = \dot{M}_1 \, . \tag{3.25}
$$

Similar expressions can be derived for $\dot{p}_2$, $\dot{q}_2$ and $\dot{m}_2$. Again, to obtain a relation between the instantaneous incremental end-force vector in local coordinates, $\underline{\dot{p}}$, and the instantaneous incremental end-force vector in member coordinates, $\underline{\dot{s}}$, $\underline{\dot{d}}$ is set to zero. Hence, if $\mathbf{B}$ is as defined in Eq.(3.22), then Eq.(3.25) reduces to

$$
\mathbf{B}^T \, \underline{\dot{s}} + \mathbf{G}_c \, \underline{\dot{d}} = \underline{\dot{p}} , \tag{3.26}
$$

where

$$
\mathbf{G}_c = \begin{bmatrix}
0 & \frac{Q}{L} & 0 & 0 & -\frac{Q}{L} & 0 \\
 & \frac{P}{L} & 0 & -\frac{Q}{L} & -\frac{P}{L} & 0 \\
 & & 0 & 0 & 0 & 0 \\
 & & & 0 & \frac{Q}{L} & 0 \\
 & \text{Sym.} & & & \frac{P}{L} & 0 \\
 & & & & & 0
\end{bmatrix} ,
$$

$$
\underline{\dot{p}}^T = \langle \, \dot{p}_1 \quad \dot{q}_1 \quad \dot{m}_1 \quad \dot{p}_2 \quad \dot{q}_2 \quad \dot{m}_2 \, \rangle
$$

$$
\underline{\dot{d}}^T = \langle \, \dot{d}_1 \quad \dot{d}_2 \quad \dot{d}_3 \quad \dot{d}_4 \quad \dot{d}_5 \quad \dot{d}_6 \, \rangle
$$

$$
\text{and} \quad \underline{\dot{s}}^T = \langle \, \dot{P} \quad \dot{M}_1 \quad \dot{M}_2 \, \rangle \, .
$$

In Eq.(3.26), Q is the equilibrium shear force given by Eq.(3.2), and the $\mathbf{G}_c$ is the segment Geometric Stiffness corresponding to the chord rotation, which is a function of the equilibrium forces currently appearing on the segment.

Substituting Eqs.(3.19) and (3.22) in Eq.(3.26), yields

$$\mathbf{K}_t^l \, \underline{\dot{d}} = \underline{\dot{p}} \tag{3.27}$$

where

$$\mathbf{K}_t^l = \mathbf{G}_{rc} + \mathbf{G}_c \,,$$

$$\mathbf{G}_{rc} = \mathbf{B}^T \mathbf{K}_t^m \mathbf{B} \,,$$

$$\underline{\dot{d}}^T = \langle \, \dot{d}_1 \quad \dot{d}_2 \quad \dot{d}_3 \quad \dot{d}_4 \quad \dot{d}_5 \quad \dot{d}_6 \, \rangle$$

and $$\underline{\dot{p}}^T = \langle \, \dot{p}_1 \quad \dot{q}_1 \quad \dot{m}_1 \quad \dot{p}_2 \quad \dot{q}_2 \quad \dot{m}_2 \, \rangle \,.$$

In Eq.(3.27), $\mathbf{K}_t^l$ is the complete Updated Lagrangian local segment tangent stiffness matrix. The $\mathbf{G}_{rc}$ includes the segment elastic tangent stiffness and the geometric stiffness corresponding to the displacements relative to the chord.

Global Coordinates -

Let the inclination of the segment updated at each local iteration within the load step to the global coordinate frame be α, as shown in the Fig.3.7. Then, the transformation, $\mathbf{T}$, relating the local and global coordinate frames is

$$\mathbf{T} = \begin{bmatrix} a & b & 0 & 0 & 0 & 0 \\ -b & a & 0 & 0 & 0 & 0 \\ 0 & 0 & 1 & 0 & 0 & 0 \\ 0 & 0 & 0 & a & b & 0 \\ 0 & 0 & 0 & -b & a & 0 \\ 0 & 0 & 0 & 0 & 0 & 1 \end{bmatrix} \tag{3.28}$$

where

$$a = \cos\alpha$$

and $$b = \sin\alpha \,.$$

Thus, the incremental end-displacement vector, $\underline{\dot{u}}$, and the incremental end-force vector, $\underline{\dot{f}}$, in global coordinates are related to their respective local quantities as

$$\begin{aligned} \underline{\dot{d}} &= \mathbf{T} \, \underline{\dot{u}} \\ \text{and} \qquad \underline{\dot{f}} &= \mathbf{T}^T \, \underline{\dot{p}} \,. \end{aligned} \tag{3.29}$$

Thus, if $\mathbf{K}_t^s$ is the global segment tangent stiffness matrix, then Eq.(3.27) can be transformed into global coordinates using Eq.(3.29), as

$$\mathbf{K}_t^s \, \underline{\dot{u}} = \underline{\dot{f}} \tag{3.30}$$

where

$$\mathbf{K}_t^s = \mathbf{T}^T \mathbf{G}_{rc} \, \mathbf{T} + \mathbf{T}^T \mathbf{G}_c \, \mathbf{T} \, ,$$

$$\underline{\dot{u}}^T = \langle \, \dot{u}_1 \quad \dot{v}_1 \quad \dot{\theta}_1 \quad \dot{u}_2 \quad \dot{v}_2 \quad \dot{\theta}_2 \, \rangle$$

and $$\underline{\dot{f}}^T = \langle \, \dot{f}_1 \quad \dot{f}_2 \quad \dot{f}_3 \quad \dot{f}_4 \quad \dot{f}_5 \quad \dot{f}_6 \, \rangle \, .$$

The first component of $\mathbf{K}_t^s$ represents the elastic tangent stiffness and the geometric stiffness corresponding to the displacement relative to the chord, while its second component represents the geometric stiffness corresponding to the chord rotation.

3.3.3 Geometric Stiffness, Large Deformations and the Popularly Used Approximations

Geometric Stiffness is an important characteristic in the nonlinear frame analysis. It originates from the geometric nonlinearity in the frame. The geometric nonlinearity of a frame contains two aspects, namely stiffness effects of the equilibrium loads on the displaced geometry and nodal coordinate updating. For stocky members, the latter alone is sufficient to closely approximate their geometric stiffness. If the nodal coordinates are not updated, the formulation is equivalent to considering only small displacements.

The first part of geometric stiffness representing the tendency toward instability or stability of the member, depends not only on the condition of the loading but also on its deformed geometry. A tensile axial load causes the member to stabilise, while a compressive axial load causes instability in it. As the equilibrium shear force caused by the end-moments increases, the coupling between the axial and shear degrees of freedom of the member increases. The deformed geometry of the member consists of two parts, namely displacements relative to the chord and the chord rotation. Often, the term Geometric Stiffness is loosely used to represent only

one of these two constituents, instead of both. The relative chord displacements are assumed to be small while deriving the governing equations, Eq.(3.18).

The P-Δ effect is important in tall building frames. It represents the increased effects of overturning due to the gravity loads caused by the lateral deflections of the frame. The stiffness effects due to the applied loads can approximately account for the P-Δ effects as long as the lateral displacements of the frame are not large. For tall frames undergoing large sways, it is necessary to accurately account for the P-Δ effect by continuously updating the nodal coordinates during the analysis.

To specialise the Eq.(3.27) to the popularly used approximations, consider the Plastic Hinge Model beam-column segment described in the previous sections of this chapter. If the effect of bowing is neglected in Eq.(3.27), then

$$\mathbf{K}_t^l \, \underline{\dot{d}} = \underline{\dot{p}} \tag{3.31}$$

where

$$\mathbf{K}_t^l = \begin{bmatrix} \frac{EA}{L} & \frac{Q}{L} & 0 & -\frac{EA}{L} & -\frac{Q}{L} & 0 \\ & \frac{2EI(c_1+c_2)}{L^3}+\frac{P}{L} & -\frac{EI(c_1+c_2)}{L^2} & -\frac{Q}{L} & -\frac{2EI(c_1+c_2)}{L^3}-\frac{P}{L} & -\frac{EI(c_1+c_2)}{L^2} \\ & & \frac{EIc_1}{L} & 0 & \frac{EI(c_1+c_2)}{L^2} & \frac{EIc_2}{L} \\ & & & \frac{EA}{L} & \frac{Q}{L} & 0 \\ & \text{Sym.} & & & \frac{2EI(c_1+c_2)}{L^3}+\frac{P}{L} & \frac{EI(c_1+c_2)}{L^2} \\ & & & & & \frac{EIc_1}{L} \end{bmatrix},$$

$$\underline{d}^T = \langle\, d_1 \quad d_2 \quad d_3 \quad d_4 \quad d_5 \quad d_6 \,\rangle$$

$$\text{and} \qquad \underline{p}^T = \langle\, p_1 \quad q_1 \quad m_1 \quad p_2 \quad q_2 \quad m_2 \,\rangle \,.$$

If p is small, then c_1,c_2, can be approximated by

$$\begin{aligned} c_1 &\doteq 4 + \frac{2}{15}\pi^2 p \\ \text{and} \qquad c_2 &\doteq 2 - \frac{1}{30}\pi^2 p \,. \end{aligned} \tag{3.32}$$

Substituting Eq.(3.32) in Eq.(3.31) and neglecting the Q/L terms, $\mathbf{K}_t^l$ can be ap-

proximated by $\mathbf{K}_t^*$, given by

$$\mathbf{K}_t^* = \begin{bmatrix} \frac{EA}{L} & 0 & 0 & -\frac{EA}{L} & 0 & 0 \\ & \frac{12EI}{L^3}+\frac{P}{5L}+\frac{P}{L} & -\frac{6EI}{L^2}-\frac{P}{10} & 0 & -\frac{12EI}{L^3}-\frac{P}{5L}-\frac{P}{L} & -\frac{6EI}{L^2}-\frac{P}{10} \\ & & \frac{4EI}{L}+\frac{2PL}{15} & 0 & \frac{6EI}{L^2}+\frac{P}{10} & \frac{2EI}{L}-\frac{PL}{30} \\ & & & \frac{EA}{L} & 0 & 0 \\ & \text{Sym.} & & & \frac{12EI}{L^3}+\frac{P}{5L}+\frac{P}{L} & \frac{6EI}{L^2}+\frac{P}{10} \\ & & & & & \frac{4EI}{L}+\frac{2PL}{15} \end{bmatrix}$$
$$= \mathbf{K}_e^* + \mathbf{K}_g^* \tag{3.33}$$

where

$$\mathbf{K}_e^* = \begin{bmatrix} \frac{EA}{L} & 0 & 0 & -\frac{EA}{L} & 0 & 0 \\ & \frac{12EI}{L^3} & -\frac{6EI}{L^2} & 0 & -\frac{12EI}{L^3} & -\frac{6EI}{L^2} \\ & & \frac{4EI}{L} & 0 & \frac{6EI}{L^2} & \frac{2EI}{L} \\ & & & \frac{EA}{L} & 0 & 0 \\ & \text{Sym.} & & & \frac{12EI}{L^3} & \frac{6EI}{L^2} \\ & & & & & \frac{4EI}{L} \end{bmatrix}$$

and

$$\mathbf{K}_g^* = \begin{bmatrix} 0 & 0 & 0 & 0 & 0 & 0 \\ & \frac{6P}{5L} & -\frac{P}{10} & 0 & -\frac{6P}{5L} & -\frac{P}{10} \\ & & \frac{2PL}{15} & 0 & \frac{P}{10} & -\frac{PL}{30} \\ & & & 0 & 0 & 0 \\ & \text{Sym.} & & & \frac{6P}{5L} & \frac{P}{10} \\ & & & & & \frac{2PL}{15} \end{bmatrix}.$$

$\mathbf{K}_e^*$ is readily recognised as the local segment linear elastic stiffness matrix, and $\mathbf{K}_g^*$ is the local segment geometric stiffness matrix, popularly used by researchers [33], considering the effects of goemetric stiffness corresponding to effect of axial load alone on the chord rotation of the segment, the small axial load approximation of the stability functions and the absence of bowing.

In Eq.(3.33), $\mathbf{K}_t^*$ can also be obtained from $\mathbf{K}_t^l$ in Eq.(3.27), in the limit as the length of the segment becomes shorter. However, in practice, this approximation is often used for the entire beam-column element. But, it is only appropriate for the stockier beam-column members. If the members are not stocky, then subdivision of the member into smaller segments or inclusion of the neglected terms, or a combination of these two must be employed. While using $\mathbf{K}_t^*$ given by Eq.(3.33), some researchers [34,35] do not update the nodal coordinates, which could have an effect on the response. This effect is studied in Chapter 6.

3.3.4 Incremental Equilibrium Equation of a Beam-Column

While ascertaining the new state of a beam-column composed of multiple segments, given the incremental end-displacements on it and its current state, the tangent stiffness matrix of the complete beam-column is required. The degrees of freedom of a beam-column, both interior and exterior, are shown in Fig.3.9. The incremental equilibrium matrix equation of the whole beam-column is formed by assembling those of all its segments. Symbolically, if $\mathbf{K}_t$ is the complete global tangent stiffness matrix of the beam-column representing all its degrees of freedom, and $\mathbf{K}_t^s$ is the segment global tangent stiffness matrix from Eq.(3.30), then using the assembly operator $\sum$,

$$\mathbf{K}_t = \sum_{s=1}^{N_s} \{ \mathbf{K}_t^s \} \tag{3.34}$$

where N_s is the number of segments in the beam-column.

3.4 Inelastic Effects

Inelastic effects stem from the characteristic load-deformation relation, which simply reflects the material nonlinearity. Under inelastic conditions, the load-deformation relation is nonlinear or at least bi-linear. Also, the loading path cannot be retraced, once plastic deformations are accumulated during the loading process.

3.4.1 Origin of Inelastic Effects : *P-M* Interaction

Two origins for inelastic effects are considered, namely axial load and bending moment. Inelastic effects due to shear are not included. Given a member of specified dimensions and material, the yield axial load capacity, P_y, and the plastic moment capacity, M_p, are automatically defined. It is assumed that the tensile and compressive yield axial load capacities are equal in magnitude, and that the plastic moment capacities are same irrespective of the sense of rotation, positive or negative. When the yield axial load or the plastic moment capacities are reached, then any additional axial displacement or rotation, respectively, accrue as plastic

deformations. The strain-hardening in the material is neglected. The individual idealised load-deformation curves for these two forces are shown in Fig.3.10.

In reality, the axial load and the bending moments appear simultaneously with interaction between them. The actual strength interaction diagram obtained from test results for a typical hot-rolled W section normally adopted in building frames are shown in Fig.3.11 along with the idealised curve. For an axial load, P, at a cross-section in a member, the reduced plastic moment capacity, M_{pr}, is given by

$$M_{pr} = \begin{cases} M_p & \text{if } |P| \leq 0.15P_y \\ \frac{M_p}{0.85}\left\{1 - \frac{|P|}{P_y}\right\} & \text{if } |P| > 0.15P_y \end{cases} . \tag{3.35}$$

When the state of a member reaches the strength interaction surface, then one of three paths is possible - further increase in axial load with decrease in bending moment, further increase in bending moment with decrease in axial load, or neither axial load nor bending moment change.

In the first case, there is an increase in the plastic rotations at the ends of the member as it tends to straighten-up. The elastic rotations within the plastic hinges reduce to zero when the yield axial load, P_y, is reached, and the segment becomes perfectly straight. The axial displacement in the segment is equal to the yield axial displacement, $u_y = P_y L/EA$. If the axial displacement, u, exceeds u_y in magnitude, either in tension or in compression, then the axial displacement beyond the yield displacement, u_y, accumulates as axial plastic displacement, u_p, given by

$$u_p = \begin{cases} u - u_y & \text{if } P = +P_y \\ u + u_y & \text{if } P = -P_y \end{cases} . \tag{3.36}$$

In the second case, the elastic end-rotations within the plastic hinges increase. When the axial load reduces to zero, these elastic end-rotations reach a maximum value. On further application of end-rotations, the elastic end-rotations remain constant, but the additional end-rotations applied accrue as plastic end-rotations. Mathematically, if θ is the total applied end-rotation and ϕ is the elastic end-rotation within the plastic hinges, then the plastic end-rotation, κ, is

$$\kappa = \theta - \phi . \tag{3.37}$$

In the third case, any additional incremental axial displacements and incremental bending rotations accrue as plastic displacements and rotations, repectively.

3.4.2 Characteristic States of a Beam-Column Segment

Consider the beam-column segment shown in Fig.3.9b. Plastic hinges may be formed at its two ends. Further, these hinges could be positive or negative. For each segment, this leads to nine possible states, henceforth called the *characteristic states*, shown in Fig.3.12. Obviously, at the end of any load step, if the segment is not in axial yield, it must be in one of these nine states.

A closer look at these nine states reveals that, in effect, there are only three typical cases, namely no hinge case, one hinge case and two hinge case. The axial load equation of the segment, Eq.(3.14), in the non-dimensional form is

$$\frac{u}{L} = \frac{\pi^2}{(L/r)^2}\, p - b_1(\phi_1+\phi_2)^2 - b_2(\phi_1-\phi_2)^2\,, \tag{3.38}$$

where $r = \sqrt{I/A}$ is the radius of gyration in the plane of bending. The singularities in Eq.(3.38) corresponding to the critical buckling loads are evident from Fig.3.13. To obtain Fig.3.13, both ϕ_1 and ϕ_2 must be specified in the no hinge case, either ϕ_1 or ϕ_2 must be specified in the one hinge case, while neither ϕ_1 nor ϕ_2 need be specified in the two hinge case. In the one hinge and two hinge cases, for each axial load ordinate, the reduced plastic moment, calculated using Eq.(3.35), is applied at the appropriate end of the segment.

3.4.3 Cyclic Loading of Plastic Hinges

The beam-column model [10] discussed in Sec.3.1, does not incorporate the cyclic loading of inelastic effects, and is limited to static and monotonic loading only. The Plastic Hinge Model incorporates the case of transient loading by effectively utilising the two internal rotational degrees of freedom of the segment, corresponding to the two elastic end-rotations between the plastic hinges. This distinction between the total end-rotation, θ, and the elastic end-rotation, ϕ, is clarified in Fig.3.14.

Consider the segment with plastic hinges, if any, formed at its ends. The segment between these plastic hinges is deformed elastically. At an end, ϕ may be smaller than or equal to θ. If $\phi = \theta$, no plastic rotation accrues, but $\phi < \theta$, plastic rotation, κ, accumulates. Mathematically, within a load step, if $\dot{\theta}$ is the applied incremental end-rotation on the segment, and $\dot{\phi}$ is the increment in the elastic rotation within the plastic hinges, then the increment in κ, is

$$\dot{\kappa} = \dot{\theta} - \dot{\phi}\,. \tag{3.39}$$

This simple equation is used to check whether the plastic hinges in the segment are loading in a positive sense or in a negative sense.

As stated earlier, at any given instance, a segment lies in only one of the nine characteristic states discussed in Sec.3.4.3. To decide the state of the segment at the end of the load step, the nine characteristic states are ordered as noted in Fig.3.12. The elastic case appears first, followed by the one hinge states and then by the two hinge states. The axial load equation, Eq.(3.38), is solved assuming the final state of the segment to be one of these states starting from the first. A detailed account of the solution procedure is discussed in Sec.3.5.1. The end-moments, M_1,M_2, are computed using Eq.(3.7), and the incremental plastic rotations, $\dot{\kappa}$, within the load step at each end are computed using Eq.(3.39).

If computed plastic end-rotation increments and the end-moments are such that the basic criteria of the assumed final state listed in Table 3.1 are violated, then the next characteristic state in the order is tried. However, if for a state, the computed plastic end-rotation increments, if any, and the end-moments are in agreement with the corresponding criteria of the assumed final state, then that state is chosen as the final state of the segment at the end of the load step.

3.4.4 Segment Characteristic States in Multi-Segment Beam-Columns

A beam-column composed of multiple segments must be modelled carefully. Two segments neighbouring an interior node of the beam-column, may carry differ-

ent axial loads. Consequently, the reduced moment capacities of these two segments could be different. In effect, two plastic moment hinges, one for each segment may be formed at the interior node. Under such circumstances, during the Newton iterations for solving the interior nodal unknowns, one may encounter convergence difficulties with the residual moment quantity associated with that interior node.

To overcome such difficulties, it is ensured that only one plastic hinge is formed at each interior node. This is made possible by forcing one of the two segments at each interior node to remain elastic. Fig.3.15 shows one possible way of achieving this for beam-columns with two, three and four segments. Similar designs can be arrived at for beam-columns with five or more segments.

It may be noted here that a beam-column segment which must have one of its ends necessarily elastic, has only three characteristic states corresponding to the characteristic states 1, 2 and 3 of the regular beam-column segment discussed in Sec.3.4.2. And, obviously, a beam-column segment which must have both of its ends necessarily elastic, has only one characteristic state corresponding to the characteristic state 1 of the regular beam-column segment.

3.5 Numerical Implementation

Some of the salient features associated with the numerical implementation of the Plastic Hinge Model are discussed in this section.

3.5.1 Adjacent Point Method - Segment Level Iteration Scheme

A beam-column may be composed of a single segment or more. In either case, a basic computational tool is required to ascertain the updated segment equilibrium forces (P, M_1, M_2) due to specified incremental end-displacements $(\dot{u}, \dot{\phi}_1, \dot{\phi}_2)$ on its inital state. Owing to the implicit nature of the governing equations, the equilibrium forces can only be ascertained through an iterative procedure. This sub-section describes the iteration scheme used at the segment level.

Of the three governing equations listed in Eq.(3.18), the axial load equation must be solved first, because of the implicit dependence of b_1, b_2 on P itself via c_1, c_2. And, once P is known, M_1, M_2 are obtained by mere substitution. Thus, consider the axial load equation in the normalised form, Eq.(3.38), shown in Fig.3.13. Given the initial state of the segment and the incremental end-displacements, the immediate task reduces to obtaining the updated p.

Fig.3.13 concludes that for increasing tensile axial loads the slope of the (u/L)-p curve becomes asymptotic to a value of (P_e/EA). No difficulty may be experienced in solving the equation under tensile axial loads as the (u/L)-p curve is relatively flat. Under compressive axial loads the picture is completely different. The smallest critical load of a beam-column segment, magnitudewise, is $-P_e$, where P_e is the first Euler load of the segment, given by Eq.(3.10). The maximum possible compressive axial load in the segment is $-P_y$. Thus, the relative magnitudes of P_y and P_e are very important. If $P_y \leq P_e$, then, in the range from $-P_e$ up to P_y, the (u/L)-p curve has no singularities. Further, in the range $-1 \leq p \leq +4$, if the iterations to compute the axial load begin close to $p = -1$ and seek an axial load $p > -1$, the slope of the (u/L)-p curve is positive and monotonically reducing to P_e/EA. The characteristic (u/L)-p curve is of the softening type. Thus, it is proposed that the iterations to solve the axial load equation always be started at an axial load of $-0.99P_e$ or $-P_y$, whichever is smaller in magnitude.

In general, the characteristic curves corresponding to the initial and new states of the segment may or may not be different, as indicated in Fig.3.16. Softening systems are readily handled by the Newton-Raphson Iterative Scheme. It requires the tangent slope at each point along the solution path of Eq.(3.38), as indicated in Fig.3.17a, which is computationally intensive. Another possible scheme is the Secant Method, as shown in Fig.3.17b. This method requires an initial estimate of the tangent slope, which is not always convenient to produce. Thus, the *Adjacent Point Method* is proposed. Fig.3.17c shows the simple nature of this scheme.

As proposed, the iterations are begun at point A, corresponding to either $-0.99P_e$ or $-P_y$, whichever is smaller in magnitude. Another point B is picked Δp away, arbitrary but small, in the tensile direction from point A. Using Eq.(3.38), u/L is computed at point B. Now, the secant slope between points A and B is

$$k = \frac{(u/L)_B - (u/L)_A}{\Delta p} . \tag{3.40}$$

In the limit $\Delta p \rightarrow 0$, k represents the tangent slope at point A. Using this slope, as in the Newton-Raphson Method, a new approximation, point C, for the solution p is obtained. Again, point D is the *adjacent* point picked Δp away in the tensile direction from point C, and the secant slope between points C and D is estimated using Eq.(3.40). This slope is used to obtain the updated p. This procedure is continued until convergence is achieved at point N, the new state.

For stocky beam-columns or for beams with small or no axial load, the characteristic (u/L)-p curve is relatively linear with an asymptotic slope of (P_e/EA). Under these circumstances, the Modified Newton-Raphson Method may be used to further reduce the computational effort, by iterating with a constant initial slope. Sometimes, the asymptotic slope (P_e/EA) itself may prove to be adequate.

If for a beam-column member $P_y > P_e^m$, where P_e^m is the first Euler load of the member, then it may be modelled using at least two segments or more in order to make $P_y \leq P_e$ for each segment. The beam-column members of framed structures designed for seismic loads in accordance with Uniform Building Code 1988 [36] have been observed to have $P_y \ll P_e^m$. Thus, a single segment is adequate to model the complete beam-column, provided no hinges are formed between its ends.

3.5.2 Buckling

Slender beam-columns and braces, for which $P_e^m < P_y$, where P_e^m is the first Euler load of the member and P_y is its yield axial load, are prone to buckling under inelastic cycling. Buckling of frame members results in considerable degradation in its strength and stiffness. A significant redistribution of internal forces occurs,

which is not usually accounted for in conventional design.

The phenomenon of elastic buckling is only a mathematical abstraction. In practice, it is not possible to have a perfectly straight member with purely axial load acting on it. Two types of buckling occur in reality. The first is the case of elastic buckling followed by inelastic effects due to large displacements transverse to the chord. The initial geometric imperfections cause bending in the member under compressive axial load. On reaching the P-M strength interaction surface, a reduction in the axial load and an increase in the end-moments take place. The second type of buckling is initiated by the inelastic effects, like partial unsymmetric yielding of the cross-section caused by the residual stresses.

This model includes both the types of buckling. Under large compressive axial loads that appear on the member combined with any geometric imperfections or with applied flexural deformations, plastic moment hinges are formed due to the reduced plastic moment capacity. The reduced stiffness in the member due to these plastic hinges results in further flexural deformations. Thus, progressively large transverse deformations are accumulated in it owing to inelastic effects, as shown in Fig.3.18a. Under cyclic load history, these large deformations accumulated can be compensated for by possible yielding in tension. Fig.3.18b shows the P-u curve with the various stages of the buckling cycle. The corresponding inelastic path along the P-M strength interaction is traced in Fig.3.18c.

Some researchers [37] closely examined experimental hysteresis loops and developed phenomenological models. These models possess one local degree of freedom, the axial deformation. But, several input parameters are required to obtain an accurate result. The hysteresis loops are defined using a number of linear segments. Important phenomena, like deterioration of the buckling load, plastic increase in member length due to tensile deformations, formation of hinges within the member and local buckling, observed during the inelastic cycles, have been incorporated in some of the models. In trying to capture these nonlinear effects, these models be-

come computationally very tedious. They are based on simplified rules that only mimic observed behaviour and *not* on any theoretical considerations.

The Plastic Hinge Model overcomes these drawbacks associated with the phenomenological models. Potential members that may undergo buckling are modelled using two-segment elements. Buckling load deterioration, tensile plastic growth and the effect of hinges formed within the span of the member are routinely handled. However, the issue of local buckling remains unattended.

As seen in Fig.3.18b, the stiffness of the member changes during the course of the loading. Hence, in case of multi-segment beam-columns, the local iterations at the member level to compute the interior nodal unknowns, must be performed carefully. The softening and stiffening portions of the P-u curve result in slow convergence, if the Modified Newton-Raphson iterations are conducted using the initial elastic stiffness. The inclusion of the Geometric Stiffness in the iterating stiffness is very important. The Newton-Raphson Method using the member tangent stiffness, accounts for these stiffness changes, and eliminates convergence difficulties.

When a member prone to buckling enters the tensile yield region during the load cycling, it may completely compensate for the previous residual compressive deformation, if any, and become perfectly straight. At this stage, if pure axial compression is applied, it does not see any imperfection from a numerical stand point. Consequently, it reaches compressive yield instead of buckling, which may not be realistic. Thus, a numerical imperfection needs to be created in it. This is done by applying a small load transverse on it as shown in Fig.3.19. Any tendency in the member to undergo buckling, readily attracts this transverse load and results in flexural deformations which ultimately lead to inelastic buckling. A member in tension does not undergo buckling. Further, if the member is in tensile yield when such a load is applied, convergence problems will be encountered. Hence, this small transverse load is applied only when the member is under compression.

3.5.3 Member Level Iteration Scheme

In frame analysis, the most recurring computation is at the element level. At each global iteration within a load step, the incremental end-displacements, $\underline{\dot{u}}^m$, appearing on the member are known and the new member equilibrium end-force vector, $\underline{f}^m$, needs to be obtained, as discussed in Sec.2.5.5. For multi-segment beam-columns, the unknown displacements corresponding to the interior degrees of freedom are obtained first. Owing to the nonlinearities in the member constitutive relations, an iterative procedure is essential.

Newton-Raphson Method is used to conduct these iterations. During cyclic loading, the unloading stiffnesses could be significantly different from the loading stiffness, as depicted in Fig.3.20. At the start of a load step, it is not known whether loading will continue or unloading will take place. Hence, to avoid any convergence problems, first iteration is conducted using the member elastic stiffness, and the subsequent iterations using the member tangent stiffness.

The effect of the known incremental end-displacements, $\underline{\dot{u}}^m$, appears as specified forces on the interior nodes neighbouring the end nodes. Then, if $\underline{f}^{cm}$ represents the complete member residual force vector corresponding to all its degrees of freedom, both interior and exterior, and if $\mathbf{K}_t$ is the tangent stiffness matrix, given by Eq.(3.34), then the incremental equilibrium of the member can be written as

$$\mathbf{K}_t \ \underline{\dot{u}}^{cm} = -\underline{f}^{cm} , \tag{3.41}$$

where $\underline{\dot{u}}^{cm}$ is the complete member incremental displacement vector. Eq.(3.41) is solved by the Gauss Elimination Procedure.

Using the complete member incremental displacement vector, $\underline{\dot{u}}^{cm}$, the global incremental end-displacements, $\underline{\dot{u}}$, appearing on each segment are obtained using the assembly array of the segments. Then, using Eq.(3.29), the local incremental end-displacement vector, $\underline{\dot{d}}$, is computed. Again, using Eq.(3.22), the member incremental end-displacement vector, $\underline{\dot{a}}$, is computed.

Now, the segment axial load is computed according to the procedure described in Sec.3.5.1. Knowing the axial load, P, the end-moments, M_1,M_2, are computed from Eq.(3.7). Thus, the end-force vector of the segment in member coordinates, $\underline{s}$, is known. Using the strain-deformation matrix, $\mathbf{B}$, given by Eq.(3.22), the segment local end-force vector, $\underline{p}$, is computed by

$$\underline{p} = \mathbf{B}^T \, \underline{s} \, . \tag{3.42}$$

Again, using the coordinate tranformation matrix, $\mathbf{T}$, given by Eq.(3.28), the segment global end-force vector, $\underline{f}$, is computed by

$$\underline{f} = \mathbf{T}^T \, \underline{p} \, . \tag{3.43}$$

The assembly of these global end-force vector, $\underline{f}$, of each segment using the assembly array, results in the updated complete member residual force vector, $\underline{f}^{cm}$. The above procedure is iterated until this residual force vector quantities associated with the interior nodes reduce to within the tolerances. Once convergence is achieved, the new member equilibrium end-force vector, $\underline{f}^m$, is formed using the global end-force vectors of the two end segments.

3.5.4 External Transverse Loads on Beam-Columns

If external concentrated loads are applied transversely within the span of the beam-columns instead of at its ends and plastic hinges occur at these locations, then such members must be composed of multiple segments. At least, as many interior nodes as the external loads on the member, should be chosen. Further, the locations of these nodes is so chosen as to coincide with those of the external loads themselves. This allows the concentrated load to be directly included in the nodal force vector while conducting the iterations at the element level.

If no plastic hinges form at the locations within the span of the beam-column, where the external transverse concentrated loads are applied, then the corresponding fixed-end forces of such transverse loads may be applied at the end of the

members. The rest of the analysis does not differ from before. Similar approach can be employed to approximately include distributed loads applied transversely on the beam-column. But, for an accurate solution, a new set of Stability Functions and Bowing Functions corresponding to the distributed loads, need to be derived.

3.5.5 Artificial Unloading during Member Iterations

The possibility of artificial unloading during inelastic global iterations was discussed in Sec.2.5.6. Artificial unloading can also occur during local iterations at the member level. In the process of updating the global $\underline{p}^{k+1}(t+\Delta t)$ vector at the end of each global iteration, the interior nodal unknowns of each beam-column need to be iteratively solved. Under inelastic conditions, the unloading stiffness is different from the loading stiffness, and *artificial unloading* may be caused by the numerical scheme, as shown in Fig.2.4. As a remedial measure, the cumulative of the displacement sub-increments from all the local iterations is applied to the member state at the start of the load step, as discussed in Sec.2.5.6.

3.6 Numerical Results

Validating the analytical model using a variety of numerical examples forms a very important part of its development. Three special problems are discussed in this section to evaluate the above model. Each of these problems is designed to elicit an important feature of the proposed model.

3.6.1 Control on Tolerances

The tolerance on local and segment iterations discussed in Sec.2.8 are adopted in the numerical examples discussed below.

3.6.2 Single Member Examples

The three different problems, wherein single beam-columns composed of multi-

ple segments are subjected to displacement-controlled loadings, are described below.

Buckling Problem

In the past, a considerable amount of experimental research was dedicated solely to study the inelastic cyclic behaviour of axially loaded members. One such study is chosen [38] to demonstrate the effectiveness of this model. A solid rectangular steel bar of cross-section 25.4 mm × 12.7 mm and of length 860 mm, *i.e.*, $kl/r = 120$, is rigidly fixed at its ends against rotational and lateral translational deformations. The Plastic Hinge Model uses two segments. A concentrated lateral load of 2 N is applied at mid-span to create an imperfection in the member.

Under the displacement-controlled axial loading history prescribed, the P-u curve for the member as obtained from experiments and as predicted by the Plastic Hinge Model are shown in Fig.3.21. The general features are very well captured in the overall sense. The smaller buckling load as seen in the experiments may be attributed to the possible initial imperfections in the geometry of the bar resulting in an eccentric loading. On the tensile side, the smooth transition from the elastic reversal regime to the inelastic reversal regime, and from the inelastic reversal regime to the tensile yield regime is not captured by the Plastic Hinge Model, since partial plastification of the cross-section is beyond its scope.

Snap-Through Problem

In the elastic behaviour of slender beam-columns, there is an important phenomenon called the *Snap-through*. This phenomenon occurs when an infinitesimal perturbation in the member end-displacements produces a finite change in the member end equilibrium forces. Consider the hot-rolled steel section W14 × 132 [39] of length 50000 mm, with $P_e/P_y = 0.08$ and fixed at its ends. The Plastic Hinge Model uses two segments. Since the deformations applied are within elastic range and since the governing equations are exact for an elastic segment, more than two segments are not required.

The three stage loading history prescribed is : equal rotational deformations

at its ends causing single curvature in the member, followed by a pure axial compressive displacement, and finally equal rotations of opposite nature to the ones prescribed in the first stage. Fig.3.22 shows the variation in the axial load, P, and in the member end-moment, M_1, with the member end-rotation, θ, for different amounts of axial compressive displacement applied in the second stage. The M-θ and P-θ curves show a marked change as the magnitude of the axial compressive displacement increases. The snap-through situation is evident particularly when the axial compressive displacement is close to or exceeds $4u_e$, where u_e is the axial displacement, which when applied in the member results in an axial load of P_e, the first Euler Load of the member.

The case where $u = -5u_e$ throws light on an additional aspect, the elastic post-buckling large deformational strength. The theoretical prediction for the maximum elastic compressive load in a fixed-ended slender beam-column, as obtained from the elastic governing equations, is $-4P_e$. Hence, while using the Plastic Hinge Model, one would expect a maximum compressive axial load of $4P_e$. However, Fig.3.22 indicates a higher load than this, magnitudewise. Since the snap-through problem is an elastic one, the governing (u/L)-p curve does not have a singularity at $p = -1$, as shown in Fig.3.13a. Further, the curve is rather flat up to $p = -3$. Hence, even for the case of a member with two segments, one can notice an increase in the magnitude of the axial load up to about $-4.52P_e$, *i.e.,* up to about $-1.13P_e^s$, where P_e^s is the first Euler Load of the segment.

Lateral Translation Problem

The problem of the cyclic lateral translation of a column member in a building frame under dynamic lateral load conditions is of utmost importance owing to its frequent occurrence in reality. Consider a beam-column made of the hot-rolled steel section W14 × 132 [39] of length 5000 *mm* fixed at its ends against rotation. The displacement time history considered is a pure axial displacement followed by cyclic lateral translations. Figs.3.23, 3.24 and 3.25 show the effect of axial displacements

on the response of the beam-column.

The model successfully captures the softening of the member at tensile axial yield load. Further, the uniform cyclic lateral translations result in a uniform variation in the member axial load, irrespective of the sense and magnitude of the axial deformation in the beam-column. With reference to the bilinear P-M interaction diagram, as the member approaches the yield corners, both in tension and in compression, the relative chord rotational deformations reduce. In the limit, when the corner is reached, the member is perfectly straight. This agrees with the physical intuition for lumped plasticity models without strain-hardening that a member cannot have any relative chord rotations at its ends while carrying the yield axial load. It is important to recognize here that the Plastic Hinge Model does not consider partial elastic unloading and strain-hardening.

...

Chapter 4

THE FIBRE MODEL

4.1 Introduction

The Plastic Hinge Model described in Chapter 3 has limitations in accurately describing the true nonlinear behaviour of a beam-column. Firstly, the strain hardening property of the material is not incorporated. Strain-hardening causes more spatial spread of plasticity along the length and cross-section of the member causing an increase in its strength. Secondly, the axial and flexural stiffnesses are elastic. The model does not account for possible inelastic effects that may be developed during the course of the loading. The partial yielding and the elastic unloading of the yielded portions of the member cross-sections change its axial and flexural stiffnesses. Thirdly, the moment-curvature relationship is not accurately represented. The complex stress distribution within the member cross-section, that may be generated through partial elastic unloading during arbitrary cyclic loading, is not reflected. Finally, the Plastic Hinge Model does not include the effect of the realistic residual stresses present in the hot-rolled structural steel sections.

Thus, a need arises [8,11,31] for a *Distributed Plasticity Model*, which is detailed enough to encompass the above inelastic effects. Since plastic behaviour is dependent on the loading path, the desired model must be capable of handling cyclic behaviour. The model must be general enough to be applicable for arbitrary material constitutive law and also to capture the geometric effects. The *Fibre Model* is developed based on the Finite Element Approach to estimate the above effects more realistically than the Plastic Hinge Model.

4.2 Model Description

In the Fibre Model, a beam-column is discretised into segments along the length, and further, each segment is sub-divided into fibres within the cross-section, as shown in Fig.4.1. Thus, the beam-column is physically replaced by an assembly of smaller discrete elements, *the fibres.*

The idea of discretising a beam-column into a number of fibres was introduced as early as in 1970 [8]. Soon, a general procedure for obtaining the tangent stiffness matrix of a segment composed of fibres was presented [11]. However, till today, the models based on this approach use approximate load-deformation relations for each fibre, *e.g.,* elastic-perfectly plastic relations and later bilinear relations with strain-hardening. Further, these models are restricted to monotonic loading only. Being computationally intensive, these models are popular only with researchers.

In the proposed model, each fibre is capable of withstanding axial load applied normal to its cross-section. The axial strain and axial stress in each fibre are computed as the average values at its centroid. A uniaxial cyclic contitutive law is used to control the hysteretic loading of the fibres. It is assumed that the fibres do not buckle under compression. Thus, the Fibre Model does not incorporate local buckling in the member, though it includes the overall buckling of the member. The behaviour of each fibre is modelled independently by a one-dimensional load-deformation relation. The flexural load-deformation relation of the segment is obtained by combining the axial load-deformation relationships of the fibres in it. All the fibres at the cross-section of a segment carry the shear force elastically, without any strength interaction with the bending moment and axial force.

The Fibre Model follows the steps noted below to arrive at the solution for the new state of the member :

(1) Discretize the beam-column into segments, and further, the segments into fibres. Identify the nodal unknowns corresponding to the two translations and a rotation at each node, either interior or exterior.

(2) Evaluate segment tangent stiffness matrices. Assemble the member tangent stiffness matrix and the member residual force vector.

(3) Introduce boundary conditions, *i.e.,* the specified member-end displacements as concentrated nodal forces on the interior nodes adjacent to end nodes. Solve incremental equilibrium equations for incremental interior nodal unknowns. Calculate strain and stress in each fibre. Update member residual force vector.

(4) Check for convergence. If not achieved, repeat from step 2.

The Fibre Model is general enough to incorporate irregularities in material, geometry and loading. Material nonlinearity and cyclic loading are included through the uniaxial cyclic material constitutive law for the axial stress-strain behaviour of fibres. The irregularities in member geometry, *e.g.,* the partially prismatic nature of stepped columns, is incorporated through the properties of the segment.

4.3 Special Features

There are two notable features of the Fibre Model, namely the uniaxial cyclic constitutive law of steel and the residual stresses in the hot-rolled sections.

4.3.1 Uniaxial Cyclic Constitutive Law for Axial Stress-Strain Behaviour of Structural Steel

Each fibre is essentially a one-dimensional member, with its entire area concentrated at its centroid. Its load-deformation relationship can be derived using the material constitutive law. For the cyclic response of *steel* beam-columns, a uniaxial cyclic constitutive law for the axial stress-strain behaviour of steel is required. In the literature, many analytical hysteretic load-deformation models are proposed to describe general hysteretic behaviour of structures. Though some of them are in conformity with the Extended Masing's Hypothesis [40] relevant for metals, they are inadequate to model structural steel, as they do not include the predominant yield plateau present in its monotonic stress-strain curve.

Experimental data collected from load tests on steel bars may be studied to propose the uniaxial cyclic constitutive law. In the past, a number of attempts were made to propose the cyclic constitutive law for structural steel [41,42,43,44]. These models are based either on curve fitting techniques or on phenomenological plasticity theory. The applicability of either kinematic hardening or isotropic hardening is yet to be established [45] in the models based on plasticity theory. However, a bias toward isotropic hardening is evident in the experimental data [46]. Also, most of these models result in hysteresis loops that approach the ultimate load asymptotically, which is contrary to reality. Steel has an ultimate strain and a rupture strain, which is not reflected in most of the available models. In addition to being computationally very intensive, they are burdened by the numerous loading-regime-dependent cumbersome hysteretic rules.

Proposed Model -

After carefully reviewing the merits and the drawbacks of the existing models, a simple model, namely *Cubic Ellipsoidal Model*, is proposed for the uniaxial cyclic constitutive law of structural steel. This physically motivated model significantly simplifies the numerical implementation under arbitrary transient loading.

The monotonic stress-strain curves, or the *virgin curves*, obtained from uniaxial tests on structural steel bars, are characterised by eight distinct properties shown in Fig.4.2. They are, namely, Yield Stress σ_y, Ultimate Stress σ_u, Yield Strain ε_y, Strain Hardening Strain ε_{sh}, Ultimate Strain ε_u, Rupture Strain ε_r, Elastic Modulus E and Modulus at Strain Hardening Strain E_{sh}. The proposed analytical model *explicitly* defines the virgin curve beyond strain-hardening strain by a *cubic ellipse*, shown in Fig.4.3 and given by

$$\begin{aligned} -\frac{(\varepsilon-\varepsilon_0)^3}{a^3}+\frac{(\sigma-\sigma_0)^3}{b^3}&=1 \qquad \text{in tension} \\ \text{and} \qquad \frac{(\varepsilon-\varepsilon_0)^3}{a^3}-\frac{(\sigma-\sigma_0)^3}{b^3}&=1 \qquad \text{in compression,} \end{aligned} \tag{4.1}$$

where ε_0 and σ_0 are the strain and stress, respectively, at the centre of the cubic ellipse, whose semi-major and semi-minor axes are a and b, respectively. ε_0, σ_0, a

and b are obtained using the eight material properties noted above. Further, the hysteresis loops, or the *branch curves*, are also defined by cubic ellipses given by Eq.(4.1), as shown in Fig.4.4. The quantities ε_0, σ_0, a and b for the branch curves are determined by the hysteretic rules.

Structural steel is assumed to strain-harden isotropically resulting in symmmetric hysteresis loops about the strain axis, *i.e.*, $\sigma = 0$ axis, under equal cyclic plastic excursions, which is in agreement with the experimental data [47]. The hysteresis loops are bounded by envelopes, henceforth referred to as the *backbone curves*. These backbone curves, in tension and in compression, are simply the tensile and compressive virgin curves, respectively, translated along the strain axis, as shown in Fig.4.5. The amount of strain translation is determined by the plastic strain history. This process, known as *Envelope Strain Shift* [42], ensures that the hysteresis loops do not intersect [47] under gradual increase in the cyclic plastic excursions, at least, until the ultimate load is reached.

The analytical representation of the strain-hardening part of the virgin curve given by Eq.(4.1) closely agrees with the experimental data [41] obtained from a uniaxial test on a steel bar, as shown in Fig.4.6. Using the backbone curve properties, the experimental hysteresis loops [41] of another bar with the same properties are shown in Fig.4.7 along with the model prediction. In an independant experiment [45], the cyclic hysteresis loops of a bar, whose properties were determined by a monotonic test, are shown in Fig.4.8 along with the model prediction. The general features are well captured.

Extended Masing's Hypothesis -

Masing's Hypothesis, originally proposed for steady-state response [48] between two fixed limits, was recently extended to arbitrary transient response [40]. This Extended Masing's Hypothesis stipulates two rules for hysteretic loops :

Rule 1 : Incomplete Loops

The equation of any hysteretic response curve, irrespective of the steady-state

or transient response, can be obtained simply by applying the original Masing's rule to the virgin loading curve using the latest point of reversal.

Rule 2 : Completed Loops

The ultimate fate of an interior curve under continued loading or unloading can be determined as follows : Once an interior curve meets a curve from the previous load cycle, the load-deformation curve then follows that of the previous cycle.

These rules are intended for smooth virgin curves with C^1 continuity. But, the virgin curve of structural steel possesses only C^0 continuity, due to a linear regime, a yield plateau and a nonlinear strain-hardening regime. Thus, the application of these rules to the material at hand is not direct.

Rule 1 is based on the original Masing's rule, which simply suggests a functional similarity between the virgin curve and the branch curves. The proposed model does incorporate this functional similarity in a slightly modified form, which is evident from the hysteretic rules described below. Rule 2 requires that the information regarding the points of reversal, called as *turning points*, be systematically handled and updated while deciding the fate of nested loops. The characteristics of the Extended Masing's Hypothesis are demonstrated through the arbitrary but general stress-strain history shown in Fig.4.9.

Hysteretic Rules -

The proposed model employs the following rules as guidelines to define the transient response of structural steel :

(1) The virgin curves in tension and in compression are identical.

(2) A sharp yield transition exists between the elastic regime and the yield regime only at the time of initial yielding, when the response is linearly elastic until the yield stress is reached, either in tension or in compression.

(3) New plastic strains are accumulated *only* by progressing along the virgin curve,

and *not* by traversing the branch curves.

(4) Under strain reversals, the branch curve originating from the virgin curve is linearly elastic until zero stress is reached, and is nonlinear thereafter. This branch curve is referred as the *first branch curve.*

(5) The destination of the first branch curve leaving a positive virgin curve is a symmetric stress point on the translated negative backbone curve. Similarly, the destination of the first branch curve leaving a negative virgin curve is a symmetric stress point on the translated positive backbone curve.

(6) All the subsequent branch curves originating from the first branch curve have the same amount of linear elastic unloading as the first branch curve. Further, the cubic ellipses describing the nonlinear portions of all these nested branch curves have the same radii, until either the destination point is reached or all the nested branch loops are closed, thus returning to the first turning point.

(7) The slope at which a branch curve approaches its destination is the slope of the *Equivalent Convex Virgin Curve* at the same strain at the turning point from which it departed. The equivalent convex virgin curve of structural steel is shown in Fig.4.10.

(8) The branch curve originating from the receding part of the virgin curve beyond the ultimate strain approaches its destination backbone curve at zero slope, instead of the negative slope at the turning point along the receding part of the virgin curve, as stated in Rule 7.

(9) When unloading takes place very early in the yield regime, the formation of a cubic ellipse for the nonlinear part of the hysteresis loop within the above constraints, may not be possible. In such a case, the linear elastic unloading is continued beyond zero stress till the formation of a cubic ellipse is possible.

Merits of the Proposed Model -

The proposed Cubic Ellipsoidal Uniaxial Cyclic Constitutive Law for Struc-

tural Steel is significantly superior to the currently used models. This physically motivated model is based on real uniaxial test data on structural steel bars. It provides smooth and *explicit* expressions for stress in terms of strain, unlike most of the currently used models which require iterations to arrive at the same result. The availability of explicit expressions for stress, and hence for the instantaneous stiffness, is very convenient for inclusion in displacement based Finite element models.

The absence of numerous cumbersome loading-regime-dependent rules makes the model simple and computationally efficient, yet descriptive enough to adequately represent the features of real hysteretic behaviour. The proposed model does not incorporate stiffness degradation. However, this feature can be incorporated very easily, if required. With the wide range of hysteretic behaviour included, this model is an excellent choice for the analytical modelling of structural steel.

4.3.2 Residual Stresses and Discretisation of Cross-section

All the standard hot-rolled steel sections exhibit a non-zero initial state of stress locked in them during the manufacturing process. These stresses, known as the *residual stresses*, have an effect on the tangent stiffness and the yield load of members. They can decrease the ultimate load of biaxially loaded members by as much as 20% in the range of intermediate slenderness ratio [33]. Hence, these stresses must be included in the analysis of structures formed with such sections.

The actual stress distribution of the residual stresses used in this study is given in Fig.4.11 along with the idealised summary. The idealisation of the residual stresses assumes that the tensile and compressive parts in the flanges and the web are equal in area. This idealised residual stress pattern suggests a very convenient discretisation of the cross-section into fibres. In the flanges, the tensile and compressive parts are modelled by one fibre each. The entire web is discretised into eight equal parts. Hence, by discretising the cross-section into 12 fibres, as shown in Fig.4.11, the residual stresses can be included in the analysis without any pro-

gramming difficulty. In fact, different number of fibres were tried, and the above discretisation with 12 fibres provided adequate accuracy.

The Fibre Model has the capability to include the residual stresses in the hot-rolled steel sections. This is achieved by assigning the fibre stresses at the start of the analysis to be equal to the residual stresses. The fibre strains are set to be zero at the same time. While doing so, it is ensured that the virgin stress-strain curve is given a strain shift by an amount corresponding to the elastic strain that would produce the assigned residual stress. Though available, this feature is not utilised in the numerical studies discussed in Chapter 7.

4.4 Equilibrium Equation

The *Principle of Virtual Work* is used to derive the incremental equilibrium equations valid for both elastic and plastic responses. Incremental relations between generalised stress and generalised strain are derived for each fibre, as shown in Fig.4.12. Such relations of all the fibres at a cross-section are combined to form the incremental equilibrium equation for a segment. Finally, the incremental equilibrium equation of the entire beam-column element is obtained by assembling those of all the segments in it. The assumption of *large-displacements and small-strains* and the Euler-Bernoulli kinematic assumption, that *plane sections normal to the centroidal axis before bending, remain plane and normal to it even after bending*, are made. The Updated Lagrangian approach is used. Let the cross-section of each segment be discretised into N_f fibres.

4.4.1 Incremental Equilibrium Equation of a Fibre

Each fibre is essentially a beam-column member without any flexural capability. Thus, eliminating the rotational degree of freedom, only the in-plane translational degrees of freedom remain at each end of the fibre, as shown in Fig.4.12. Hence, the fibre incremental matrix equilibrium equation is of order four.

The incremental equilibrium equation of the Plastic Hinge Model beam-column segment decribed in Chapter 3 are specialised for a fibre by dropping the moment equations. While doing so, it is meaningful to replace the Elastic Modulus, E, of the material by its Tangent Modulus, E_t. Hence, the incremental equilibrium equation, Eq.(3.30), of the beam-column segment in global coordinates, is reduced to form the incremental equilibrium equation of a fibre in global coordinates, as

$$ {}^{f}\mathbf{K}_t \, \underline{\dot{g}} = \underline{\dot{h}} \tag{4.2} $$

where

$$ {}^{f}\mathbf{K}_t = {}^{f}\mathbf{K}_t^{TS} + {}^{f}\mathbf{K}_t^{GS}, $$

$$ {}^{f}\mathbf{K}_t^{TS} = \frac{E_t A}{L} \begin{bmatrix} a^2 & ab & -a^2 & -ab \\ & b^2 & -ab & -b^2 \\ & & a^2 & ab \\ \text{Sym.} & & & b^2 \end{bmatrix}, $$

$$ {}^{f}\mathbf{K}_t^{GS} = \frac{P}{L} \begin{bmatrix} (1-a^2) & -ab & -(1-a^2) & ab \\ & (1-b^2) & ab & -(1-b^2) \\ & & (1-a^2) & -ab \\ \text{Sym.} & & & (1-b^2) \end{bmatrix}, $$

$$ \underline{\dot{g}}^T = \langle \, \dot{g}_1 \quad \dot{g}_2 \quad \dot{g}_3 \quad \dot{g}_4 \, \rangle $$

and $$ \underline{\dot{h}}^T = \langle \, \dot{h}_1 \quad \dot{h}_2 \quad \dot{h}_3 \quad \dot{h}_4 \, \rangle . $$

In Eq.(4.2), ${}^{f}\mathbf{K}_t$ is the tangent stiffness matrix, $\underline{\dot{g}}$ is the incremental end- displacement vector and $\underline{\dot{h}}$ is the incremental end-force vector of the fibre. ${}^{f}\mathbf{K}_t^{TS}$ and ${}^{f}\mathbf{K}_t^{GS}$ are its truss stiffness matrix and geometric stiffness matrix, respectively.

4.4.2 Incremental Equilibrium Equation of a Segment

The segment incremental equilibrium equation is obtained by assembling those of the constituent fibres, derived in Sec.4.4.1. The segment equilibrium so obtained does not possess any stiffness under a pure lateral translation. Hence, shear stiffness is added to the segment.

Incremental Equation without Shear Stiffness -

The end-displacement and end-force quantities of a fibre are shown in Fig.4.12a, and those of a segment are shown in Fig.4.12b. The translations indicated at the

end of the fibre correspond to the translations at its centroidal axis. If h is the distance of the fibre centroid from the centroidal axis of the cross-section, then the incremental fibre end-displacement vector, $\underline{\dot{g}}$, and the incremental segment end-displacement vector, $\underline{\dot{u}}$, are related through fibre transformation matrices, $\mathbf{R}$, as

$$\begin{Bmatrix} \vdots \\ \underline{\dot{g}} \\ \vdots \end{Bmatrix} = \begin{bmatrix} \vdots \\ \mathbf{R} \\ \vdots \end{bmatrix} \underline{\dot{u}}, \tag{4.3}$$

where

$$\mathbf{R} = \begin{bmatrix} 1 & 0 & h\cos\alpha & 0 & 0 & 0 \\ 0 & 1 & h\sin\alpha & 0 & 0 & 0 \\ 0 & 0 & 0 & 1 & 0 & h\cos\alpha \\ 0 & 0 & 0 & 0 & 1 & h\sin\alpha \end{bmatrix},$$

$$\underline{\dot{g}}^T = \langle\, \dot{g}_1 \quad \dot{g}_2 \quad \dot{g}_3 \quad \dot{g}_4 \,\rangle$$

and $$\underline{\dot{u}}^T = \langle\, \dot{u}_1 \quad \dot{v}_1 \quad \dot{\theta}_1 \quad \dot{u}_2 \quad \dot{v}_2 \quad \dot{\theta}_2 \,\rangle .$$

Further, the fibre incremental end-force vector, $\underline{\dot{h}}$, and the segment incremental end-force vector, $\underline{\dot{f}}$, are related through the same transformation matrices, $\mathbf{R}$, as

$$\underline{\dot{f}} = [\ldots \quad \mathbf{R}^T \quad \ldots] \begin{Bmatrix} \vdots \\ \underline{\dot{h}} \\ \vdots \end{Bmatrix}. \tag{4.4}$$

where

$$\underline{\dot{h}}^T = \langle\, \dot{h}_1 \quad \dot{h}_2 \quad \dot{h}_3 \quad \dot{h}_4 \,\rangle$$

and $$\underline{\dot{f}}^T = \langle\, \dot{f}_1 \quad \dot{f}_2 \quad \dot{f}_3 \quad \dot{f}_4 \quad \dot{f}_5 \quad \dot{f}_6 \,\rangle .$$

Append the incremental equations of all fibres together to form

$$\begin{bmatrix} \ddots & \underline{0} & \underline{0} \\ \underline{0} & {}^{f}\mathbf{K}_t & \underline{0} \\ \underline{0} & \underline{0} & \ddots \end{bmatrix} \begin{Bmatrix} \vdots \\ \underline{\dot{g}} \\ \vdots \end{Bmatrix} = \begin{Bmatrix} \vdots \\ \underline{\dot{h}} \\ \vdots \end{Bmatrix}. \tag{4.5}$$

Combine Eqs.(4.3), (4.4) and (4.5) to form the segment incremental equilibrium equations in the global coordinate frame. If $\underline{\dot{u}}$ is the segment incremental global end-displacement vector, $\underline{\dot{f}}$ is the segment incremental global end-force vector and ${}^{ab}\mathbf{K}_t$ is the tangent stiffness matrix corresponding to axial and bending effects, then

$${}^{ab}\mathbf{K}_t\ \underline{\dot{u}} = \underline{\dot{f}} \tag{4.6}$$

where

$$ {}^{ab}\mathbf{K}_t = \sum_{1}^{N_f} \mathbf{R}^T \, {}^{f}\mathbf{K}_t \, \mathbf{R} = \sum_{1}^{N_f} \begin{bmatrix} \Lambda & -\Lambda \\ -\Lambda & \Lambda \end{bmatrix} , $$

$$ \Lambda = \frac{E_t A}{L} \begin{bmatrix} a^2 & ab & ah \\ ab & b^2 & bh \\ ah & bh & h^2 \end{bmatrix} + \frac{P}{L} \begin{bmatrix} (1-a^2) & -ab & 0 \\ -ab & (1-b^2) & 0 \\ 0 & 0 & 0 \end{bmatrix} , $$

$$ a = \cos\alpha \, , $$

$$ b = \sin\alpha \, , $$

$$ \underline{\dot{u}}^T = \langle \, \dot{u}_1 \quad \dot{v}_1 \quad \dot{\theta}_1 \quad \dot{u}_2 \quad \dot{v}_2 \quad \dot{\theta}_2 \, \rangle $$

and $$ \underline{\dot{f}}^T = \langle \, \dot{f}_1 \quad \dot{f}_2 \quad \dot{f}_3 \quad \dot{f}_4 \quad \dot{f}_5 \quad \dot{f}_6 \, \rangle . $$

Incremental Equation for Shear Stiffness -

A pure lateral translation of the segment has no shear stiffness to oppose it. Hence, the shear deformation properties of the segment are included seperately. The Fibre Model does not consider the interaction of shear force with either axial force or bending moment, *i.e.*, the shear deformation behaviour is considered elastic. The incremental equilibrium equations associated with shear deformations are derived and appended with Eq.(4.6) to form the complete incremental equilibrium equations of the segment. The Euler-Bernoulli kinematic assumption is partially relaxed in the Fibre Model. Thus, *plane sections normal to the centroidal axis before bending remain plane after bending though not normal to it.*

Let the lateral translation and rotational degrees of freedom of the segment in the local coordinates be w and θ, respectively, and let z represent the axial coordinate in the local frame of reference, as shown in Fig.4.13. Let G be the Bulk or Shear Modulus of Elasticity of steel, and A_* be the segment cross-sectional area effective in resisting shear. Then, the shear strain due to shear deformation is $(\partial w/\partial z - \theta)$, where $\partial w/\partial z$ is the rotation of the current normal to the centroidal axis and θ is the rotation of the original normal. Therefore, the incremental equilibrium shear, $\dot{Q}$, at any cross-section of the segment is

$$ GA_* \left(\frac{\partial \dot{w}}{\partial z} - \dot{\theta} \right) = \dot{Q} \, . \tag{4.7} $$

Consider the domain $\mathcal{V}$ and it's boundary $\partial\mathcal{V}$ of the segment. Let $\underline{\dot{p}}$ be the incremental end-force vector. Then, the virtual work done by the incremental virtual end-displacements, $\underline{\hat{\dot{d}}}$, on the segment is

$$\int_{\mathcal{V}} \left(\frac{\partial \hat{\dot{w}}}{\partial z} - \hat{\dot{\theta}} \right) \dot{Q} \; d\mathcal{V} = \int_{\partial\mathcal{V}} \underline{\hat{\dot{d}}}^T \; \underline{\dot{p}} \; d(\partial\mathcal{V}) \,. \tag{4.8}$$

Impose the finite element approximation of the segment using a single straight two-noded element as shown in Fig.4.13. Then, substituting Eq.(4.7) in Eq.(4.8),

$$\int_{-L/2}^{+L/2} \left(\frac{\partial \hat{\dot{w}}}{\partial z} - \hat{\dot{\theta}} \right) GA_* \left(\frac{\partial \dot{w}}{\partial z} - \dot{\theta} \right) \; dz = \underline{\hat{\dot{d}}}^T \; \underline{\dot{p}} \tag{4.9}$$

where

$$\underline{\dot{d}}^T = \langle \, \dot{d}_1 \quad \dot{d}_2 \quad \dot{d}_3 \quad \dot{d}_4 \quad \dot{d}_5 \quad \dot{d}_6 \, \rangle$$

and $$\underline{\dot{p}}^T = \langle \, \dot{p}_1 \quad \dot{q}_1 \quad \dot{m}_1 \quad \dot{p}_2 \quad \dot{q}_2 \quad \dot{m}_2 \, \rangle \,.$$

Customarily, $\dot{w}$ and $\dot{\theta}$ are expressed in terms of shape functions as

$$\begin{Bmatrix} \dot{w} \\ \dot{\theta} \end{Bmatrix} = \begin{bmatrix} 0 & {}^{w}N_1 & 0 & 0 & {}^{w}N_2 & 0 \\ 0 & 0 & {}^{\theta}N_1 & 0 & 0 & {}^{\theta}N_2 \end{bmatrix} \begin{Bmatrix} \dot{d}_1 \\ \dot{d}_2 \\ \dot{d}_3 \\ \dot{d}_4 \\ \dot{d}_5 \\ \dot{d}_6 \end{Bmatrix} \tag{4.10}$$

where the shape functions are given by

$${}^{w}N_1 = {}^{\theta}N_1 = \frac{1}{2} + \frac{z}{L}$$

and $${}^{w}N_2 = {}^{\theta}N_2 = \frac{1}{2} - \frac{z}{L} \,.$$

Hence, the incremental shear strains in Eq.(4.9) reduce to

$$\left(\frac{\partial \hat{\dot{w}}}{\partial z} - \hat{\dot{\theta}} \right) = \langle \, 0 \quad \tfrac{1}{L} \quad -(\tfrac{1}{2} + \tfrac{z}{L}) \quad 0 \quad -\tfrac{1}{L} \quad -(\tfrac{1}{2} - \tfrac{z}{L}) \, \rangle \begin{Bmatrix} \hat{\dot{d}}_1 \\ \hat{\dot{d}}_2 \\ \hat{\dot{d}}_3 \\ \hat{\dot{d}}_4 \\ \hat{\dot{d}}_5 \\ \hat{\dot{d}}_6 \end{Bmatrix} = \underline{b}^T \; \underline{\hat{\dot{d}}}$$

$$\text{and} \qquad \left(\frac{\partial \dot{w}}{\partial z} - \dot{\theta}\right) = \langle 0 \quad \tfrac{1}{L} \quad -(\tfrac{1}{2} + \tfrac{z}{L}) \quad 0 \quad -\tfrac{1}{L} \quad -(\tfrac{1}{2} - \tfrac{z}{L}) \rangle \begin{Bmatrix} \dot{d}_1 \\ \dot{d}_2 \\ \dot{d}_3 \\ \dot{d}_4 \\ \dot{d}_5 \\ \dot{d}_6 \end{Bmatrix} = \underline{b}^T \, \underline{\dot{d}}. \tag{4.11}$$

Substituting Eq.(4.11) in Eq.(4.9),

$$\int_{-L/2}^{+L/2} \widehat{\dot{d}}^T \, \underline{b} \, GA_* \, \underline{b}^T \, \underline{\dot{d}} \; dz = \widehat{\dot{d}}^T \, \underline{\dot{p}}.$$

Since $\widehat{\dot{d}}^T$ is arbitrary, the above equation yields

$$\left(\int_{-L/2}^{+L/2} \underline{b} \, GA_* \, \underline{b}^T \, dz \right) \underline{\dot{d}} = \underline{\dot{p}}. \tag{4.12}$$

Hence , if ${}^{sh}\mathbf{K}_t^l$ is the segment tangent shear stiffness matrix in local coordinates, then the segment incremental equilibrium equation is

$${}^{sh}\mathbf{K}_t^l \; \underline{\dot{d}} = \underline{\dot{p}} \tag{4.13}$$

where

$${}^{sh}\mathbf{K}_t^l = \int_{-L/2}^{+L/2} \underline{b} \, GA_* \, \underline{b}^T \, dz = GA_* \begin{bmatrix} 0 & 0 & 0 & 0 & 0 & 0 \\ & \frac{1}{L} & -\frac{1}{2} & 0 & -\frac{1}{L} & -\frac{1}{2} \\ & & \frac{L}{4} & 0 & \frac{1}{2} & \frac{L}{4} \\ & & & 0 & 0 & 0 \\ & \text{Sym.} & & & \frac{1}{L} & \frac{1}{2} \\ & & & & & \frac{L}{4} \end{bmatrix}.$$

While evaluating the above integral to obtain the local segment tangent shear stiffness matrix, ${}^{sh}\mathbf{K}_t^l$, one-point Gauss Quadrature is used to avoid the contribution of the shear stiffness to the flexural mode.

Let the inclination of the segment in the global coordinates be α. Then, the transformation, $\mathbf{T}$, relating the local and global coordinate frames is

$$\mathbf{T} = \begin{bmatrix} a & b & 0 & 0 & 0 & 0 \\ -b & a & 0 & 0 & 0 & 0 \\ 0 & 0 & 1 & 0 & 0 & 0 \\ 0 & 0 & 0 & a & b & 0 \\ 0 & 0 & 0 & -b & a & 0 \\ 0 & 0 & 0 & 0 & 0 & 1 \end{bmatrix} \tag{4.14}$$

where

$$a = \cos\alpha$$

$$\text{and} \qquad b = \sin\alpha\,.$$

Using this transformation, $\mathbf{T}$, the incremental end-displacement vector, $\underline{\dot{u}}$, and the incremental end-force vector, $\underline{\dot{f}}$, of the segment in the global coordinates, are related to the respective local quantities through Eq.(4.14), as

$$\begin{aligned} \underline{\dot{d}} &= \mathbf{T}\,\underline{\dot{u}} \\ \text{and} \qquad \underline{\dot{f}} &= \mathbf{T}^T \underline{\dot{p}}\,. \end{aligned} \tag{4.15}$$

Thus, if ${}^{sh}\mathbf{K}_t$ is the global tangent shear stiffness matrix of the segment, then Eq.(4.13) transformed into the global coordinate frame using Eq.(4.15), is

$${}^{sh}\mathbf{K}_t\;\underline{\dot{u}} = \underline{\dot{f}} \tag{4.16}$$

where

$$\begin{aligned} {}^{sh}\mathbf{K}_t &= \mathbf{T}^T\,{}^{sh}\mathbf{K}_t^l\;\mathbf{T} \\ &= GA_* \begin{bmatrix} \frac{b^2}{L} & -\frac{ab}{L} & \frac{b}{2} & -\frac{b^2}{L} & \frac{ab}{L} & \frac{b}{2} \\ & \frac{a^2}{L} & -\frac{a}{2} & \frac{ab}{L} & -\frac{a^2}{L} & -\frac{a}{2} \\ & & \frac{L}{4} & -\frac{b}{2} & \frac{a}{2} & \frac{L}{4} \\ & & & \frac{b^2}{L} & -\frac{ab}{L} & -\frac{b}{2} \\ & \text{Sym.} & & & \frac{a^2}{L} & \frac{a}{2} \\ & & & & & \frac{L}{4} \end{bmatrix}, \\ \underline{\dot{u}}^T &= \langle\, \dot{u}_1 \quad \dot{v}_1 \quad \dot{\theta}_1 \quad \dot{u}_2 \quad \dot{v}_2 \quad \dot{\theta}_2 \,\rangle \\ \text{and} \qquad \underline{\dot{f}}^T &= \langle\, \dot{f}_1 \quad \dot{f}_2 \quad \dot{f}_3 \quad \dot{f}_4 \quad \dot{f}_5 \quad \dot{f}_6 \,\rangle\,. \end{aligned}$$

In the numerical study discussed in this thesis, the effective shear area, A_*, of the segment is taken as (5/6) times the web area of the hot-rolled W sections.

Complete Incremental Equation -

Hence, using the tangent stiffness matrices corresponding to axial and bending effects, ${}^{ab}\mathbf{K}_t$ from Eq.(4.6), and to shear effects, ${}^{sh}\mathbf{K}_t$ from Eq.(4.16), the complete segment incremental equilibrium equation in global coordinates is

$$\mathbf{K}_t^s\;\underline{\dot{u}} = \underline{\dot{f}} \tag{4.17}$$

where

$$\mathbf{K}_t^s = {}^{ab}\mathbf{K}_t + {}^{sh}\mathbf{K}_t\,,$$

$$\underline{\dot{u}}^T = \langle\, \dot{u}_1 \quad \dot{v}_1 \quad \dot{\theta}_1 \quad \dot{u}_2 \quad \dot{v}_2 \quad \dot{\theta}_2 \,\rangle$$

and $$\underline{\dot{f}}^T = \langle\, \dot{f}_1 \quad \dot{f}_2 \quad \dot{f}_3 \quad \dot{f}_4 \quad \dot{f}_5 \quad \dot{f}_6 \,\rangle\,.$$

In Eq.(4.17), $\mathbf{K}_t^s$ is the segment tangent stiffness matrix in global coordinate frame. Since, the shear response is assumed to be elastic and uncoupled from the axial and bending effects, the above linear superposition is conducted even under nonlinear and inelastic conditions.

4.4.3 Incremental Equilibrium Equation of a Beam-Column

The incremental equilibrium matrix equation of the whole beam-column is formed by assembling those of all its segments. All the member degrees of freedom are ordered as shown in Fig.3.9. Symbolically, if $\mathbf{K}_t$ is the complete global tangent stiffness matrix of the beam-column, $\mathbf{K}_t^s$ is the segment global tangent stiffness matrix from Eq.(4.17), and $\sum$ is the assembly operator, then

$$\mathbf{K}_t = \sum_{s=1}^{N_s} \{\, \mathbf{K}_t^s \,\} \tag{4.18}$$

where N_s is the number of segments in the beam-column.

4.5 Numerical Implementation

The Fibre Model and the multi-segment Plastic Hinge Model beam-column elements differ in substance but not in form. Though the incremental load-deformation relations are derived by completely different methods, their final matrix forms are identical. Hence, techniques and strategies similar to the ones adopted in the multi-segment Plastic Hinge Model beam-column element, are employed in the numerical implementation of the Fibre Model. The important aspects are re-iterated here.

4.5.1 Member Level Iteration Scheme

As discussed in Sec.3.5.3, at the end of each global iteration within a load

step, the immediate task is to obtain for all members, the updated end-force vector, $\underline{f}^m$, given the incremental end-displacement vector, $\underline{\dot{u}}^m$, appearing on them. To accomplish this, the unknown displacement increments corresponding to the interior degrees of freedom need to be evaluated. Owing to the nonlinearities in the member constitutive relations, an iterative procedure is essential. Newton-Raphson Method is used to conduct these iterations. To avoid convergence difficulties during cyclic loading, the first iteration is conducted with the member elastic stiffness and the subsequent iterations using the member tangent stiffness.

The effect of the known incremental end-displacements, $\underline{\dot{u}}^m$, appears as specified forces on the interior nodes neighbouring the end nodes. Then, if $\underline{f}^{cm}$ represents the complete member residual force vector corresponding to all its degrees of freedom, both interior and exterior, and if $\mathbf{K}_t$ is the tangent stiffness matrix given by Eq.(4.18), then the incremental equilibrium of the member can be written as

$$\mathbf{K}_t \ \underline{\dot{u}}^{cm} = -\underline{f}^{cm} \,, \tag{4.19}$$

where $\underline{\dot{u}}^{cm}$ is the complete member incremental displacement vector. Eq.(4.19) is solved by the Gauss Elimination Procedure to obtain the unknown displacement increments corresponding to the interior degrees of freedom, $\underline{\dot{u}}^{cm}$.

Using $\underline{\dot{u}}^{cm}$, the global incremental end-displacements, $\underline{\dot{u}}$, appearing on each segment are obtained through the assembly array of the segments. Then, from Eq.(4.15), the local incremental end-displacement vector, $\underline{\dot{d}}$, is computed. The incremental axial strain, $\dot{\varepsilon}^f$, in each fibre, f, is given by

$$\dot{\varepsilon}^f = \frac{(\dot{d}_1 - \dot{d}_4) + (\dot{d}_3 - \dot{d}_6)h}{L^s} \,, \tag{4.20}$$

where h is the normal distance of the fibre from the centroidal axis of the segment before deforming and L^s is the length of the segment. Given the initial state of the fibre and the incremental axial strain, $\dot{\varepsilon}^f$, using the proposed Cubic Ellipsoidal Model of the uniaxial cyclic constitutive law for the axial stress-strain behaviour of structural steel described in Sec.4.3.1, the new state of the fibre, σ^f, is obtained.

From the stresses of all the fibres at the cross-section of a segment, the components of the local end-force vector, $\underline{p}$, are obtained by

$$
\begin{aligned}
p_1 &= \sum_1^{N_f} \sigma^f A^f \\
q_1 &= q_0 + \frac{GA_*(\dot{d}_2 - \dot{d}_5)}{L^s} - \frac{GA_*(\dot{d}_3 + \dot{d}_6)}{2} \\
m_1 &= \sum_1^{N_f} \sigma^f A^f h - \frac{q_1 L^s}{2} \\
p_2 &= -p_1 \\
q_2 &= -q_1 \\
m_2 &= -\sum_1^{N_f} \sigma^f A^f h - \frac{q_1 L^s}{2},
\end{aligned}
\tag{4.21}
$$

where N_f is the number of fibres at the segment cross-section and q_0 is the segment shear force at the start of the load step. Using the coordinate transformation, $\mathbf{T}$, given by Eq.(4.14), the segment global end-force vector, $\underline{f}$, is computed by

$$
\underline{f} = \mathbf{T}^T \underline{p}. \tag{4.22}
$$

The assembly of these $\underline{f}$ vectors, of each segment results in the updated complete member residual force vector, $\underline{f}^{cm}$. The above procedure is iterated until these residual force quantities associated with the interior nodes are within the tolerance. Once convergence is achieved, the updated member end-force vector, $\underline{f}^m$, is formed using the global end-force vectors of the two end segments.

4.5.2 External Transverse Loads on Beam-Columns

The Fibre Model also accommodates the external transverse loads applied within its span, as the Plastic Hinge Model as discussed in Sec.3.5.4. If external concentrated loads are applied transversely within the span of the beam-columns instead of the global nodes, then plastic hinges can occur at these locations. Such members are composed of multiple segments. At least, as many interior nodes as

the external loads on the member, are chosen. Further, the locations of these nodes is so chosen as to coincide with those of the external loads themselves. This allows the concentrated load to be directly included in the nodal force vector while conducting the iterations at the element level.

If no plastic hinges form at the locations within the span of the beam-column, where the external transverse concentrated loads are applied, then the corresponding fixed-end forces of such transverse loads may be applied at the end of the members. The rest of the analysis does not differ from before. Similar approach can be employed to approximately include distributed loads applied transversely on the beam-column.

4.5.3 Artificial Unloading during Member Iterations

The possibility of artificial unloading during local iterations at the member level is noted in Sec.3.5.5 while discussing the Plastic Hinge Model. The same remedial measure is employed in the case of the Fibre Model too. The cumulative of the displacement sub-increments from all the local iterations is applied to the member state at the start of the load step as discussed in Sec.2.5.6.

4.6 Numerical Results

The Fibre Model beam-column element is validated using comparisons with the results of Plastic Hinge Model beam-column element, discussed in Sec.3.6. The same three numerical problems used in Sec.3.6 are repeated here to compare the relative performances of the two models.

4.6.1 Control on Tolerances

Tthe tolerances on residual force quantities discussed in Sec.2.7 are adopted in the numerical examples below.

4.6.2 Material Properties

In this thesis, unless stated otherwise, all numerical studies using the Fibre Model beam-column element use the following values for the eight characteristic properties of structural steel required in the proposed uniaxial cyclic constitutive law for the axial stress-strain behaviour of structural steel :

$$\sigma_y = 250\,N/mm^2\,, \qquad \varepsilon_y = 0.00125\,,$$
$$\sigma_u = 400\,N/mm^2\,, \qquad \varepsilon_{sh} = 0.01400\,,$$
$$E = 200000\,N/mm^2\,, \qquad \varepsilon_u = 0.16000\,,$$
$$E_{sh} = 4000\,N/mm^2\,, \qquad \text{and} \quad \varepsilon_r = 0.30000\,,$$

Further, to obtain the Shear Modulus G, a Poisson's Ratio of 0.3 is used.

4.6.3 Effect of Discretisation

Before presenting the results from the single member problems, the effect of the number of segments, N_s, in the Fibre Model beam-column element on the member response is studied. The problem of the cyclic lateral translation of a column member is chosen for this study. Consider a beam-column made of the hot-rolled steel section W14 $\times$ 132 [39] of length 3660 mm, fixed at its ends against rotation. Three different discretisations shown in Fig.4.14a are considered. The displacement time history includes a pure axial compressive displacement, $u = -0.5u_y$, followed by cyclic lateral translations keeping the axial displacement constant. Fig.4.14b shows the axial load *vs.* bending moment diagram for the three cases. The case of $N_s = 30$ and $N_s = 100$ yield identical responses. However, the case with $N_s = 6$ gives a marginally different member response.

It is considered appropriate to use $N_s = 30$ while using the Fibre Model beam-column element. The Fibre Model results discussed in Chapters 4 and 6 are obtained using $N_s = 30$ segments. However, in the analysis of planar MRFs discussed in Chapter 7, while using the Fibre Model beam-column element, $N_s = 6$ is used. This compromise is made in order to accommodate the analysis of the twenty-storey

planar MRF within the hard disk memory of the available computing environment of a *Micro VAX II*.

4.6.4 Single Member Examples

The single member problems with the different displacement time histories detailed in Sec.3.6.2 while discussing the Plastic Hinge Model element are studied again using the Fibre Model elements.

Buckling Problem -

The response of the member composed of Fibre Model beam-column elements, to the axial displacement time history discussed in Sec.3.6.2, is also shown in Fig.3.21. The Fibre Model provides a very good match to the experimental data in the entire displacement cycle. The marginal departure in the neighbourhood of the tensile yield regime may be attributed to the difference between the actual cyclic stress-strain behaviour of steel and the Cubic Ellipsoidal Hysteretic Model used. Further, the predicted response using the Fibre Model is better than that obtained using the Plastic Hinge Model owing to the distributed nature of the inelastic effects in the Fibre Model. The partial yielding of the cross-section, partial elastic unloading and strain-hardening are beyond the scope of the Plastic Hinge Model.

Snap-Through Problem -

The three-stage displacement and rotation time history discussed in Sec.3.6.2, is applied on the fixed-fixed member composed of the Fibre Model beam-column elements. Fig.3.22 shows the responses of the member using the Fibre Model elements, along with the corresponding responses using the Plastic Hinge Model elements. The responses are identical for smaller magnitudes of the compressive axial displacement, u. In the vicinity of snap-through, *i.e.*, when u is close to or greater than $-4u_e$, where $u_e = P_e L/EA$, P_e being the first Euler Load of the member, there is a very small difference in the two model responses. Since, the snap-through problem is an elastic one, this difference may be attributed to the discretisation

error and the inclusion of shear deformation in the Fibre Model.

Lateral Translation Problem -

The lateral displacement time history described in Sec.3.6.2, is applied on the member composed of the Fibre Model beam-column elements. The displacement time history is such that yielding takes place in the member ends. As described in Sec.4.1, the Fibre Model is capable of capturing partial yielding, partial elastic unloading and strain-hardening of the member. Consequently, the responses obtained from the Fibre Model to the lateral displacement problem are different from those obtained from the Plastic Hinge Model. Figs.4.15, 4.16 and 4.17 show the effect of different tensile and compressive axial displacements on the response of the member. In comparison with Figs.3.23, 3.24 and 3.25, these responses are better representations of the true member characteristics.

...

Chapter 5

THE JOINT HYSTERESIS MODEL

5.1 Introduction

The terms *panel zone* and *connection* appear often in the literature describing studies associated with junctions of the beam and the columns. The panel zone, or the *joint*, refers to the finite-sized area of the junction into which the beams and the columns frame-in. On the other hand, the connection refers to the means by which the beams and the columns are connected to these panel zones. The common methods for connection are welding, bolting and combinations of the two. Understandably, nonlinearities may arise in a frame from either the joint panel zones or the connections. This study assumes that the connections between the beam-columns and the joint panel zones are rigid, and that nonlinearities arise only from the joints. This chapter discusses the inelastic behaviour and analytical modelling of the flexible joint panel zones.

5.2 Behaviour of a Joint in a Frame

The lateral resistance of a steel MRF depends on how well the bending moments are transferred between the beams and the columns. This is decided by the joints. The summary of loads transferred through a joint is presented through the free body diagram shown in Fig.5.1. Under the action of these forces, experiments have shown that the in-plane and flexural deformations of the joint are small. The primary deformation is shear distortion. Hence, the predominant stress in the joint is due to shear caused by the unbalance of beam moments. Usually, this unbalance

exists at exterior and corner joints even under gravity loads, while at the interior joints, it is experienced under wind or seismic load conditions. These high shear forces result in large joint shear strains, which affect the storey-drift and the overall structural response.

The primary responsibilities of a joint in a moment-resisting frame are :

(1) to resist the interaction of multi-directional forces (axial load, shear force, bending moment and torsion), which the connected members transfer through it,

(2) to possess adequate ductility to carry large deformations to facilitate the redistribution of forces in the frame, without any brittle failure in it or without the collapse of the frame, and

(3) to possess good energy-dissipating qualities.

5.3 Code Specifications for Design of Joints

There are three specifications concerning the design of steel joint panel zones in the Uniform Building Code 1991 [19]. These provisions are essentially the recommendations made by the SEAOC [20] for lateral force requirements. The first one requires that the shear strength of the joint, given by

$$V = 0.55\sigma_y d_c t \left[1 + \frac{3b_{cf}t_{cf}^2}{d_b d_c t}\right], \tag{5.1}$$

where

σ_y = yield stress

d_c = depth of the column

d_b = depth of the beam

t = thickness of the joint including doubler plates

b_{cf} = breadth of the column flange

and t_{cf} = thickness of the column flange,

shall be sufficient to resist the beam moments due to gravity loads plus 1.85 times the prescribed seismic forces, but the shear strength need not exceed that required to

develop $0.8 \sum M_p$ of the girders framing into the column flanges at the joint, where M_p is the plastic moment capacity. Lesser panel zone strengths are permitted, but when used, it is required that the additional loading and panel zone stress and their extra contribution to the drift, and thus to the P-Δ effects, be accounted for. In addition, the large kink rotations that may be developed at the girder to column flange connections due to increased shear strains in the joint must be accounted for.

The shear strength of the panel zone given by Eq.(5.1) was proposed [49] as an *empirical* estimate for the ultimate shear strength of the joint at a shear strain of $4\gamma_y$. Experimental investigations [50] have indicated much larger values for the ultimate shear strength of the joints and smaller values for the yield shear strength. Hence, the use of this expression for either the yield strength or the ultimate strength of the joint seems inconsistent.

The second provision ensures that the thickness of the panel zone plate is adequate to avoid buckling of the panel under shear. The panel zone thickness, t, shall conform to the following formula

$$t \geq \frac{d_z + w_z}{90}, \tag{5.2}$$

where

$$d_z = d_b - t_{bf}$$

$$w_z = d_c - t_{cf}$$

and $\quad t_{bf} =$ thickness of beam flange.

The third provision is concerning the relative proportioning of the beams, columns and joints. At any moment frame joint, the following relationships shall be satisfied :

$$\frac{\sum Z_c(F_{yc} - f_a)}{\sum Z_b F_{yb}} > 1.0 \tag{5.3a}$$

or

$$\frac{\sum Z_c(F_{yc} - f_a)}{1.25 \sum M_{pz}} > 1.0, \tag{5.3b}$$

where

Z_c = plastic modulus of the column,

Z_b = plastic modulus of the beam,

F_{yc} = yield stress of the column,

F_{yb} = yield stress of the beam,

f_a = maximum axial compressive stress

and M_{pz} = sum of beam moments when joint panel zone reaches the value specified in Eq.(5.1).

In the above codal provision, Eq.(5.3a) attempts to restrict the plastic hinges to within the beams. The columns are not expected to form any hinges. However, Eq.(5.3b) suggests that even the beams need not develop their full plastic moment capacities, and that the joints may yield even before them. Hence, the ductility of the joint enters into the frame response. Since columns under axial loads do not possess good hysteretic properties, the ductility demands of the frame must be restricted to the joint panel zones with excellent hysteretic properties and to the beams. Hence, the relative proportioning of the beams, columns and the panel zones is critical in the design of Special Moment Resisting Frames.

5.4 Hysteretic Beam-Column Joint Behaviour

The joints in a frame were assumed to be rigid in the earlier nonlinear dynamic analysis of frames until their hysteretic properties were revealed [50] experimentally. For typical code-designed buildings, the joints are flexible enough to be included as flexible elements in the analysis of a frame. Further, their yield strength as given by Eq.(5.1) may be low enough so that they undergo considerable yielding under strong earthquake loads, possibly even before the plastic hinges occur in the beams. The true strength and stiffness of the joints play a very important role in the nonlinear behaviour of steel planar MRFs. Thus, an adequate mathematical model to analytically describe this nonlinear response of the joints is essential for

inclusion in realistic frame analyses.

The detailed experimental [17,50,51] and analytical [15,16,17,18] studies conducted on beam-column joints in the past two decades resulted in a much better understanding of its hysteretic behaviour. At low force levels, the shear stresses in the joint, as shown in Fig.5.2a, are in the elastic range. These stresses are highest at the centre of the joint, but with a more nearly uniform variation than the parabolic variation predicted by the elastic theory. The elastic analysis is simplified to the extent that it does not exactly account for the boundary effects of the joint panel. Under increased unbalance of beam moments, the centre of the joint reaches yield. The yielding then propagates towards the edges of the joint panel, resulting in an almost uniform state of stress in the panel, as shown in Fig.5.2b.

The column axial force and bending moments are primarily carried by the two column flanges only. The influence of column axial force on the general yielding of the joint is usually small [52]. But, there are other factors that contribute to the shear stiffness of the joint. The moment on the joint is resisted by the joint panel zone by, at least, four different components, given below :

(1) Shear resistance of the panel zone plate to unbalanced beam moments, as shown in Fig.5.3a, upto yield.

(2) Resistance of the panel boundary elements [16], *i.e.*, the flanges of the beams and of the columns, to the unbalanced beam moments, as shown in Fig.5.3b.

(3) Restraint of the panel zone flexural deformation [17] by the adjacent beam and column webs, as shown in Fig.5.3c.

(4) Strain hardening of the panel zone plate under continued shear.

Some researchers argue that the contributions to the resistance offered by the joint are necessarily in the above sequential order.

The monotonic load-deformation curves for the shear response of joints, obtained from numerous experimental research projects, are summarised [17] in Fig.

5.5. The well-defined knee in the early inelastic regime, is a significant feature of all these tests. The yielding of the joint is found to occur before the theoretical shear yield is reached [53]. This effect is attributed to the combined action of the above mentioned components resisting the joint moment. The joint shows a remarkable increase in strength beyond yield. Its post-yield stiffness is noteworthy over a long range of inelastic deformation, and it exhibits remarkable ductility. Further, under cyclic loading, repetitive hysteresis loops are observed for its shear behaviour with no drop in strength even under very large inelastic joint distortions. Thus, the joint demonstrates excellent energy dissipating characteristics.

5.5 Degrees of Freedom

The physical idealisation of a joint in a planar MRF are shown in Fig.5.4. If μ and ν are the end-rotations of the adjoining beams and columns, respectively, then the shear strain in the joint is given by

$$\gamma = \mu - \nu \,. \tag{5.4}$$

Since μ and ν are considered positive if counter-clockwise, the shear strain, γ, is automatically defined as positive or negative. The moment in the joint, M, is considered positive if it causes a positive γ.

The joint has two degrees of freedom - the beam rotation, μ, and the column rotation, ν, as shown in Fig.2.4. Therefore, the incremental displacement vector, $\underline{\dot{u}}$, of the joint is

$$\underline{\dot{u}} = \left\{ \begin{array}{c} \dot{\mu} \\ \dot{\nu} \end{array} \right\} , \tag{5.5}$$

and its total force vector, $\underline{f}$, is

$$\underline{f} = \left\{ \begin{array}{c} M_\mu \\ M_\nu \end{array} \right\} , \tag{5.6}$$

where M_μ and M_ν are the sum of the beam and column moments, respectively. Further, from the moment equilibrium of the joint,

$$M_\nu = -M_\mu \,. \tag{5.7}$$

5.6 Joint Hysteresis Model

In the literature, there are a number of analytical models [15,16,17,18] describing the hysteretic behaviour of beam-column joints. They are reasonable approximations, but can be improved in several ways. The ultimate load is underestimated in the Krawinkler-Popov Model [53]. The post-yield joint stiffness is applicable only over a small range of inelastic behaviour, *i.e.*, only up to 4 times the yield strain. The Kato Model [17], overcomes this difficulty by defining the virgin curve over the entire possible range of inelastic behaviour, but it uses a multi-linear virgin curve. The Fielding-Chen Model [18] uses a simplified bilinear virgin curve, which over-estimates the post-yield stiffness.

After studying the available models, a simple model is proposed for the hysteretic behaviour of beam-column joints. This model is semi-empirical and is convenient for numerical implementation, even under cyclic loading. The following is a detailed account of the proposed *Ellipsoidal Joint Hysteresis Model* for use in the analysis of steel planar moment-resisting frames with joint elements.

5.6.1 Proposed Model

The starting point is the summary [17] of the monotonic test data on panel zones shown in Fig.5.5. Based on this data, the proposed model empirically defines a virgin curve for the joint hysteresis behaviour, as shown in Fig.5.6. This curve is essentially a function of the joint shear yield moment, M_y, and the joint shear yield strain, γ_y. If d_c is the depth of the column, d_b is the depth of the beam and t is the thickness of the panel zone plate, then M_y and γ_y are given by

$$\begin{aligned} M_y &= \tau_y \, d_c \, d_b \, t \\ \text{and} \qquad \gamma_y &= \frac{\tau_y}{G} , \end{aligned} \tag{5.8}$$

where

$$\tau_y = \frac{\sigma_y}{\sqrt{3}}$$

$$\text{and} \qquad G = \frac{E}{2(1+\nu)} .$$

In Eq.(5.8), σ_y, E and ν are the elastic properties of structural steel.

The linear range of the joint behaviour is restricted to within $0.8M_y$ corresponding to a strain of $0.8\gamma_y$. The ultimate joint moment is specified as $2.35M_y$ corresponding to an ultimate strain of $100\gamma_y$. Owing to a lack of adequate experimental information, the post-ultimate behaviour is assumed to be perfectly-plastic. The curve between the joint shear strain limits of $0.8\gamma_y$ and $100\gamma_y$, is defined by a *quadratic ellipse*, as shown in Fig.5.7, and given by

$$\frac{(\gamma-\gamma_0)^2}{a^2}+\frac{(M-M_0)^2}{b^2}=1\,, \tag{5.9}$$

where M_0 and γ_0 are the joint moment and shear strain, respectively, at the centre of the quadratic ellipse, whose semi-major and semi-minor axes are a and b, respectively. Further, the hysteresis loops or the *branch curves*, are defined by *cubic ellipses*, as shown in Fig.5.7, and given by Eq.(5.10) below :

$$\begin{aligned} &-\frac{(\gamma-\gamma_0)^3}{a^3}+\frac{(M-M_0)^3}{b^3}=1 \qquad \text{for positive curve} \\ \text{and} \quad &\frac{(\gamma-\gamma_0)^3}{a^3}-\frac{(M-M_0)^3}{b^3}=1 \qquad \text{for negative curve}\,. \end{aligned} \tag{5.10}$$

The hysteresis modelling in the Ellipsoidal Joint Hysteresis Model is identical in form to the hysteresis modelling proposed for the Cubic Ellipsoidal Model of the uniaxial cyclic constitutive law for the axial stress-strain behaviour of structural steel described in Sec.3.3.1.

There are a few assumptions behind the hysteretic model of the joint. The structural steel beam-column joint is assumed to strain-harden isotropically, which results in symmetric hysteresis loops about the shear strain axis, *i.e.*, $M=0$ axis, under equal cyclic plastic excursions, as seen in the experimental data [53]. The hysteresis loops are bounded by envelopes, the *backbone curves*. These positive and negative backbone curves are simply the corresponding virgin curves translated along the shear strain axis, as shown in Fig.5.8. The amount of shear strain translation is determined by the plastic shear strain history. This process is already

recognised as *Envelope Strain Shift* in Sec.3.3.1. This shift ensures that the hysteresis loops do not intersect [53] under gradual increase in the cyclic plastic excursions, at least, until the ultimate joint moment is reached.

In Fig.5.9, a typical experimental joint hysteresis loop [16] is shown along with the corresponding analytical prediction. These comparisons show a close fit to the experimental data and hence provide some validation of the model.

5.6.2 Hysteretic Rules

The Extended Masing's Hypothesis discussed in Sec.4.3.1 is very general and can be used to describe most structural load-deformational characteristics. But, the applicability of Rule 1 to the cyclic behaviour of steel joints is not clear. However, Rule 2 concerning the ultimate fate of the branch loops is used as a guideline while forming, handling and updating the joint hysteresis loops. The proposed model employs the following rules to define the cyclic response of structural steel joints :

(1) The virgin curves in the positive and the negative sense are identical.

(2) The response is linearly elastic until the modified joint yield moment is reached, either in the positive or in the negative sense.

(3) New plastic strains are accumulated *only* by progressing along the virgin curve, and *not* by traversing the branch curves.

(4) Under strain reversals, the branch curve originating from the virgin curve is linearly elastic until zero joint moment is reached, and is nonlinear thereafter. This branch curve is referred as the *first branch curve.*

(5) The destination of a branch curve leaving a positive virgin curve is a symmetric point on the translated negative backbone curve. Similarly, the destination of a branch curve leaving a negative virgin curve is a symmetric point on the translated positive backbone curve.

(6) All the subsequent branch curves originating from the first branch curve have

the same amount of linear elastic unloading as the first branch curve. Further, the cubic ellipses describing the nonlinear portions of all these nested branch curves have the same radii until either the destination point is reached or all the nested branch loops are closed, thus returning to the first turning point.

(7) The slope at which a branch curve approaches its destination is the slope of the virgin curve at the turning point from which it departed.

(8) When loading takes place very early in the inelastic regime, the formation of a cubic ellipse, for the nonlinear part of the hysteresis loop, within the above constraints, may not be possible. In such a case, the linear elastic unloading is continued beyond zero joint moment till the formation of a cubic ellipse is possible.

5.6.3 Merits of the Proposed Model

The proposed Ellipsoidal Joint Hysteresis Model for steel beam-column joints in moment-resisting plane frames is significantly superior to the currently used models. This model is based on the macroscopic view of the overall joint behaviour and is supported by test data from steel beam-column sub-assemblages. It provides smooth and *explicit* expressions for joint moment in terms of the shear strain. The few non-cumbersome hysteretic rules make the model simple and computationally efficient, yet descriptive enough to adequately represent the features of real hysteretic behaviour. The smooth virgin curve, and a realistic estimate of the ultimate capacity and the possible inelastic range of the joint are the strengths of this model. With hysteretic behaviour defined up to $100\gamma_y$, this model is an excellent choice for the analytical modelling of structural steel beam-column joints.

5.7 Numerical Implementation

The numerical implementation of the joint element is very simple, and needs no detailed description. However, the following comments are considered necessary.

5.7.1 Elastic Joint Stiffness

As noted in Sec.2.3.6, the global iterations are conducted using elastic frame stiffness. Thus, only the elastic stiffness of the joint needs to be evaluated. Using Eq.(5.8), the joint elastic stiffness, ${}^{j}K_e$, is

$$ {}^{j}K_e = \frac{M_y}{\gamma_y} = G\, d_c\, d_b\, t\,. \tag{5.11} $$

However, this stiffness is associated with the shear strain, γ, of the joint. In terms of the two joint global degrees of freedom, the beam rotation, μ, and the column rotation, ν, the elastic stiffness matrix of the joint becomes

$$ \mathbf{K}_e^J = \begin{bmatrix} {}^{j}K_e & -{}^{j}K_e \\ -{}^{j}K_e & {}^{j}K_e \end{bmatrix}\,. \tag{5.12} $$

5.7.2 Joint Force Vector

To update the global stiffness force vector, $\underline{p}^{k+1}(t+\Delta t)$, at the end of each global iteration within a load step, the incremental displacement vector, $\underline{\dot{u}}^m$, is given and the joint total force vector, $\underline{f}^m$, is required. This vector is simply the vector $\underline{f}$, given by Eq.(5.6). The incremental beam and column rotations, $\dot{\mu}$ and $\dot{\nu}$, respectively, are obtained from $\underline{\dot{u}}^m$. Using Eq.(5.4), the joint incremental shear strain, $\dot{\gamma}$ is obtained. Using the current state of the joint and $\dot{\gamma}$, the updated joint moment is ascertained through the proposed Joint Hysteresis Model. Finally, Eqs.(5.6) and (5.7) result in the required joint total force vector, $\underline{f}^m$.

5.8 Numerical Results

The effects of joint flexibility on the response of MRFs are studied in Chapter 7 through the dynamic analysis of a building frame under specified ground motions.

...

Chapter 6

EVALUATION OF SOME MODELLING ASSUMPTIONS FOR BEAM-COLUMNS IN FRAME ANALYSIS

6.1 Introduction

In the analysis of planar moment-resisting frames (MRFs), considerable computational economy is achieved by making some very basic assumptions. For a designer, it is important to know how far these assumptions can be stretched without significantly corrupting the response of the frame. This chapter aims at studying the effect of some of these assumptions with specific reference to a building frame chosen from the literature [26] under the Holiday Inn ground motion discussed in Sec.2.7, scaled to 0.4g(peak). Further, the frame used for this numerical study is discretised into beam-column members only without any joint elements.

6.2 Significant Geometric Effects in a Frame

The sources of nonlinearities in the behaviour of planar frames are discussed in general in Sec.2.2. The significant geometric effects in a frame may be recast as given below. Approximations of these effects are detailed in Sec.6.4.

6.2.1 Large Deformations

The application of external loads on an undeformed frame produces equilibrium forces in its members, called *primary forces*, and also causes the frame to deform. Further, the external loads now acting on this deformed configuration of the frame produce additional forces in it, called *secondary forces*. These secondary forces

become significant in frames which have large column loads or which undergo large lateral deformation. In frame analysis, this effect is automatically included by continuously updating the nodal coordinates of the frame. If the nodal coordinates are not updated, only small deformations are said to be considered in the frame.

6.2.2 Geometric Stiffness

The effect of member deformed geometry on its own stiffness is understood as Geometric Stiffness. The deflections relative to the member chord are reflected through the stiffness quantities - Stability Functions c_1,c_2, given by Eq.(3.7), and Bowing Functions b_1,b_2, given by Eq.(3.10). The overall member chord rotation results in the P-Δ Effect. Often, in stocky members, Geometric Stiffness may have only a marginal effect on its response, and hence on the response of the frame.

6.2.3 P-Δ Effect due to Other Supported Structures

In the design of buildings, often all frames are not designed to resist the lateral load. This necessitates that some frames support only the gravity loads and seek lateral resistance from the neighbouring MRFs. Under these conditions, the MRFs must carry additional lateral forces originating from the P-Δ effect of these other laterally supported non-MRFs. The realistic analyses of buildings must not neglect these P-Δ forces originating from the non-MRFs.

If P_i is the total gravity load in the i^{th} storey non-MRF columns, h_i is the deformed i_{th} storey height, then the horizontal floor load magnitude, H_i, to be applied at the i^{th} and $(i-1)^{th}$ floor nodes of the MRF is

$$H_i = \frac{P_i \Delta_i}{h_i}, \tag{6.1}$$

where Δ_i is the relative drift of the i^{th} floor with respect to the $(i-1)^{th}$ floor.

6.3 Frame Description

The structure selected for this analytical study is taken from the literature

[26]. It is a twenty-storey, three-bay by four-bay rectangular office building shown in Figs.6.1 and 6.2. When the report [26] was released, this structure was to be built in downtown San Francisco, California. The building was designed for seismic loads in accordance with UBC 1988 [36]. The lateral load on the building is resisted by the exterior moment-resisting frames along its perimeter. The gravity load is supported by the interior core columns in conjunction with the perimeter frames.

6.3.1 Geometry and Idealisation

The critical direction of the frame from the lateral resistance point of view is the shorter direction with three bays. This study will focus on the response of the building in this critical direction. Hence, the frame of interest is a three-bay twenty-storey exterior frame, whose dimensions are shown in Fig.6.3. The frame is symmetric with respect to its centerline. The two exterior three-bay frames alone carry the lateral load, while all the five planar frames in the shorter direction carry the gravity loads. Thus, each of these exterior MRFs laterally supports one half of the building. Consequently, the gravity loads on the one and a half interior frames appear in the computation of the P-Δ forces due to the adjacent non-MRFs on the lateral load resisting MRF.

For analytical modelling purposes, the retaining wall in the basement is assumed to provide restraint to the frame against horizontal translation at the ground level. Hence, the two exterior nodes at the ground level are free to translate vertically and rotate, but are constrained from translating horizontally. Further, the soil and foundation conditions are assumed to be such that the columns are pin-jointed to the foundation at the basement level. Soil-structure interaction is neglected.

The structural idealisation is given in Fig.6.3. It is discretised into beam-columns spanning between the global nodes, without any joint elements. All members are made of A36 grade structural steel. The member cross-sections adapted from the Design 1 MRF in reference [26] are shown in Fig.6.4.

The relative proportioning of the beams and columns in a MRF are controlled in the UBC 1991 [19] by the following provision. At any moment frame joint, the following relationship shall be satisfied :

$$\frac{\sum Z_c(F_{yc} - f_a)}{\sum Z_b F_{yb}} > 1.0\,, \tag{6.2}$$

where

Z_c = plastic modulus of the column,

Z_b = plastic modulus of the beam,

F_{yc} = yield stress of the column,

F_{yb} = yield stress of the beam

and f_a = maximum axial compressive stress.

Eq.(6.2) attempts to restrict the plastic hinges to the beams and keep the columns elastic. The frame under study was designed in accordance with the above specification. Table 6.1 gives the list of the axial load capacity, P_y, and the bending moment capacity, M_p, for each of the frame members.

6.3.2 Loading

The weight of the building floor, including partitions, ceiling and mechanical piping, is assumed to be 4.79 kN/m^2 for the typical floor and roof. The weight of the MRF is computed using the properties of the hot-rolled sections of the members. The exterior window wall system is assumed to weigh 1.67 kN/m^2 average over the exterior surface of the building. The design live loads are 3.84 kN/m^2 and 0.96 kN/m^2 for the typical floor and roof, respectively.

As discussed in Sec.2.5.1, only 20% of the specified live load in the frames is used to compute the nodal masses of the frame. The effect of the wind load on the building under consideration, is assumed to be less significant than the earthquake forces, and hence is not considered in this study. The ground motion selected for this study, the Holiday Inn record of the San Fernando Earthquake 1971 scaled to 0.4g(peak), is discussed in Sec.2.7.

6.3.3 Damping Matrix

For the frame used in the present study, 2% of critical damping is assumed to be present at frequencies of 0.25 Hz and 2.0 Hz. Hence, using Eq.(2.6), the Rayleigh damping coefficients a_0 and a_1 are evaluated to be

$$\begin{aligned} a_0 &= 0.05585 \\ \text{and} \qquad a_1 &= 0.00283\,. \end{aligned} \tag{6.3}$$

The frequency dependence of damping so estimated is shown in Fig.6.5.

6.4 Cases for Performance Evaluation of the Assumptions

Five different cases, denoted **F1**, **F2**, **F3**, **F4** and **F5**, are identified to study the strength of the assumptions. A summary of these five cases is given in Table 6.2. In the first four cases, single segment Plastic Hinge Model elements are used to model all the beam-columns. A preliminary run with two segments per member resulted in no internal hinges, in addition to providing results identical to the case with a single segment. Hence, the use of two segments per member in the Plastic Hinge Model elements is considered unnecessary while modelling this frame. The fifth case uses Fibre Model elements to model the columns in the bottom three storeys of the building. In all the five cases, the same ground motion, the Holiday Inn record scaled to 0.4g(peak) detailed in Sec.2.7, is used for the dynamic analysis.

Case F1

All the three effects, noted in Sec.6.2, namely large deformations, geometric stiffness and P-Δ forces from the non-MRFs, are included. While estimating the lateral forces from the P-Δ effect of the non-MRFs, the deformed or the current storey height is used. All members are composed of single segment Plastic Hinge Model beam-column elements.

Case F2

Large deformations and P-Δ forces from the non-MRFs are included as before. However, geometric stiffness is approximated. The Stability functions are approxi-

mated by the first two terms of their truncated Taylor Series Expansions given in Eq.(3.13). And, bowing is completely neglected. Thus the governing equations, Eqs.(3.7) and (3.11), reduce to

$$\begin{aligned} P &= \frac{EA}{L}\, u \\ \text{and} \qquad \begin{Bmatrix} M_1 \\ M_2 \end{Bmatrix} &= \begin{bmatrix} c_1 & c_2 \\ c_2 & c_1 \end{bmatrix} \begin{Bmatrix} \phi_1 \\ \phi_2 \end{Bmatrix}, \end{aligned} \tag{6.4}$$

where

$$\begin{aligned} c_1 &= 4 + \frac{2}{15}\pi^2 p \\ \text{and} \qquad c_2 &= 2 - \frac{1}{30}\pi^2 p . \end{aligned}$$

All members are composed of single segment Plastic Hinge Model elements.

Case F3

Only small deflections are considered. Nodal coordinates of the frame are not updated. But, the secondary forces are included approximately in the form of the shears given by $\pm Pv/L$, where v is the relative lateral translation of the member in local coordinates. P and L are the member axial load and initial undeformed length. Approximate geometric stiffness, as discussed in case **F2**, is included.

To be consistent with the small-deflection consideration, the P-Δ forces from the non-MRFs are also approximated. In Eq.(6.1), the current or deformed height of the i^{th} storey, h_i, is replaced by h_{i0}, the initial undeformed height of the i^{th} storey. Hence, the magnitude of the horizontal floor load H_i to be applied to the MRF at the i^{th} and $(i-1)^{th}$ floors is given by

$$H_i = \frac{P_i \Delta_i}{h_{i0}}, \tag{6.5}$$

where P_i and Δ_i are as defined in Eq.(6.1). All members are composed of single segment Plastic Hinge Model elements.

Case F4

Frame nodal coordinates are not updated, thus considering only small deflections. Secondary shear terms noted in case **F3** are neglected. The P-Δ forces from

the non-MRFs are completely neglected. Hence, the magnitude of the horizontal force H_i to be applied at the i^{th} and $(i-1)^{th}$ floors of the MRF is zero. No geometric stiffness is considered. The constant terms in the truncated Taylor Series Expansions, given in Eq.(3.13) are used for the Stability Functions c_1,c_2. Thus, the governing equations excluding geometric nonlinearities are

$$P = \frac{EA}{L} u$$
$$\text{and} \qquad \begin{Bmatrix} M_1 \\ M_2 \end{Bmatrix} = \begin{bmatrix} 4 & 2 \\ 2 & 4 \end{bmatrix} \begin{Bmatrix} \phi_1 \\ \phi_2 \end{Bmatrix}. \tag{6.6}$$

All members are composed of single segment Plastic Hinge Model elements.

Case F5

While using single segment Plastic Hinge Model elements, a collapse mechanism is observed in responses **F1 - F4** between the first floor (at the ground level) and the fourth floor. In order to examine this closely, the twelve column members in these three storeys are modelled using the Fibre Model beam-column elements in case **F5**. This case is identical to case **F1** in all respects except that the columns in the first, second and third storeys are composed of the Fibre Model beam-column elements, which include strain-hardening effects. See Fig.6.6. Thus, large deformations, geometric stiffness and P-Δ forces from the non-MRFs are included exactly. All the other members are composed of single segment Plastic Hinge Model elements. The twelve columns in the bottom floors are made up of thirty segments each, as discussed in Sec.4.6.2, the lengths of which are given in Fig.4.13a.

6.5 Numerical Results

The responses of the frame under the different cases mentioned in Sec.6.4 are presented in this section. The performance of the different assumptions that may be made during frame analysis are evaluated in light of these responses.

6.5.1 Natural Periods of the Frame

The elastic natural periods of the first three undamped modes of vibration

of the frame without joint elements, are estimated using the Subspace Iteration Method and are listed in Table 6.3. The elastic pseudo-acceleration response spectrum of the Holiday Inn record scaled to 0.4g(peak) for 2% damping indicates good acceleration content in the neighbourhood of the elastic first natural period of the frame, as seen in Fig.2.7a.

6.5.2 Overall Frame Responses

A summary of the frame responses **F1 - F5** is shown in Fig.6.7, in the form of lateral and vertical roof displacements. Clearly, except in case **F4**, the frame develops a collapse mechanism and subsequently fails. Fig.6.8 shows a schematic of the collapse mechanism. The progressive deformed profiles on the verge of collapse are shown in Fig.6.9. The lateral and vertical displacement time histories of all the floors of MRF0 from response **F1** are shown in Fig.6.10, which correspond to the right exterior global nodes of the frame.

The typical response time histories along with their strength envelopes of the members in the lower storeys of the frame, shown in Fig.6.11, are presented. At any instant, the moment envelope follows the bending moment on the P-M strength interaction surface, shown in Fig.3.11, corresponding to the axial load in the member at that instant. Similarly, the axial load envelope follows the axial load on the P-M surface corresponding to the absolute maximum of the two end-moments in the member. The member response time histories from case **F5** of the first storey interior and exterior columns, and the second floor interior and exterior beams, are presented in Figs.6.12, 6.13, 6.14 and 6.15, respectively. The variation in the axial load of the first storey exterior column is about P_y. In Figs.6.12 and 6.13, these response envelopes are exceeded owing to the fact that the Fibre Model undergoes strain-hardening beyond the P-M strength interaction surface.

In spite of the codal provision given in Eq.(6.2), the columns develop plastic hinges in all the five cases. One major reason why plastic moment hinges form in

the columns is that the points of inflection are not always located at mid-storey. Eq.(6.2) is based on this assumption. Also, in Eq.(6.2), the maximum axial stress, f_a, in the columns cannot be precisely computed at the design stage. The responses of the frames are sensitive to the ground motion used in the dynamic analyses. The large fluctuations in the column axial loads obtained under dynamic conditions are not reflected in the maximum axial stress, f_a, in the columns estimated by the equivalent static lateral load procedure for design. Hence, Eq.(6.2) does not strictly ensure that plastic moment hinges do not form in the columns.

6.5.3 Geometric Stiffness

A comparison of responses **F1** and **F2** concludes that approximating the geometric stiffness of the frame members does not effect the overall frame response. In fact, beam-column members of framed structures designed for seismic loads in accordance with UBC 1991 [19] have been observed to have a yield axial load much smaller in magnitude than their first Euler buckling load. This suggests that the members are usually stocky. And, for stocky members, bowing is very small and can be neglected. Consequently, the geometric effects may be insignificant for code designed members. Hence, approximate geometric stiffness is adequate in the analysis of such frames.

6.5.4 Large Deformations

The primary difference between cases **F2** and **F3** is that the former includes large deflections, unlike the latter. With reference to Fig.6.7, the responses are almost identical. This means that the strength of the collapse-causing earthquakes for models **F2** and **F3** would be almost the same. Thus, the approximation of the large deflections by the secondary shear terms is adequate in capturing collapse.

6.5.5 P-Δ Forces from MRF and non-MRFs

The case **F4** is the simplest formulation of frame analysis with the absence of

all geometric nonlinearities. The comparison of **F3** and **F4** is pertinent to asses the effect of the P-Δ forces from the MRF and the non-MRFs.

While **F3** indicates a collapse of the frame, **F4** does not show any such tendency. This may be attributed to the only un-accounted effect of P-Δ forces from the members of the MRFs and from the non-MRFs. Hence, in the realistic analysis of MRFs which laterally support other non-MRFs, the P-Δ forces originating from the lateral sway of the non-MRFs are important along with the member P-Δ forces, which must be included to better represent the frame behaviour.

6.5.6 Frame with Fibre Model Elements

The collapse mechanism between the first floor (at the ground level) and the fourth floor, observed in responses **F1 - F3**, encourages the use of Fibre Model elements to model the columns in these floors. Case **F5** is intended to see if the additional features of the Fibre Model, especially strain-hardening of the member cross-section, help the frame to overcome the collapse mechanism. Also, the effect of yielding from bending on axial stiffness is included.

The comparison of responses **F1** and **F5** shows only marginal differences. Thus, the above features of the Fibre Model did not help the frame in overcoming the collapse. It may be pointed out that the beams in these three floors should have been modelled with the Fibre Model elements. The strain-hardening in the beams may have helped by increasing the strength and stiffness of those three storeys. Further, it is observed that no internal hinges are formed in the columns modelled with Fibre Model elements. This strengthens the common notion that the inelasticities are concentrated only at the end of the code-designed seismic frame members.

6.6 Conclusions

The salient conclusions recorded from the above numerical study in light of the twenty-storey MRF are :

(1) Code designed frames classify as short columns, and hence approximate geometric stiffness is adequate.

(2) Large deformations are important.

(3) P-Δ forces originating from the MRF members and from the other laterally supported non-MRFs, if any, are critical and they must be included.

(4) Effect of yielding from bending stresses on the axial stiffness is not significant, though present, in code designed seismic frames. Surprisingly, strain-hardening does not seem to significantly strengthen the frame against collapse. The overall response of the frame with 12 Fibre Model beam-column elements is not too different from the frame modelled without Fibre Model elements.

(5) No interior member plastic hinges are formed in code designed seismic frame columns. Thus, multiple segments are not required in the Plastic Hinge Model beam-column elements.

(6) If plastic moment hinge must be avoided in the columns, then in Eq.(6.2), the maximum axial stress, f_a, obtained from static analysis under code recommended minimum lateral forces, must be appropriately increased by a factor to account for the fluctuations in the column axial loads under dynamic conditions. The interior columns demonstrate much smaller axial load fluctuations than the exterior columns.

...

Chapter 7

NUMERICAL RESULTS FROM ANALYSES OF FLEXIBLE JOINT MRFs

7.1 Introduction

Buildings deform into their inelastic range under severe earthquakes. To arrive at building codes which ensure that tall buildings are safe under big earthquakes, the inelastic behaviour of such buildings must be well understood. In this regard, nonlinear analyses of building frames incorporating the material and geometric nonlinearities discussed in Chapters 2 and 6 need to be performed. This chapter presents one such study through the specific case of a planar moment-resisting frame (MRF). The approximations noted in Chapter 6 are not considered here. Thus, large deformations, geometric stiffness and P-Δ forces are exactly modelled.

The highly nonlinear load-deformational behaviour and the energy absorbing characteristics of steel beam-column joints discussed in Chapter 5 are included in the planar MRF analysis. This chapter presents a more realistic analysis of the planar MRF chosen from the literature [26] with flexible joint elements included in the discretisation. Different panel zones designs are discussed to study their effect on the inelastic response of the building frame under severe ground motions.

7.2 Frame Description

The same twenty-storey building frame [26] described in Chapter 6 is used here in the proposed study. Hence, the description of the frame given in Sec.6.3 is not reproduced here. The frame under study was originally designed in accordance with UBC 1988 [36]. However, the relevant provisions for the design of beam-columns

and joint panel zones have not been revised in UBC 1991 [19]. Hence, the discussions pertaining to the performance of the MRF are viewed in light of UBC 1991.

7.3 Panel Zone Designs

Three different panel zone designs described below are considered to assess the effects of panel zone flexibility on the inelastic response of the MRF. The basic dimensions of the joint elements are given in Table 7.1. The parameter for design is the thickness of the joint panel zone plate. Table 7.2 shows the thickness of the doubler plates required at each typical exterior and interior joint at each floor of the MRF for each of three joint panel zone designs discussed below.

7.3.1 Design I

The thickness of the joint panel zone plate, t_j, is chosen to be the same as the thickness of the column web, t_{cw}, *i.e.*, no doubler plates are added. Hence,

$$t_j = t_{cw} \,. \tag{7.1}$$

It is intended to study the performance of the panel zones, based on the beam and column sizes as obtained from the static lateral force procedure using the minimum design lateral forces recommended in the UBC 1991. This is a lower bound for the design of panel zones.

7.3.2 Design II

The thickness of the joint panel zone plate is determined by :

$$t_j = \frac{0.8 \sum^{bj} M_p}{\tau_y \, d_b \, d_c} \,, \tag{7.2}$$

where

$$\tau_y = \frac{\sigma_y}{\sqrt{3}} \,.$$

In Eq.(7.2), $\sum^{bj} M_p$ refers to the sum of the plastic moment capacities of all beams framing into that joint. σ_y is the yield stress of steel, d_b is the depth of the beam

and d_c is the depth of the column. If the thickness, t_j, as computed from Eq.(7.2) is less than the thickness of the column web, t_{cw}, then the latter is used.

The panel zone need not support the beam hinging to make a moment frame ductile. Hence, to reduce the ductility requirements on the beam-column members, the panel zone is designed for $0.8\sum^{bj} M_p$ of the beams. This is the upper-bound design suggested in UBC 1991.

7.3.3 Design III

The thickness of the joint panel zone plate is determined by :

$$t_j = \frac{1.5\sum^{bj} M_p}{\tau_y \, d_b \, d_c} \, . \tag{7.3}$$

The factor 1.5 in Eq.(7.3), is obtained from $1.2 \times (1/0.8)$. The factor 1.2 accounts for the strain-hardening of the adjoining beam moments up to 20% over their plastic moment capacities. The factor (1/0.8) ensures that the linear elastic range of the joint, which is up to $0.8M_y$, where M_y is as defined in Eq.(5.5), is not exceeded. Again, if the thickness, t_j, as computed from Eq.(7.3), is less than the thickness of the column web, t_{cw}, then the latter is used.

The panel zones are relieved of ductility demands by designing their thicknesses based on a yield moment of $1.5\sum^{bj} M_p$ of the beams. This consideration is only used to evaluate the stiffness of the flexible joint elements. The yield strength of the panel zones is set at an arbitrarily large value. This design allows for yielding in the girders and the columns, but no yielding in the joint panel zones. In effect, the joint remains in the linear elastic regime.

7.4 Cases for Numerical Study

Planar MRFs with each of the three joint designs discussed in Sec.7.3 are analysed using the computer program **NDA2** described in Sec.2.6 under the ground motions detailed in Sec.2.7. Several frame analyses are identified for numerical

study. In all these analyses, the beam-columns in the MRFs are composed of the Fibre Model elements only. To accommodate the analyses within the available computing environment of *Micro VAX II*, the beam-columns are composed of six segments only. The employed discretisation of the beam-columns with six segments, see Sec.4.6.3, is shown in Fig.4.13a.

While referring to the different analysis cases, the following nomenclature is used. MRF1, MRF2 and MRF3 refer to the twenty-storey MRF with joint panel zone design I, II and III, respectively. Further, MRF0 refers to the frame without joint elements discussed in Chapter 6.

A, B and C Series

The MRFs with different joint panel zone designs are subjected to acceleration ground motions collected from *real* earthquakes, discussed in Sec.2.7. The responses of MRF1, MRF2 and MRF3 under these ground motions are identified as series **A**, **B** and **C**, respectively. The list of different analyses showing the joint design type and peak amplitudes of the real ground motions is given in Table 7.3.

P, Q and R Series

The three MRFs are also studied under *synthetic* acceleration ground motions detailed in Sec.2.7. The analyses with the different synthetic ground motions of MRF1, MRF2 and MRF3 are identified as series **P**, **Q** and **R**, respectively, as listed in Table 7.3.

7.5 Numerical Results

While interpreting the results, the following definitions are used. The joint shear strain or shear rotation as defined by Eq.(5.4) is used here. The joint rotation ductility is defined as the shear rotation γ_p of the joint in excess of the yield rotation γ_y. For the beam-columns, the member-end curvature ductility is defined as the curvature ϕ_p of the end segment in excess of the yield curvature ϕ_y.

The ductility quantities are presented at each floor for joints and beams, and at each half-storey for columns. The ductilities are normalised with the corresponding yield values. In the case of joints, the maximum of the joint rotation ductility amongst the two exterior joints and the two interior joints are shown separately. In case of beams, the maximum of the curvature ductilities at the exterior-ends of the exterior-bay beams is represented as the exterior beam maximum curvature ductility. And, the maximum of the curvature ductilities at the interior-ends of the exterior-bay beams and at the two ends of the interior-bay beam, is represented as the interior beam maximum curvature ductility. Similarly, for columns, the maximum of the curvature ductilities at the bottom ends of the two exterior columns is represented by a bar in the bottom-half of the storey. And, the maximum of the curvature ductilities at the top ends of the two exterior columns is represented by a bar in the top-half of the storey. Similarly, the maximum curvature ductilities of the two interior columns are also represented.

The responses of the different MRFs mentioned in Sec.7.4 are presented in this section. The performance of the different frame elements and that of the frame as a whole are evaluated in light of these responses. The joint panel zone designs I and III represent the weakest and the strongest joint designs from a strength point of view. The primary thrust of this study is on the basic understanding of the effect of the joint behaviour on the MRFs. Hence, emphasis is laid on MRF1 and MRF3 in the following numerical study. Responses of the code designed frame MRF2 are compared to those of MRF1 and MRF3. Once the responses from MRF1 and MRF3 are carefully examined and understood, optimal joint panel designs between these two extrema may be arrived at.

7.5.1 Natural Periods of the Frames

The natural periods of the first three undamped elastic modes of vibration of MRF1, MRF2 and MRF3 are estimated using the Subspace Iteration Method. Table 6.3 gives these natural periods along with the corresponding values for MRF0.

The differences in the natural periods of MRF1, MRF2 and MRF3 are obvious. As the joints get stronger, the frame gets stiffer and the period becomes smaller. The difference in the natural periods of MRFs with joint elements and MRF0 is also explainable. In the analytical modelling of the joint elements, only the distortional stiffness of the joint is considered, while the in-plane deformations are not considered, as noted in Secs.2.4 and 5.5. Consequently, the dimensions of the joints do not enter the translational stiffness computations of the frame. Thus, the period of the building is underestimated to that extent. For the frame at hand, the dimensions of the joints account for 20% of the building's total height and total width. The change in the first natural period is also around 20%.

It is reiterated that these natural periods correspond to the elastic responses of the frames. The actual inelastic actions during strong shaking will significantly affect these quantities. The pseudo-acceleration elastic response spectrum of the Holiday Inn record scaled to 0.5g(peak) for 2% damping indicates good acceleration content in the neighbourhood of the elastic first natural period of MRF1, as seen in Fig.2.7.

7.5.2 Responses to Holiday Inn Ground Motion

The original Holiday Inn S90W record is scaled to different levels of peak ground motion and the responses of MRF1, MRF2 and MRF3 are studied. The following is a summary of observations from the same.

0.4g(peak) -

Under the same ground motion, Fig.7.1 shows that the lateral and vertical roof displacement responses in **A4**, **B4** and **C4** are completely different from that in **F5** without joint elements discussed earlier in Chapter 6. The difference is attributed to the inclusion of the flexible joint elements in the frame discretisation. The collapse mechanism observed involving the bottom three storeys of **F5** is totally absent here. Since the inclusion of joint elements is considered necessary in the frame

discretisation, the responses from **A4**, **B4** and **C4** are considered more realistic than that from **F5**. MRF0 has a lower period than MRF1, MRF2 and MRF3, where there is more motion in the earthquake, resulting in a collapse mechanism.

Further, amongst the frames with joint elements, **B4** and **C4** show a lateral offset unlike **A4**. Detailed comments on this aspect are presented while discussing the results from the 0.5g(peak) ground motion.

0.5g(peak) -

The lateral floor displacement time histories in **A5**, **B5** and **C5** are indicated in Fig.7.2. **A5** demonstrates good ductile behaviour and shows no lateral offset, unlike **B5** and **C5**. Further, most of the lateral offsets in **B5** and **C5** occur in the bottom few floors. In spite of the lateral offsets, none of the frames collapse. Even though MRF2 and MRF3 do not collapse at 0.5g(peak) ground motion, the displacement time history scenario suggests a probable collapse mechanism should the frames fail under higher levels of ground motion. This probable collapse mechanism is similar to the one already identified in case of MRF0 in Chapter 6 as shown in Fig.6.8.

The joints play a critical role in redistributing the inelastic effects between the various elements in the frames. The second floor interior and exterior joints identified in Fig.6.11, are chosen to observe the typical joint responses. Figs.7.3 and 7.4 show the hysteresis loops of these joints from **A5** and **B5**, respectively. The joints in **A5** and **B5** undergo considerable yielding. The joints in **C5** remain completely elastic and hence their responses are omitted here. In general, the interior joints are subjected to larger shear strains than the exterior ones. The joints in **B5** indicate a drift in the shear strains, unlike the joints in **A5** which show a symmetric pattern in the shear strain plastic excursions.

The same four members identified in Chapter 6 (see Fig.6.11) are chosen again to present typical member reponse time histories. The member response time histories of the first storey interior and exterior columns, and the second floor interior and exterior beams from **A5** are shown in Figs.7.5, 7.6, 7.7 and 7.8, respectively,

along with the strength envelopes. These strength envelopes are obtained as detailed in Sec.6.5.2. The exterior beam and interior column undergo strain-hardening and pick up axial loads and bending moments beyond the envelopes. Comparisons of responses of the same four members in **A5**, **B5** and **C5**, are given in Figs.7.9, 7.10, 7.11 and 7.12. The large lateral offsets in **B5** and **C5** are reflected in the member responses. The significant yielding in all these members suggests a drop in the storey stiffness leading to large storey displacements.

The maximum joint rotation ductilities (γ_p/γ_y) and the maximum member-end curvature ductilities (ϕ_p/ϕ_y) during the entire time history in **A5**, **B5** and **C5**, are summarised in Figs.7.13, 7.14 and 7.15, respectively. Most of the inelastic behaviour in **C5** occurs in the latter half of the time history when the frame undergoes a significant lateral offset. Hence, the associated ductility quantities are larger than the ones observed in **A5**. As expected, the joint ductilities in **A5** are absent in **C5**, since the joints remain elastic. Consequently, the curvature ductilities in the beam-column members are larger in **C5** than in **A5**. As expected, the joint rotations reduce from MRF1 to MRF2, and furthermore from MRF2 to MRF3. In general, the exterior beam-end curvature ductilities are larger than those of the interior ones.

The ratio of the relative storey lateral displacement Δ to the corresponding storey height h is hereinafter referred to as the storey-drift. The maximum storey-drifts (Δ/h) in the three MRFs are shown in Fig.7.16. Clearly, the storey-drifts are more uniform in **A5** than in **B5** and **C5**. The bottom few storeys undergo very large storey-drifts in **B5** and **C5**. The maximum allowable storey-drift by UBC 1991 for steel special MRFs is *0.0025 radians* under the prescribed design lateral forces. The maximum storey-drifts in MRF1, MRF2 and MRF3 are about *12*, *17* and *36* times the prescribed maximum storey-drift, respectively. From serviceability considerations, it is essential that no single storey undergoes unreasonably large drifts. Keeping this in mind, only MRF1 may be considered to have performed well. MRF2 and MRF3 indicate large drifts in the bottom two storeys relative to the others. The pattern in these storey-drifts suggests the possible collapse

mechanism in MRF2 and MRF3.

The performance of **B5** is in between those of **A5** and **C5**. However, its lateral offset suggests that its performance is more similar to that of **C5** than of **A5**.

0.6g(peak) -

As suspected earlier in MRF3 under 0.5g(peak) ground motion, the concentration of the lateral offset in the bottom few storeys leads to the collapse of the frame at 0.6g(peak) ground motion. The lateral displacement time histories of all the floors in **A6** and **C6** are shown in Fig.7.17. **A6** shows the first signs of a lateral offset. However, this offset in **A6** is distributed over at least half the frame height, unlike in **C6**, where it is concentrated in the bottom few floors. In spite of this lateral offset, **A6** does not collapse.

The summary of the joint and member-end ductilities during collapse in **C6** and on the verge of collapse in **A6**, are not presented as the quantities do not have any physical significance.

0.7g(peak) -

The lateral offset in MRF1 under 0.6g(peak) ground motion suggests a probable collapse under higher magnitudes of ground motion. MRF1 collapses under the increased ground motion of 0.7g(peak). The lateral displacement time histories of all the floors in **A7**, are also given in Fig.7.17.

7.5.3 Responses to Pacoima Dam Ground Motion

The lateral displacement time histories of all floors of the three MRFs under the Pacoima Dam ground motion, are shown in Fig.7.18. MRF1 has a larger offset than MRF2 and MRF3. In MRF2 and MRF3, the lateral offset is concentrated in the bottom six storeys, while it is uniformly distributed over the entire height in MRF1. Fig.7.18 indicates a very gradual collapse in MRF2 and MRF3. The collapse mechanism developed in these two frames is similar to the one observed

in the case of the Holiday Inn ground motion. Here, the bottom six storeys are involved in the sway mechanism as against the bottom three storeys only under the Holiday Inn ground motion. Even though the lateral offset is initially larger in **A0** than in **B0** and **C0**, MRF1 survives the ground motion.

The maximum ductilities in the joints and beam-columns of the three MRFs are indicated in Figs.7.19, 7.20 and 7.21. As expected, the joint ductilities are larger in **A0**, while the member-end curvature ductilities are larger in **B0** and **C0**. The increased participation of the higher floor beams is obvious in Fig.7.21. As the joints get stronger, the interior beams also form plastic moment hinges at their ends.

The maximum storey-drifts in MRF1, MRF2 and MRF3 are indicated in Fig.7.22. All the frames perform reasonably well. The maximum storey-drift in all the frames is about *12* times the maximum prescribed under the design lateral forces. However, the uniformity in the maximum storey-drifts across the height of the frames observed in **A5** is not very obvious in **A0**. As before, the joint rotations are larger in MRF1, and progressively lesser in MRF2 and MRF3.

The joints in MRF3 are stronger than those in MRF1. Consequently, the large velocity pulse in the Pacoima Dam ground motion affects MRF1 more than MRF3 by way of a larger lateral offset. But, the transfer of ductilities to the columns in MRF3 is not favourable to the overall stability of the frame. Further, the Pacoima Dam ground motion has a larger content at *1.0 second* period than at *1.2 seconds*, as per its acceleration spectrum given in Fig.2.7. Hence, MRF3 with a second natural period of *1.06 seconds* responds in second mode more than MRF1, whose second natural period is *1.20 seconds*. Also, the inelastic effects are more pronounced in MRF1 than in MRF3, causing a lesser response to the second mode.

7.5.4 Comments on Responses to Real Ground Motions

The following general observations are made regarding the responses of the frames under the two real ground motions. The lateral displacement of the roof in

A0 is smaller than in **A5**. This is owing to the fact that the Holiday Inn ground motion scaled to 0.5g(peak) has a larger content around the first natural period of MRF1, as seen in Fig.2.7.

Further, **A0** and **A5** differ in one other major aspect. The lateral offset observed in **A0** is completely absent in **A5**. This is attributed to the large velocity pulse in the Pacoima Dam ground motion which causes large strains in the lower storey columns, particularly in the first storey columns. These large strains cause yielding in the columns, which reduces their lateral stiffness. Hence, larger lateral offset results in **A0** unlike in **A5**.

Under both ground motions, MRF2 and MRF3 readily develop plastic hinges in columns and form collapse sway mechanisms nore easily than MRF1.

7.5.5 Responses to Fault-Parallel Synthetic Ground Motions

Pulses 1 to 5 in Table 7.3 correspond to the synthetic ground motions simulating the fault-parallel motion with a large pulse. The following is a summary of the numerical results obtained from the dynamic analyses of the three MRFs under these synthetic ground motions :

Pulse 1 -

The floor lateral displacement time histories from **P1**, **Q1** and **R1** are shown in Fig.7.23. Though none of the frames collapse, **P1** accumulates a much larger lateral offset. Further, the figure suggests that **R1** also vibrates in its second mode, unlike **P1** which vibrates predominantly in its first mode. The joint rotational ductilities and the member-end curvature ductilities in **P1**, **Q1** and **R1**, are given in Figs.7.24, 7.25 and 7.26, respectively. The member-end curvature ductilities in **R1** are marginally larger than those of **P1**.

Pulse 2 -

The synthetic pulse 2 has a duration of 2 seconds and a ground acceleration of

0.2g(peak), which is twice the duration of synthetic pulse 1 and half its peak ground acceleration. Fig.7.27 illustrates the floor lateral displacement time histories from **P2**, **Q2** and **R2**. **P2** behaves very similar to **P1**. But, the second mode contribution observed in **R1**, is absent in **R2**. Also, **R2** demonstrates a lateral offset like **P2**. The ductilities in the joints and beam-column members in **P2**, **Q2** and **R2**, are distributed across the frames in a similar way as observed under pulse 1. Since they are only marginally more than those observed under pulse 1, they are not presented.

Pulse 3 -

In comparison with pulse 1, pulse 3 basically has the same duration of the pulse but has twice the amplitude. Consequently, the responses also seem scaled up, though not linearly. Fig.7.28 shows the floor lateral displacement time histories in **P3**, **Q3** and **R3**. Unlike in **R1**, **R3** accumulates lateral offset. The second mode of vibration seen earlier in **R1** is not very obvious in **R3**. The element ductilities in **P3**, **Q3** and **R3** are shown in Figs.7.29, 7.30 and 7.31, respectively. Understandably, these quantities are larger than those observed under pulse 1. None of the frames show any tendency to collapse. A maximum joint rotation ductility of about *30* is recorded in the second floor exterior joint of MRF1.

Pulse 4 -

Again, with twice the duration of pulse 3 and half its peak ground acceleration, pulse 4 results in larger responses. The lateral offsets in the two frames are further increased, but **R4** has smaller lateral offset than **P4**, as seen in Fig.7.32. The ductility distributions in the frames are similar to the corresponding ones obtained under pulse 3. They are omitted for brevity. In spite of the large lateral offsets, the frames still remain stable.

Pulse 5 -

Of the five pulses representing typical fault-parallel motion, pulse 5 is the most severe one. The peak ground acceleration of about 1.6g and peak velocity of 4000 *mm/sec* are slightly on the higher side of the ground motions recorded so far during

major earthquakes. However, these quantities are explored to simulate the extreme conditions during big earthquakes.

With twice the ground motion of pulse 3, MRF1 collapses under pulse 5, unlike MRF2 and MRF3, as shown in the floor displacement time histories from **P5**, **Q5** and **R5** in Fig.7.33. The first storey interior columns are translated laterally to the extent that the extreme fibres in the bottom end segment reach ultimate strain, and start losing strength and stiffness. Consequently, the frame starts collapsing. This suggested collapse mechanism in Fig.7.33, is similar to the one indicated in Fig.6.8.

On the other hand, **Q5** and **R5** with stiffer joints withstand the jolt and remain stable, as seen in Fig.7.33. The collapse of MRF2 and MRF3 is imminent on further increase in the amplitude of ground motion, as suggested by the concentration of the lateral offset in the bottom few floors. The ductilities recorded are not meaningful under collapse conditions, and hence omitted.

7.5.6 Responses to Fault-Normal Synthetic Ground Motions

Pulses 6 to 9 in Table 7.3 correspond to the synthetic ground motions simulating the fault-normal motion with a large pulse. The following is a summary of the numerical results obtained from the dynamic analyses of the three MRFs under these synthetic ground motions :

Pulse 6 -

The floor displacement time histories from **P6**, **Q6** and **R6** are shown in Fig.7.34. Clearly, all of them demonstrate similar responses. Since the joints in **R6** are stiffer and hence the frame, the amplitude of the response is greater in **R6**. None of the frames collapse. The lateral offsets in **Q6** and **R6** are marginally more than those in **P6**. The joint rotation ductilities and the member-end curvature ductilities from **P6**, **Q6** and **R6** are given in Figs.7.35, 7.36 and 7.37, respectively. The ductility distributions indicate that as the joints get stronger, the higher mode participation is increased. The location of the large ductilities exactly coincides

with the floors 15 to 17, where the doubler plate thicknesses are suddenly reduced. The beams and columns in the higher floors participate much more in **Q6** and **R6** than in **P6** owing to stronger joints.

Pulse 7 -

The effect of a longer duration pulse is evident here. The displacement excursions are larger in **P7**, **Q7** and **R7** than those under pulse 6, as shown in Fig.7.38. One major difference in the responses under the pulses 6 and 7 is regarding the distribution of the lateral offset along the height of the frames. Under pulse 6, the lower floors are subjected to higher inter-storey drifts. However, under pulse 7, the floors displace uniformly relative to each other. Further, the lateral offset in **P7** are smaller than those in **Q7** and **R7**.

Pulse 8 -

The responses of the three MRFs under pulse 8 are identical in form to those obtained under pulse 6, as seen in Fig.7.39. Obviously, the amplitudes of the responses are larger. However, the concentration of the lateral offset in the bottom few floors is further accentuated under pulse 8 in comparison with the reponses under pulse 6. The tendency towards the collapse mechanism identified in Chapter 6 (see Fig.6.8) may be observed. The ductilities from **P8**, **Q8** and **R8** are given in Figs.7.40, 7.41 and 7.42, respectively.

Pulse 9 -

Response **P9** is predictable from the trend in the above responses. The amplitudes are larger than in **P7**, as seen in Fig.7.43. Even with twice the duration of pulse 8 and the same peak velocity, the MRFs do not collapse under pulse 9, as seen in Fig.7.43.

7.5.7 Comments on Responses to Synthetic Ground Motions

Based on the responses under pulses 1 to 5, it is observed that the duration

of the pulse affects the participation of the higher modes, while the amplitude of ground motion affects the response amplitudes. The response is greater under the larger amplitudes of ground motion. MRF3 performs better than MRF1 on the whole with lesser lateral offsets. The non-unifomity in the inter-storey drift is seen in all the frames as the strength of the ground motion is increased.

Based on the responses under pulses 6 to 9, the shorter duration pulses, *i.e.,* the pulses 6 and 8, seem to cause lesser lateral offsets in the frames. For a given peak velocity of the pulse, the shorter duration pulses cause non-uniform inter-storey drift in the building with larger drift concentrated in the lower floors. Secondly, the larger the peak ground velocity, the greater is the response. The response of MRF3 is larger than that of MRF1 under these ground motion pulses.

In summary, while both MRF1 and MRF3 take the fault-normal ground motion very well, MRF3 performs better under the fault-parallel ground motion in comparison to MRF1.

7.6 Conclusions

The above numerical studies of the twenty-storey MRF suggests that the non-linear dynamic response of a high-rise MRF is very sensitive to the panel zone design as well as to the input acceleration ground motion. The MRF analyses provide an insight into and help better understand the behaviour of the twenty-storey MRF. The following conclusions are noted with respect to the design and analyses of the twenty-storey MRF :

(1) The proposed Cubic Ellipsoidal Hysteretic Model of the uniaxial cyclic constitutive law for the axial stress-strain behaviour of structural steel is very efficient and convenient.

(2) The performance of a MRF with flexible joint elements in its discretisation is different from that of a MRF without joint elements. The inclusion of flexible joint elements in realistic frame analysis is essential.

(3) In general, MRF2 and MRF3 perform very similarly under the various ground motions. However, the perfomance of MRF1 is different depending on the type of ground motion.

(4) Strain-hardening is successfully incorporated in the analysis of planar MRFs through the Fibre Model beam-column element. The first storey interior column and the second floor exterior beam undergo strain-hardening and pick up additional moments up to about 10% of M_p in MRF1 under the Holiday Inn ground motion scaled to 0.5g(peak). In MRF2 and MRF3, these members strain-harden to pick up additional moments up to about 50% of M_p.

(5) The axial load fluctuates from peak to peak by about $0.8P_y$ in the first storey exterior column, and by about $0.1P_y$ in the first storey interior column in MRF1 under the Holiday Inn ground motion scaled to 0.5g(peak). In both MRF2 and MRF3, the axial loads in the first storey exterior and interior columns fluctuate by about $1.2P_y$ and $0.2P_y$, respectively.

(6) The MRF with strong joints performs satisfactorily under the synthetic ground motions with large pulses. However, owing to the stronger joints, the columns, which do not possess the desirable stable hysteretic properties of the joints, are forced into larger inelastic excursions. Consequently, large undesirable inter-storey drifts occur in the bottom storeys of the frame.

(7) On the other hand, the MRF with yielding joints performs well under ground motions with large acceleration content in the proximity of the first natural period of the frame, and under fault-normal synthetic ground motions. However, under fault-parallel synthetic ground motions, the displacement jump in the ground motion caused by the half-cycle velocity pulse results in excessive lateral offsets of the frame owing to the yielding joint panel zones.

(8) In the case of the fault-parallel synthetic ground motion, the duration of the pulse affects the modal participation, while the amplitude of the pulse affects the response amplitude. But, in the case of the fault-normal synthetic ground

motions, the shorter duration pulses cause lesser lateral offsets, but larger non-uniform distribution of the inter-storey drift with larger concentrations in the lower floors. However, in general, the closer the duration of the pulse to the first natural period of the frame, the larger the response.

(9) The Pacoima Dam ground motion has a velocity pulse typical of the fault-parallel ground motion. Thus, as stated in conclusions (6) and (7) above, MRF1 undergoes larger lateral offset than MRF3. But, in MRF3, the stronger joints force the plastic moment hinges to occur in the columns, leading to reduced storey stiffness. Consequently, MRF3 develops a collapse mechanim.

(10) Under the Holiday Inn ground motion scaled to different levels, the overall performance of MRF1 is superior to those of MRF2 and MRF3. The absence of sharp and large velocity pulses in the ground motion is favourable to MRF1 with yielding joint panel zones.

(11) MRF3 has a higher participation of the second mode, unlike MRF1 which predominantly elicits the first mode response. The participation of the beams and columns in the higher floors is obvious in MRF3 from the ductility plots obtained from the analyses using the different types of ground motions. This may be attributed to the sudden reduction in the doubler plate thicknesses in MRF3 around floors 15 to 17.

(12) The performances of the MRFs with joint designs I and III are quite varied under the different ground motions studied. MRF1 does not respond well to the displacement jumps in the ground motions. On the other hand, MRF3 forces undesirable plastic moment hinges to occur in the columns. A MRF with joints stronger than those in MRF1 and with the columns protected against formation of plastic moment hinges seems to be a good design philosophy that needs to be explored for tall buildings to withstand ground motions with large displacement jumps.

(13) The above study indicates that code suggested design of the joint panel zone,

i.e., design II in MRF2, does not perform as well as joint design I in MRF1, under the Holiday Inn ground motion. The possibility of a weaker joint panel zone design than that adopted in MRF2 must be considered to reduce the ductility demands on the columns.

(14) Frame ductility distribution between the joints, beams and columns can be controlled through the design of the joints or through the design of beams. For the twenty-storey MRF, the numerical study shows the effect of the joint panel zone design on the MRF ductility distibution. Stronger joints throw more ductility demands on the columns, while yielding joints attract the ductility towards themselves and do not perform well under ground motions with displacement jumps.

...

Chapter 8
SUMMARY AND CONCLUSIONS

8.1 Summary of Research

This thesis attempts to provide realistic and efficient analytical tools to aid the study of the hysteretic inelastic response of steel planar moment-resisting frames. The following is the summary of the contributions of this thesis :

(1) A uniaxial cyclic constitutive law valid under arbitrary transient loading, is proposed for structural steel. This physically motivated model incorporates the initial yield plateau and strain-hardening. It is based on simple hysteretic rules and is computationally efficient.

(2) Two beam-column models which include material and geometric nonlinearities are proposed, based on large-displacement small-strain formulation. These models incorporate features to include dynamic and hysteretic effects. The first model is based on the Beam-Column Approach with the capability of multiple segments. Features like buckling, internal hinging and plastic growth of the span are easily introduced. It accurately represents the strength of beam-columns. The second model is a comprehensive one based on the Finite Element Approach. It accurately models the stiffness as affected by yielding in hinge regions in addition to the strength.

(3) A simple semi-empirical phenomenological model is proposed to analytically describe the inelastic hysteretic behaviour of flexible joints in steel planar MRFs. This two parameter model is general and defines the joint behaviour over a wide inelastic range.

(4) A steel planar MRF without joint elements is studied to evaluate the performance of the various assumptions that may be made for beam-columns in order to reduce the computational effort in the frame analysis. Decisive conclusions are obtained.

(5) A steel planar MRF with flexible joints is studied for the effect of the panel zone design on the frame collapse. The effect of the panel zone plate thickness and the strength of the beams on the re-distribution of ductility demands between the beam-columns and joints is carefully examined.

8.2 Conclusions

The following are the salient conclusions of this thesis :

(1) The proposed Cubic Ellipsoidal Hysteretic Model for the uniaxial cyclic constitutive law for the axial stress-strain behaviour of structural steel is computationally very efficient and convenient.

(2) The proposed Plastic Hinge Model and Fibre Model beam-column elements simulate planar beam-column members very well.

(3) The proposed Joint Hysteresis Model successfully captures the highly nonlinear and hysteretic load-deformation characteristics of steel planar joint panel zones.

(4) For code designed beam-column members of seismic MRFs, approximate geometric stiffness is adequate. Large deformations must be included in the collapse analyses of frames. Inclusion of the P-Δ forces is critical in the realistic analyses of MRFs.

(5) Under moderate shaking, the Plastic Hinge Model and the Fibre Model beam-column elements result in almost identical frame responses. However, under severe shaking, the Fibre Model beam-column element is superior owing to its capability to handle strain-hardening.

(6) The design of flexible joint panel zones and the input ground motion signifi-

cantly affect the frame response. Ground motions with long-period acceleration content and large pulses, which are characteristic of big earthquakes, have a marked effect on the frame response. The yielding joints perform well except under ground motions with displacement jumps. The strong joints force plastic moment hinges to occur in the columns, which results in the collapse sway mechanisms in the frames.

(7) Plastic moment hinges in columns are detrimental to the stability of the frame.

8.3 Recommendations for Future Work

Based on the conclusions of this thesis, the following specific recommendations are made for future work in this area :

(1) The capability of the Plastic Hinge Model beam-column element to capture buckling and plastic growth in members under planar conditions may be extended to the inelastic hysteretic behaviour of planar rigid-jointed trusses.

(2) The idea of multi-segment Plastic Hinge Model and Fibre Model beam-column elements may be extended to the case of three-dimensional analysis. The inelastic hysteretic response of space frames and space trusses is a potential area of research.

(3) While contemplating realistic three-dimensional analysis, a need arises to thoroughly understand two-dimensional and three-dimensional material constitutive behaviour. Analytical models may be proposed to simulate them.

(4) The effect of soil-structure interaction is very crucial to the stability of tall building frames even under uniform ground motions. The rotation of the base of the building under soft soil conditions increases the contribution of the P-Δ forces on the frames. It is essential to include this effect in the collapse analyses of frames. Further, under non-uniform ground motion, the analyses become even more involved. However, the nonlinear response of tall buildings can be simulated more realistically by including this aspect also in the formulation of

frame analysis.

(5) From a design point of view, concentrated ductility demands in the columns are detrimental to frames under strong seismic excitation. To attract the ductility demands away from the columns, the excellent hysteretic properties of *flexible-joints* can be used to distribute the inelastic actions in the frame to as many different elements as possible that possess stable energy dissipating characteristics. Also, the design of the beams may also be changed to achieve the same end result. Based on this philosophy, design criteria, which make optimum use of panel zones and beams for earthquake resistance and seismic energy dissipation, need to be proposed for steel MRFs.

(6) For designing tall buildings to withstand big earthquakes, the design response spectra in the building codes must reflect the characteristics of all critical and relevant ground motions that are applicable for each geological region. Further, a need arises for an inelastic design response spectrum characteristic of each geological region. The elastic design response spectra in the UBC 1991 currently in use, does not cater to the specific case of tall buildings under severe ground motions.

...

REFERENCES

[1] Housner, G. W., "Limit Design of Structures to Resist Earthquakes," Proceedings of The First World Conference on Earthquake Engineering, Berkeley, California, June 1956.

[2] Berg, G. V., "The Analysis of Structural Response to Earthquake Forces," thesis presented to the University of Michigan, Ann Arbor, Michigan, in partial fulfillment of the requirements for the degree of Doctor of Philosophy, May 1958.

[3] Penzien, J., "Dynamic Response of Elasto-Plastic Frames," Journal of the Structural Division, Proceedings of the ASCE, Vol. 86, No. ST7, Proc. Paper 2545, July 1960, pp. 81-94.

[4] Jennings, P. C., "Response of Simple Yielding Structures to Earthquake Excitation," thesis presented to the California Institute of Technology, Pasadena, California, in partial fulfillment of the requirements for the degree of Doctor of Philosophy, 1963.

[5] Clough, R. W., and Benuska, K. L., "Nonlinear Earthquake Behaviour of Tall Buildings," Journal of the Engineering Mechanics Division, Proceedings of the ASCE, Vol. 93, No. EM3, Proc. Paper 5292, June 1967, pp. 129-146.

[6] Zienkiewicz, O. C., *The Finite Element Method in Engineering Science*, McGraw-Hill Book Company, Inc., London, 1971.

[7] Powell, G. H., and Chen, P. F., "3-D Beam-Column Element with Generalized Plastic Hinges," Journal of the Engineering Mechanics Division, Proceedings of the ASCE, Vol. 112, No. EM7, Proc. Paper 20711, July 1986, pp. 627-641.

[8] Latona, R. W., "Nonlinear Analysis of Building Frames for Earthquake Loading," thesis presented to Massachussetts Institute of Technology, Cambridge, Massachussetts, in partial fulfillment of the requirements for the degree of Doctor of Philosophy, Report No.: R70-65, September 1970.

[9] Goel, S. C., "P-Δ and Axial Column Deformation in Aseismic Frames,"

Journal of the Structural Division, Proceedings of the ASCE, Vol. 95, No. ST8, Proc. Paper 6738, August 1969, pp. 1693-1711.

[10] Kassimali, A., "Large Deformation Analysis of Elastic-Plastic Frames," Journal of the Structural Division, Proceedings of the ASCE, Vol. 109, No. ST8, Proc. Paper 18177, August 1983, pp. 1869-1886.

[11] Santhathadaporn, S., and Chen, W. F., "Tangent Stiffness Method for Biaxial Bending," Journal of the Structural Division, Proceedings of the ASCE, Vol. 98, No. ST1, Proc. Paper 8637, January 1972, pp. 153-163.

[12] Popov, E. P., "U.S. Seismic Steel Codes," Engineering Journal, American Institute of Steel Construction, Vol. 28, No. 3, 1991, pp. 119-128.

[13] Chen, P. F., and Powell, G. H., "Generalized Plastic Hinge Concepts for 3-D Beam-Column Elements," Report No.: UCB/EERC 82-20, Earthquake Engineering Research Centre, University of California, Berkeley, California, November 1982.

[14] Krawinkler, H., Bertero, V. V., and Popov, E. P., "Inelastic Behaviour of Steel Beam-to-Column Subassemblages," Report No.: UCB/EERC 71-7, Earthquake Engineering Research Centre, University of California, Berkeley, California, October 1971.

[15] Pinkney, R. B., "Cyclic Plastic Analysis of Structural Steel Joints," Report No.: UCB/EERC 73-15, Earthquake Engineering Research Centre, University of California, Berkeley, California, August 1973.

[16] Krawinkler, H., Bertero, V. V., and Popov, E. P., "Shear Behaviour of Steel Frame Joints," Journal of the Structural Division, Proceedings of the ASCE, Vol. 101, No. ST11, Proc. Paper 11717, November 1975, pp. 2317-2334.

[17] Kato, B., "Beam-to-Column Connection Research in Japan," Journal of the Structural Division, Proceedings of the ASCE, Vol. 108, No. ST2, Proc. Paper 16852, February 1982, pp. 343-360.

[18] Fielding, D. J., and Chen, W. F., "Steel Frame Analysis and Connection Shear Deformation," Journal of the Structural Division, Proceedings of the ASCE, Vol. 99, No. ST1, Proc. Paper 9481, January 1973, pp. 1-18.

[19] Uniform Building Code (UBC), International Conference of Building Officials, Whittier, California, 1991.

[20] "Recommended Lateral Force Requirements and Commentary," Seismology Committee, Structural Engineers Association of California (SEAOC), Sacramento, California, 1990.

[21] Meyer, C., "Inelastic Dynamic Analysis of Tall Buildings," Journal of Earthquake Engineering and Structural Dyanmics, John Wiley and Sons, Ltd., Vol. 2, 1974, pp. 325-342.

[22] Caughey, T. K., "Classical Normal Modes in Damped Linear Dynamic Systems," Journal of Applied Mechanics, Vol. 27, 1960, pp. 269-271.

[23] "Strong Motion Earthquake Accelerograms :: Digitized and Plotted Data," Vol. II, Part C, Report No.: EERL 72-51, Earthquake Engineering Research Laboratory, California Institute of Technology, Pasadena, California, February 1973.

[24] Heaton, T.H., "Near-Field Ground Motions in Large Earthquakes and Base-Isolated Structures," Seismological Research Letters, Vol. 62, Number 1, January-March 1991, pp. 49.

[25] Hartzell, S., and Heaton, T.H., "San Andreas Deterministic Fault Problem Green's Function Summation for a Finite Source," EPRI/STANFORD/USGS Workshop on Earthquake Ground Motions at Close Distances, Palo Alto, California, 5-6 September 1990.

[26] Tsai, K-C., and Popov, E. P., "Steel Beam-Column Joints in Seismic Moment Resisting Frames," Report No.: UCB/EERC 88-19, Earthquake Engineering Research Centre, University of California, Berkeley, California, November 1988.

[27] Clough, R. W., Benuska, K. L., and Wilson, E. L., "Inelastic Response

of Tall Buildings," Proceedings of The Third World Conference on Earthquake Engineering, Auckland and Wellington, New Zealand, Vol. I, 1965, pp. 68-89.

[28] Porter, F. L., and Powell, G. H., "Static and Dynamic Analysis of Inelastic Framed Structures," Report No.: UCB/EERC 71-03, Earthquake Engineering Research Centre, University of California, Berkeley, California, June 1971.

[29] Giberson, M. F., "The Response of Nonlinear Multi-Storey Structures subjected to Earthquake Excitation," thesis presented to the California Institute of Technology, Pasadena, California, in partial fulfillment of the requirements for the degree of Doctor of Philosophy, Earthquake Engineering Research Laboratory, May 1967.

[30] Hays, Jr., C. O., and Matlock, H., "Nonlinear Discrete Element Analysis of Frames," Journal of the Structural Division, Proceedings of the ASCE, Vol. 99, No. ST10, Proc. Paper 10091, October 1973, pp. 2011-2030.

[31] Powell, G. H., and Chen, P. F., "3-D Beam-Column Element with Generalized Plastic Hinges," Journal of the Engineering Mechanics Division, Proceedings of the ASCE, Vol. 112, No. EM7, Proc. Paper 20711, July 1986, pp. 627-641.

[32] Ekhande, S. G., Selvappalam, M., and Madugula, M. K. S., "Stability Functions for Three-Dimensional Beam-Columns," Journal of the Structural Division, Proceedings of the ASCE, Vol. 115, No. ST2, Proc. Paper 23230, February 1989, pp. 467-479.

[33] Chen, W. F., and Atsuta, T., *Theory of Beam-Columns, Vols.: 1 and 2*, McGraw-Hill International Book Company, Inc., New York, 1977.

[34] Oran, C., "Tangent Stiffness in Plane Frames," Journal of the Structural Division, Proceedings of the ASCE, Vol. 99, No. ST6, Proc. Paper 9810, June 1973, pp. 973-985.

[35] Kassimali, A., "Nonlinear Static and Dynamic Analysis of Frames," thesis presented to the University of Missouri, Columbia, Missouri, in partial fulfillment

of the requirements for the degree of Doctor of Philosophy, August 1976.

[36] Uniform Building Code (UBC), International Conference of Building Officials, Whittier, California, 1988.

[37] Ikeda, K., Mahin, S. A., and Dermitzakis, S. N., "Phenomenological modelling of Steel Braces under Cyclic Loading," Report No.: UCB/EERC 84-09, Earthquake Engineering Research Centre, University of California, Berkeley, California, May 1984.

[38] Kahn, L. F., and Hanson, R. D., "Inelastic Cycles of Axially Loaded Steel Members," Journal of the Structural Division, Proceedings of the ASCE, Vol. 102, No. ST5, Proc. Paper 12111, May 1976, pp. 947-959.

[39] *Manual of Steel Construction : Load and Resistance Factor Design*, 1st Edition, American Institute of Steel Construction, Inc., 1986.

[40] Jayakumar, P., "Modelling and Identification in Structural Dynamics," thesis presented to the California Institute of Technology, Pasadena, California, in partial fulfillment of the requirements for the degree of Doctor of Philosophy, Earthquake Engineering Research Laboratory, Report No.: EERL 87-01, May 1987.

[41] Kent, D. C., "Inelastic Behaviour of Reinforced Concrete Members with Cyclic Loading," thesis presented to University of Canterbury, Christchurch, New Zealand, in partial fulfillment of the requirements for the degree of Doctor of Philosophy, 1969.

[42] Stanton, J. F., and McNiven, H. D., "The Development of a Mathematical Model to Predict the Flexural Response of Reinforced Concrete Beams to Cyclic Loads, Using System Identification," Earthquake Engineering Research Centre, Report No.: UCB/EERC 79-02, University of California, Berkeley, California, January 1979.

[43] Hays, Jr., C. O., "Inelastic Material Models in Earthquake Response," Journal of the Structural Division, Proceedings of the ASCE, Vol. 107, No. ST1,

Proc. Paper 15971, January 1981, pp. 13-28.

[44] Santhanam, T. K., "Model for Mild Steel in Inelastic Frame Analysis," Journal of the Structural Division, Proceedings of the ASCE, Vol. 105, No. ST1, Proc. Paper 14333, January 1979, pp. 199-215.

[45] Petersson, H., and Popov, E. P., "Constitutive Relations for Generalised Loadings," Journal of the Engineering Mechanics Division, Proceedings of the AS CE, Vol. 103, No. EM4, Proc. Paper 13144, August 1977, pp. 611-627.

[46] Filippou, F. C., Popov, E. P., and Bertero, V. V., "Effects of Bond Deterioration on Hysteretic Behaviour of Reinforced Concrete Joints," Report No.: UCB/EERC 83-19, Earthquake Engineering Research Centre, University of California, Berkeley, California, August 1983, pp. 34-35.

[47] Popov, E. P., and Petersson, H., "Cyclic Metal Plasticity : Experiments and Theory," Journal of the Engineering Mechanics Division, Proceedings of the ASCE, Vol. 104, No. EM6, Proc. Paper 14257, December 1978, pp. 1371-1388.

[48] Masing, G., "Eigenspannungen Und Verfestigung Beim Messing," Proceedings of the Second International Congress for Applied Mechanics, Zurich, Switzerland, 1926 (in German), pp. 332-335.

[49] Krawinkler, H., "Shear in Beam-Column Joints in Seismic Design of Steel Frames," Engineering Journal, Proceedings of the AISC, No. 3, 1978, pp. 82-91.

[50] Bertero, V. V., Popov, E. P., and Krawinkler, H., "Beam-Column Sub-Assemblages under Repeated Loading," Journal of the Structural Division, Proceedings of the ASCE, Vol. 98, No. ST5, Proc. Paper 8915, May 1972, pp. 1137-1159.

[51] Becker, R., "Panel Zone Effect on the Strength and Stiffness of Steel Rigid Frames," Engineering Journal, American Institute of Steel Construction, Inc., New York, No. 1, 1975, pp. 19-29.

[52] Nakao, M., "Experiment of the Behaviour of Steel Beam-to-Column Con-

nections with Large Axial Force of Column," Annual Report of Engineering Research Institute, University of Tokyo, Tokyo, Japan, Vol. 32, July 1973.

[53] Krawinkler, H., and Popov, E. P., "Seismic Behaviour of Moment Connections and Joints," Journal of the Structural Division, Proceedings of the ASCE, Vol. 108, No. ST2, Proc. Paper 16865, February 1982, pp. 373-391.

...

Table 2.1 : Duration, T, peak ground acceleration, a_0, peak ground velocity, v_0, and peak ground displacement, d_0, of the synthetic ground motions with a large velocity pulse simulating fault-parallel (SP) motion, see Fig.2.8, and fault-normal (SN) motion, see Fig.2.9.

Type of Pulse	No.	T	a_0	v_0	d_0
		(sec)	(mm/sec^2)	(mm/sec)	(mm)
SP	1	1.0	4000.0	1000.0	500.0
	2	2.0	2000.0	1000.0	1000.0
	3	1.0	8000.0	2000.0	1000.0
	4	2.0	4000.0	2000.0	2000.0
	5	1.0	16000.0	4000.0	2000.0
SN	6	1.0	8000.0	1000.0	292.0
	7	2.0	4000.0	1000.0	583.0
	8	1.0	16000.0	2000.0	583.0
	9	2.0	8000.0	2000.0	1167.0

Table 3.1 : Criteria for validating a characteristic state as the final state of the segment. $\dot{\theta}$ is the applied incremental end-rotation, and $\dot{\phi}$ is the increment in the elastic end-rotation within the plastic hinge.

	Criterion	
State	@ Node 2	@ Node 1
1	$\lvert M_2\rvert < M_{pr}$	$\lvert M_1\rvert < M_{pr}$
2	$\lvert M_2\rvert < M_{pr}$	$\dot{\theta}_1 - \dot{\phi}_1 \geq 0$
3	$\lvert M_2\rvert < M_{pr}$	$\dot{\theta}_1 - \dot{\phi}_1 \leq 0$
4	$\dot{\theta}_2 - \dot{\phi}_2 \geq 0$	$\lvert M_1\rvert < M_{pr}$
5	$\dot{\theta}_2 - \dot{\phi}_2 \leq 0$	$\lvert M_1\rvert < M_{pr}$
6	$\dot{\theta}_2 - \dot{\phi}_2 \geq 0$	$\dot{\theta}_1 - \dot{\phi}_1 \geq 0$
7	$\dot{\theta}_2 - \dot{\phi}_2 \geq 0$	$\dot{\theta}_1 - \dot{\phi}_1 \leq 0$
8	$\dot{\theta}_2 - \dot{\phi}_2 \leq 0$	$\dot{\theta}_1 - \dot{\phi}_1 \geq 0$
9	$\dot{\theta}_2 - \dot{\phi}_2 \leq 0$	$\dot{\theta}_1 - \dot{\phi}_1 \leq 0$

Table 6.1 : List of axial load capacity, P_y, and bending moment capacity, M_p, for each of the MRF members. The units for axial load is $10^6 N$, and for bending moment is $10^9 N-mm$.

Storey	Columns			
	Interior		Exterior	
	P_y	M_p	P_y	M_p
20	5.79	1.26	5.16	0.79
19	5.79	1.26	5.16	0.79
18	6.93	1.71	6.26	0.96
17	6.93	1.71	6.26	0.96
16	6.93	1.71	7.53	1.18
15	6.93	1.71	7.53	1.18
14	7.69	1.92	8.35	1.31
13	7.69	1.92	8.35	1.31
12	7.69	1.92	10.00	1.60
11	7.69	1.92	10.00	1.60
10	7.69	1.92	12.19	2.00
9	7.69	1.92	12.19	2.00
8	8.44	2.32	13.44	2.22
7	8.44	2.32	13.44	2.22
6	8.44	2.32	14.74	2.47
5	8.44	2.32	14.74	2.47
4	8.44	2.32	16.29	2.75
3	8.44	2.32	16.29	2.75
2	9.05	2.76	17.58	3.02
1	9.05	2.76	17.58	3.02
B	9.05	2.76	17.58	3.02
Floor	Beams			
	Interior		Exterior	
	P_y	M_p	P_y	M_p
Roof	4.00	1.00	4.00	1.00
20	4.00	1.00	4.00	1.00
19	4.69	1.28	4.69	1.28
18	4.69	1.28	4.69	1.28
17	4.69	1.28	4.69	1.28
16	4.69	1.28	4.69	1.28
rest	5.52	1.55	5.52	1.55

Table 6.2 : List of MRF analyses indicating the assumptions made regarding the significant frame effects.

Analysis	Geometric Stiffness	Deformations	P-Δ Effect
F1	Exact	Large	Exact
F2	Approx.	Large	Exact
F3	Approx.	Small	Approx.
F4	-	Small	-
F5	Exact	Large	Exact

Table 6.3 : Natural Periods of the first three modes of the MRF without and with joint elements, in seconds.

	No Joint Elements	Joint Elements		
Mode		Design I	Design II	Design III
1	3.80	3.54	3.34	3.17
2	1.27	1.20	1.12	1.06
3	0.72	0.68	0.64	0.60

Table 7.1 : Joint dimensions of the MRF with joint elements, in millimeters.

	Exterior Joints			Interior Joints		
Floor	d_c	d_b	t	d_c	d_b	t
21	363.73	678.43	13.34	550.67	678.43	15.24
20	363.73	678.43	13.34	550.67	678.43	15.24
19	372.36	753.11	16.38	628.40	753.11	16.51
18	372.36	753.11	16.38	628.40	753.11	16.51
17	380.49	753.11	18.92	628.40	753.11	16.51
16	380.49	753.11	18.92	628.40	753.11	16.51
15	386.59	762.25	21.08	635.00	762.25	17.91
14	386.59	762.25	21.08	635.00	762.25	17.91
13	399.29	762.25	24.89	635.00	762.25	17.91
12	399.29	762.25	24.89	635.00	762.25	17.91
11	416.05	762.25	29.85	635.00	762.25	17.91
10	416.05	762.25	29.85	635.00	762.25	17.91
9	425.20	762.25	32.77	706.37	762.25	18.42
8	425.20	762.25	32.77	706.37	762.25	18.42
7	434.85	762.25	35.81	706.37	762.25	18.42
6	434.85	762.25	35.81	706.37	762.25	18.42
5	445.52	762.25	39.12	706.37	762.25	18.42
4	445.52	762.25	39.12	706.37	762.25	18.42
3	455.17	762.25	42.04	779.27	762.25	18.03
2	455.17	762.25	42.04	779.27	762.25	18.03
1	455.17	762.25	42.04	779.27	762.25	18.03

Table 7.2 : Doubler plate thicknesses provided in the three joint panel zone designs of the MRF with joint elements, in millimeters.

	Exterior Joints			Interior Joints		
Floor	Design I	Design II	Design III	Design I	Design II	Design III
21	-	9.12	28.76	-	14.42	40.37
20	-	9.12	28.76	-	14.42	40.37
19	-	8.88	30.99	-	13.43	39.63
18	-	8.88	30.99	-	13.43	39.63
17	-	5.80	27.43	-	13.43	39.63
16	-	5.80	27.43	-	13.43	39.63
15	-	8.05	33.53	-	17.56	48.59
14	-	8.05	33.53	-	17.56	48.59
13	-	3.31	27.98	-	17.56	48.59
12	-	3.31	27.98	-	17.56	48.59
11	-	-	20.90	-	17.56	48.59
10	-	-	20.90	-	17.56	48.59
9	-	-	16.89	-	13.47	41.36
8	-	-	16.89	-	13.47	41.36
7	-	-	12.74	-	13.47	41.36
6	-	-	12.74	-	13.47	41.36
5	-	-	8.27	-	13.47	41.36
4	-	-	8.27	-	13.47	41.36
3	-	-	4.35	-	10.87	36.15
2	-	-	4.35	-	10.87	36.15
1	-	-	4.35	-	10.87	36.15

Table 7.3 : List of analyses of the three MRFs indicating the type of acceleration ground motion (See Sec.2.7). HI, PD, SP and SN stand for Holiday Inn record, Pacoima Dam record, synthetic fault-parallel pulse and synthetic fault-normal pulse, respectively.

Ground Motion	Scaled to	Analyses		
		MRF1	MRF2	MRF3
HI	0.4g(peak)	A4	B4	C4
	0.5g(peak)	A5	B5	C5
	0.6g(peak)	A6	-	C6
	0.7g(peak)	A7	-	-
PD	original	A0	B0	C0
SP 1	-	P1	Q1	R1
SP 2	-	P2	Q2	R2
SP 3	-	P3	Q3	R3
SP 4	-	P4	Q4	R4
SP 5	-	P5	Q5	R5
SN 6	-	P6	Q6	R6
SN 7	-	P7	Q7	R7
SN 8	-	P8	Q8	R8
SN 9	-	P9	Q9	R9

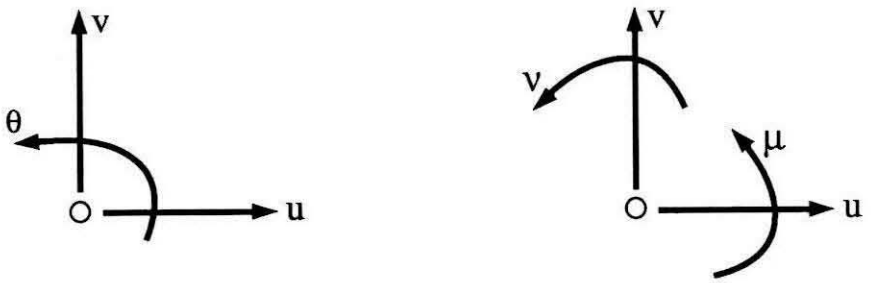

(a) Frame without joint elements (b) Frame with joint elements

Figure 2.1 : Degrees of freedom of global nodes in the discretisation of planar moment resisting frames.

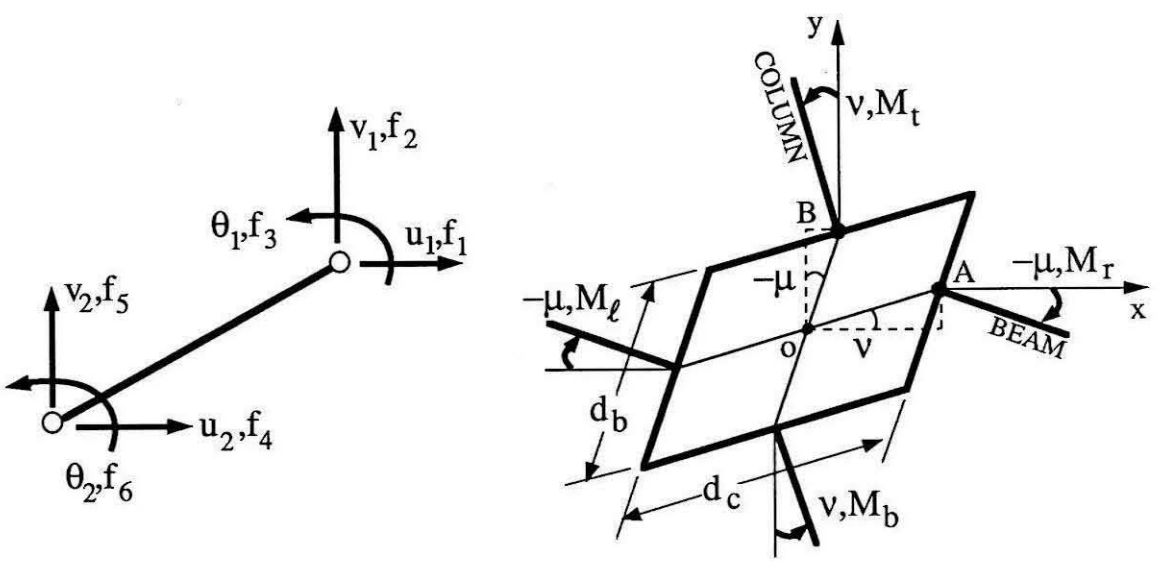

(a) Beam-column (b) Joint

Figure 2.2 : Degrees of freedom of the planar beam-column and joint elements.

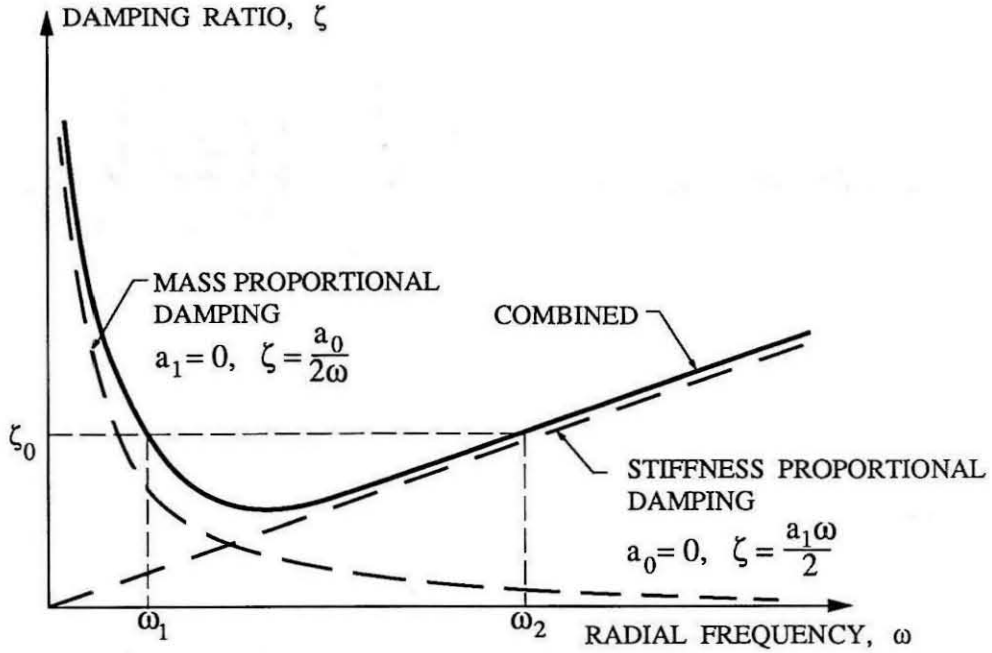

Figure 2.3 : Frequency dependance of viscous damping as estimated using Rayleigh damping terms of the Caughey Damping Series.

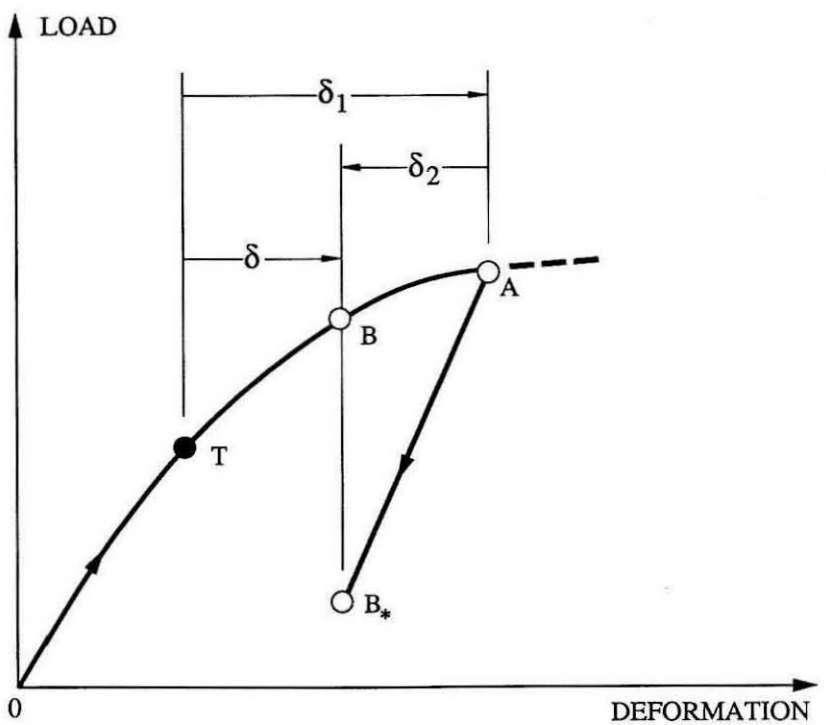

Figure 2.4 : Undesirable artificial unloading during iterations in direct stiffness approach.

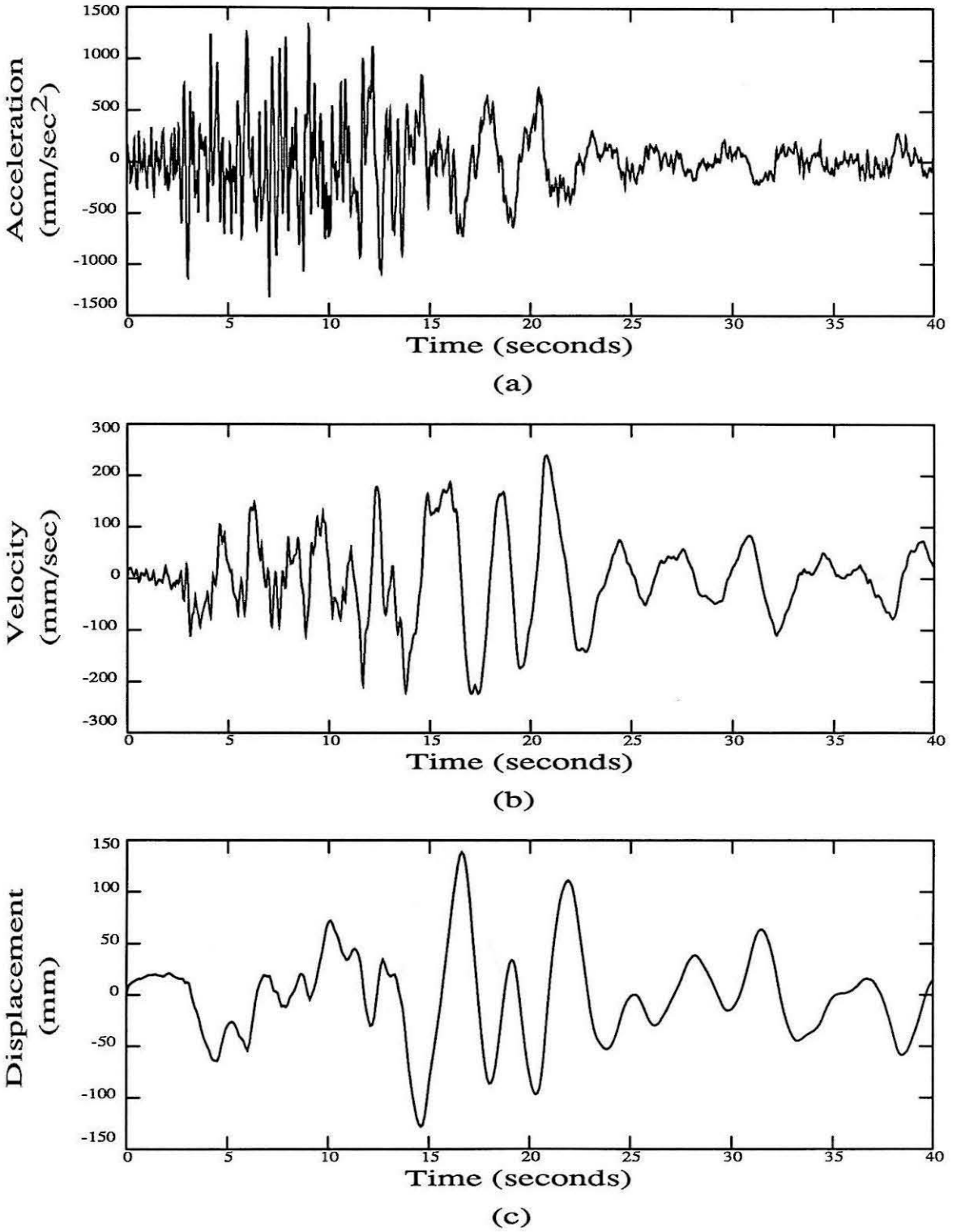

Figure 2.5 : Corrected and digitized data [23] of the 9th February 1971 San Fernando Earthquake recorded at the Holiday Inn, Ground Floor, 8244 Orion Blvd., Los Angeles, California, S90W component.

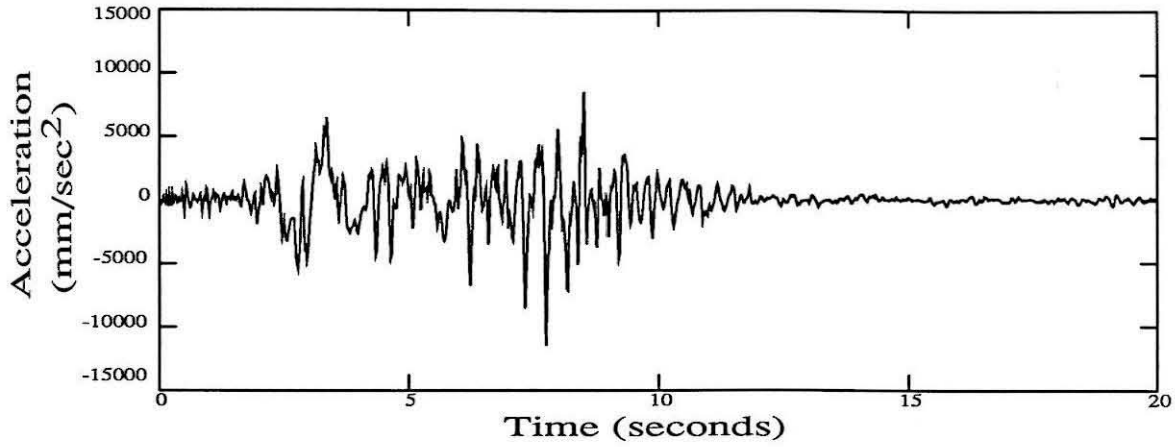

(a)

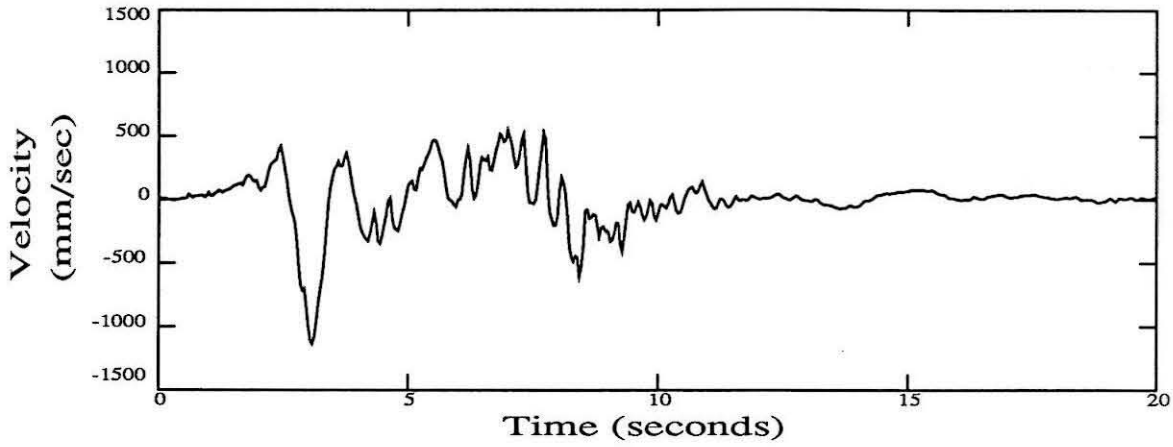

(b)

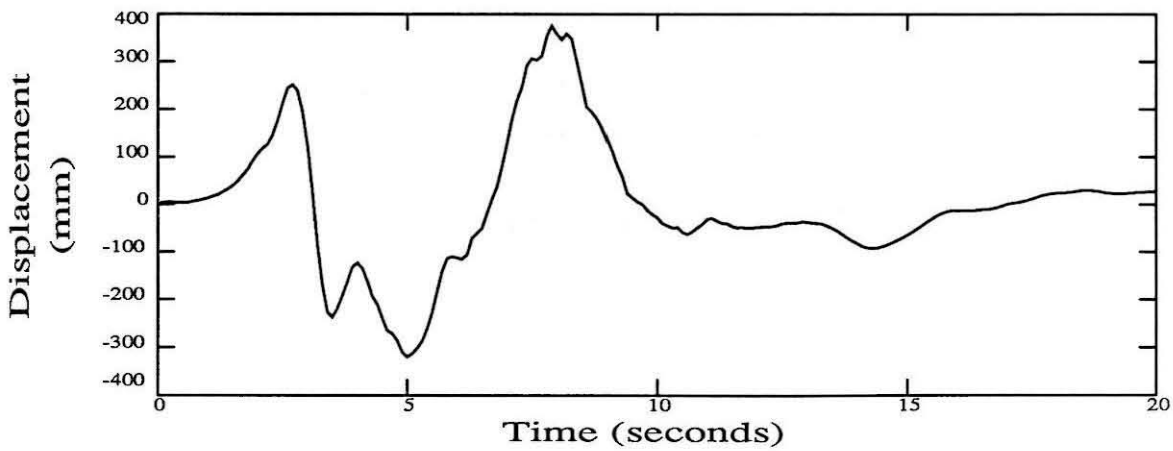

(c)

Figure 2.6 : Corrected and digitized data [23] of the 9th February 1971 San Fernando Earthquake recorded at the Pacoima Dam, California, S16E component.

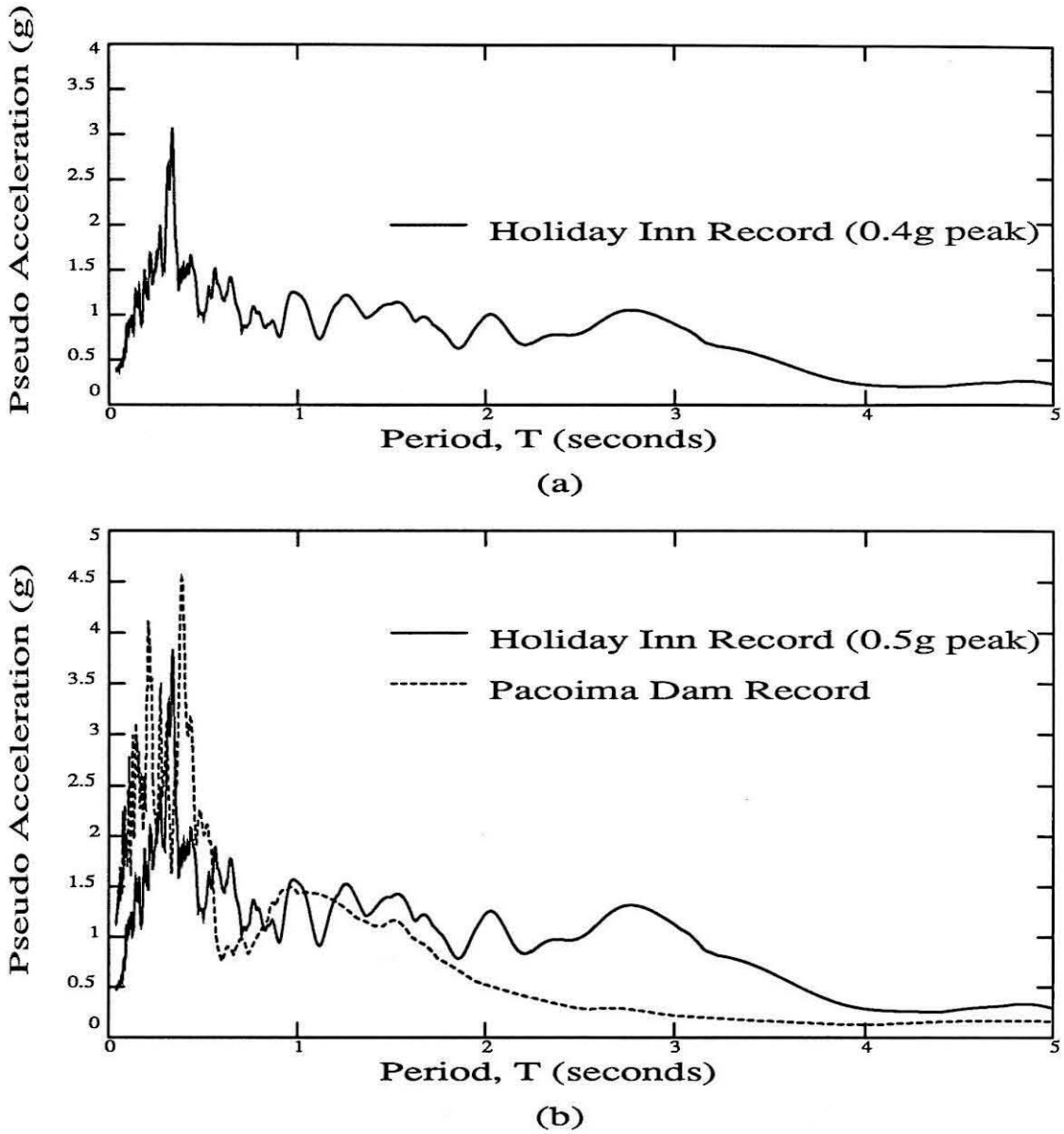

Figure 2.7 : Pseudo-acceleration spectra normalised with acceleration due to gravity for 2% damping of the 9th February 1971 San Fernando Earthquake :

(a) Holiday Inn record, Ground Floor, 8244 Orion Blvd., Los Angeles, California, S90W component, scaled to 0.4g (peak), and

(b) Holiday Inn record, Ground Floor, 8244 Orion Blvd., Los Angeles, California, S90W component, scaled to 0.5g (peak), and Pacoima Dam record, California, S16E component, unscaled.

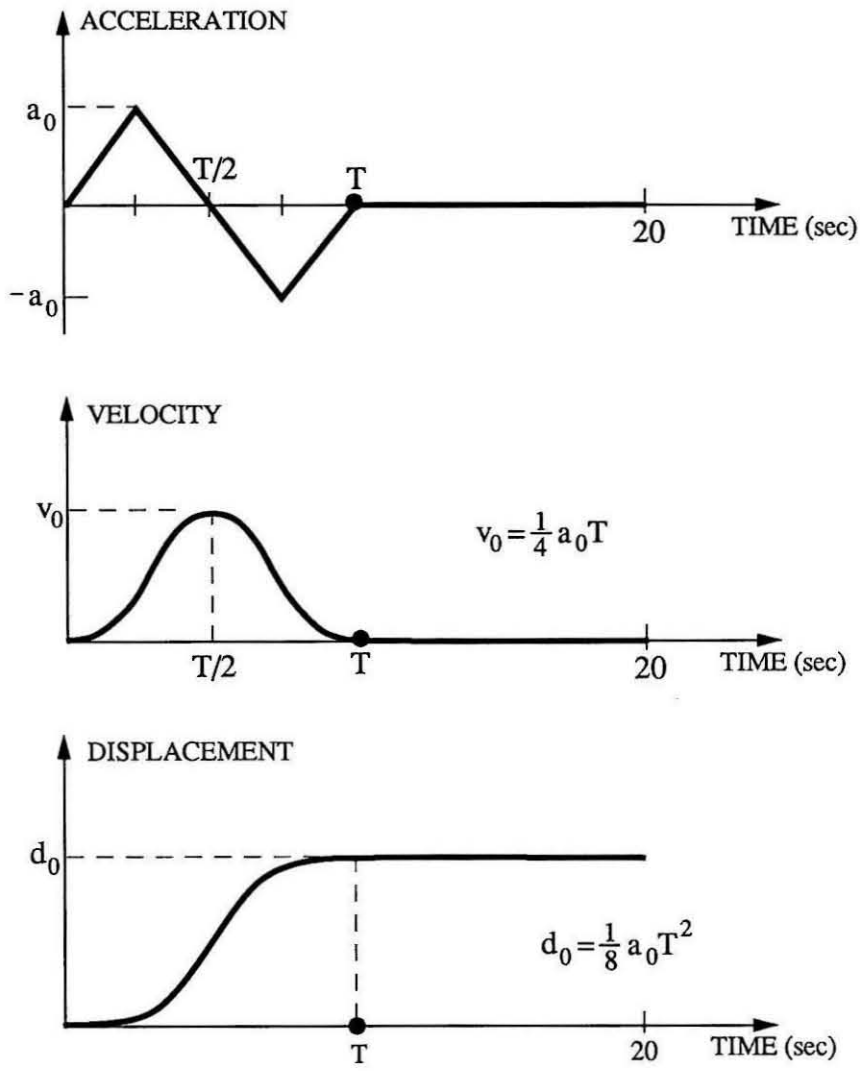

Figure 2.8 : Synthetic ground motion simulating fault-parallel motion with a large velocity pulse.

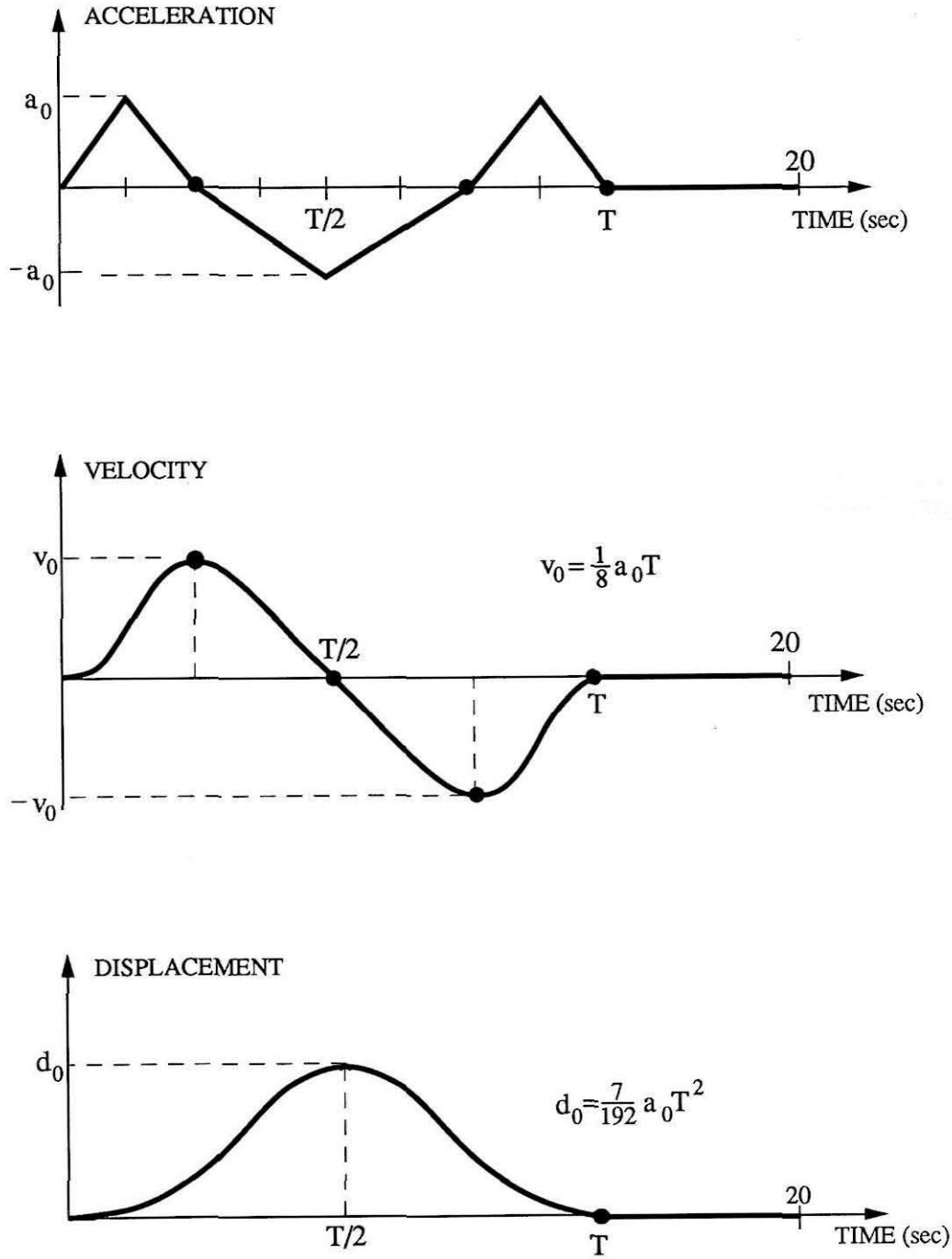

Figure 2.9 : Synthetic ground motion simulating fault-normal motion with a large velocity pulse.

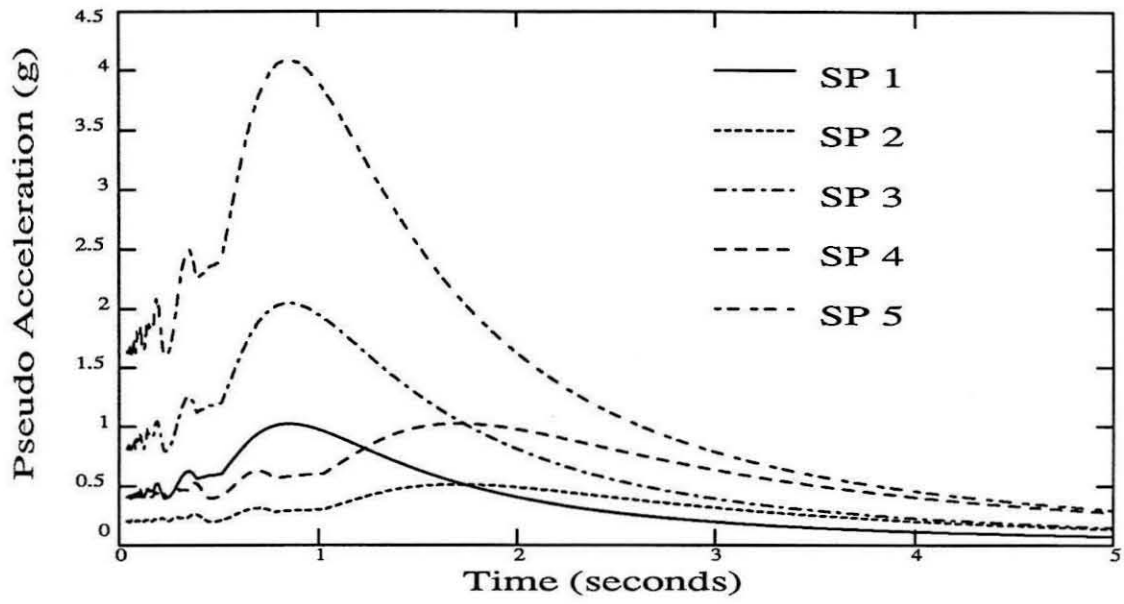

(a) Fault-parallel pulses

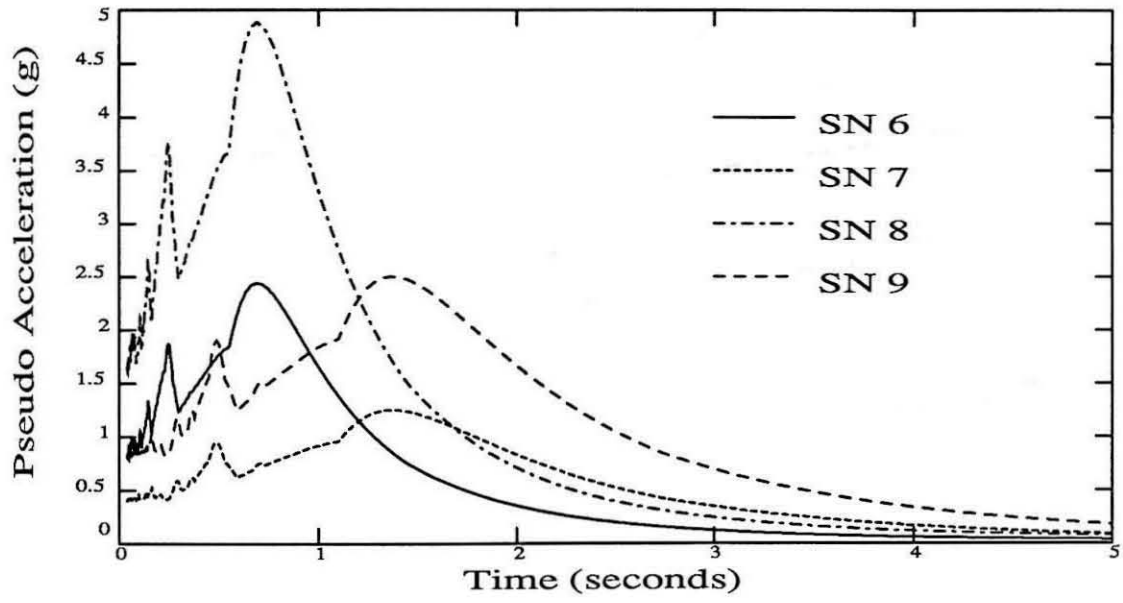

(b) Fault-normal pulses

Figure 2.10 : Pseudo-acceleration response spectra normalised with acceleration due to gravity, of the synthetic ground motions simulating fault-parallel and fault-normal motions.

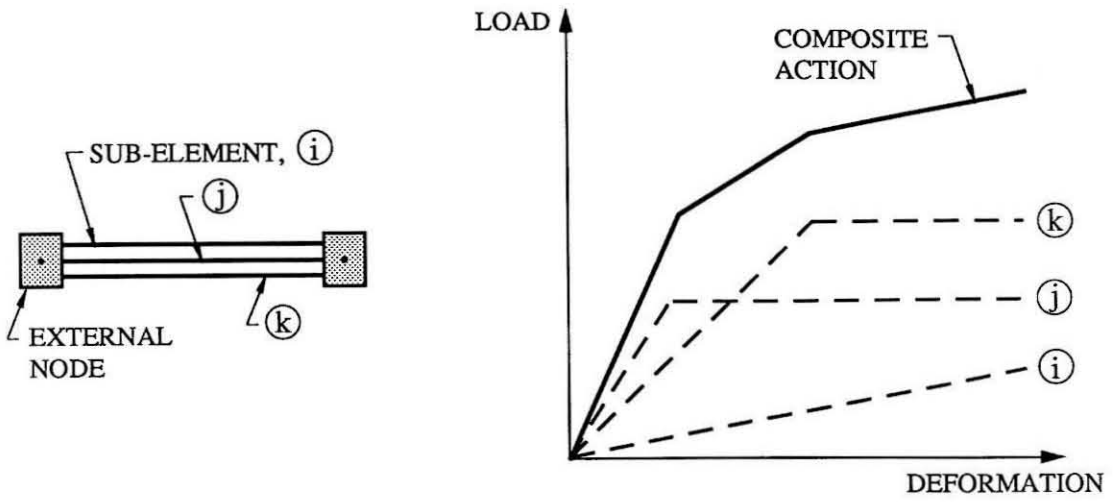

(a) Parallel Element Model

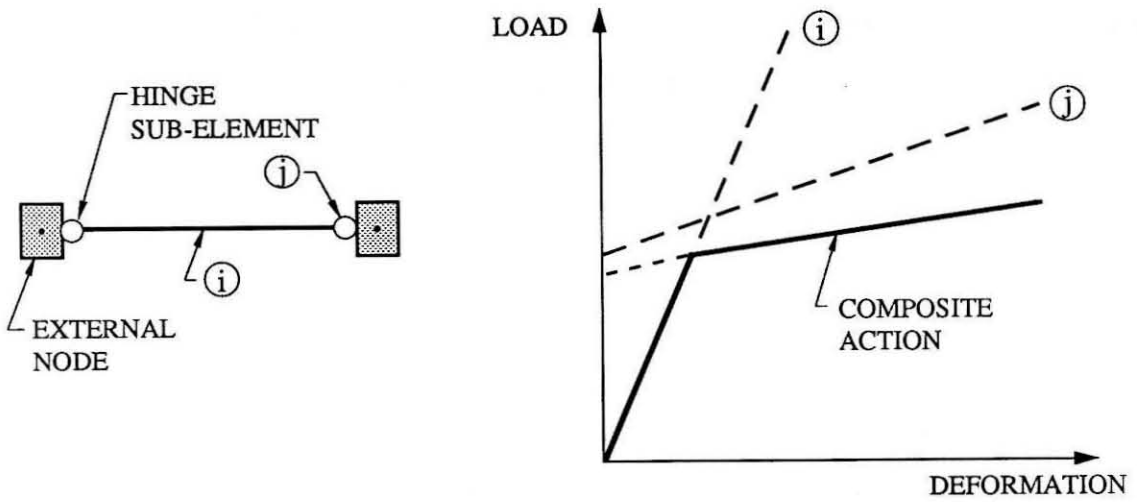

(b) Series Element Model

Figure 3.1 : Physical idealisation and load-deformation curves of the two types of simplified lumped plasticity models for beam-columns.

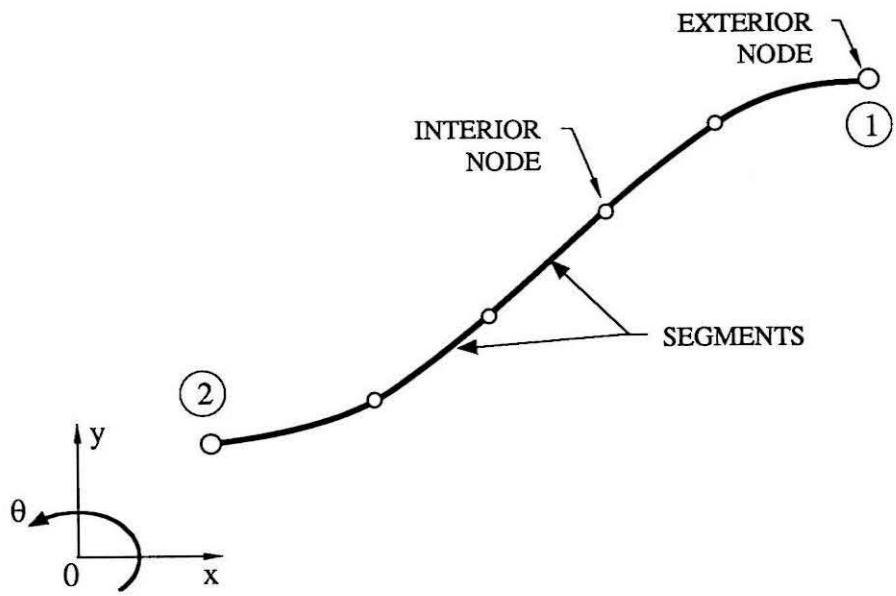

Figure 3.2 : Exterior and interior nodes of a Plastic Hinge Model beam-column element composed of multiple segments.

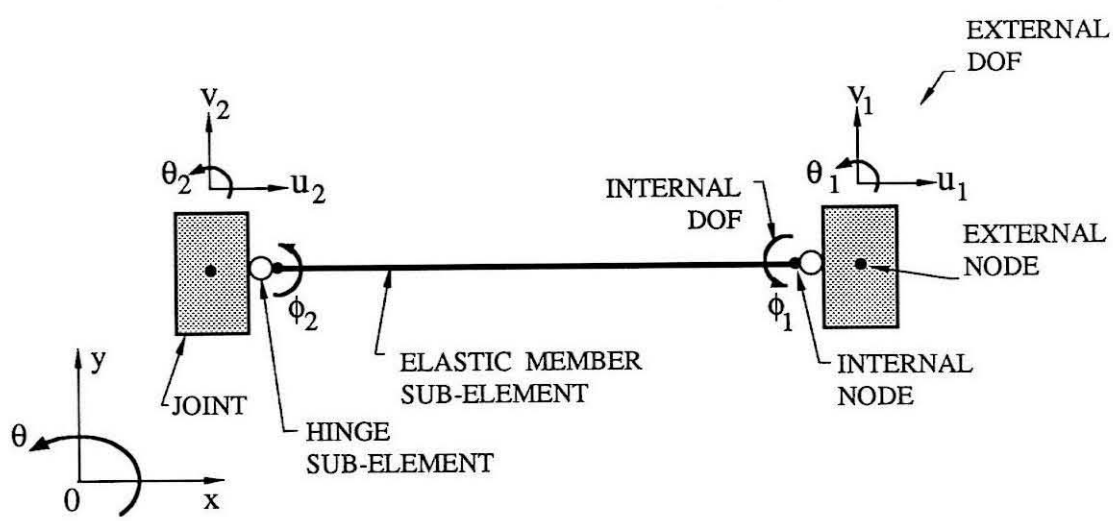

Figure 3.3 : Idealisation of a Plastic Hinge Model beam-column segment indicating its sub-elements and degrees of freedom.

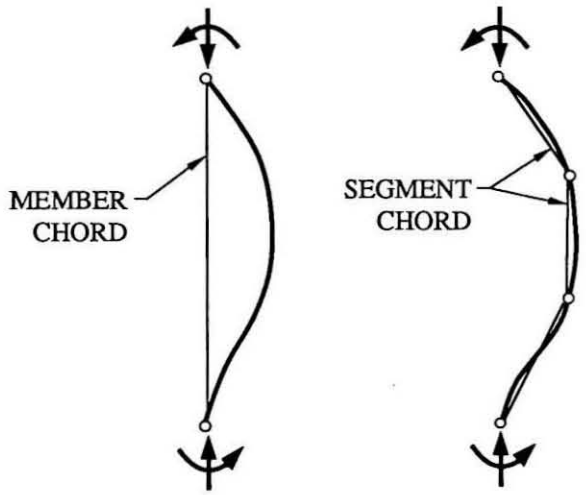

(a) Chord Definitions

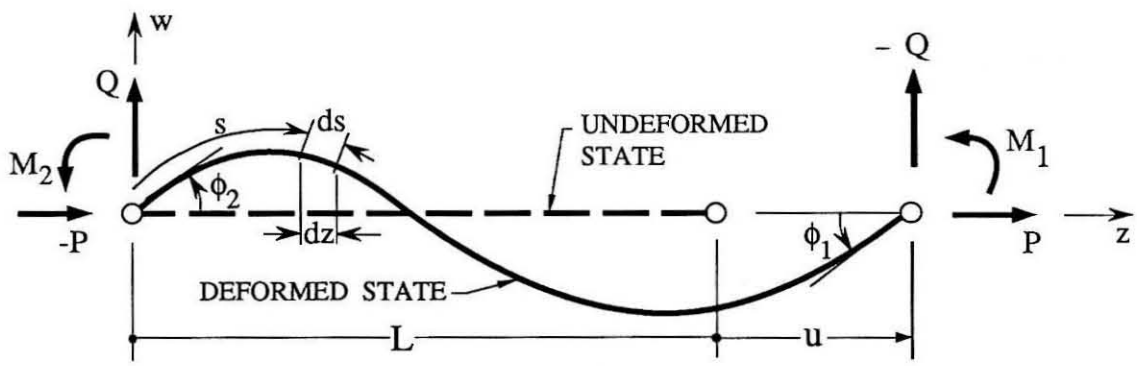

(b) Beam-column Segment in Member Coordinates

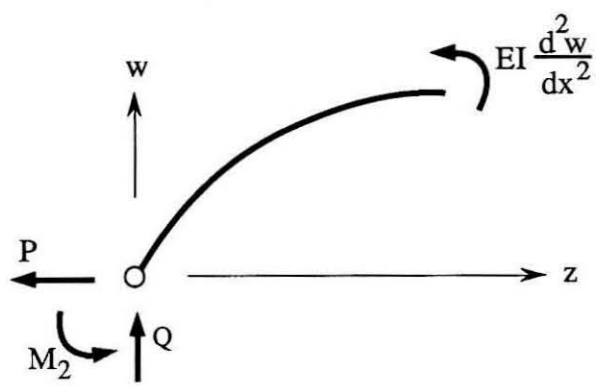

(c) Free-body Diagram for Moment Equlibrium

Figure 3.4 : Deformed and undeformed configurations of a Plastic Hinge Model beam-column segment in member coordinates.

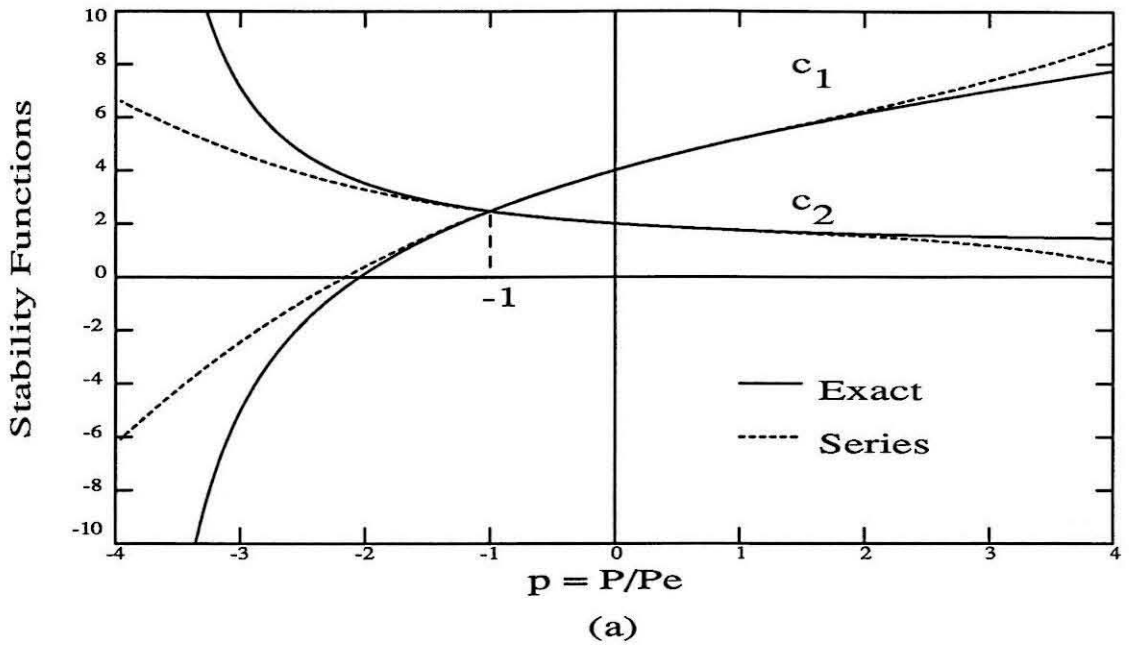

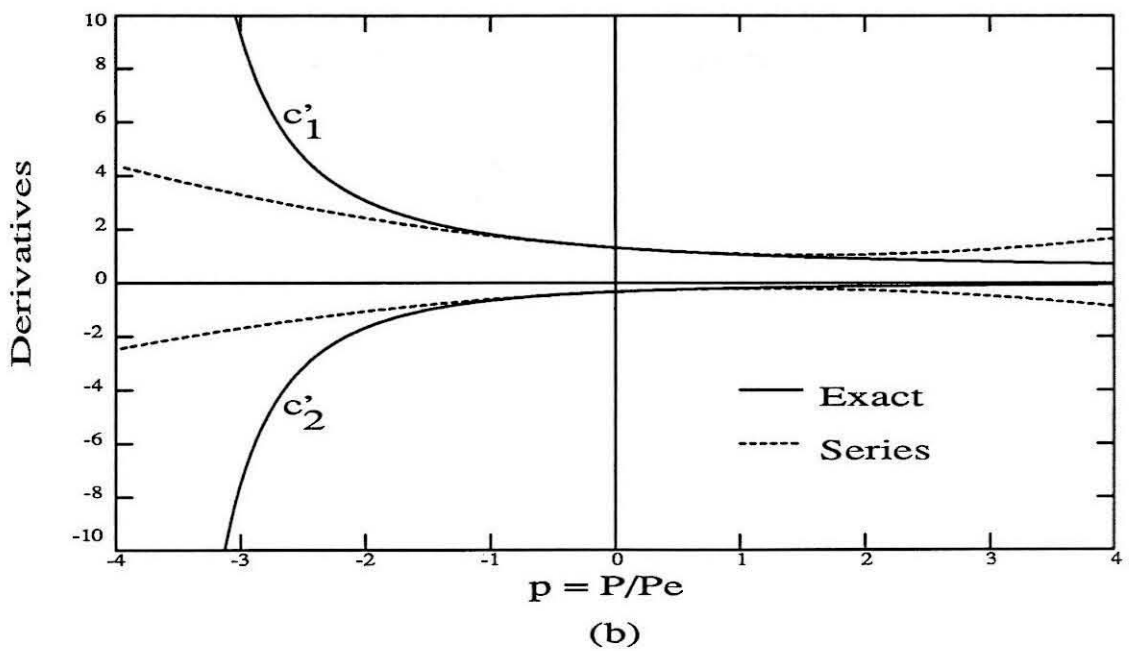

Figure 3.5 : Stability functions and their derivatives with the corresponding series expansions about $p = 0$ as a function of the normalised axial load.

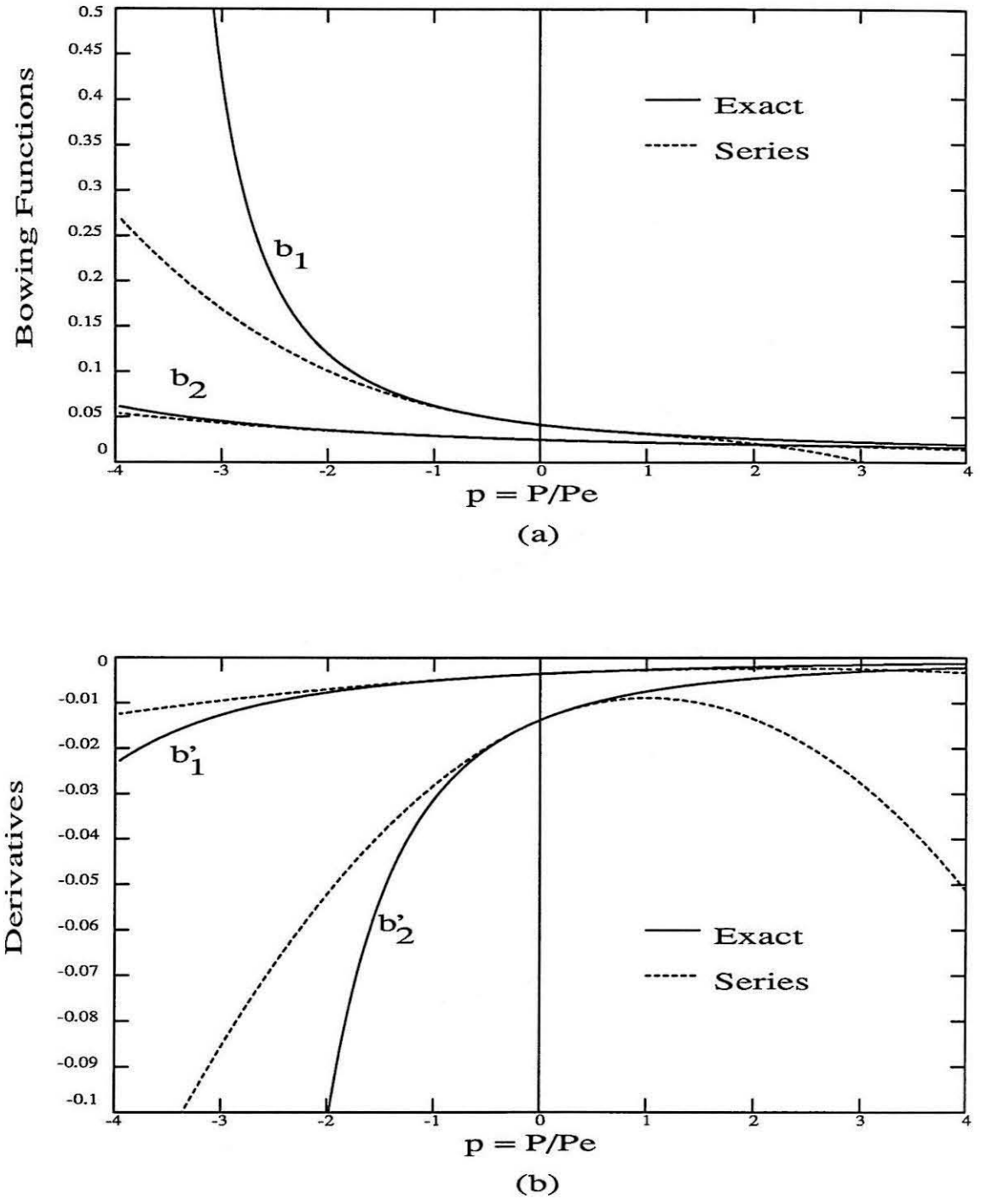

Figure 3.6 : Bowing functions and their derivatives with the corresponding series expansions about $p = 0$ as a function of the normalised axial load.

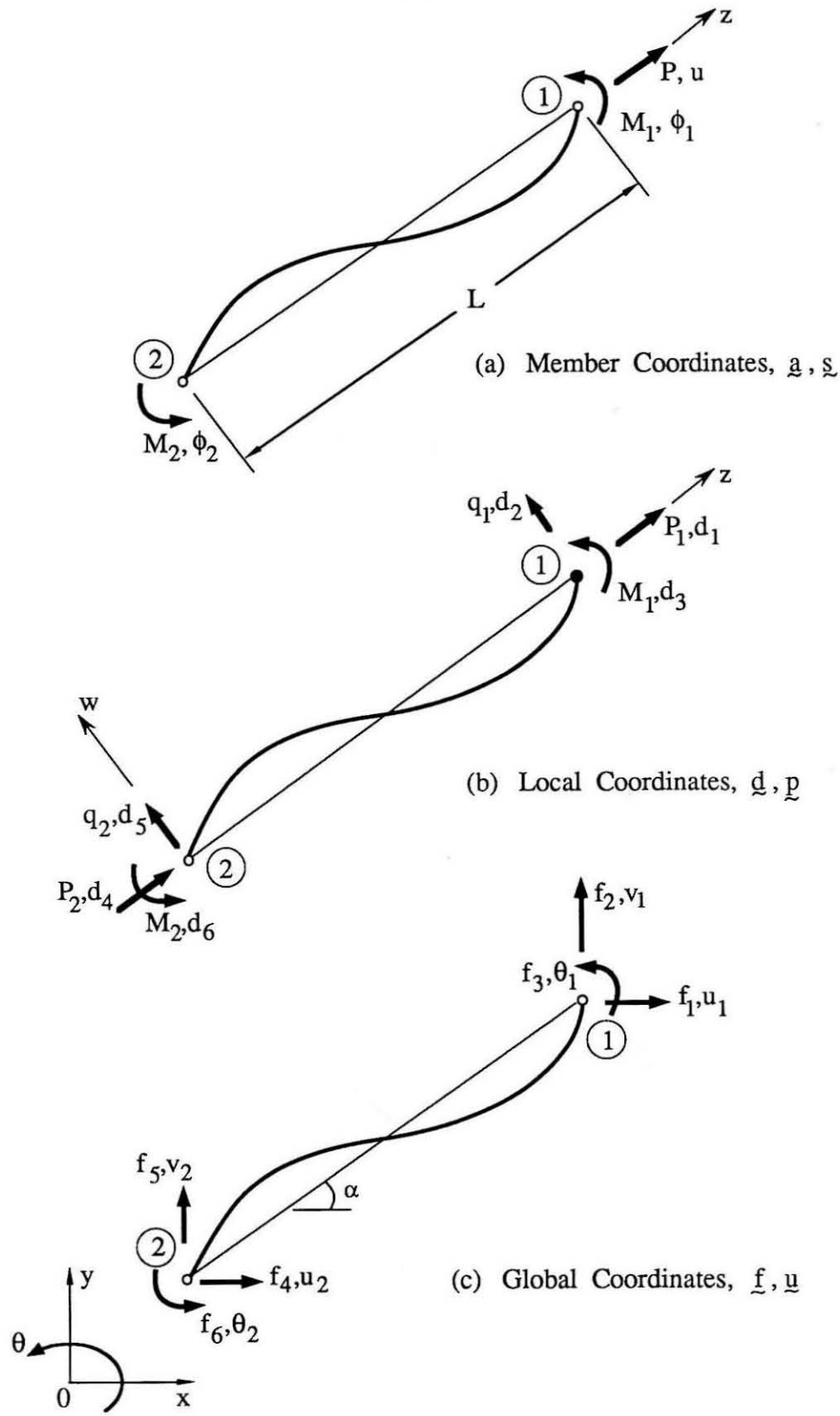

Figure 3.7 : Degrees of freedom and end-forces in different coordinate frames of a Plastic Hinge Model beam-column segment.

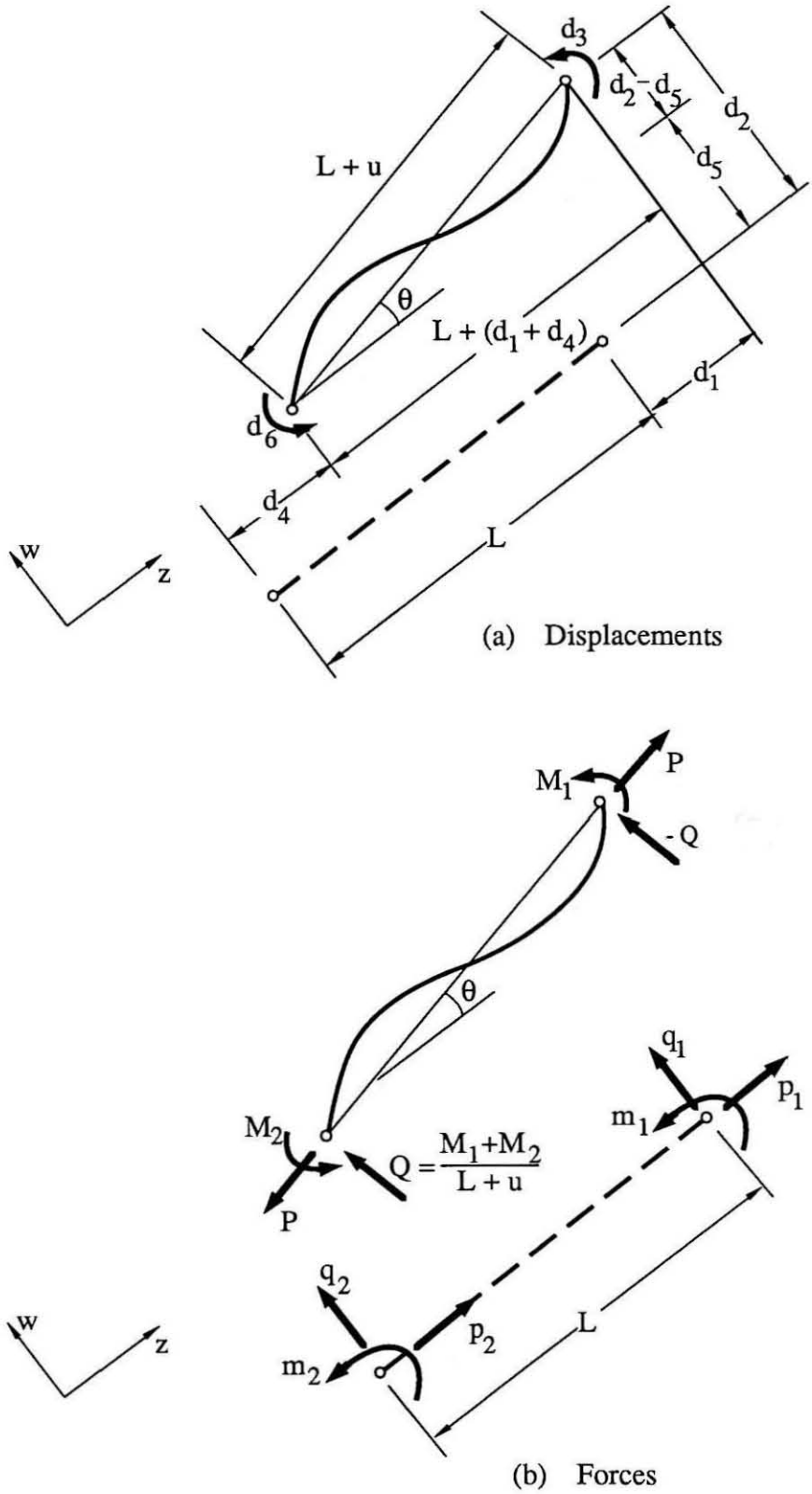

Figure 3.8 : Geometry and end-forces in member and local coordinate frames of a Plastic Hinge Model beam-column segment.

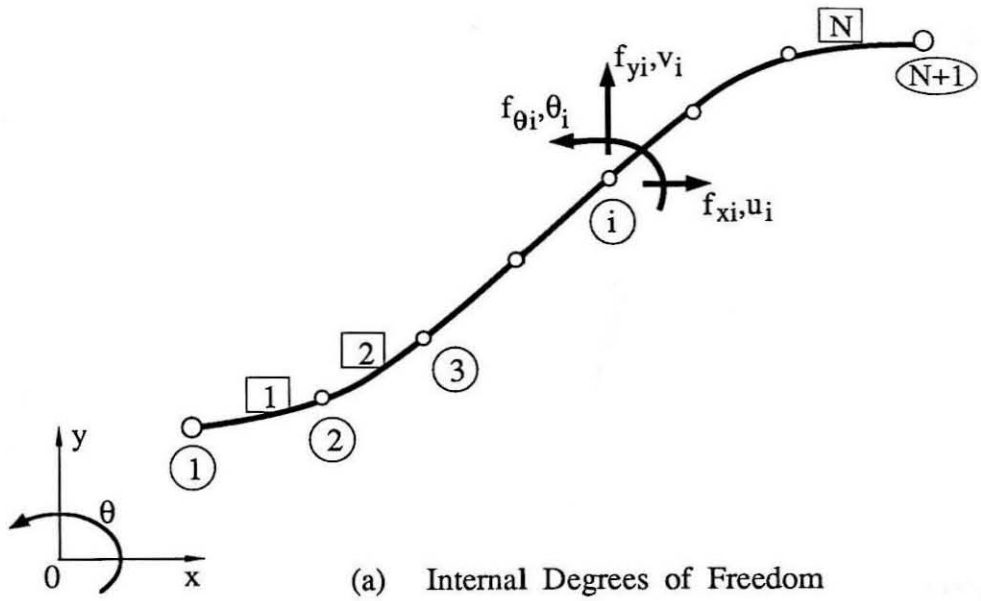

(a) Internal Degrees of Freedom

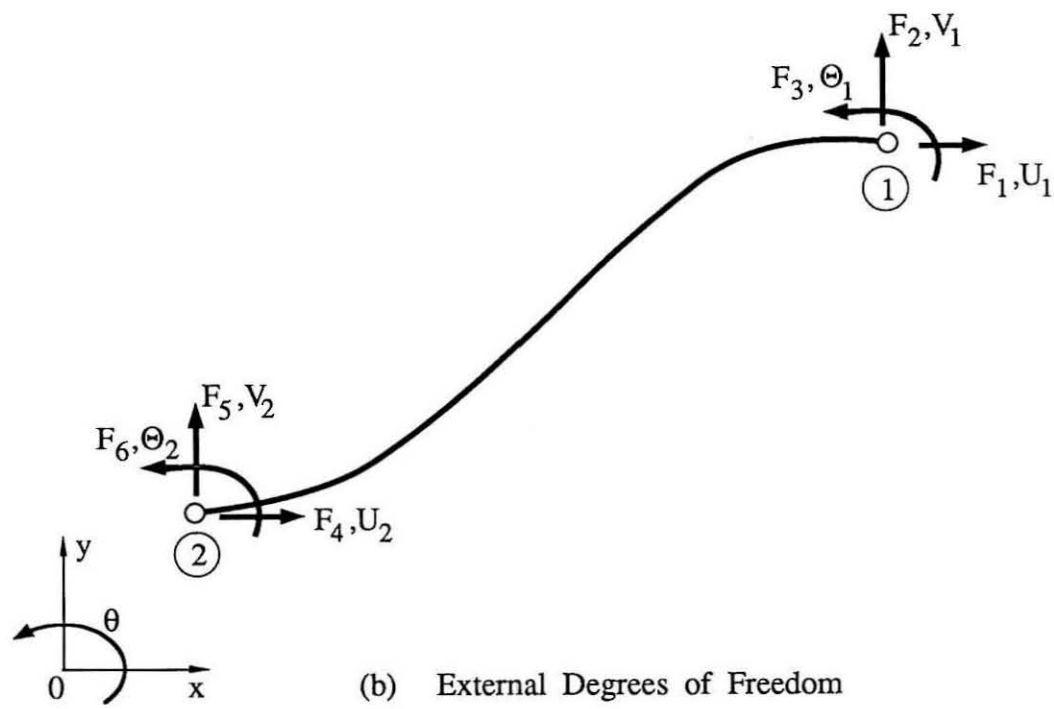

(b) External Degrees of Freedom

Figure 3.9 : External and internal degrees of freedom and corresponding forces in global coorinates of a multi-segment beam-column.

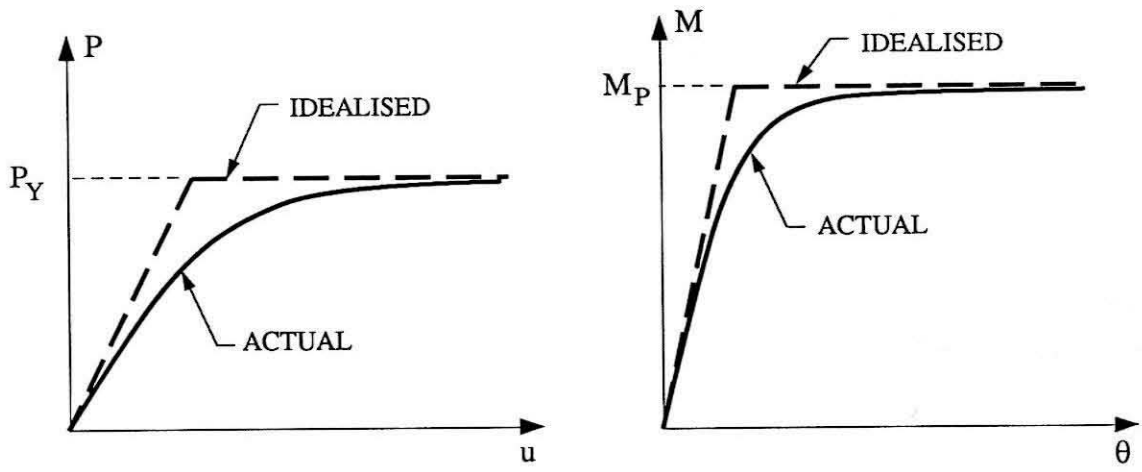

(a) Axial Load Only (b) Bending Moment Only

Figure 3.10 : Actual and idealised axial load and bending moment load-deformation relationships of hot rolled W sections.

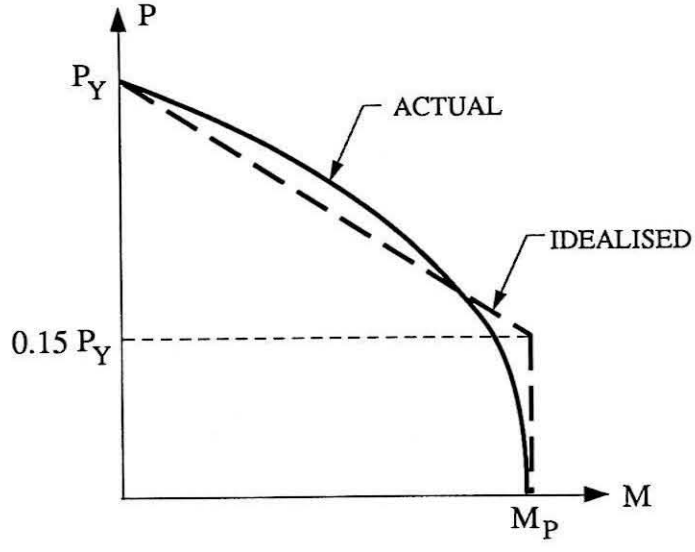

Figure 3.11 : Actual *P-M* strength interaction surface of hot-rolled W sections and idealisation used in the Plastic Hinge Model.

State 1

(a) Elastic Segment

State 2

State 3

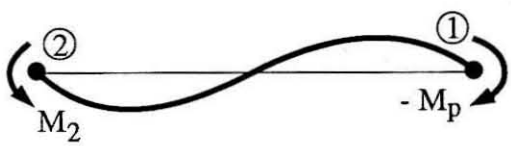

State 4

State 5

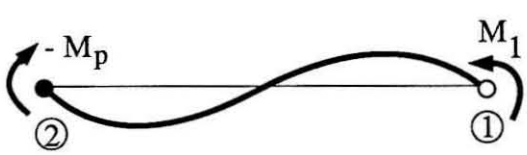

(b) One Hinge Segment

State 6

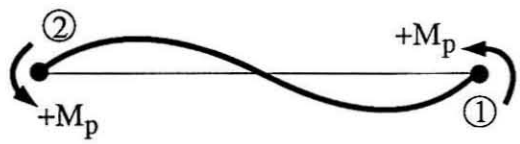

State 7

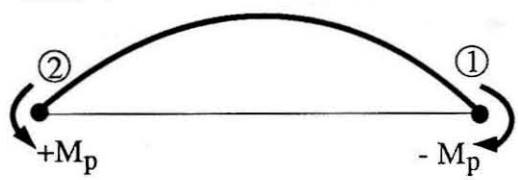

State 8

State 9

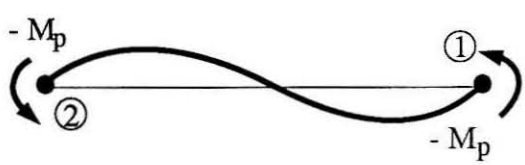

(c) Two Hinge Segment

Figure 3.12 : Characteristic states of a Plastic Hinge Model segment.

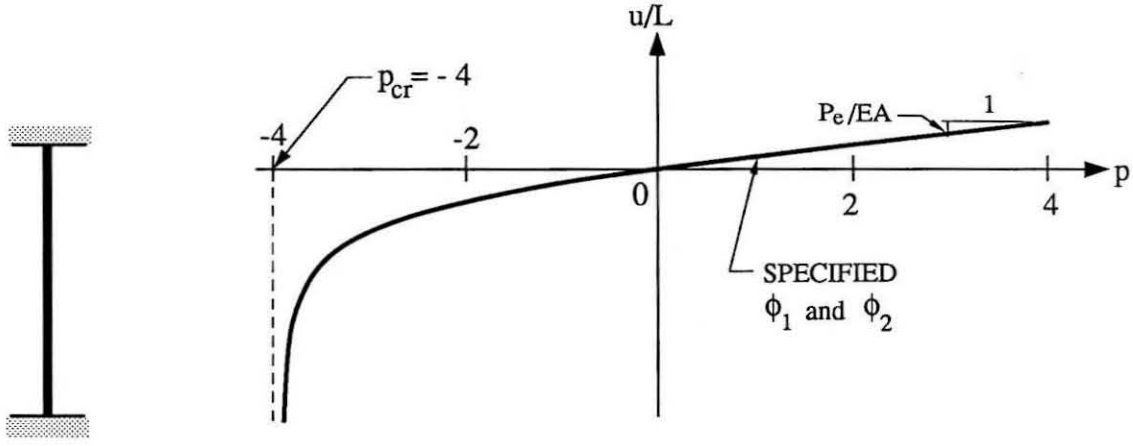

(a) Elastic Segment

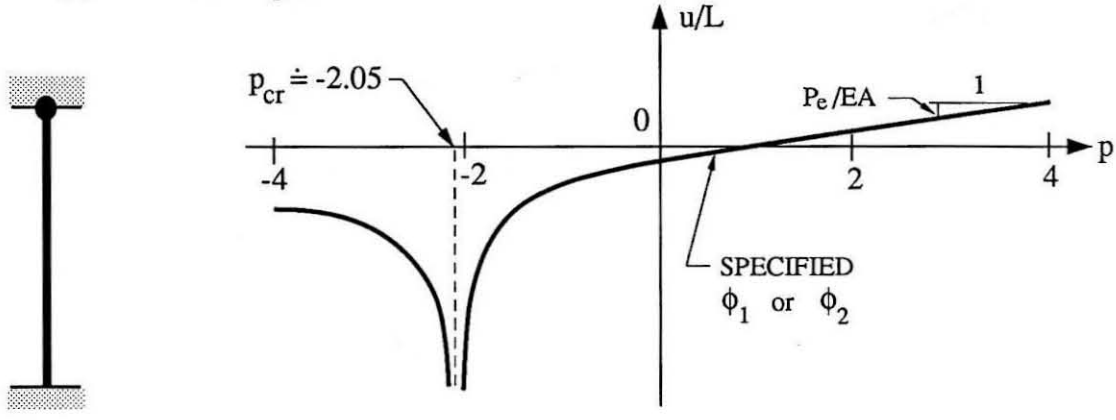

(b) One Hinge Segment

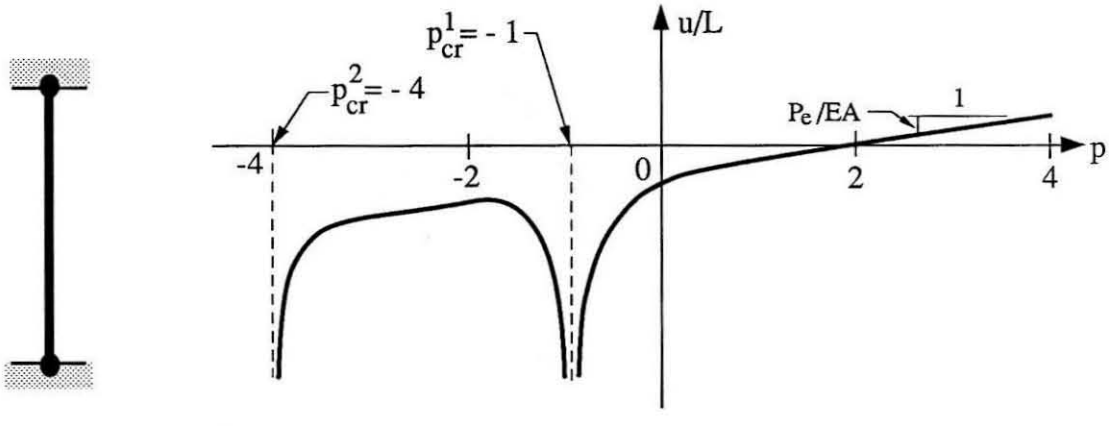

(c) Two Hinge Segment

Figure 3.13 : Singularities in the axial load equation of a Plastic Hinge Model segment under different end-conditions and the corresponding critical axial loads.

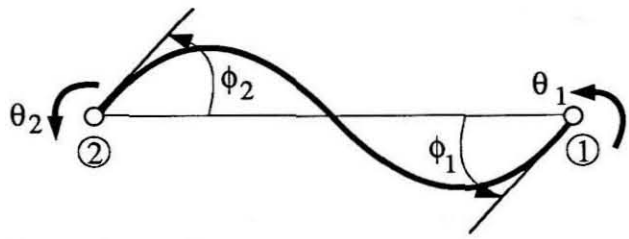

(a) Internal and External Rotational Degrees of Freedom

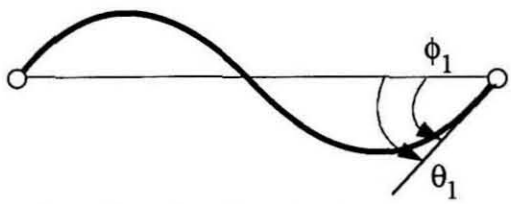

NO
PLASTIC ROTATION
$\kappa \equiv 0$

(b) Rotationally elastic end

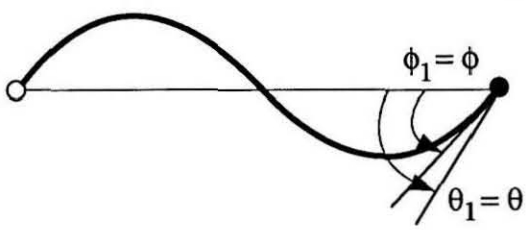

POSITIVE
PLASTIC ROTATION
$\kappa = \theta - \phi$

(c) Positive plastic - moment hinge

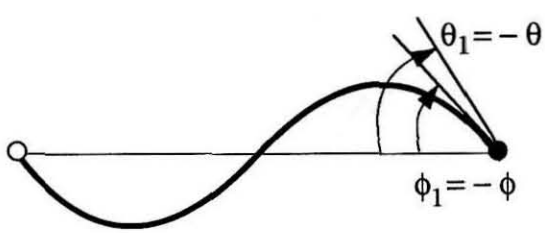

NEGATIVE
PLASTIC ROTATION
$\kappa = -\theta - (-\phi)$

(d) Negative plastic - moment hinge

Figure 3.14 : Definitions for positive and negative plastic rotation at the ends of a Plastic Hinge Model beam-column segment.

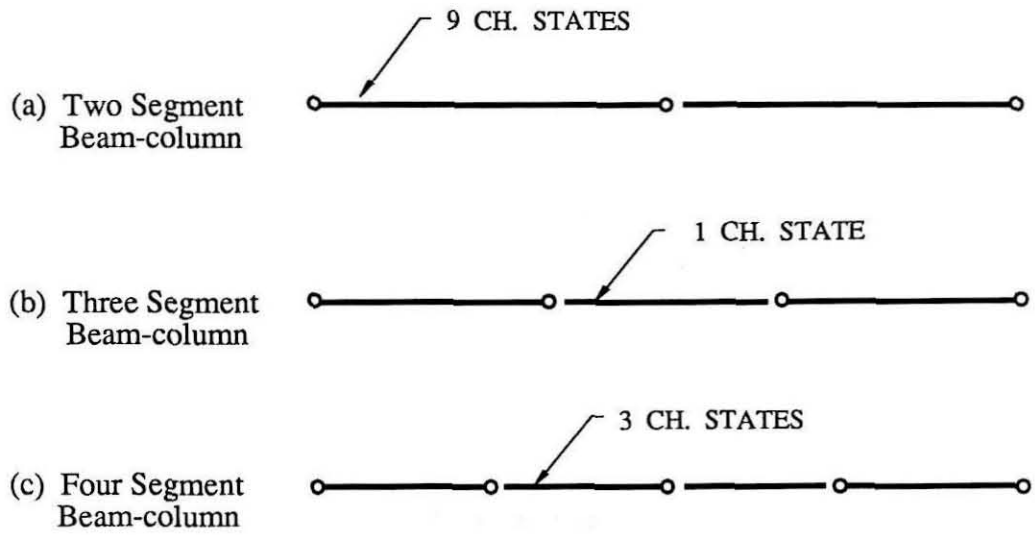

Figure 3.15 : *Formation of multi-segment beam-columns with Plastic Hinge Model segments having different characteristic states to ensure that only one plastic hinge can be formed at any interior node.*

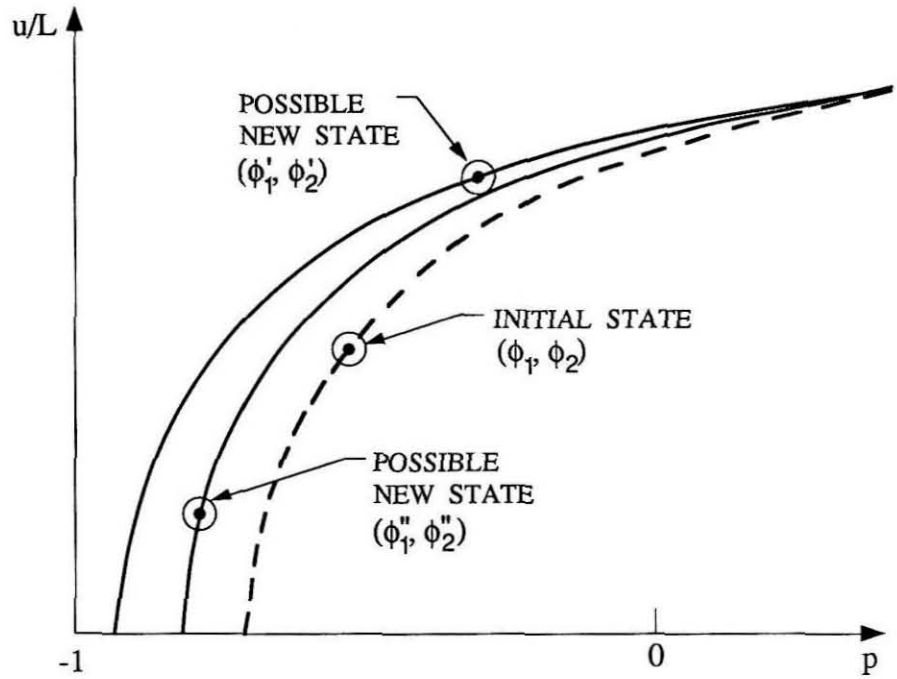

Figure 3.16 : *Characteristic states corresponding to the current and possible new states of a Plastic Hinge Model beam-column segment.*

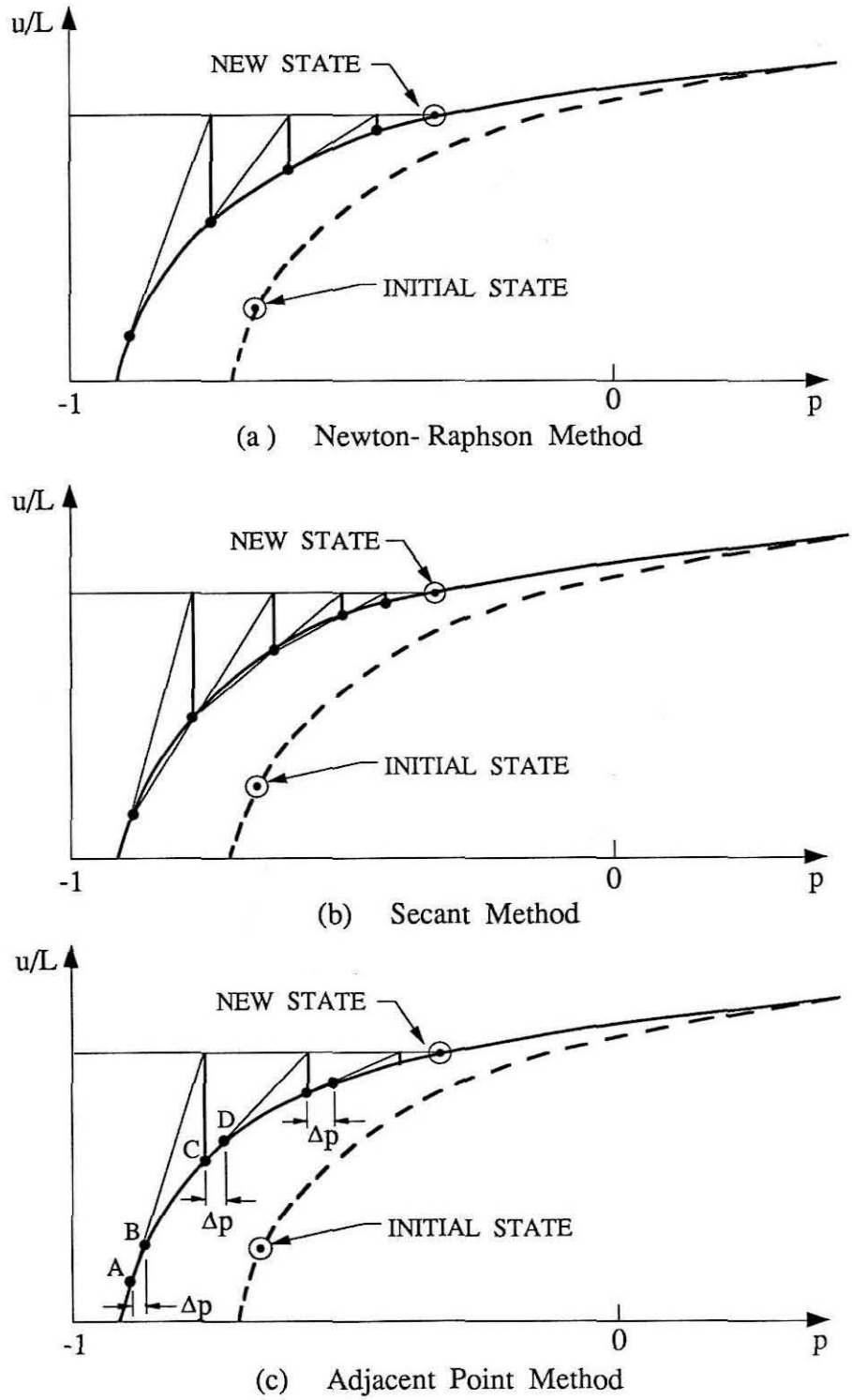

Figure 3.17 : Popular and proposed iterative schemes used to solve softening type nonlinear governing equations.

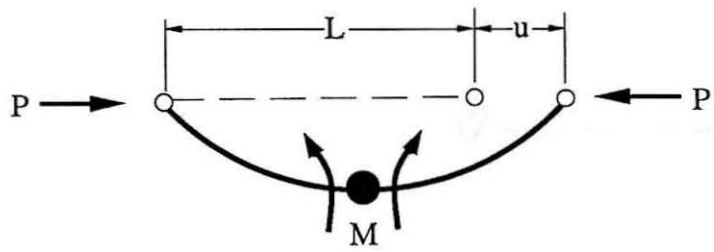

(a) Member under axial load cycles with possible moment hinge due to buckling

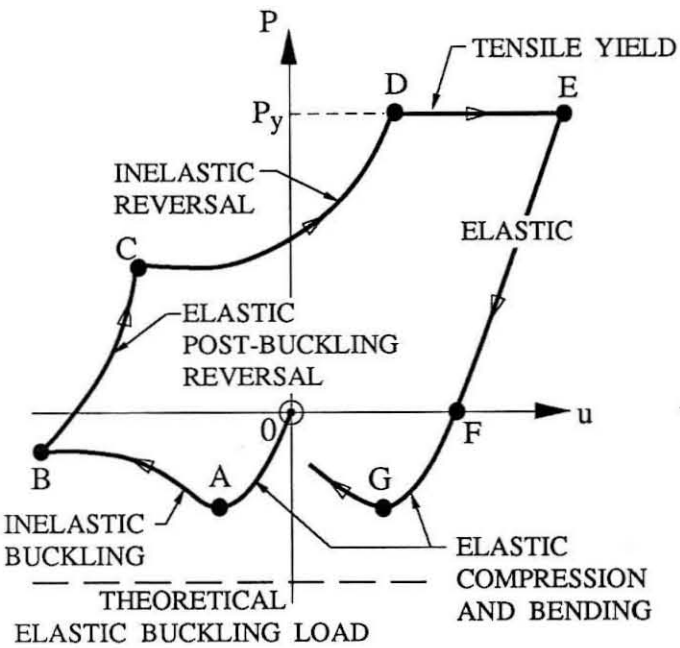

(b) P - u Cycle

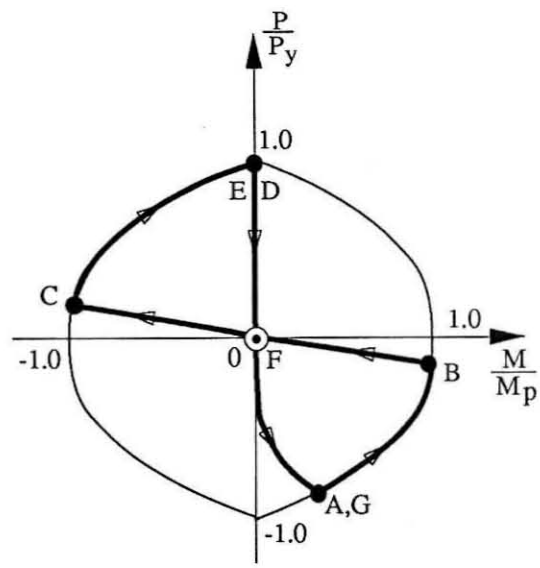

(c) Inelastic Path

Figure 3.18 : Geometry, load-deformation relation and the P-M interaction surface of a pin-ended brace member during buckling.

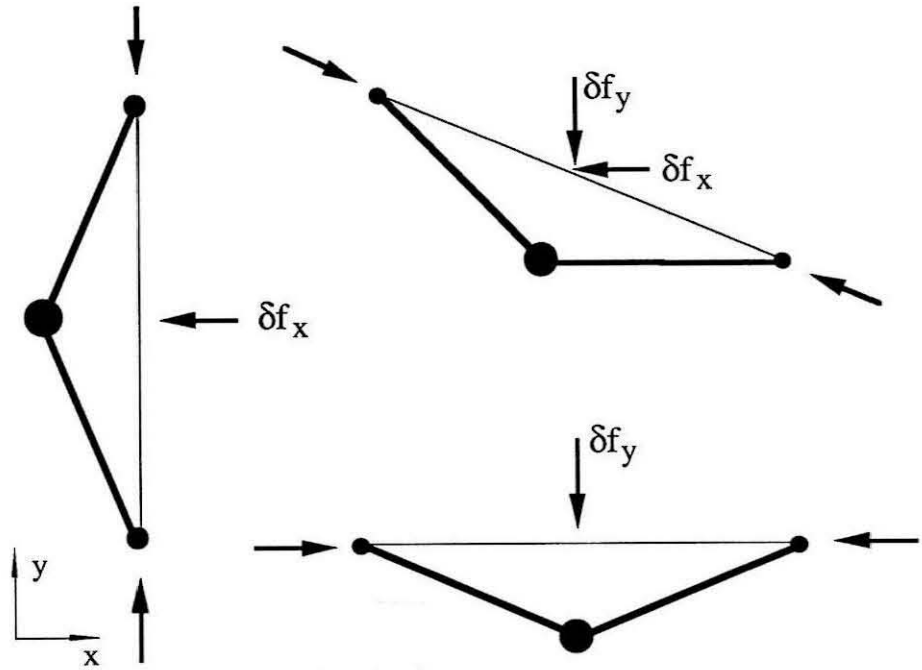

Figure 3.19 : Application of the infinitesimal load to create a numerical imperfection in the brace member to initiate buckling.

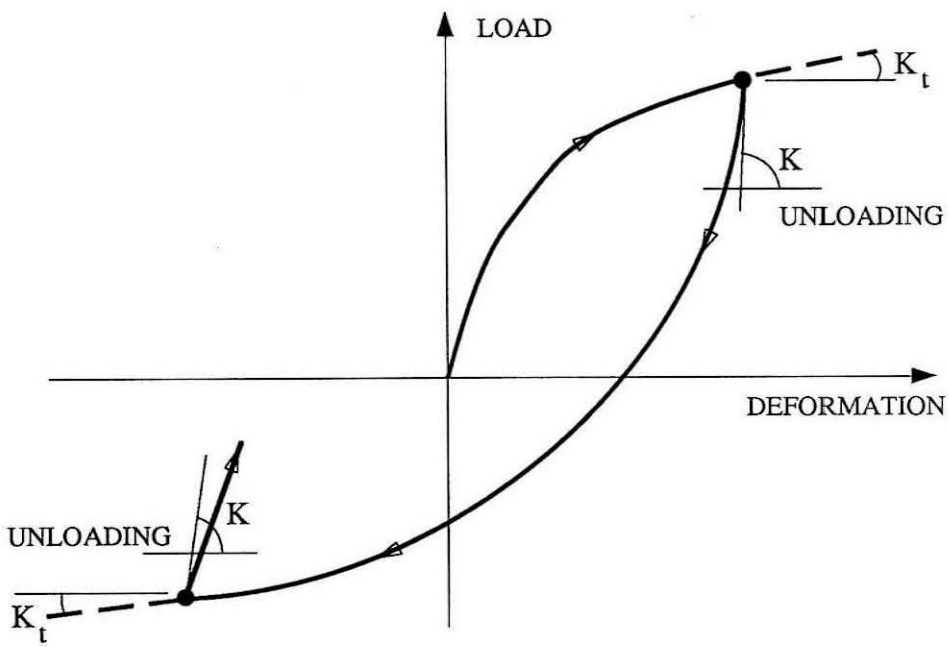

Figure 3.20 : Changing stiffnesses during unloading in direct stiffness approach.

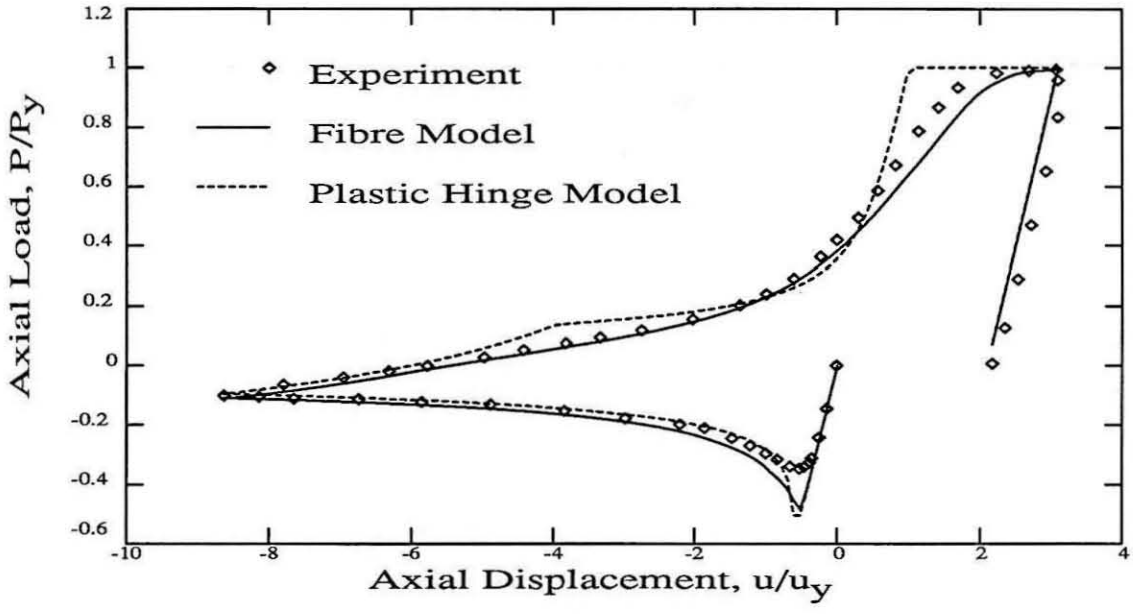

Figure 3.21 : Comparison of the experimental data [36] of the axial cyclic load performance of a fixed-ended brace, $kL/r = 120$, with the theoretical predictions using the Fibre Model and the Plastic Hinge Model.

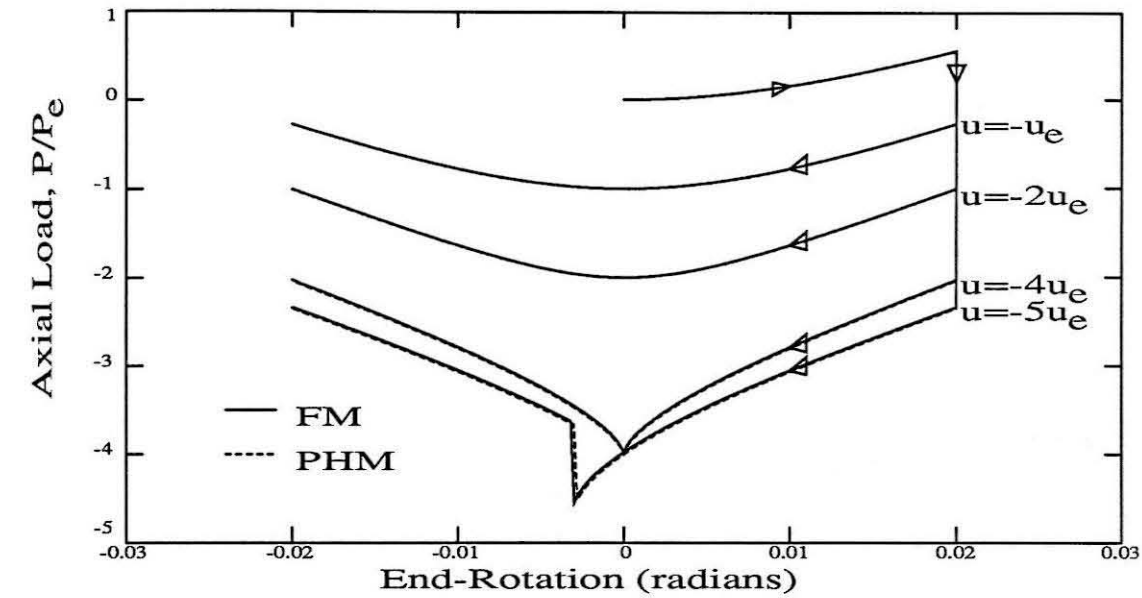

(a)

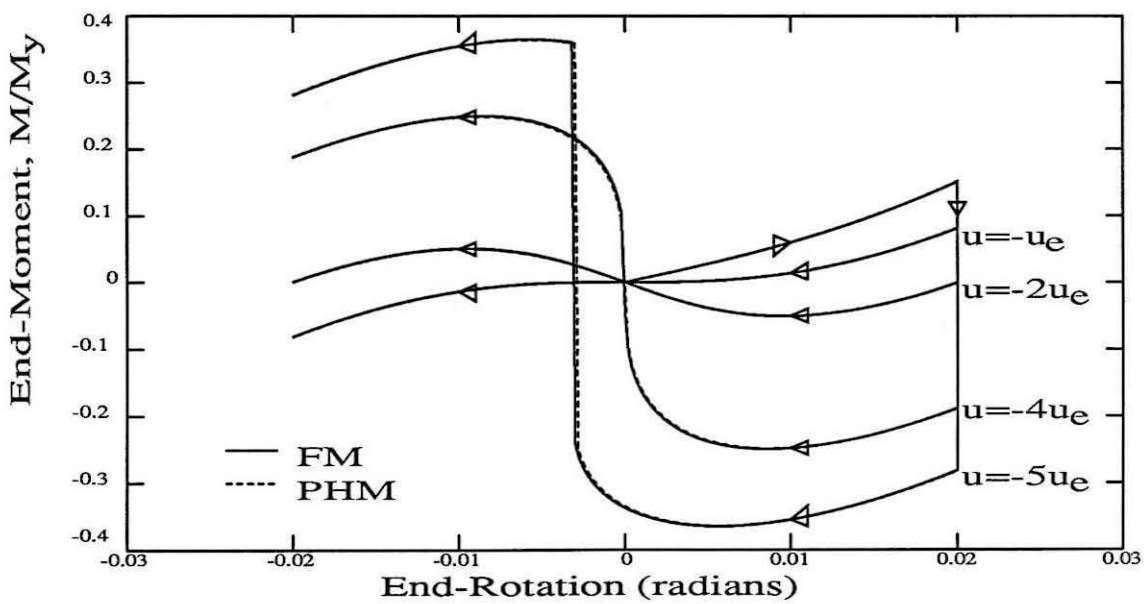

(b)

Figure 3.22 : Comparison of the theoretically predicted responses to the snap-through problem of a slender member using the Fibre Model and the Plastic Hinge Model beam-column elements.

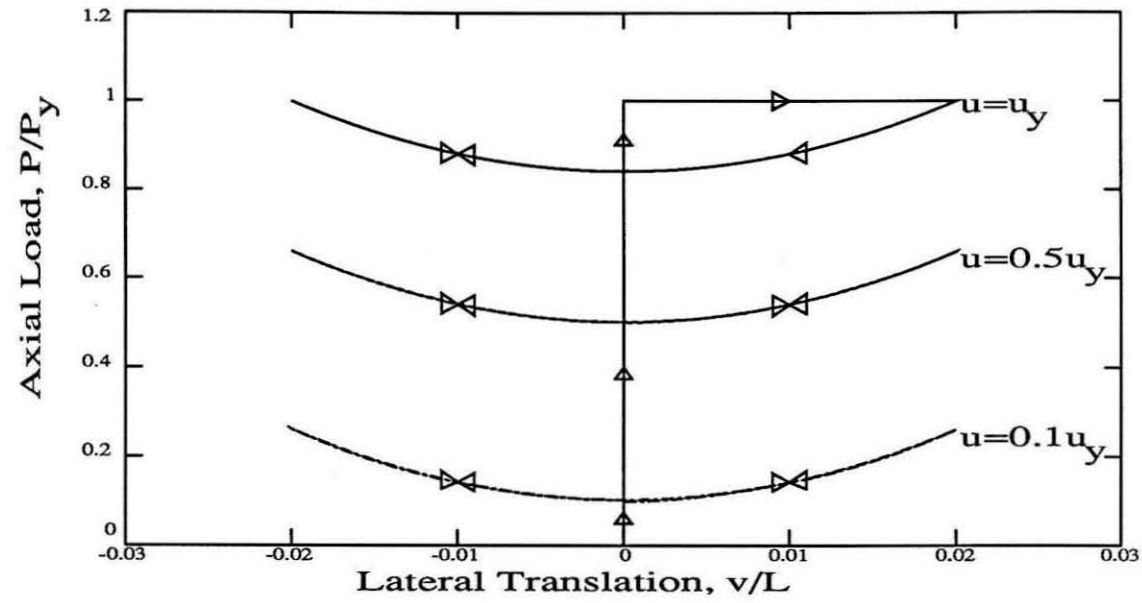

(a)

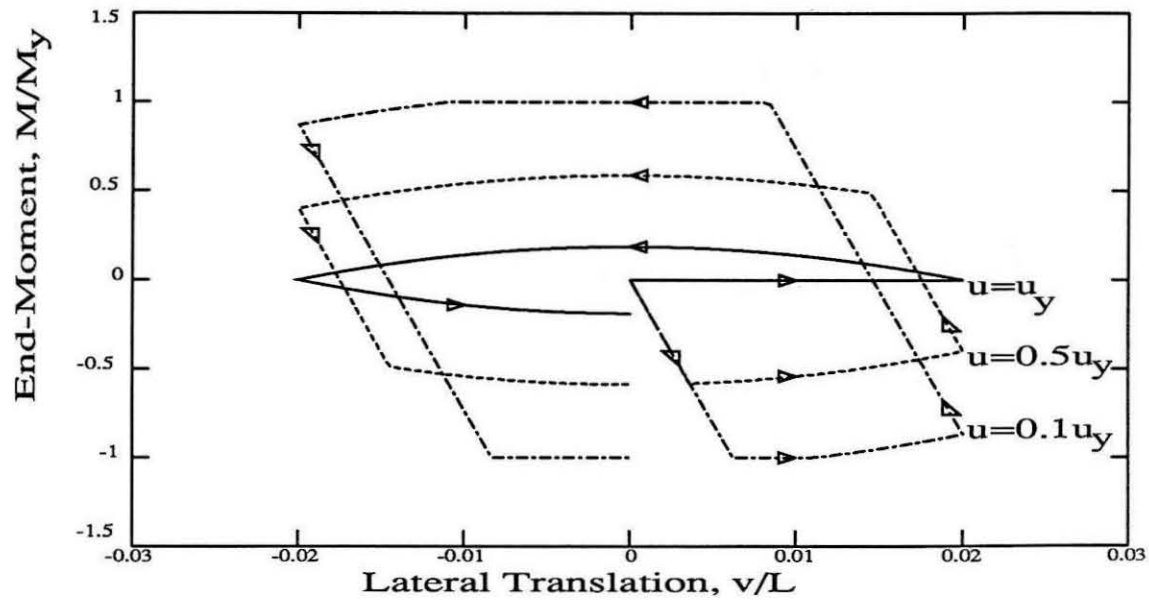

(b)

Figure 3.23 : Effect of tensile axial displacement on the response to the lateral translation problem of a beam-column modelled using the Plastic Hinge Model element.

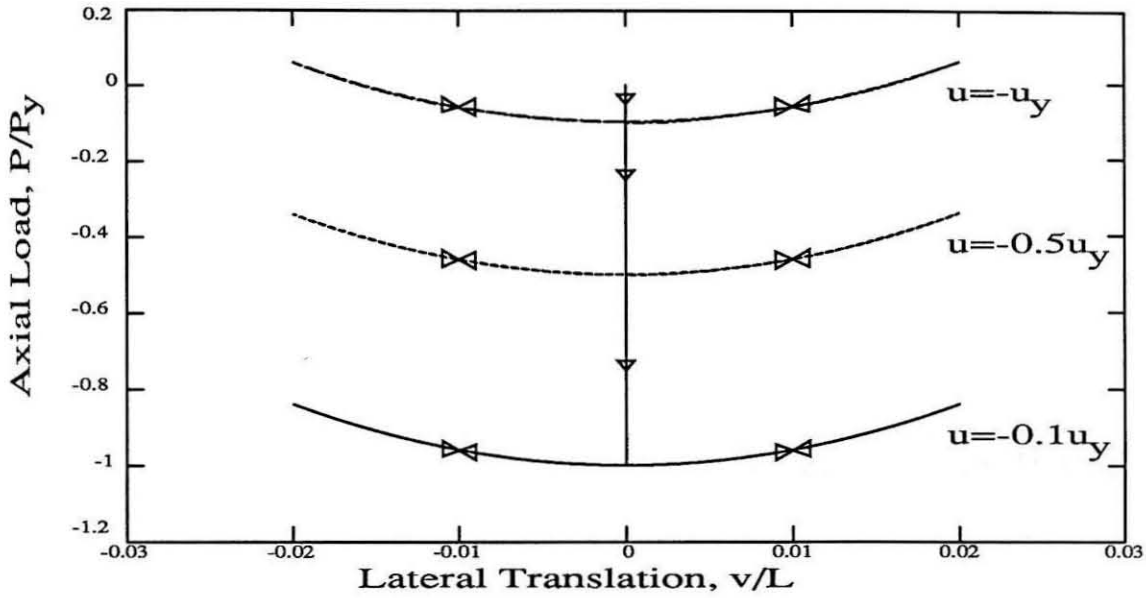

(a)

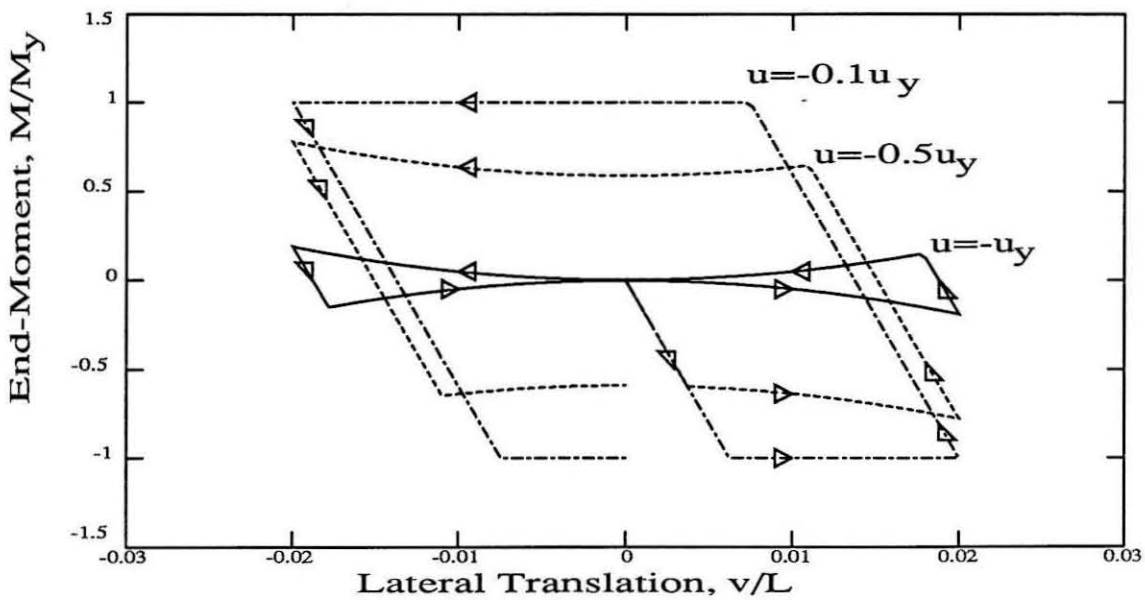

(b)

Figure 3.24 : Effect of compressive axial displacement on the response to the lateral translation problem of a beam-column modelled using the Plastic Hinge Model.

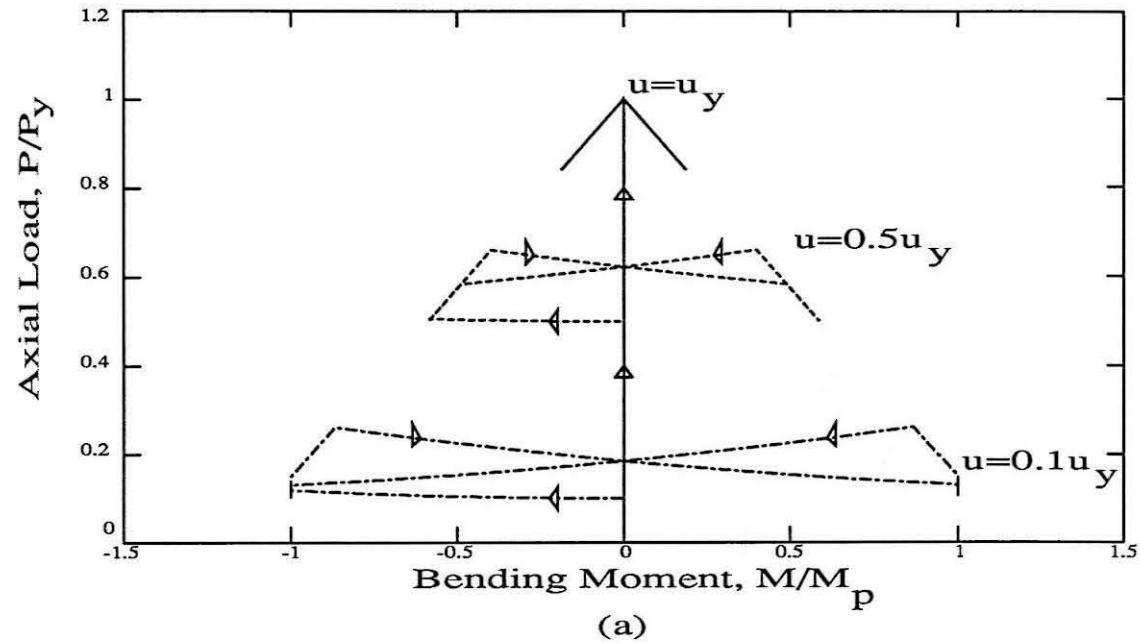

Figure 3.25 : Effect of tensile and compressive axial displacement on the *P-M* strength interaction to the lateral translation problem of a beam-column modelled using the Plastic Hinge Model element.

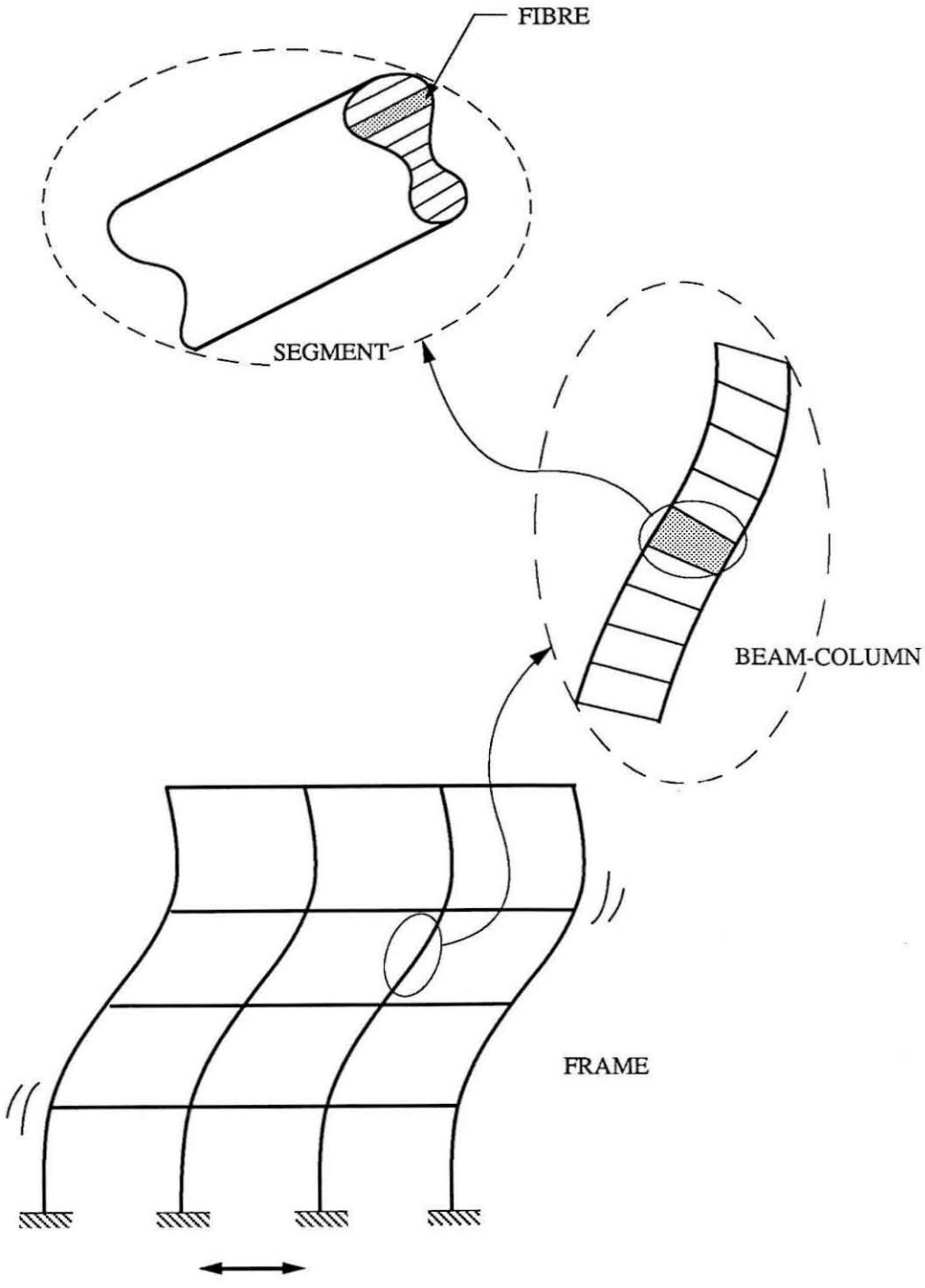

Figure 4.1 : Schematic defining a fibre and a segment in a Fibre Model beam-column element, and showing how an assemblage of one-dimensional fibres forms a planar moment resisting frame.

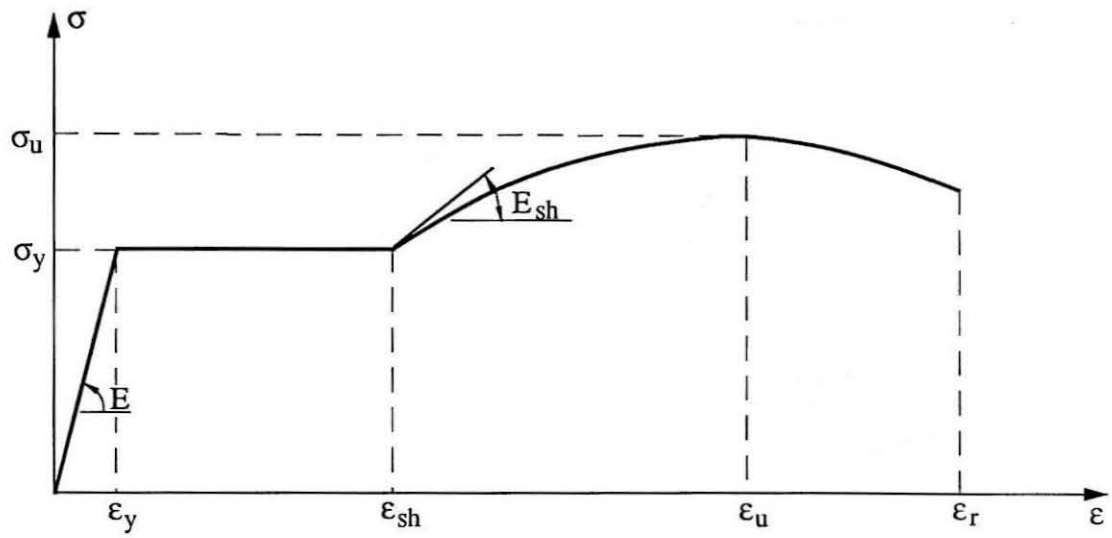

Figure 4.2 : Typical monotonic stress-strain curve for structural steel and the associated characteristic properties.

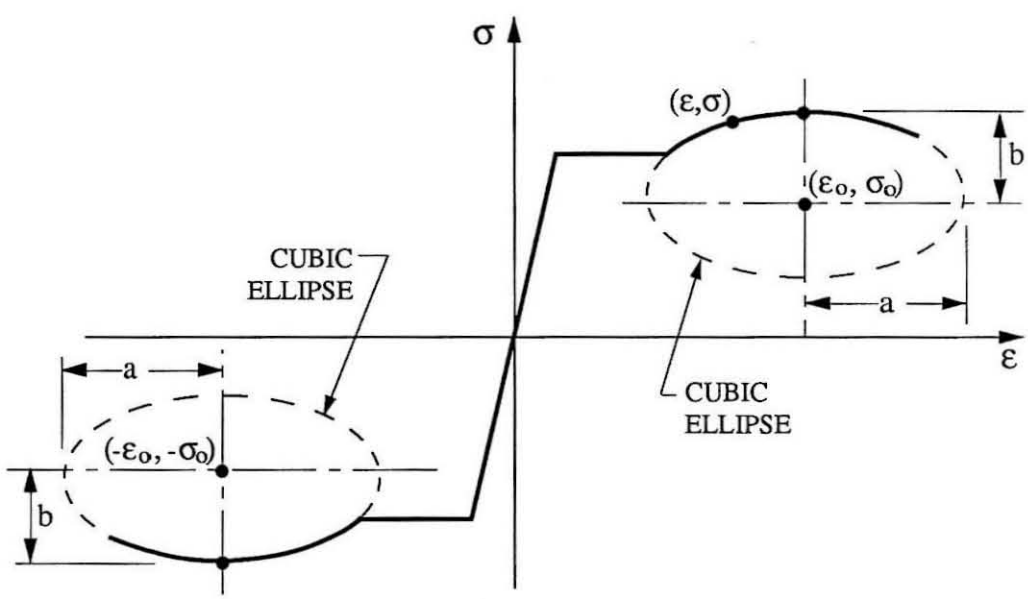

Figure 4.3 : Geometry of the cubic ellipses modelling the strain-hardening part of the virgin curves in the Cubic Ellipsoidal Model.

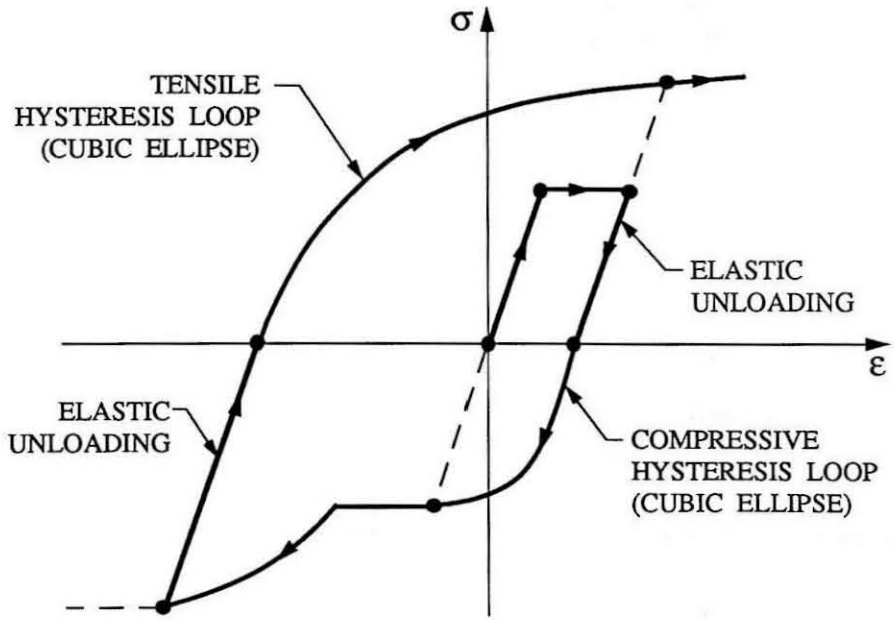

Figure 4.4 : Geometry of the cubic ellipses modelling the hysteresis loops in the Cubic Ellipsoidal Model.

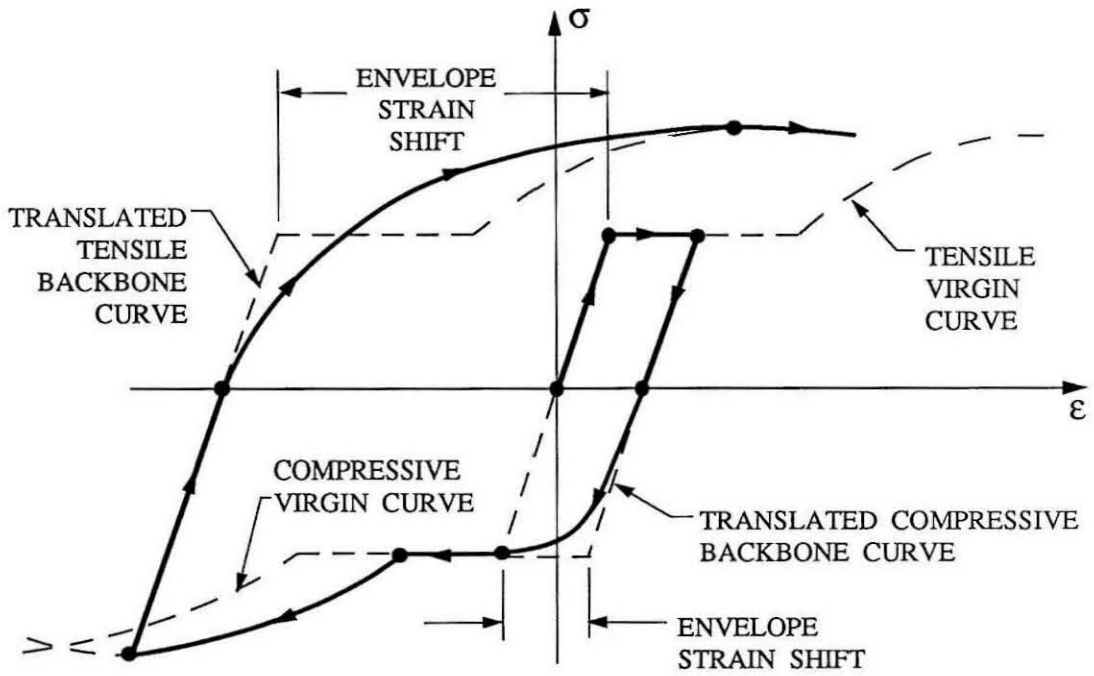

Figure 4.5 : Envelope strain shift under arbitrary cyclic strain history.

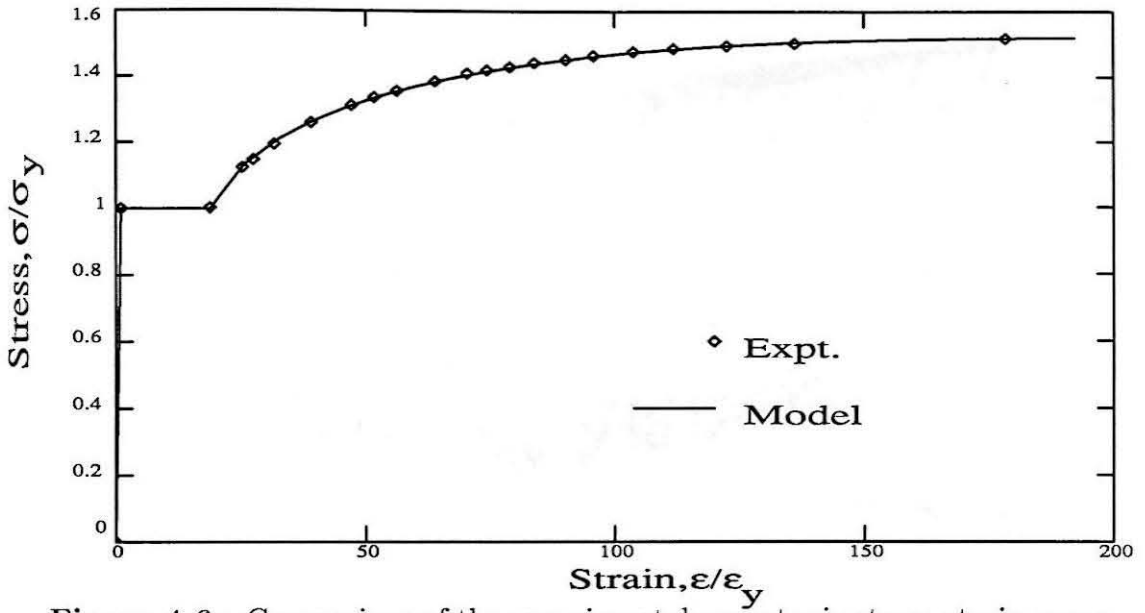

Figure 4.6 : Comparison of the experimental monotonic stress-strain curve [41] from the uniaxial test on a steel bar, with the theoretical prediction using the Cubic Ellipsoidal Model.

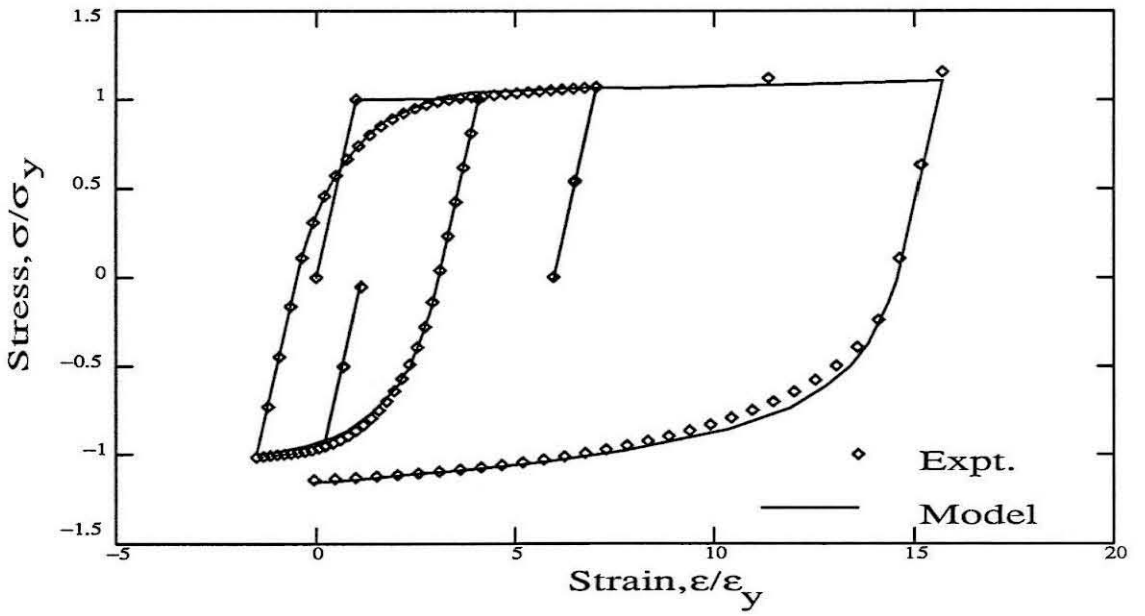

Figure 4.7 : Comparison of the experimental hysteresis loops [41] from the uniaxial test on a steel bar, with the theoretical prediction using the Cubic Ellipsoidal Model.

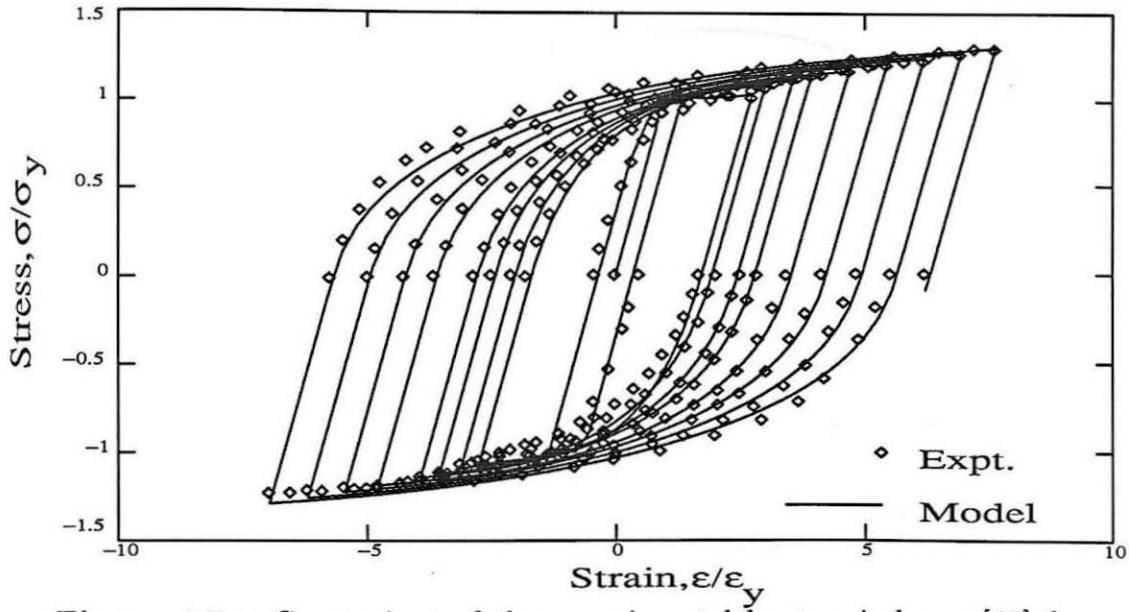

Figure 4.8 : Comparison of the experimental hysteresis loops [45] from the uniaxial test on a steel bar, with the theoretical prediction using the Cubic Ellipsoidal Model.

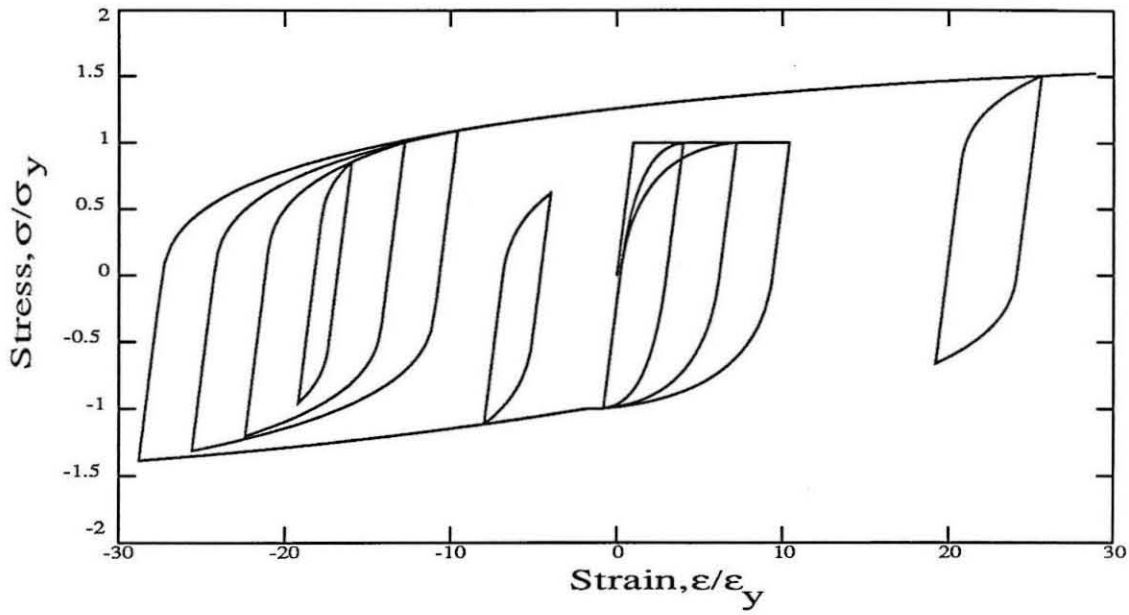

Figure 4.9 : General stress-strain history of a steel bar demonstrating the rules governing the incomplete and completed hysteresis loops in the Cubic Ellipsoidal Model.

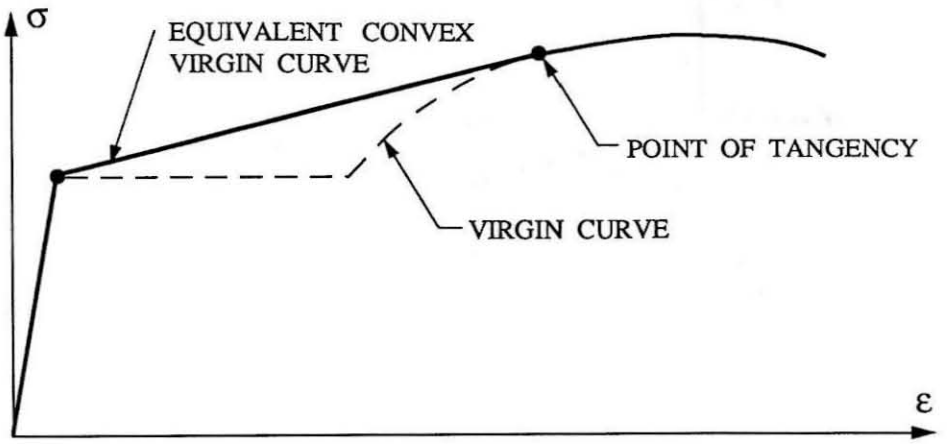

Figure 4.10 : Equivalent convex virgin curve for structural steel.

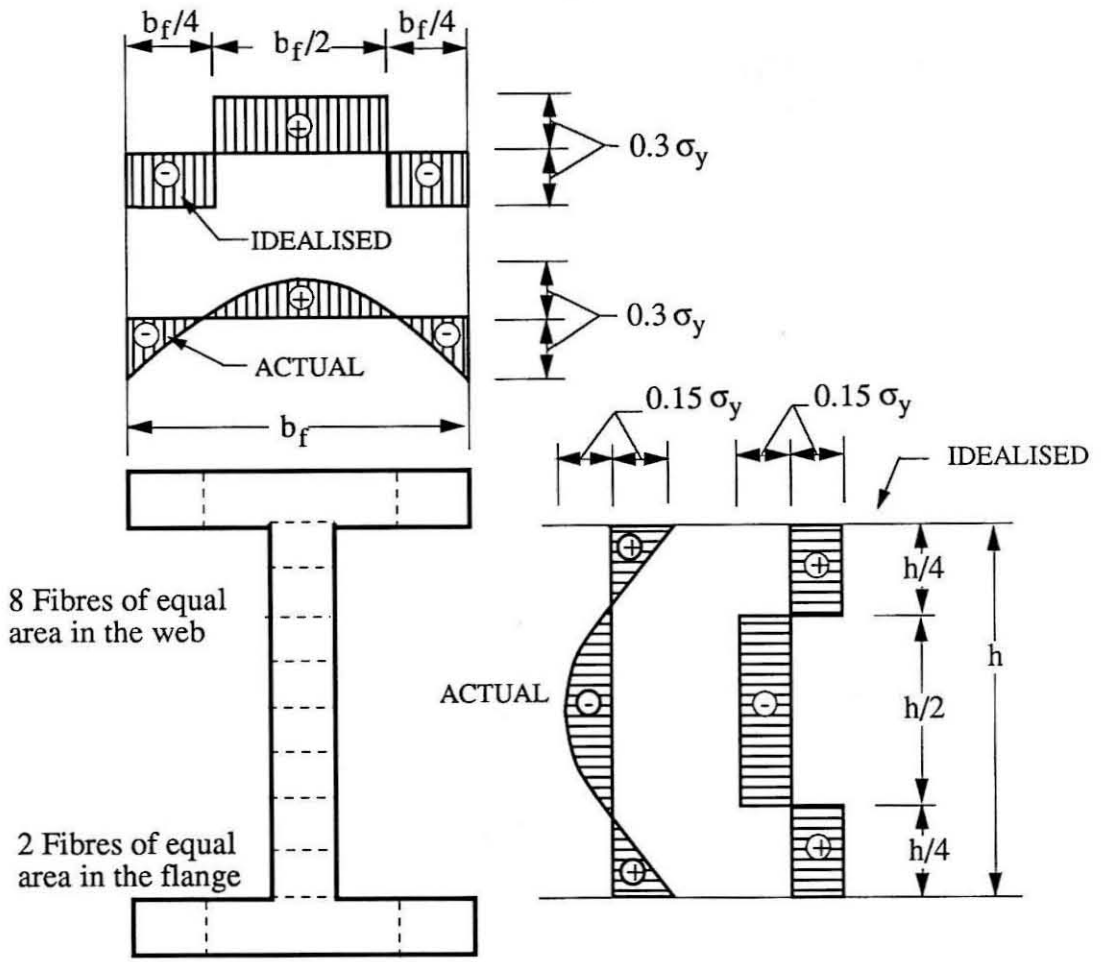

Figure 4.11 : Proposed discretisation of the cross-section into 12 fibres in view of the actual and idealised residual stresses in standard hot-rolled W sections commonly used as beam-columns.

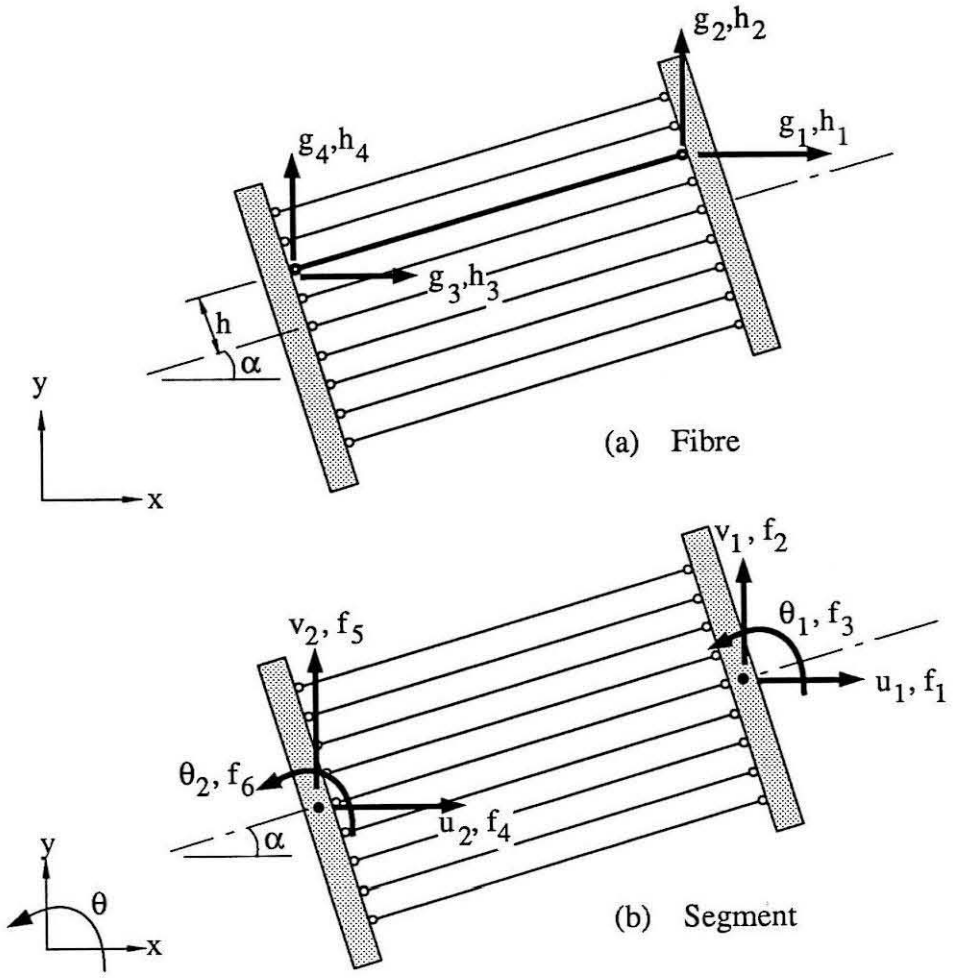

Figure 4.12 : Global degrees of freedom and end-forces on a fibre and a segment of the Fibre Model beam-column element.

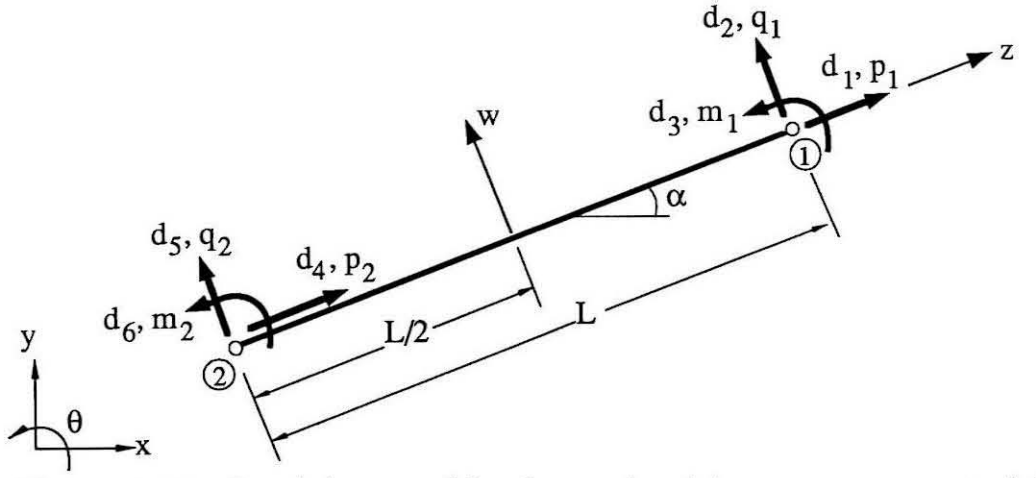

Figure 4.13 : Local degrees of freedom and end-forces on a segment of the Fibre Model beam-column element.

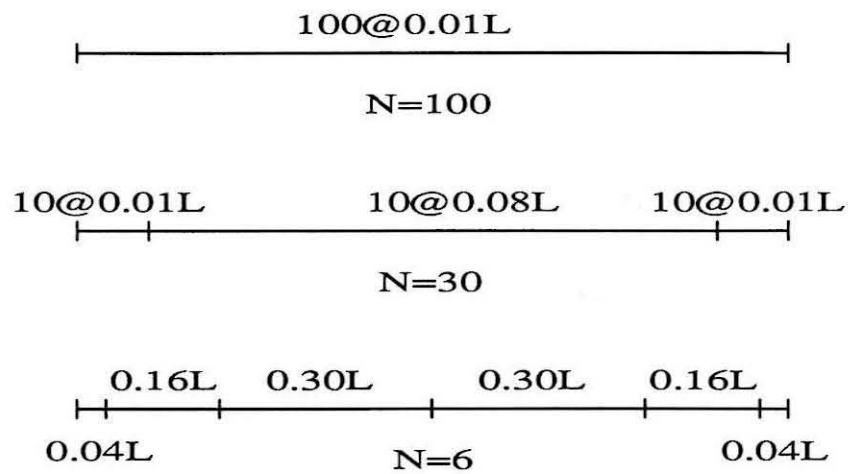

(a) Discretisations studied

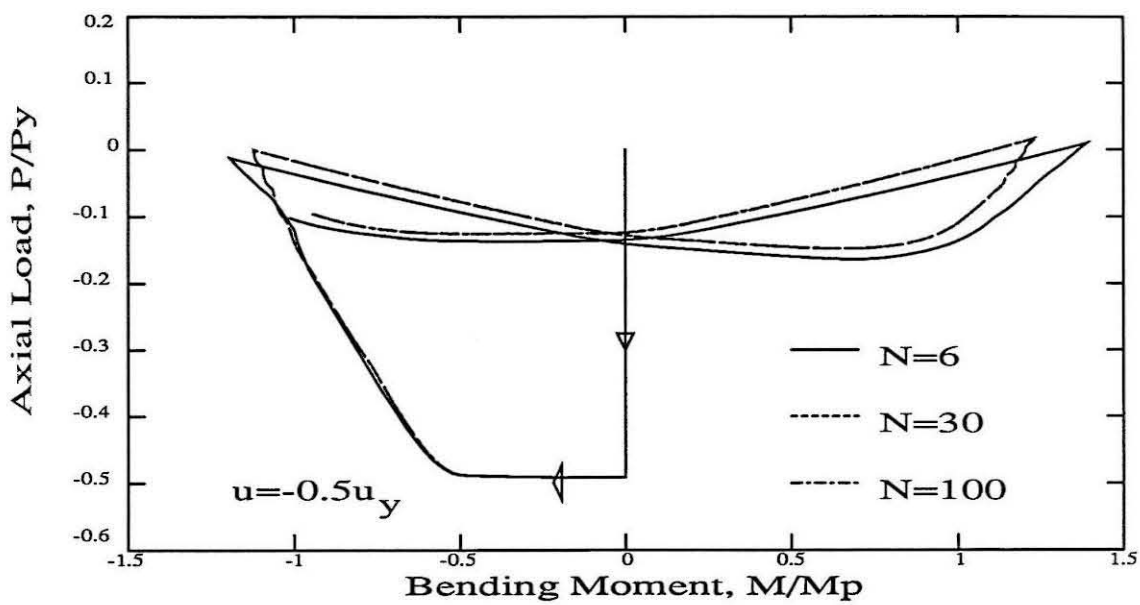

(b)

Figure 4.14 : Effect of discretisation on the P-M interaction diagram response to the lateral translation problem of a member modelled using the Fibre Model.

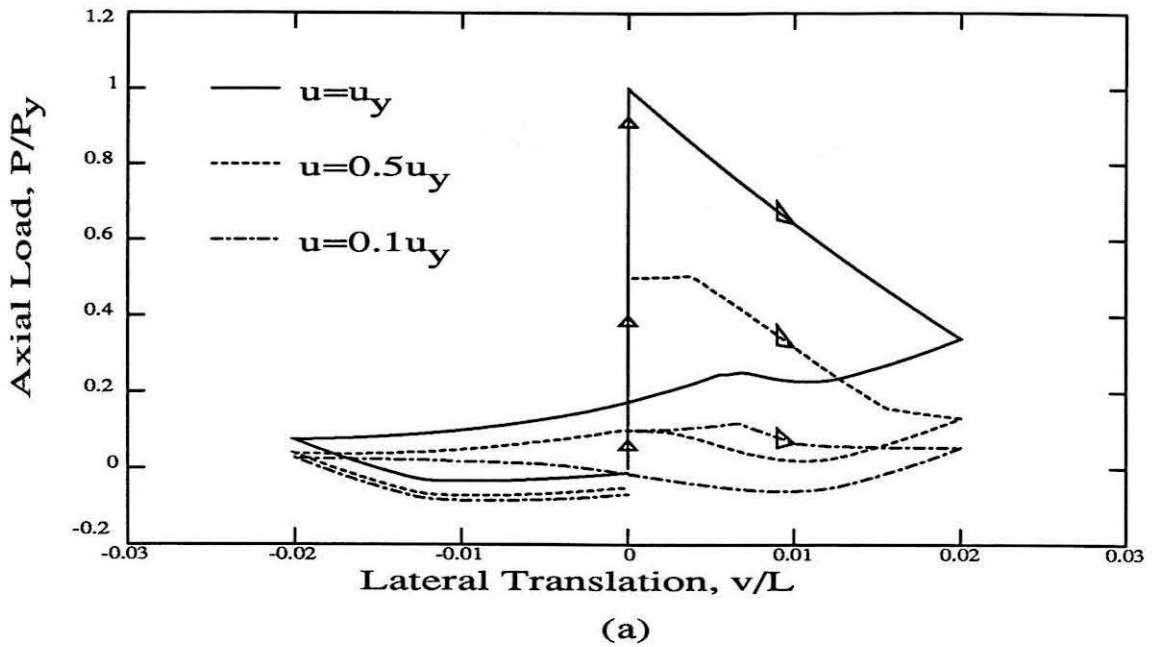

(a)

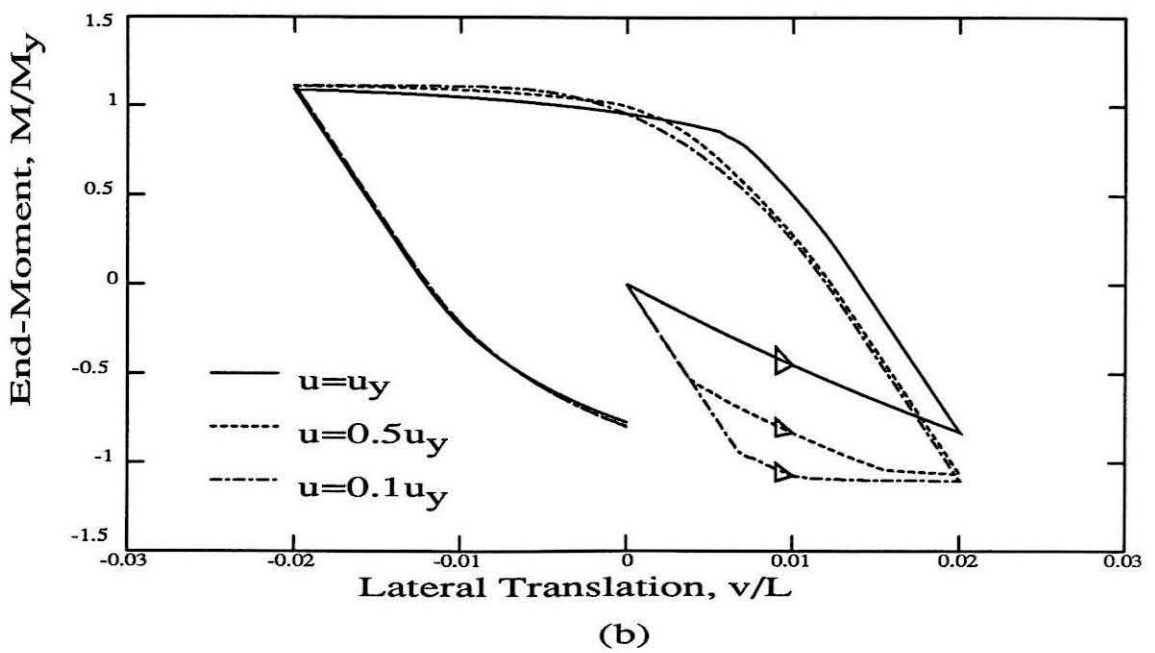

(b)

Figure 4.15 : Effect of tensile axial load on the response to the lateral translation problem of a member modelled using the Fibre Model.

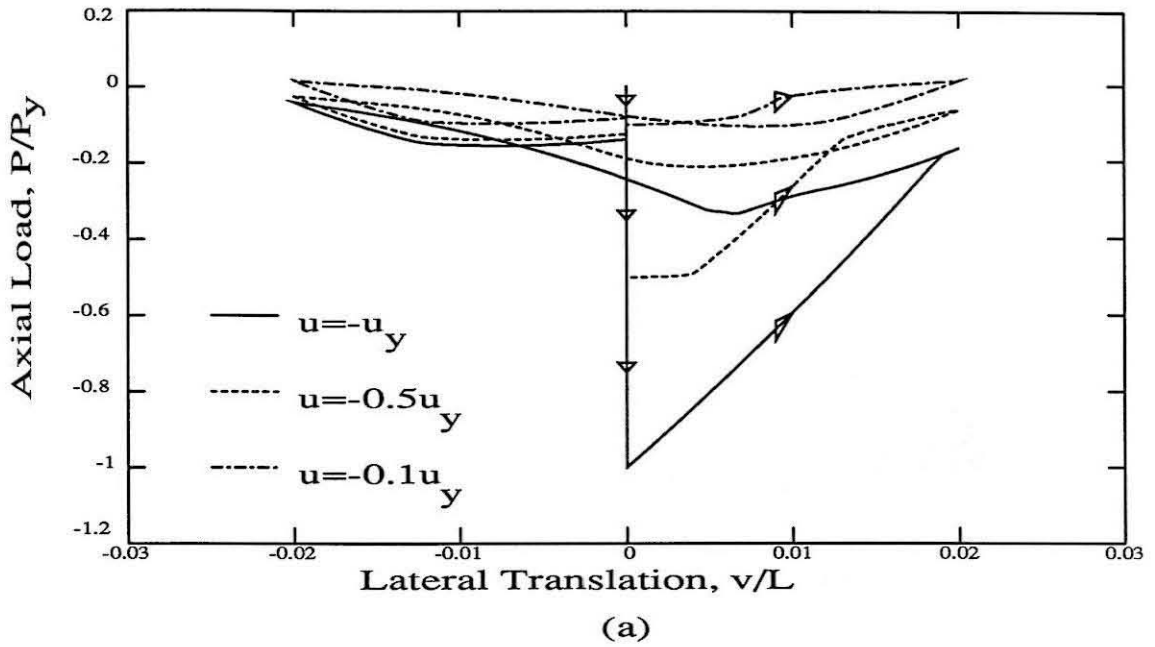

(a)

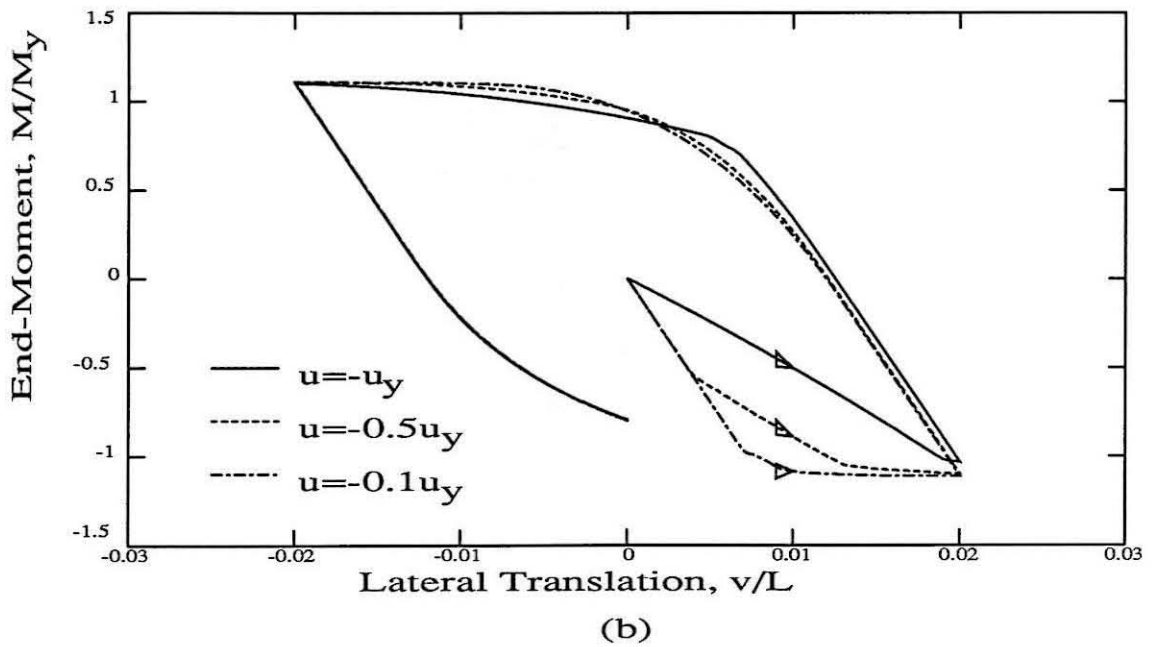

(b)

Figure 4.16 : Effect of compressive axial load on the response to the lateral translation problem of a member modelled using the Fibre Model.

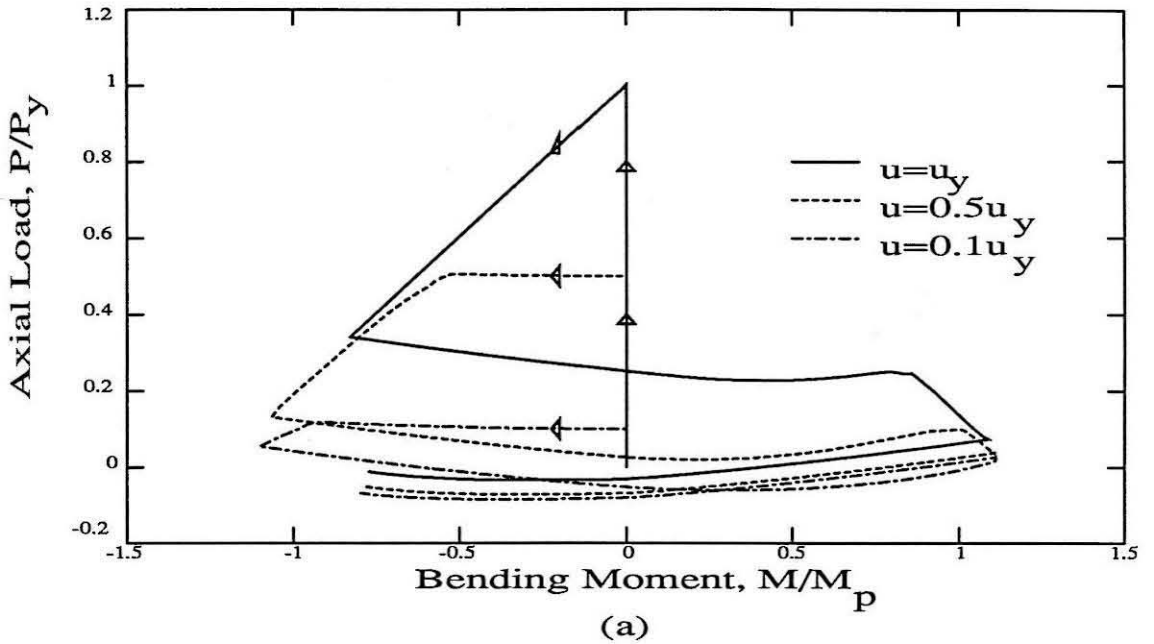

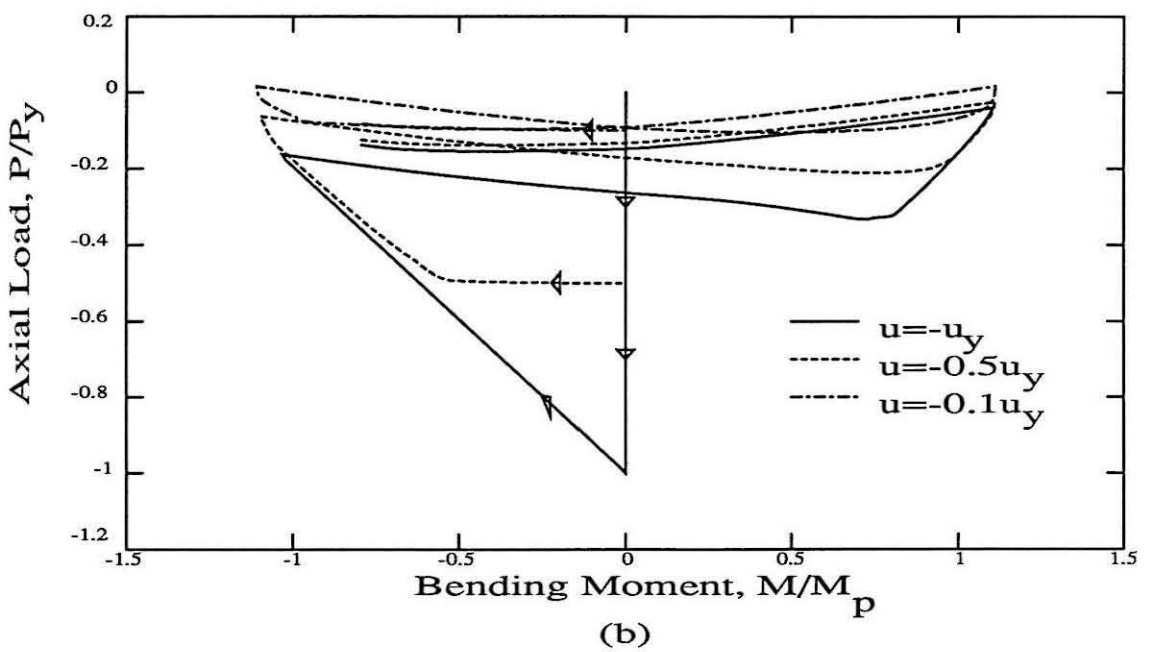

Figure 4.17 : Effect of tensile and compressive axial load on the P-M interaction surface response to the lateral translation problem of a member modelled using the Fibre Model.

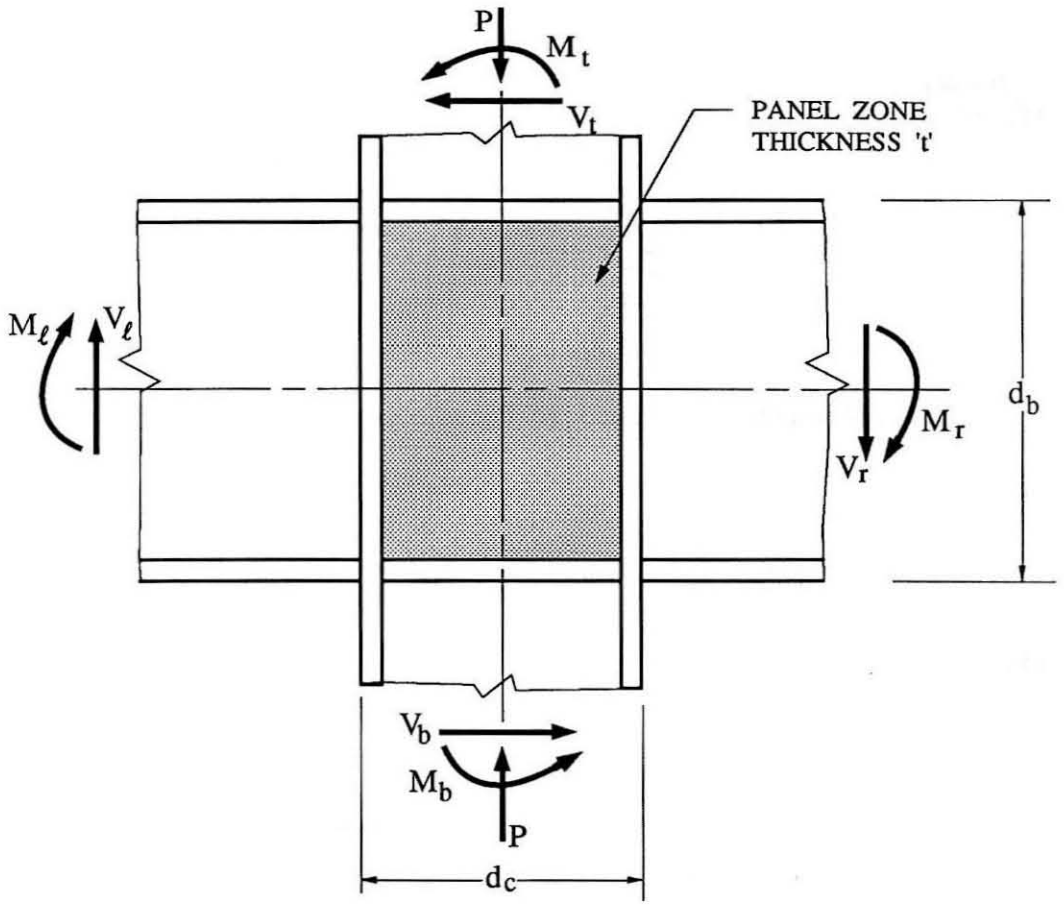

Figure 5.1 : Geometry and the loads transferred through a planar joint.

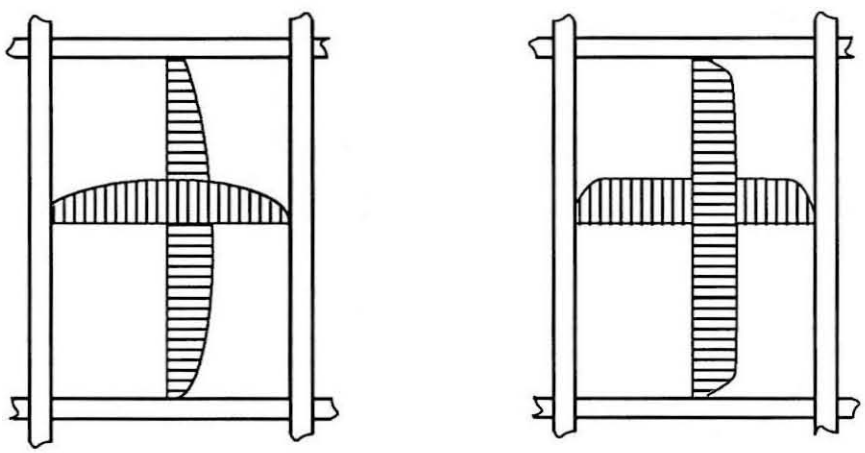

(a) Elastic Range (b) Inelastic Range

Figure 5.2 : Shear stress distribution in a planar joint.

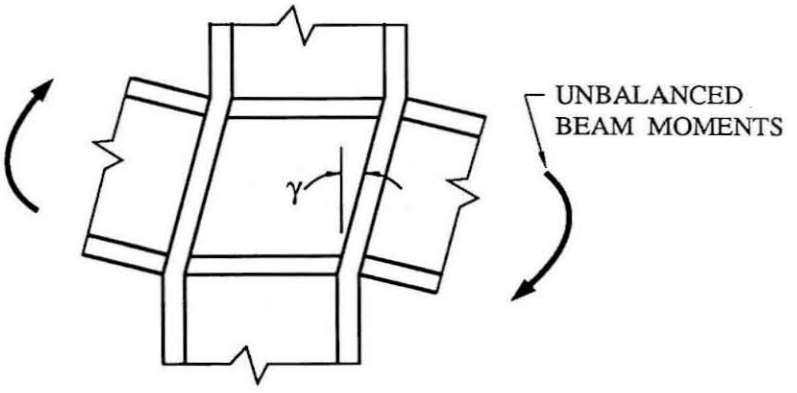

(a) Shear Behaviour Caused by Unbalanced Beam Moments

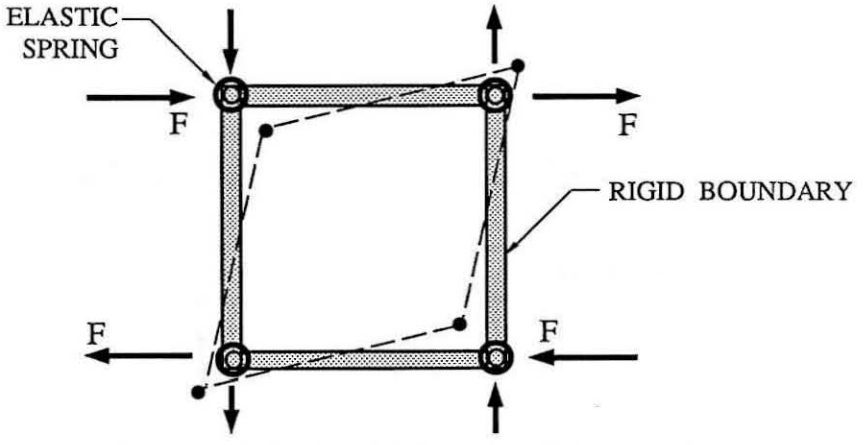

(b) Resistance of the Panel Boundary Elements [16]

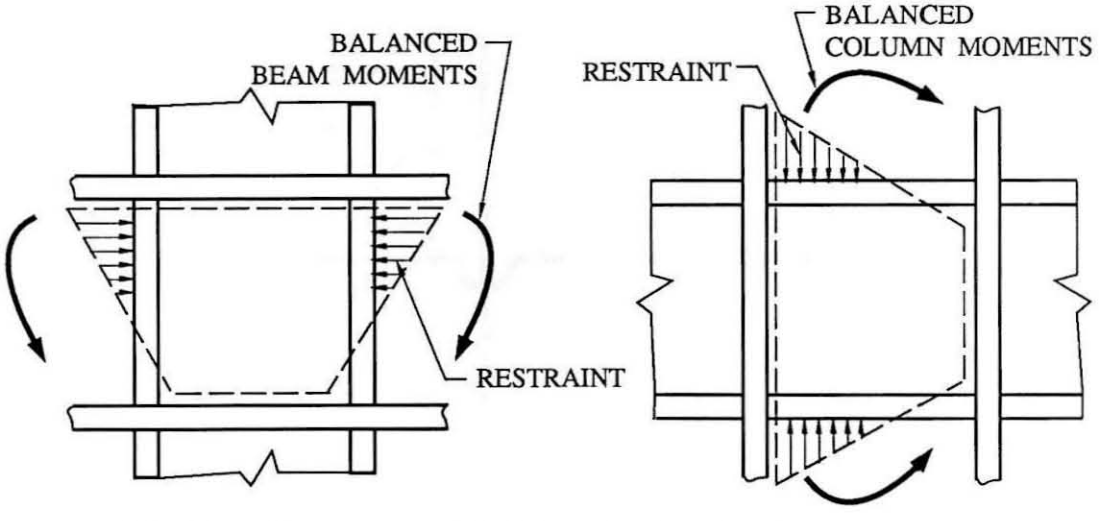

(c) Restraint to Flexural Deformation by the Adjacent Beam and Column Webs [17]

Figure 5.3 : Joint moment contributed by various surrounding elements.

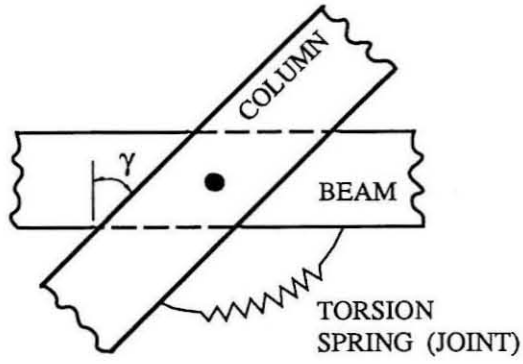

(a) Physical Idealisation

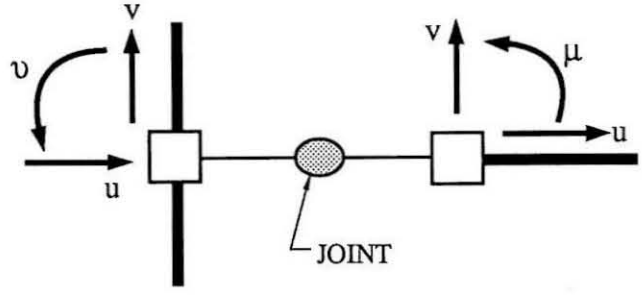

(b) End-Bay Joint

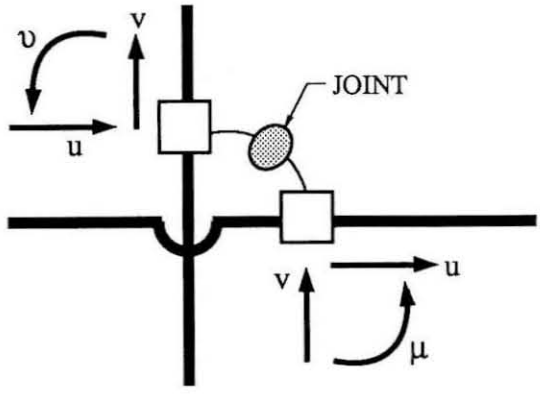

(c) Interior-Bay Joint

Figure 5.4 : Physical idealisation a joint and the degrees of freedom of a typical global node of a planar MRF with joint elements.

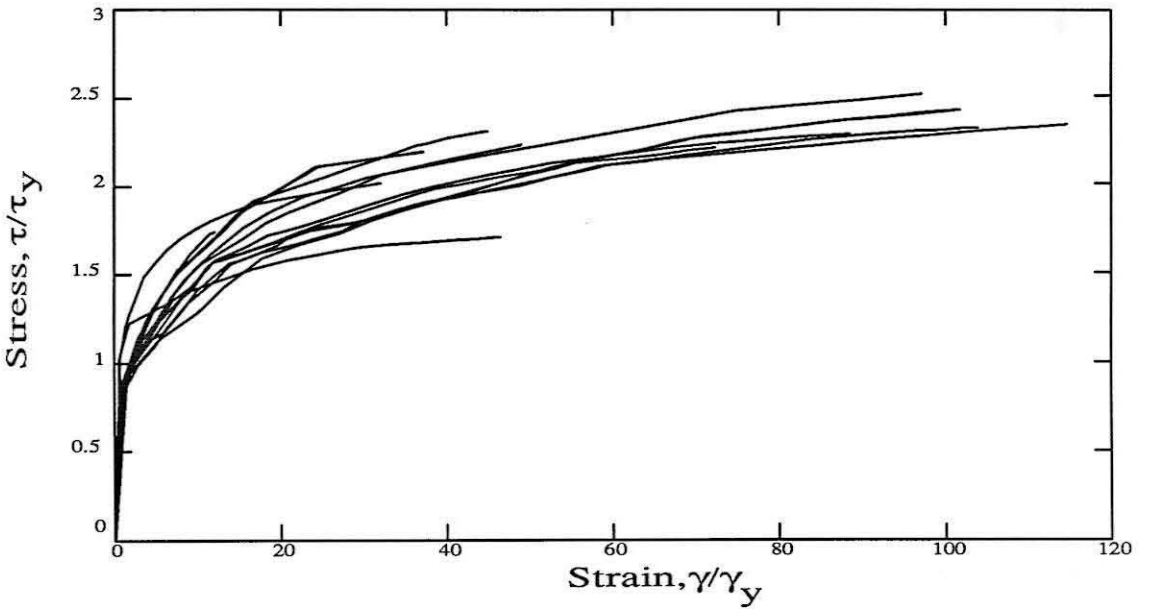

Figure 5.5 : Summary of the experimental data [17] of the monotonic stress-strain curves of the joint shear responses from steel beam-column sub-assemblage tests.

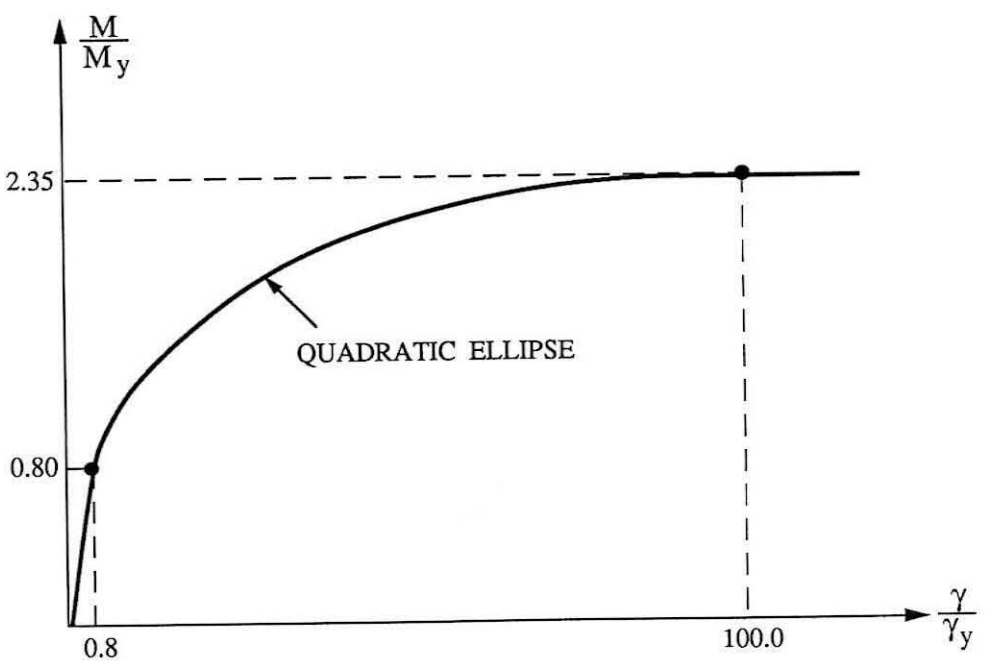

Figure 5.6 : Joint moment vs joint shear strain curve used as the backbone curve in the proposed joint model.

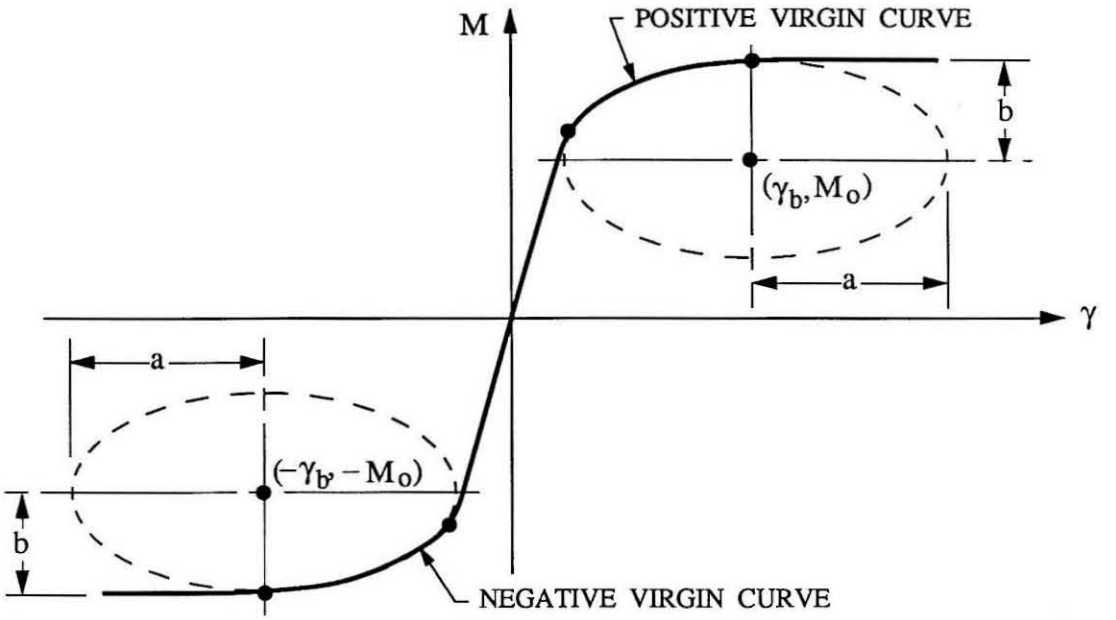

Figure 5.7 : Geometry of the quadratic ellipses modelling the nonlinear virgin curve in the Joint Hysteresis Model.

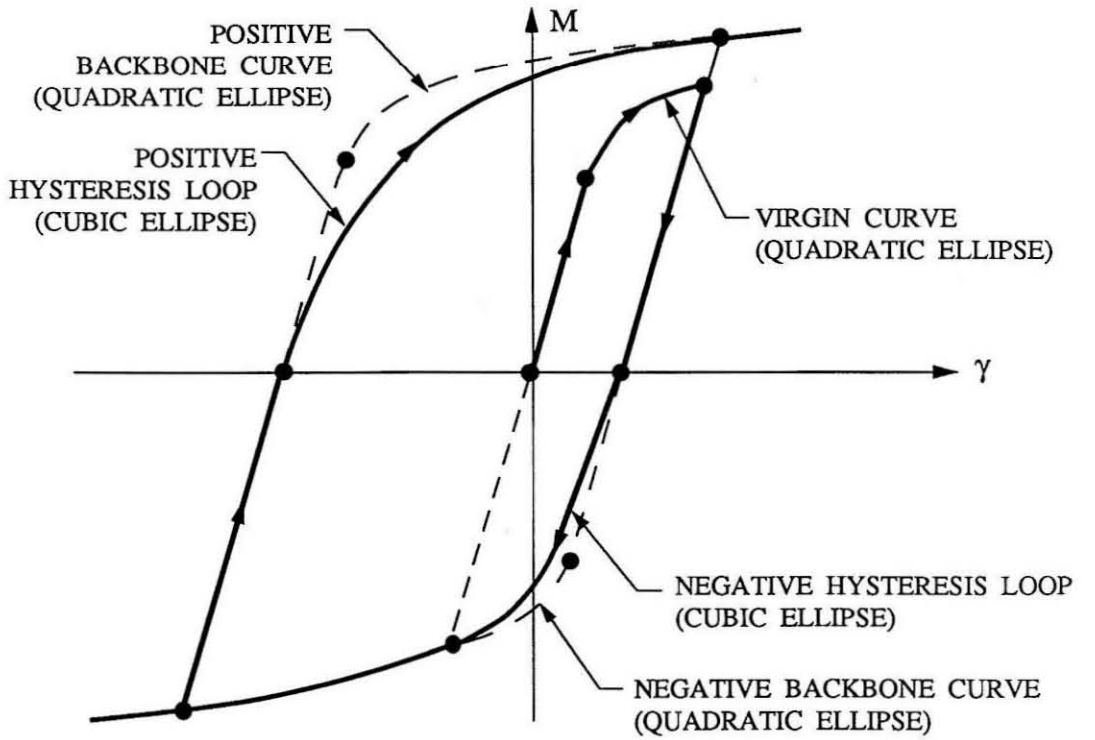

Figure 5.8 : Quadratic ellipses for virgin curves and backbone curves, and cubic ellipses for positive and negative hysteresis loops in the Joint Hysteresis Model.

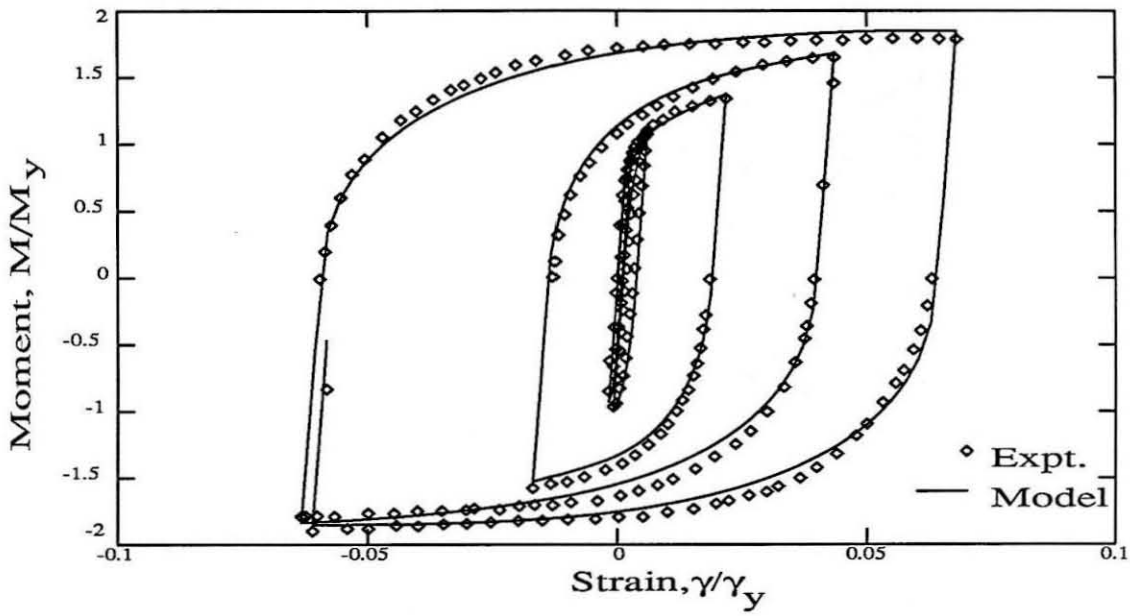

Figure 5.9 : Comparison of the experimental hysteresis loops [16] of the shear response of a steel joint from the sub-assemblage test, with the theoretical prediction using the Joint Hysteresis Model.

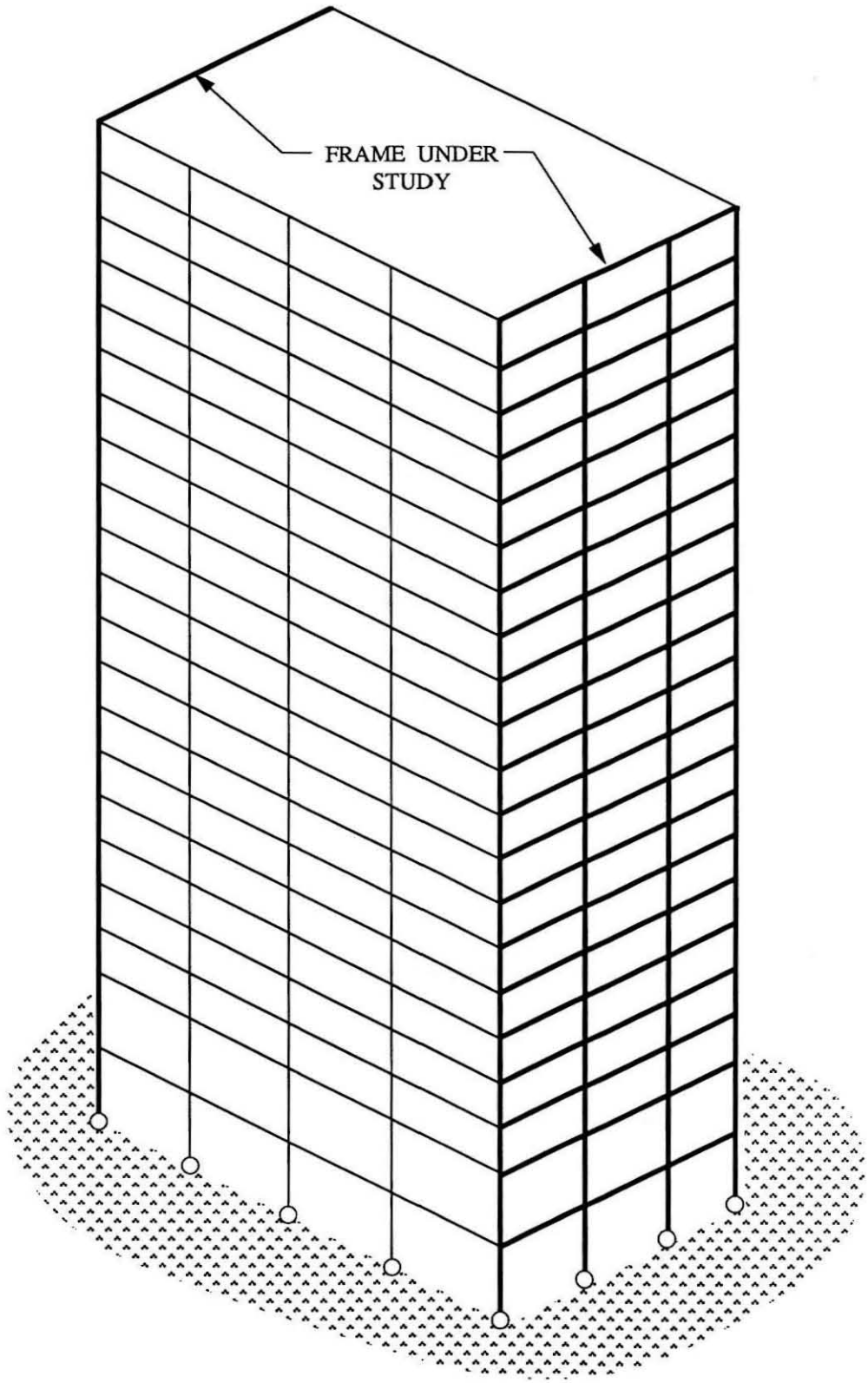

Figure 6.1 : Isometric view of the twenty-storey office building with specific reference to the moment resisting frame under consideration.

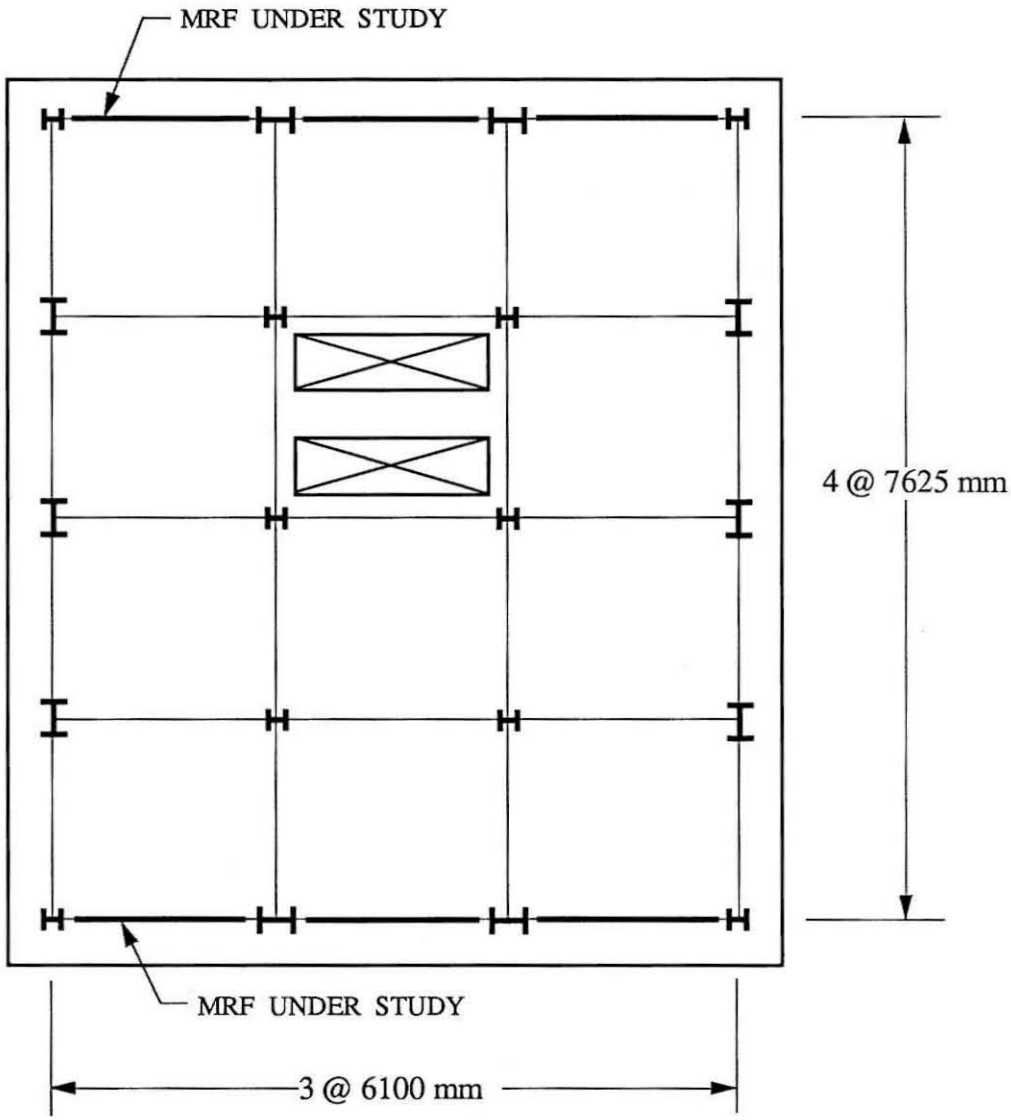

Figure 6.2 : Typical floor plan showing the framing in the twenty-storey office building.

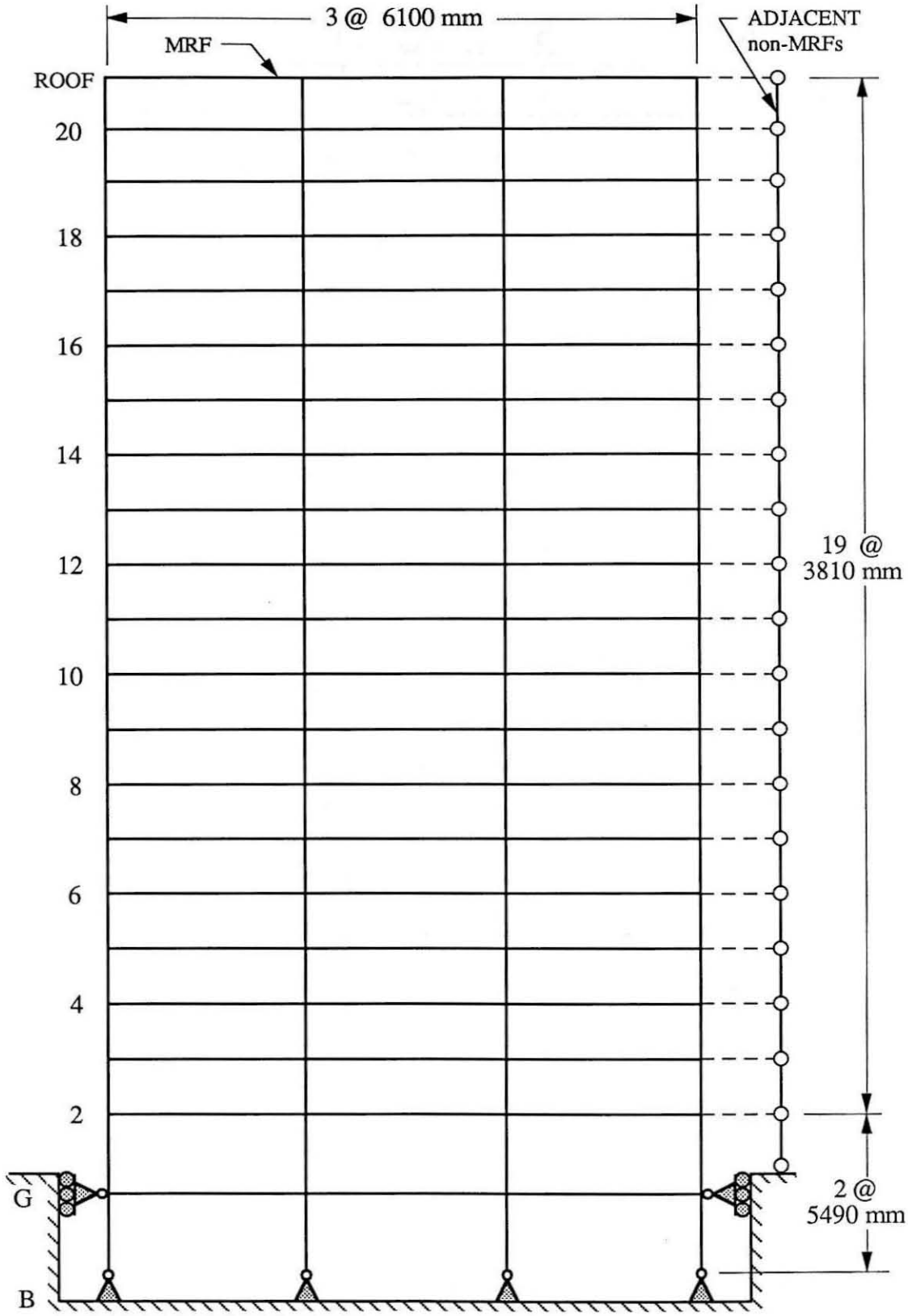

Figure 6.3 : Structural idealisation and dimensions of the planar MRF with adjacent non-MRFs.

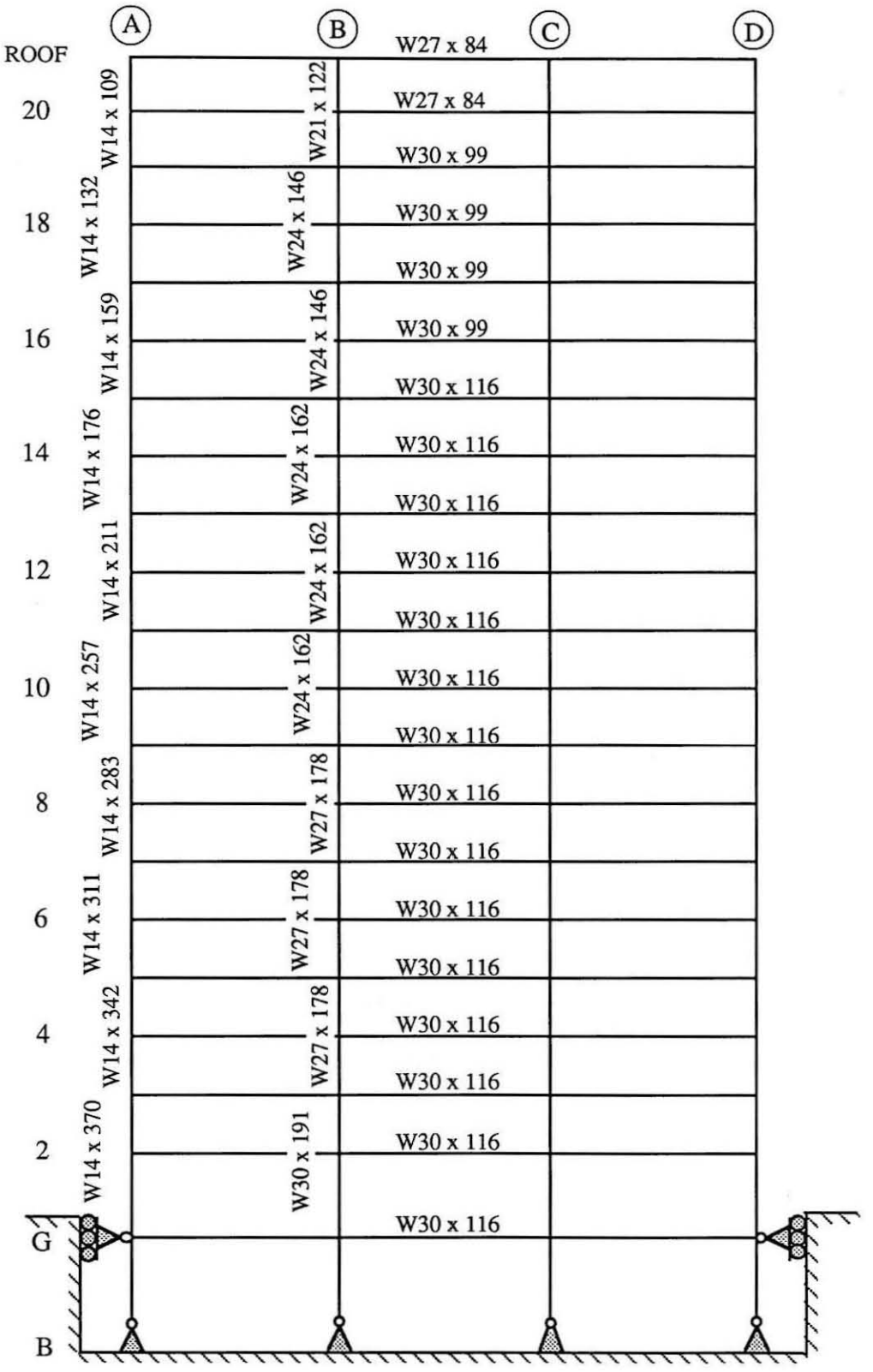

Figure 6.4 : Member cross-section sizes of the planar MRF.

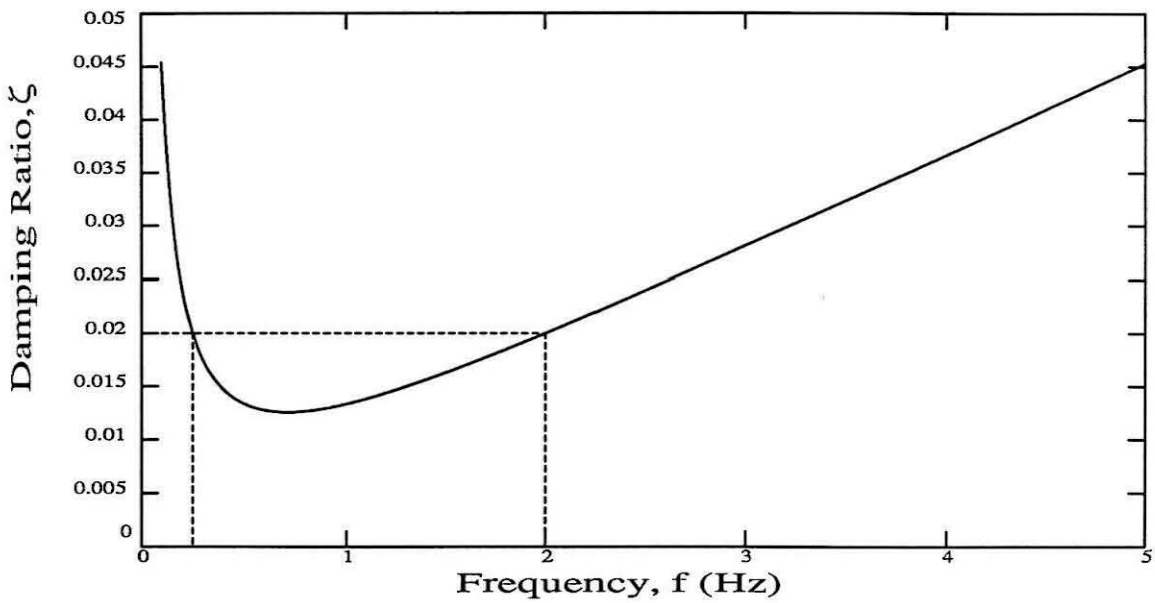

Figure 6.5 : Frequency dependence of the Rayleigh Damping estimated for the planar MRF.

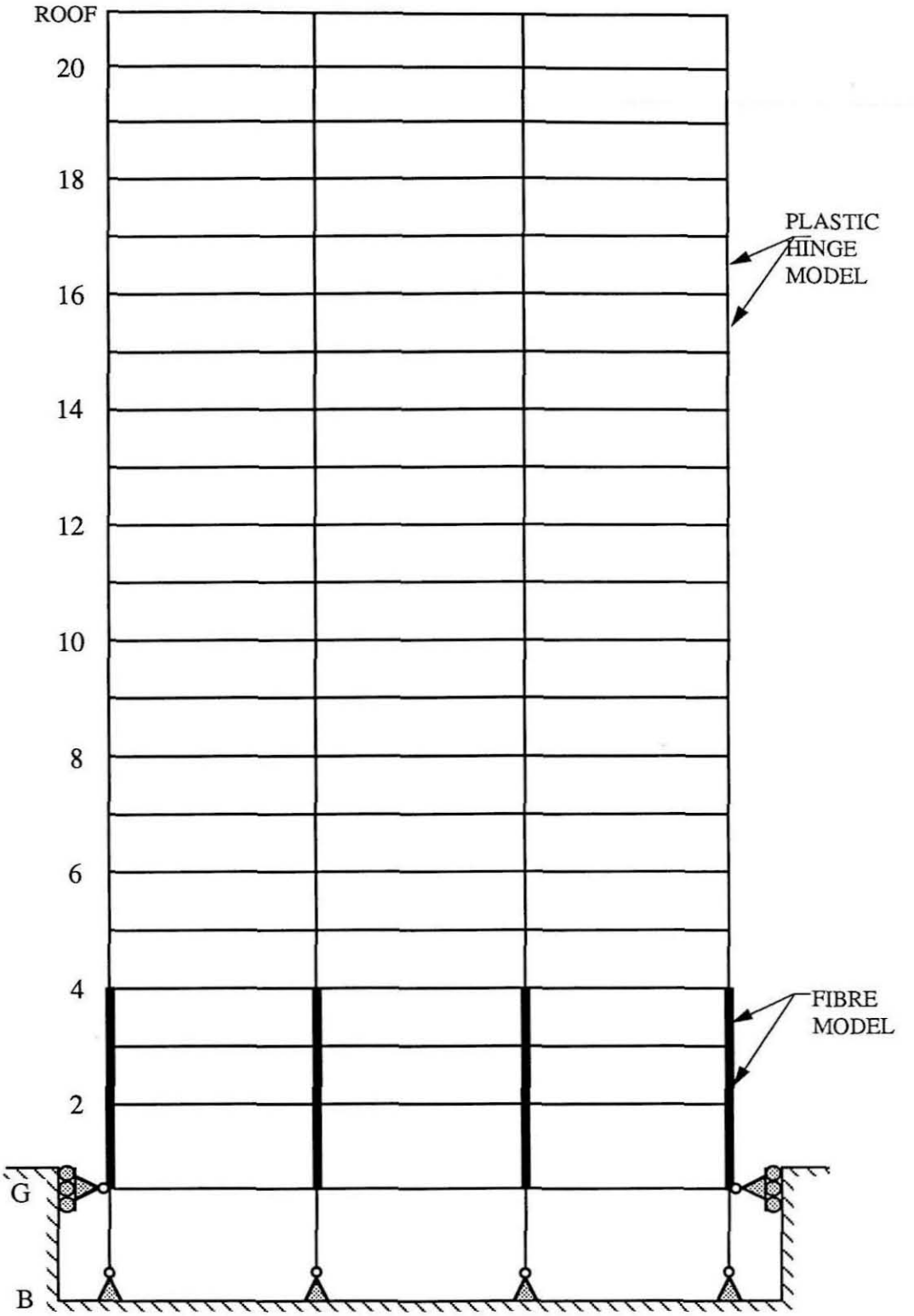

Figure 6.6 : The planar MRF showing the twelve columns modelled using the Fibre Model beam-column element.

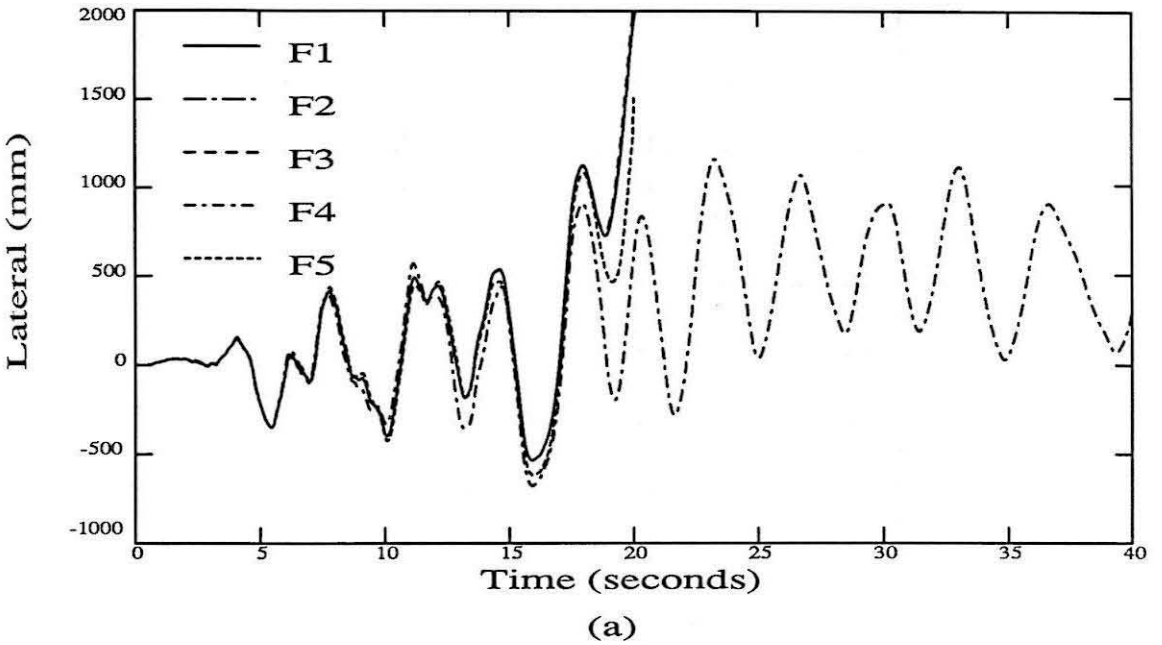

(a)

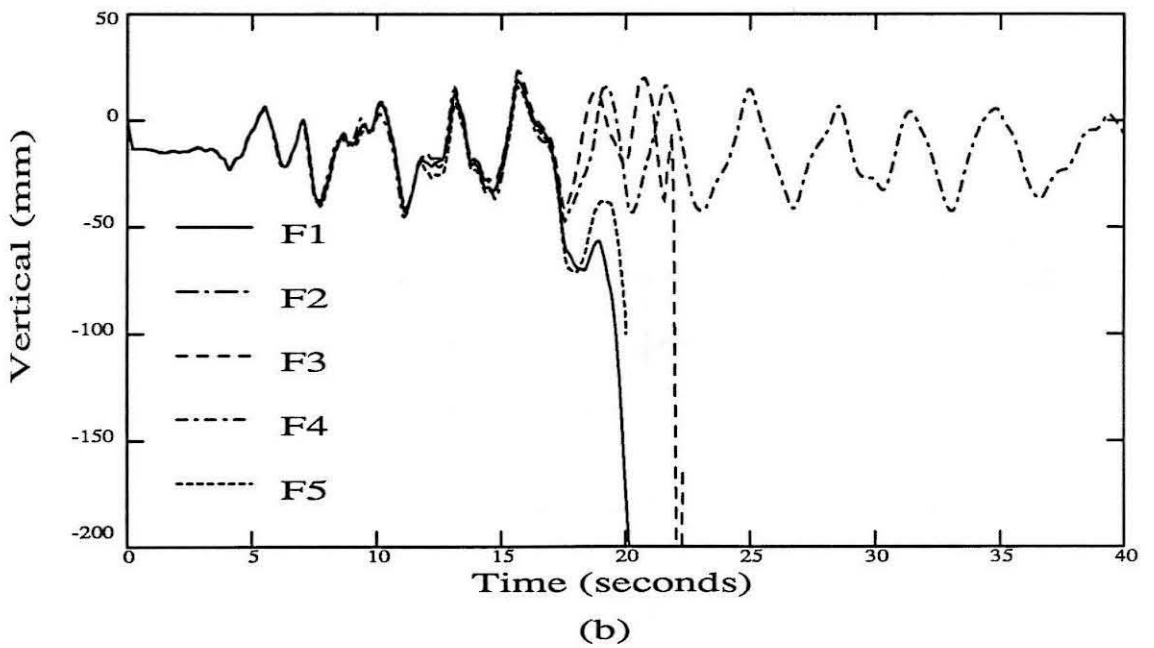

(b)

Figure 6.7 : Roof displacement time history summary of MRF0 from responses **F1** to **F5**.

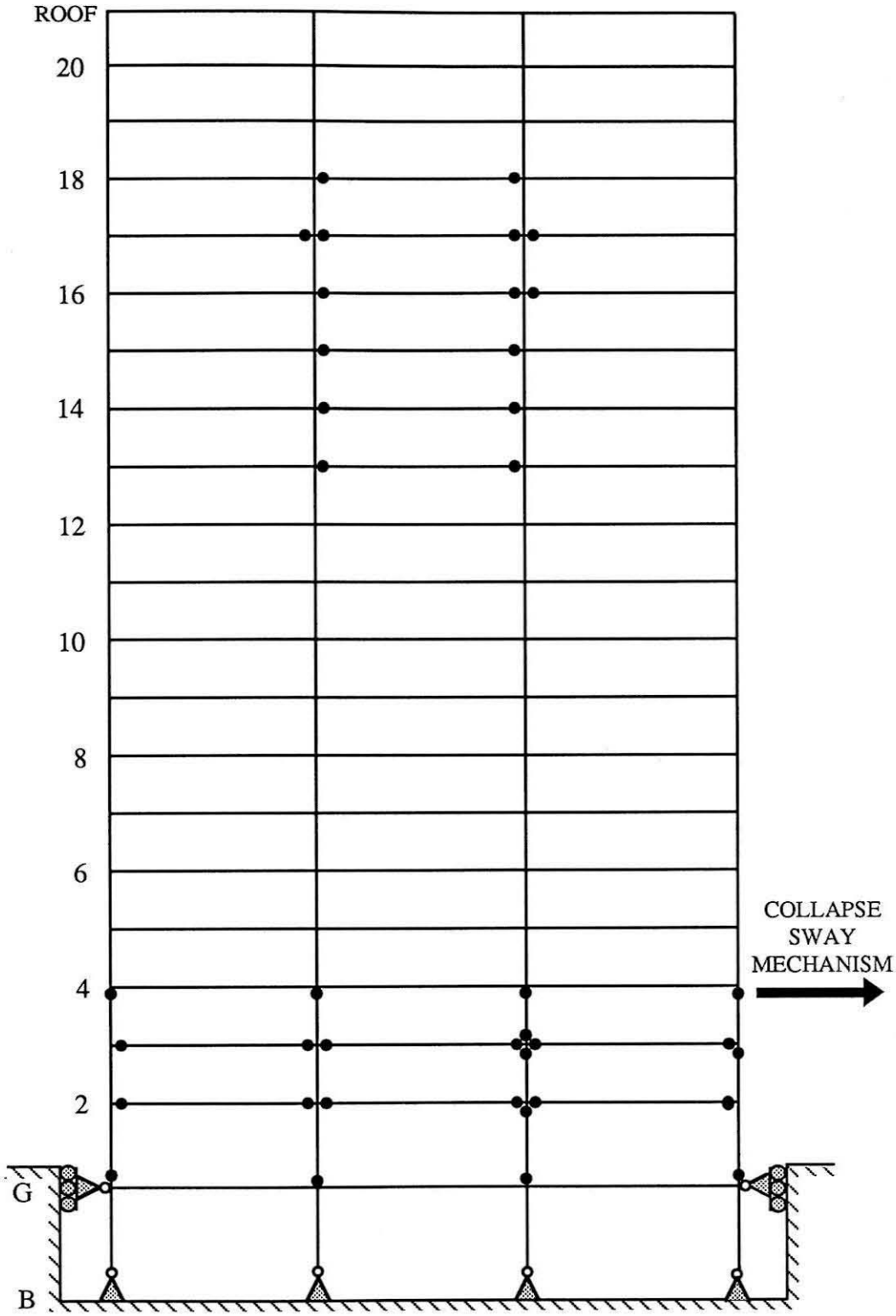

Figure 6.8 : The planar MRF showing the plastic hinges at the ends of the members resulting in the collapse mechanism in response **F1** at time 17.52 seconds.

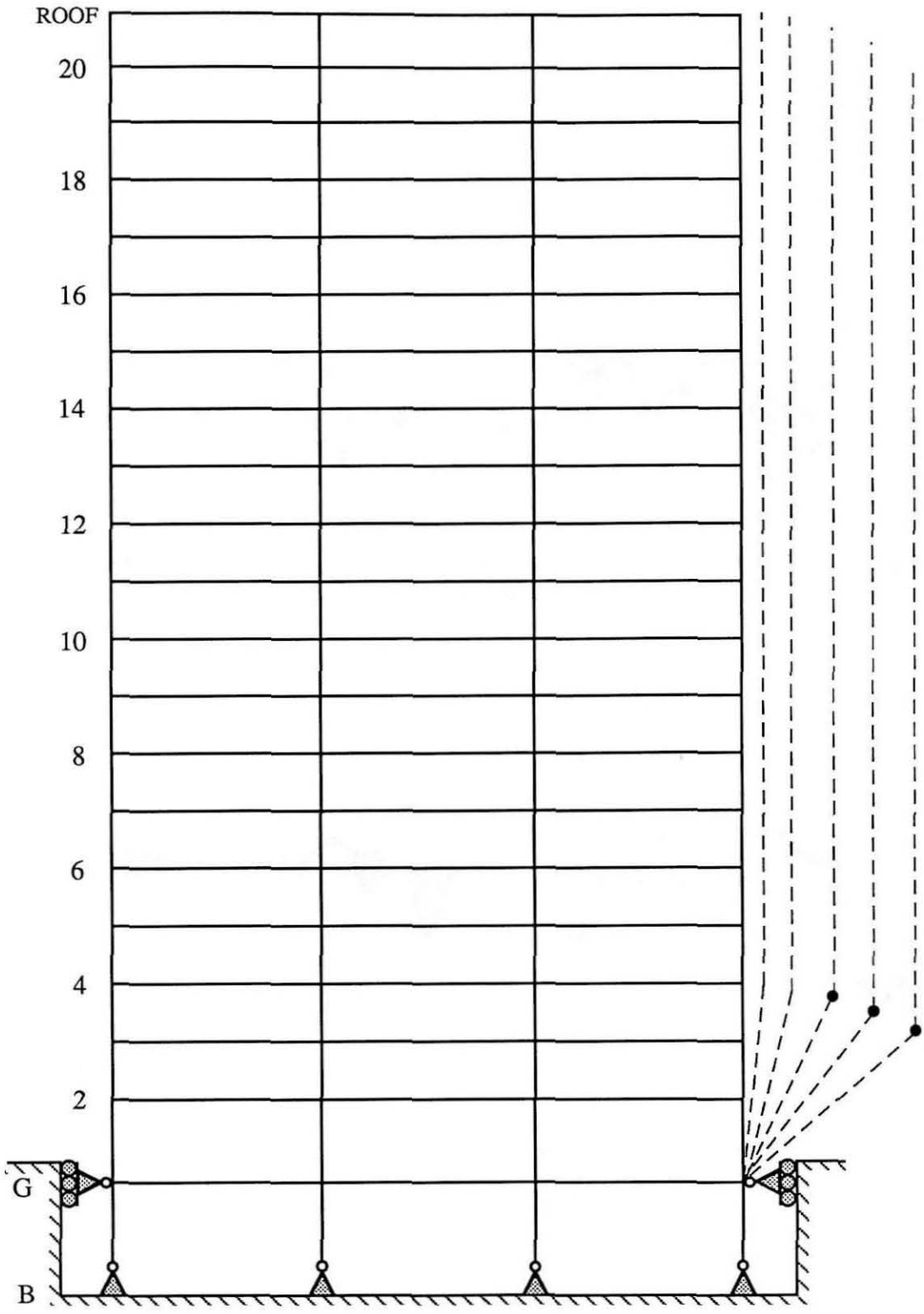

Figure 6.9 : The planar MRF showing the deformed profile (exaggerated scale) during collapse indicating the collapse sway mechanism in response **F1** between time 16 seconds and 20 seconds.

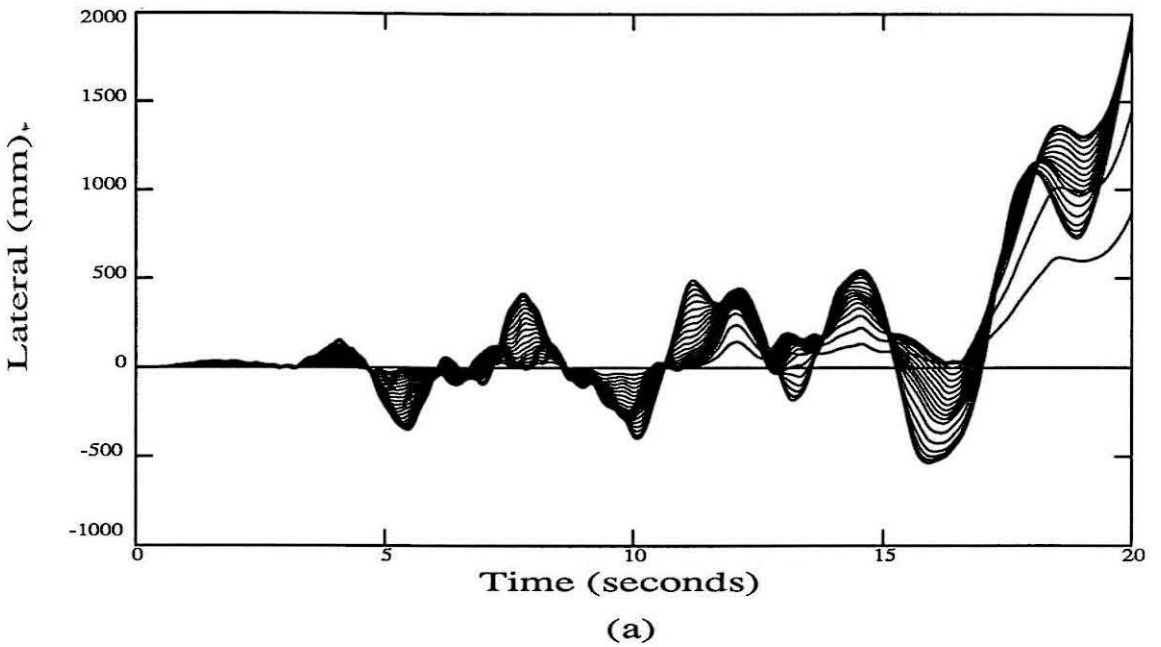

(a)

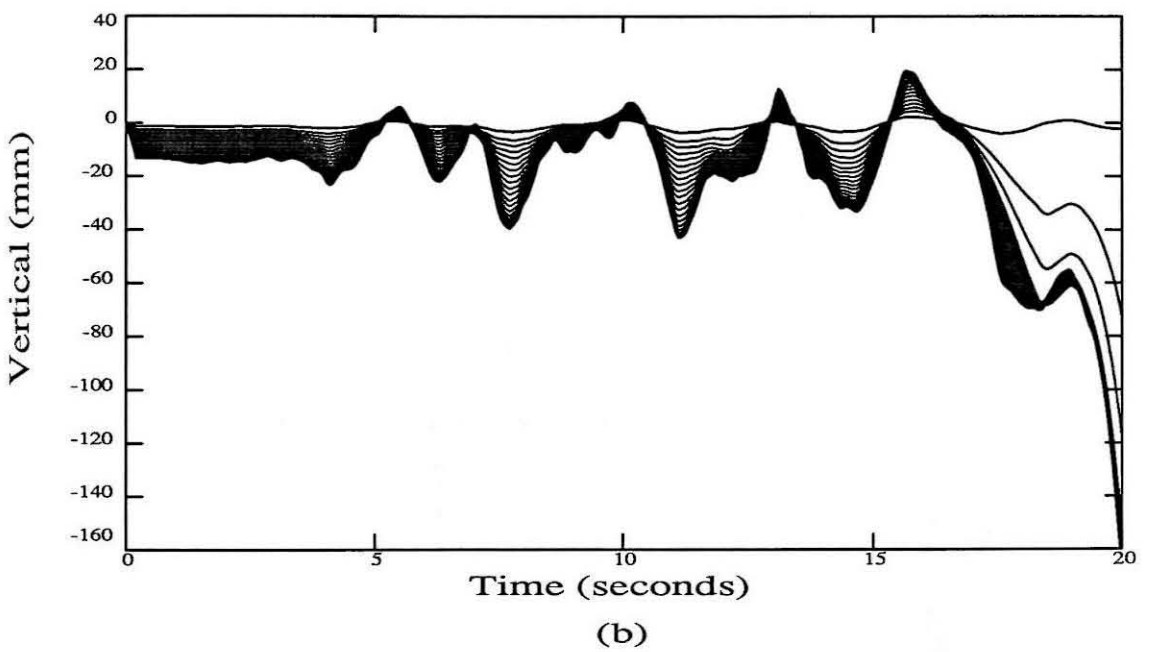

(b)

Figure 6.10 : Displacement time histories of all floors of MRF0 from response **F1**. The outermost curves correspond to the roof, while the innermost curves correspond to the first floor.

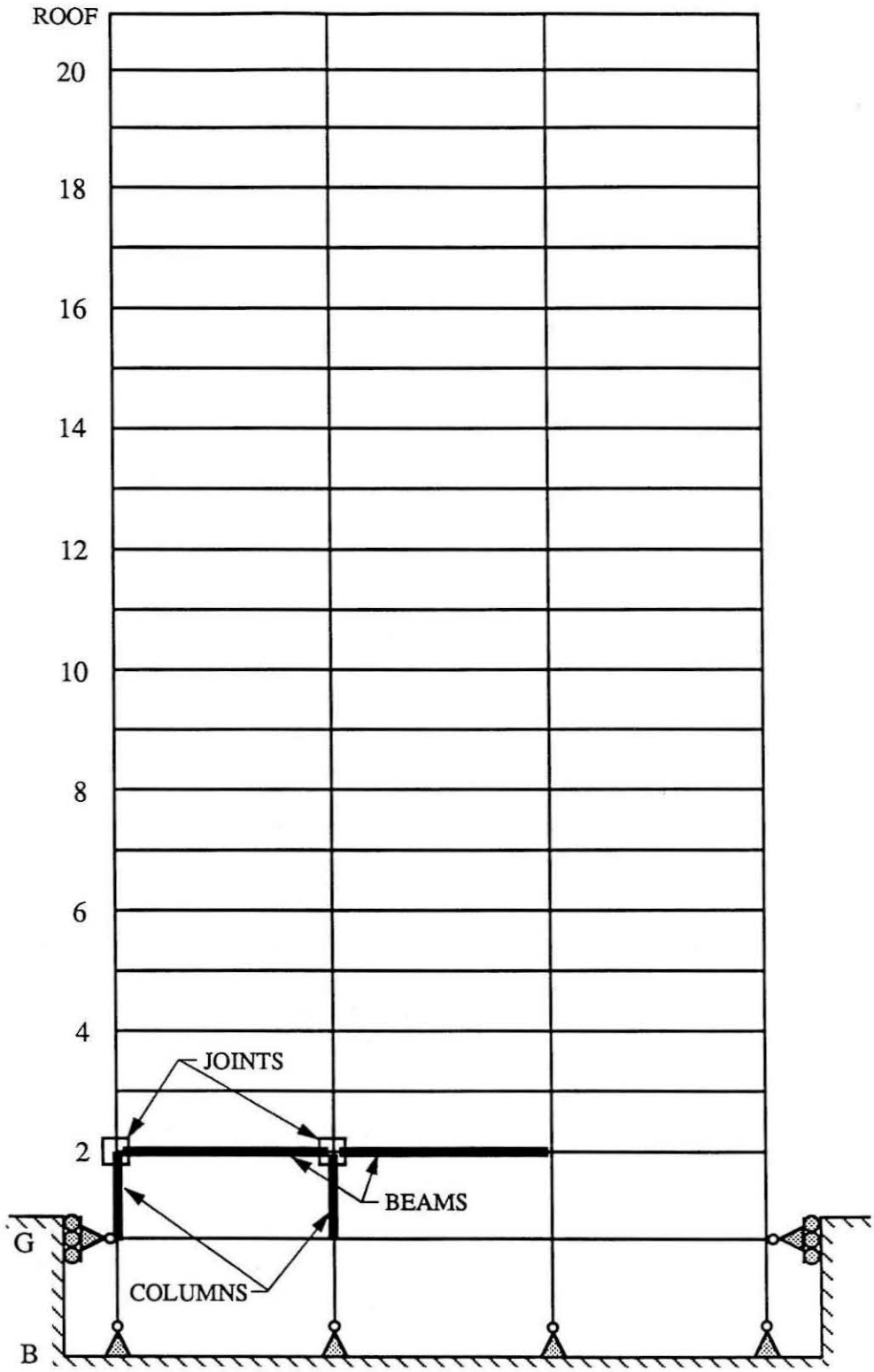

Figure 6.11 : The planar MRF elevation showing the beam-column members and the joints (in Chapter 7) for which the response time histories are presented.

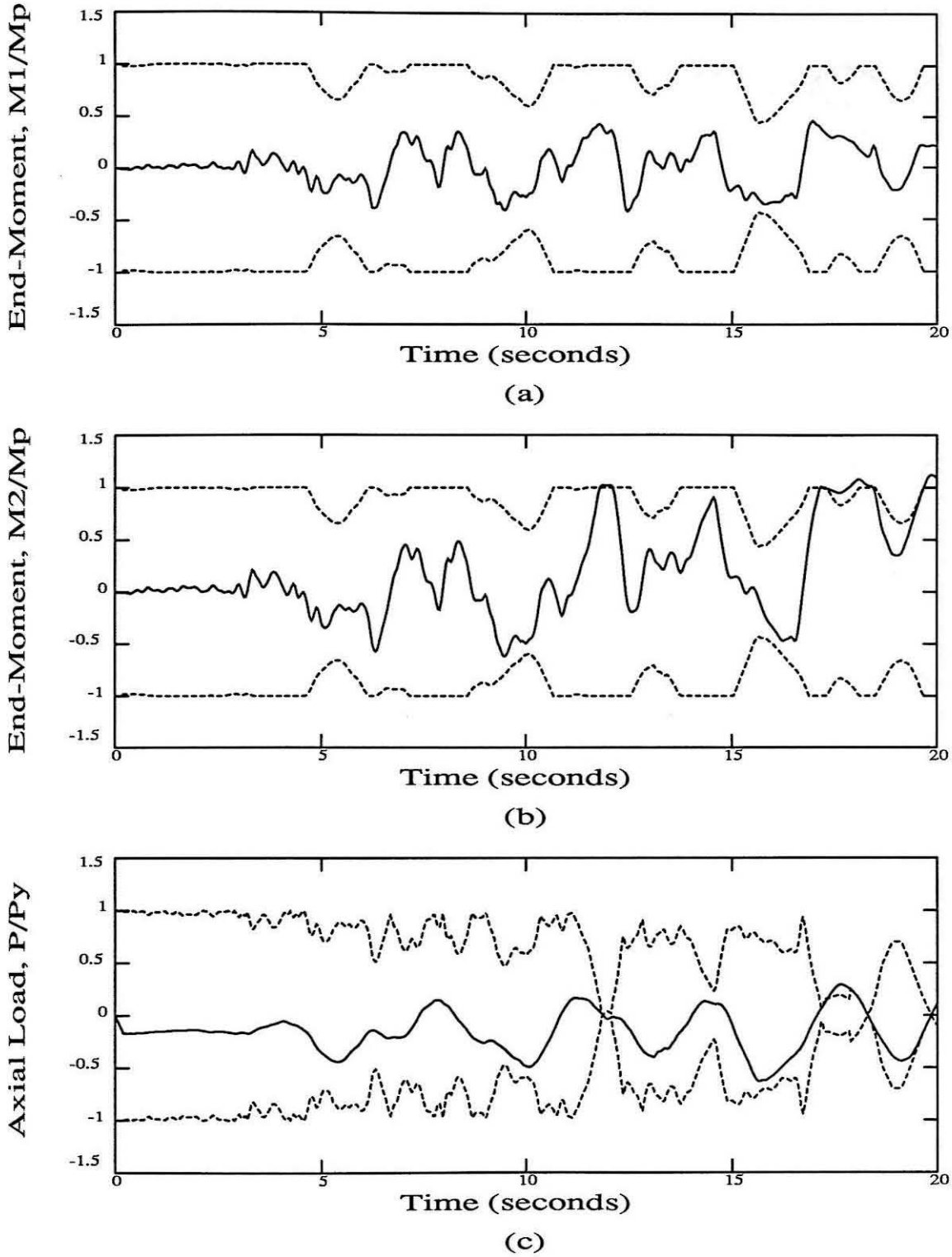

Figure 6.12 : Member response time histories of the first storey exterior column from response **F5**. The full lines represent the time histories and the dashed lines represent the envelopes.

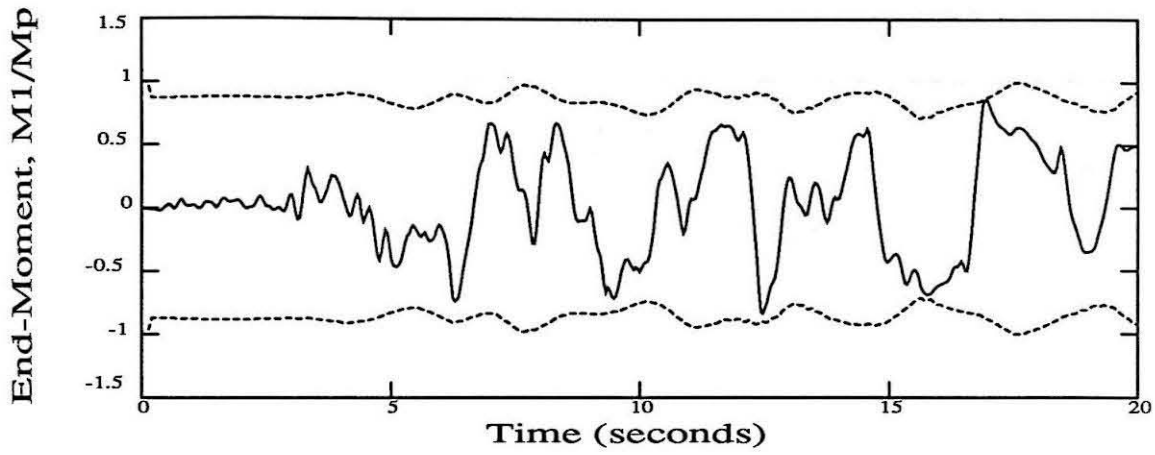

(a)

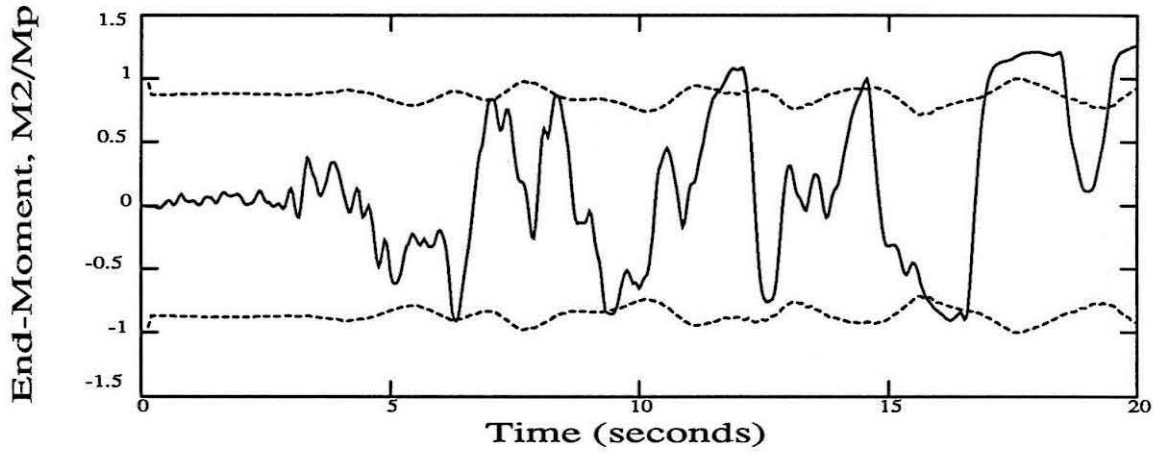

(b)

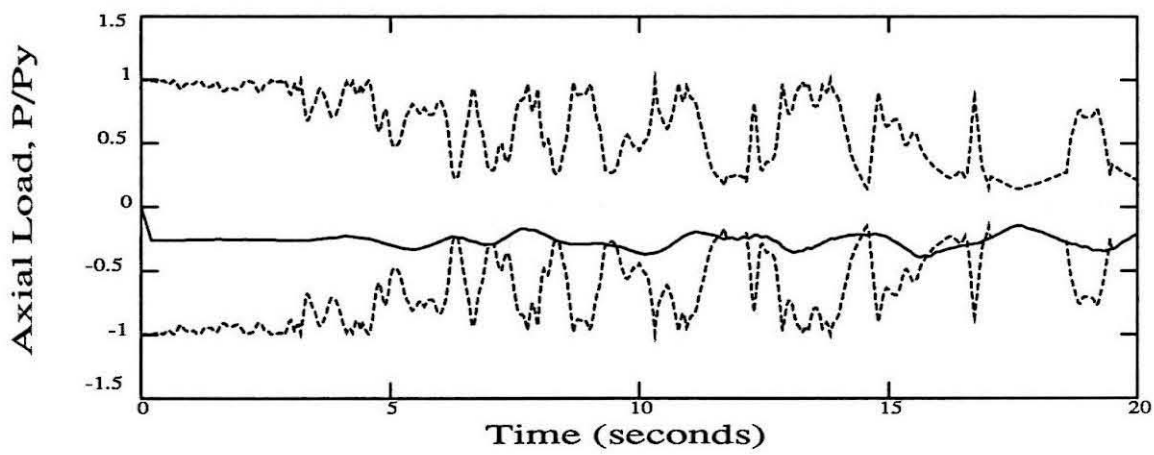

(c)

Figure 6.13 : Member response time histories of the first storey interior column from response **F5**. The full lines represent the time histories and the dashed lines represent the envelopes.

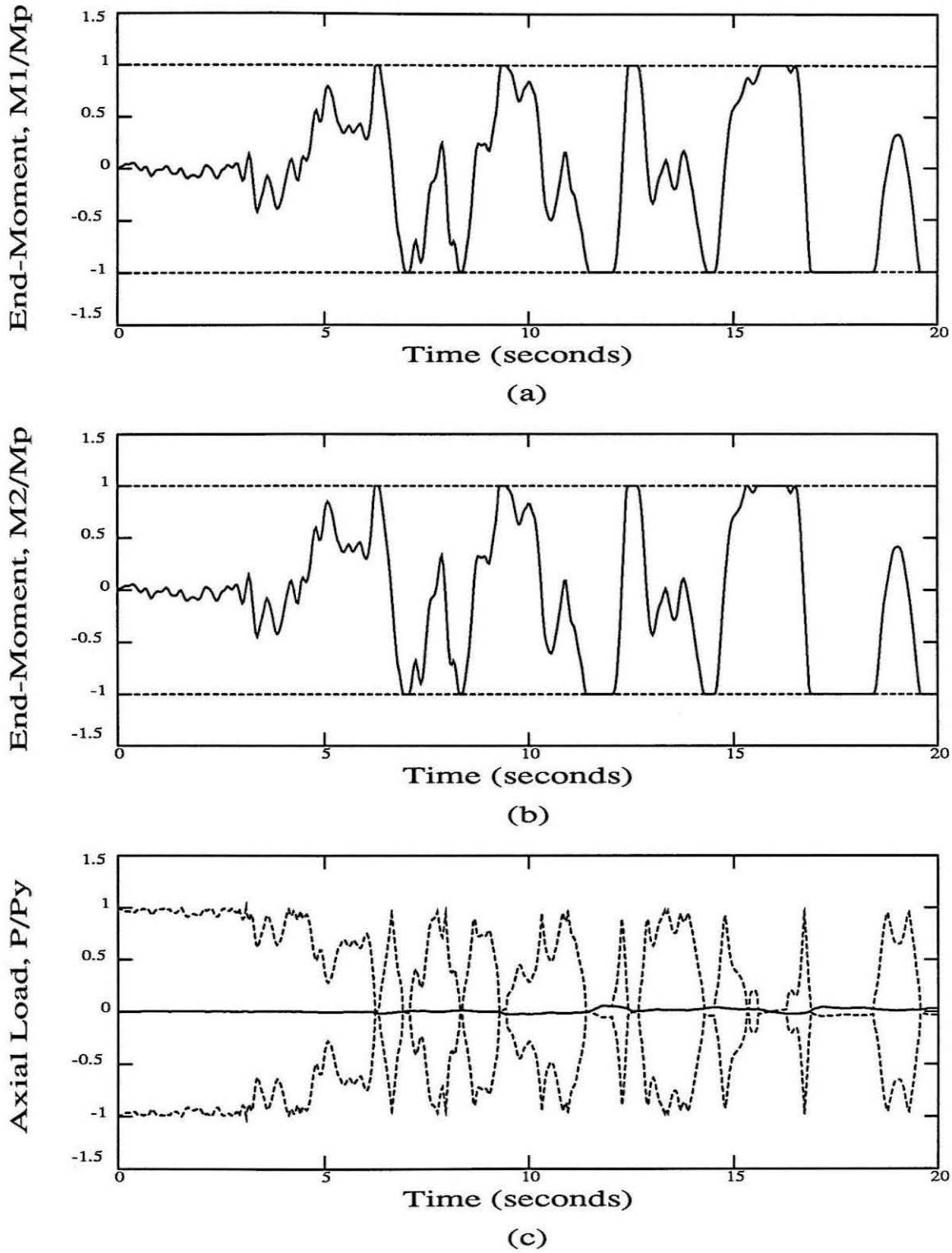

Figure 6.14 : Member response time histories of the second floor exterior beam from response **F5**. The full lines represent the time histories and the dashed lines represent the envelopes.

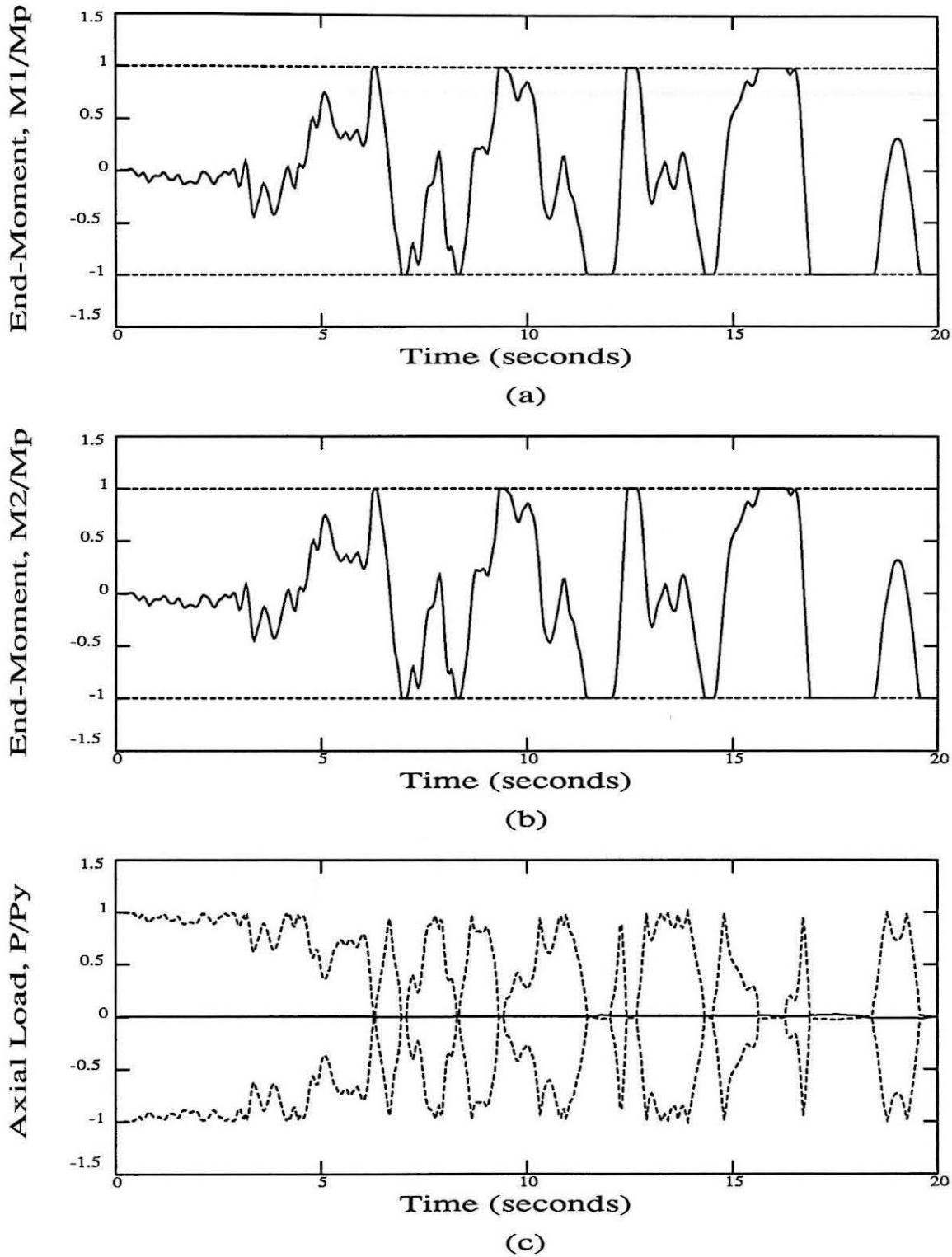

Figure 6.15 : Member response time histories of the second floor interior beam from response **F5**. The full lines represent the time histories and the dashed lines represent the envelopes.

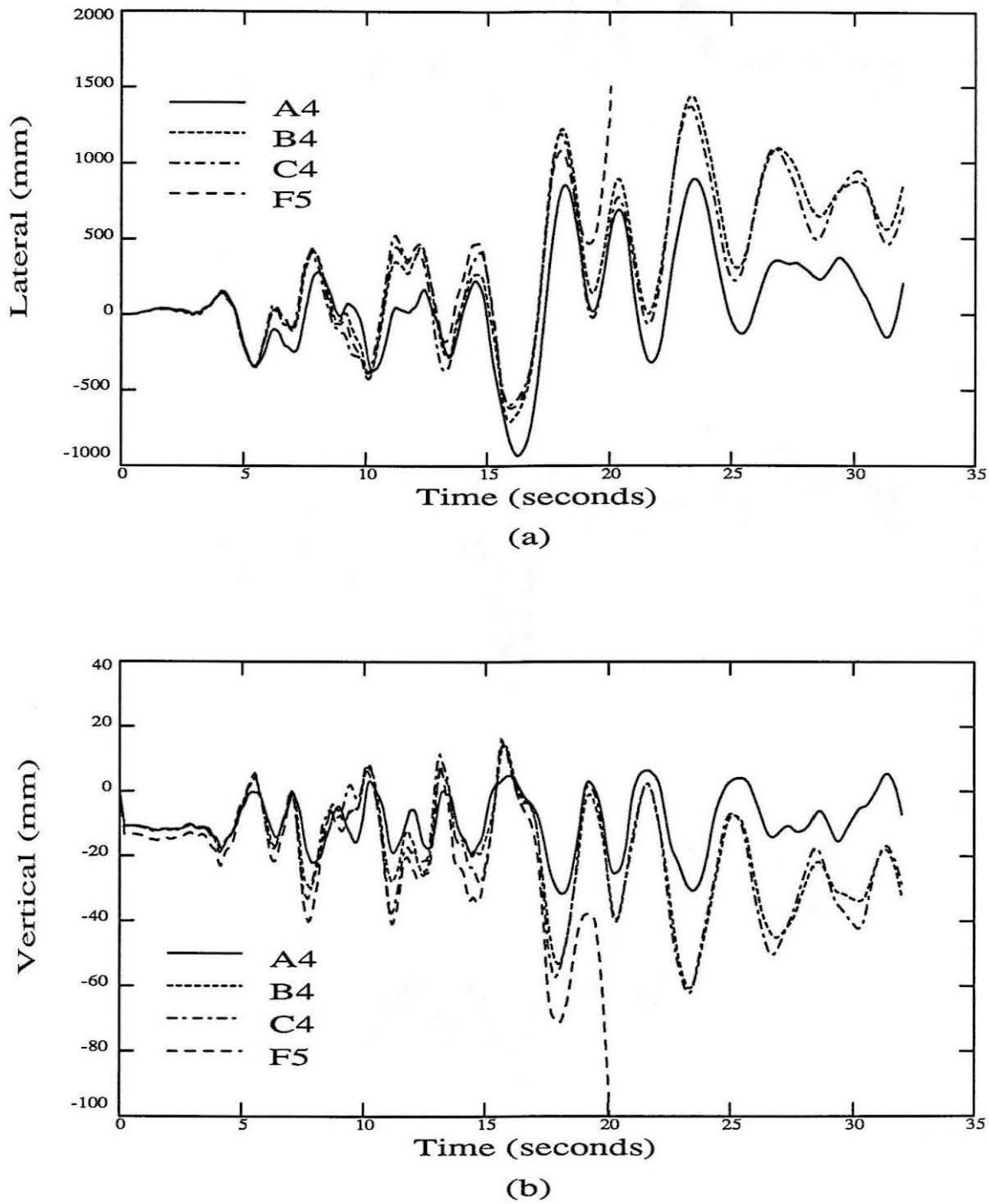

Figure 7.1 : Roof displacement time history summary of MRF1, MRF2, MRF3 and MRF0 from responses **A4**, **B4**, **C4** and **F5**, respectively.

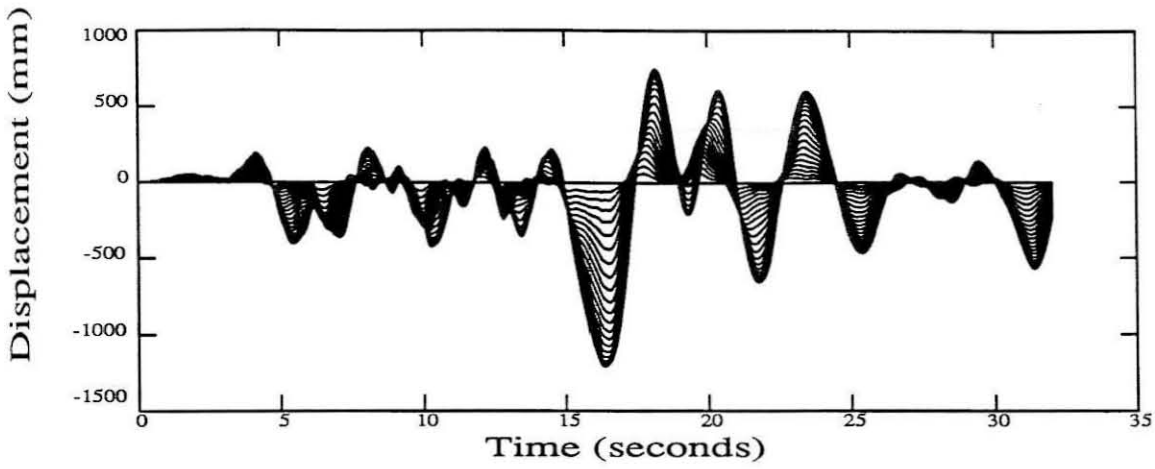

(a) MRF1

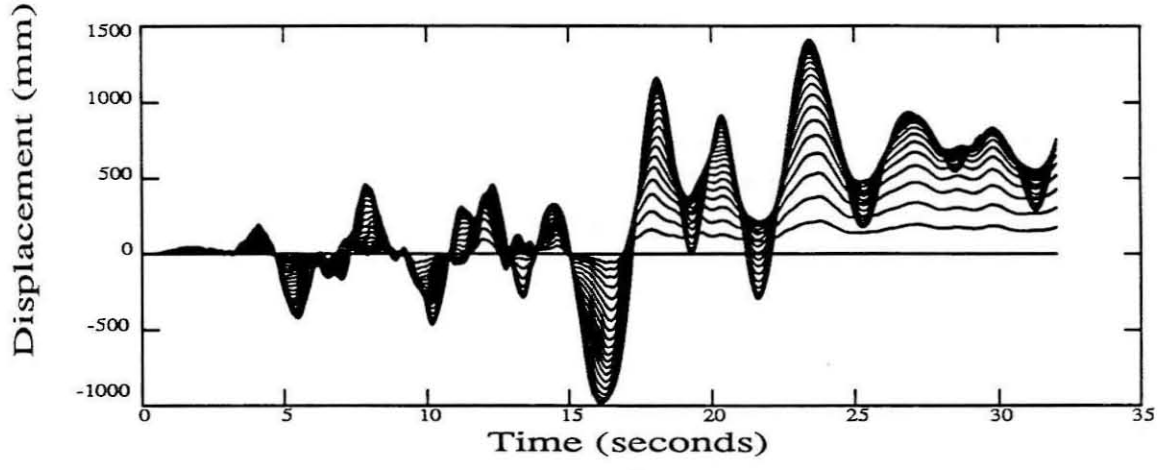

(b) MRF2

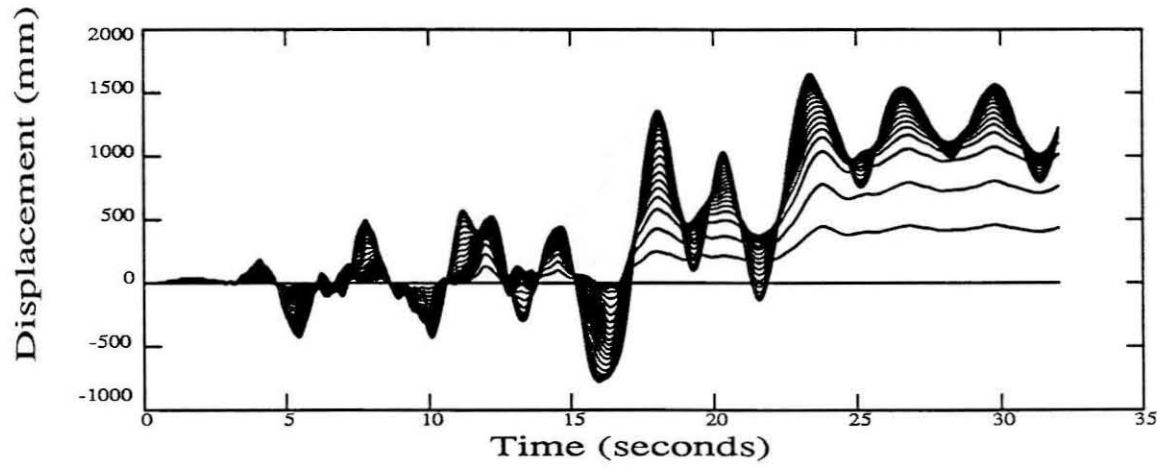

(c) MRF3

Figure 7.2 : Lateral displacement time histories of all floors of the three MRFs from responses **A5**, **B5** and **C5**. The outermost curves correspond to the roof, while the innermost curves correspond to the first floor.

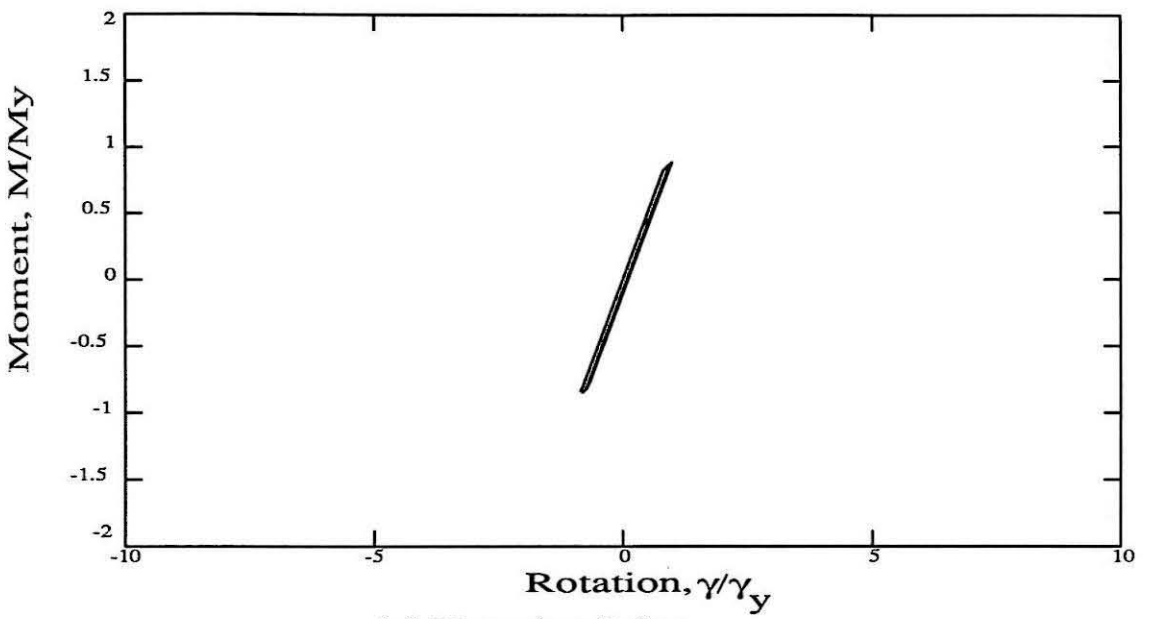

(a) Exterior Joint

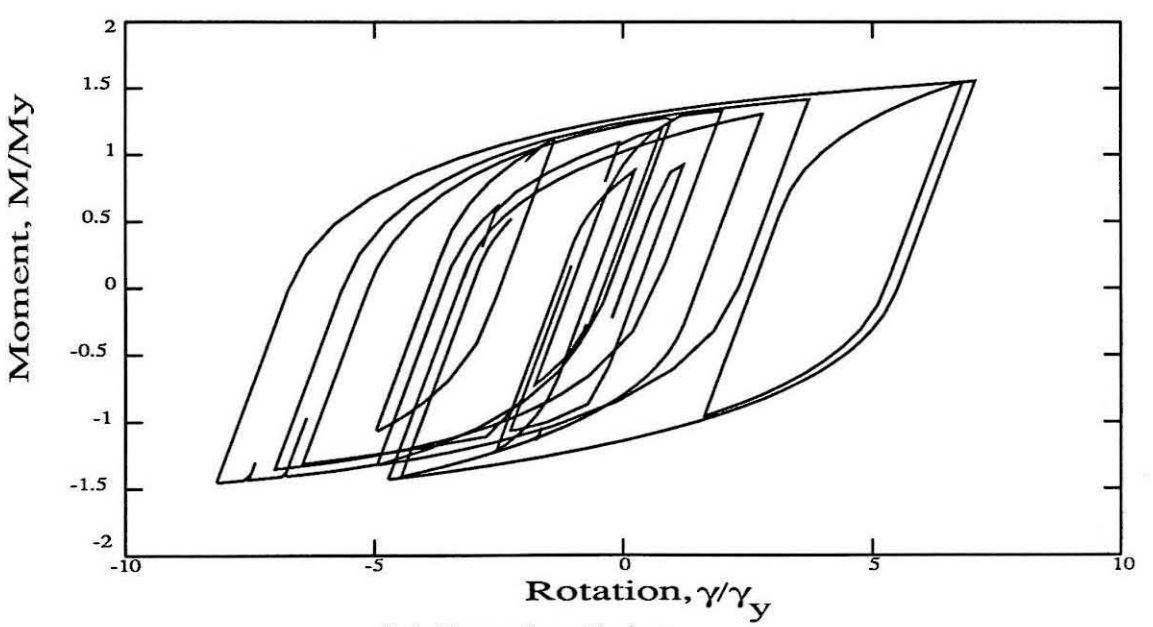

(b) Interior Joint

Figure 7.3 : Hysteresis loops of the second floor exterior and interior joints of MRF1 from response **A5**.

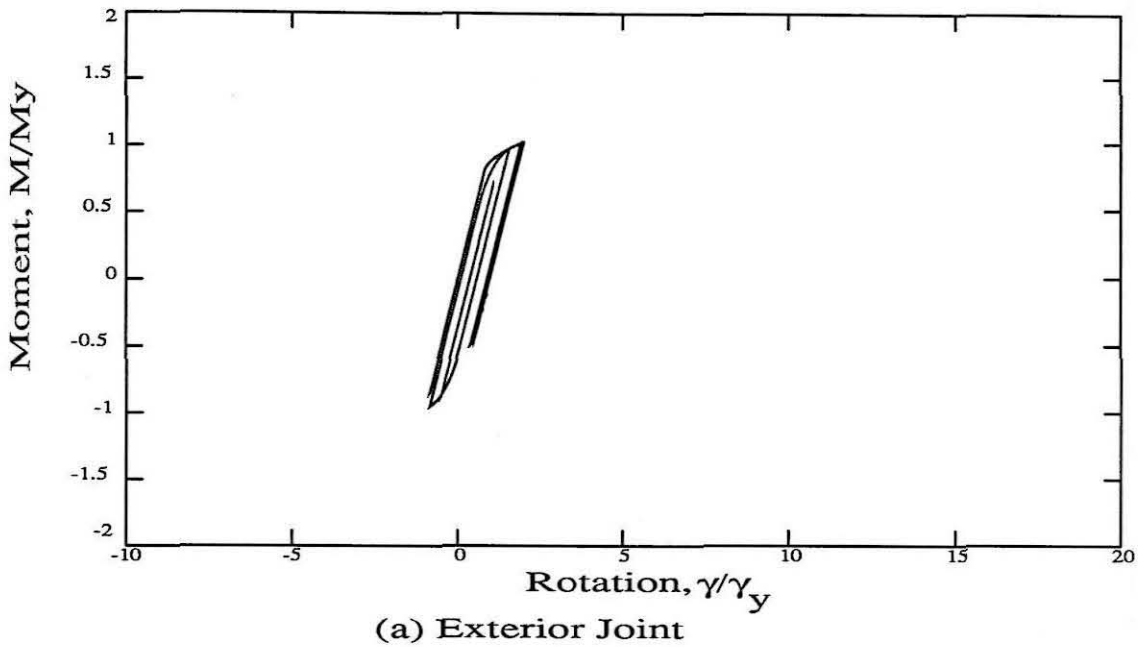

(a) Exterior Joint

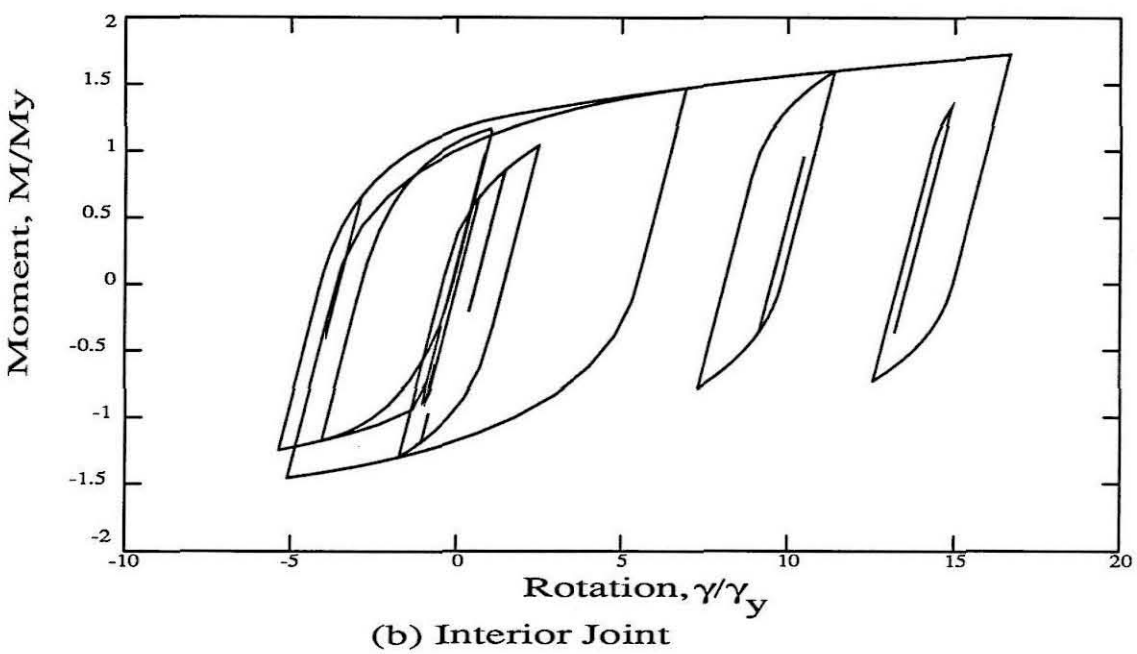

(b) Interior Joint

Figure 7.4 : Hysteresis loops of the second floor exterior and interior joints of MRF2 from response **B5**.

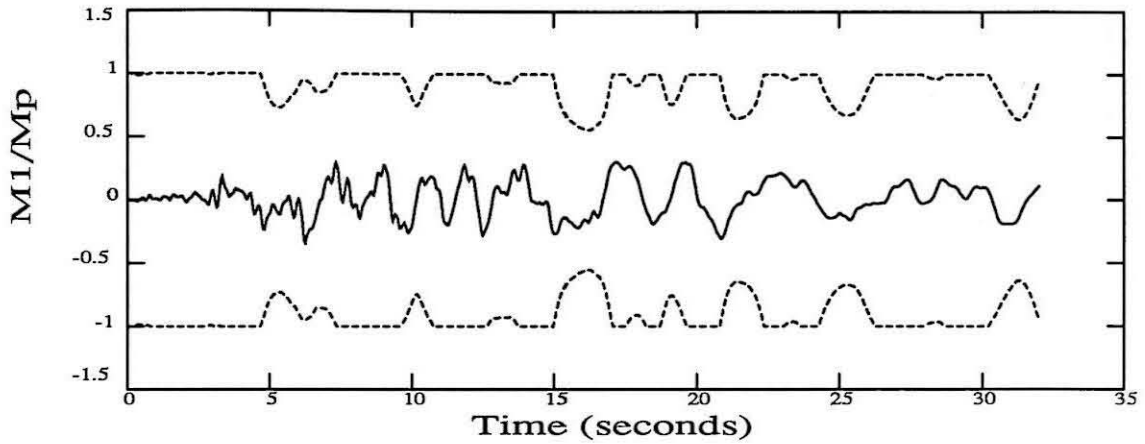

(a)

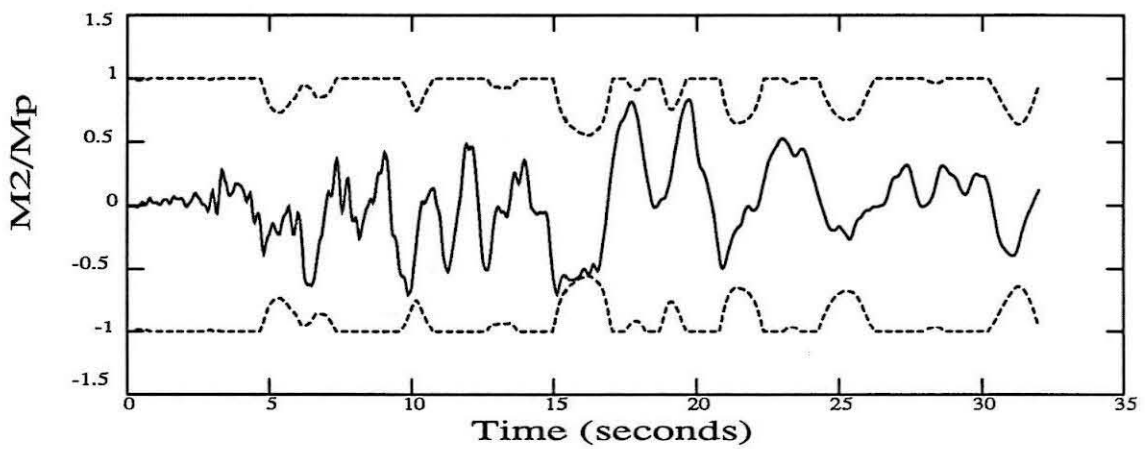

(b)

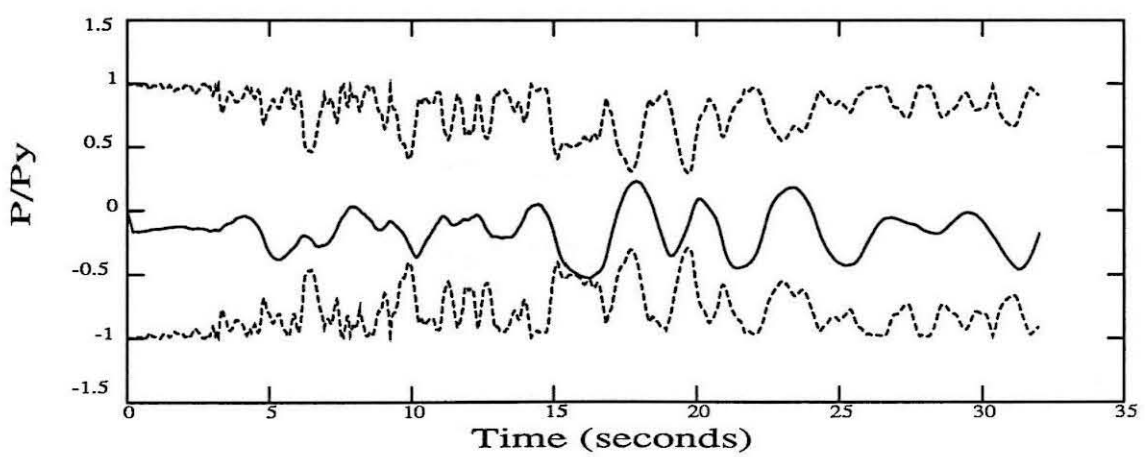

(c)

Figure 7.5 : Response time histories of the first storey exterior column of MRF1 from response **A5**. The full lines represent the responses, while the dashed lines represent the envelopes.

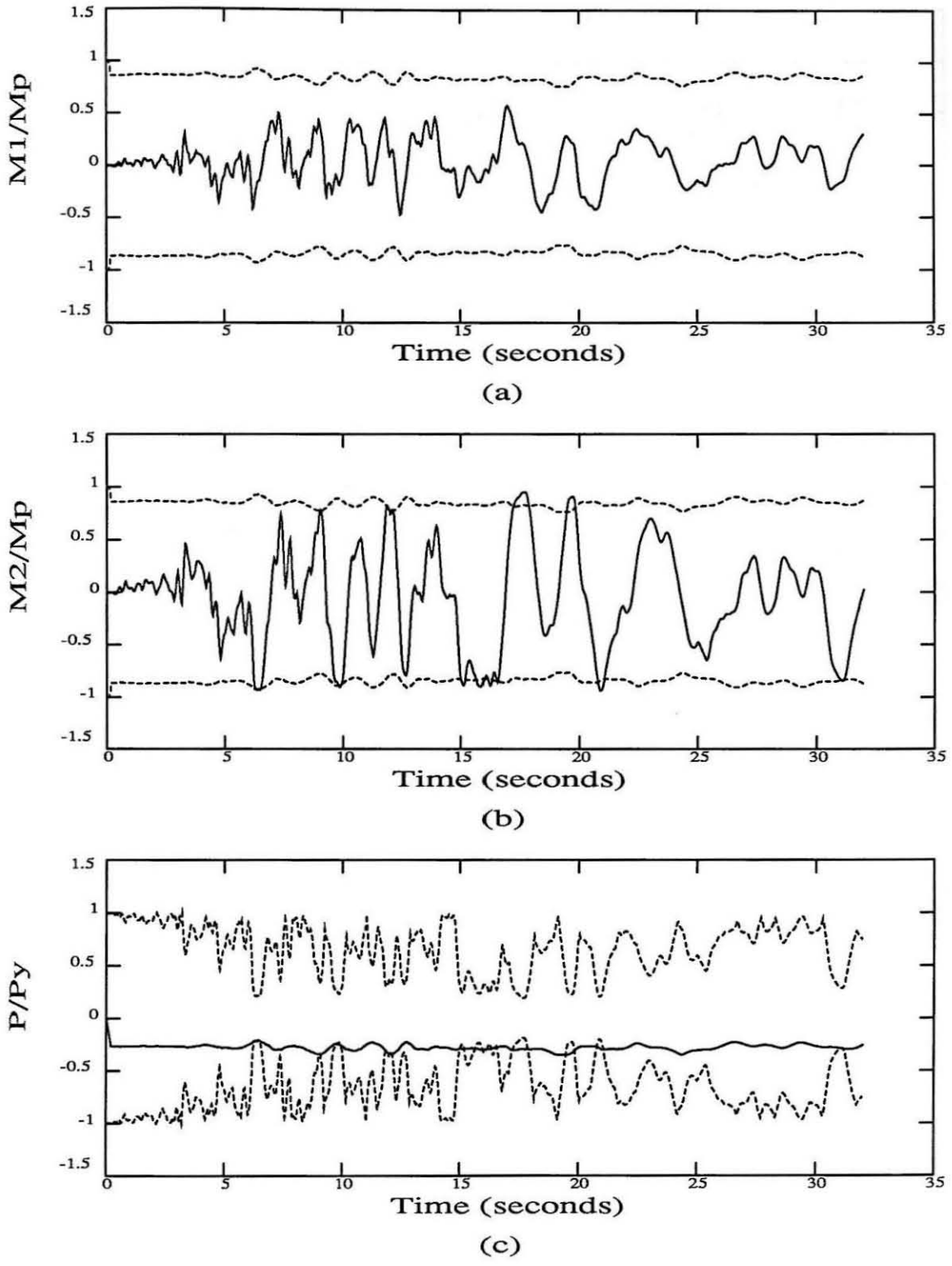

Figure 7.6 : Response time histories of the first storey interior column of MRF1 from response **A5**. The full lines represent the responses, while the dashed lines represent the envelopes.

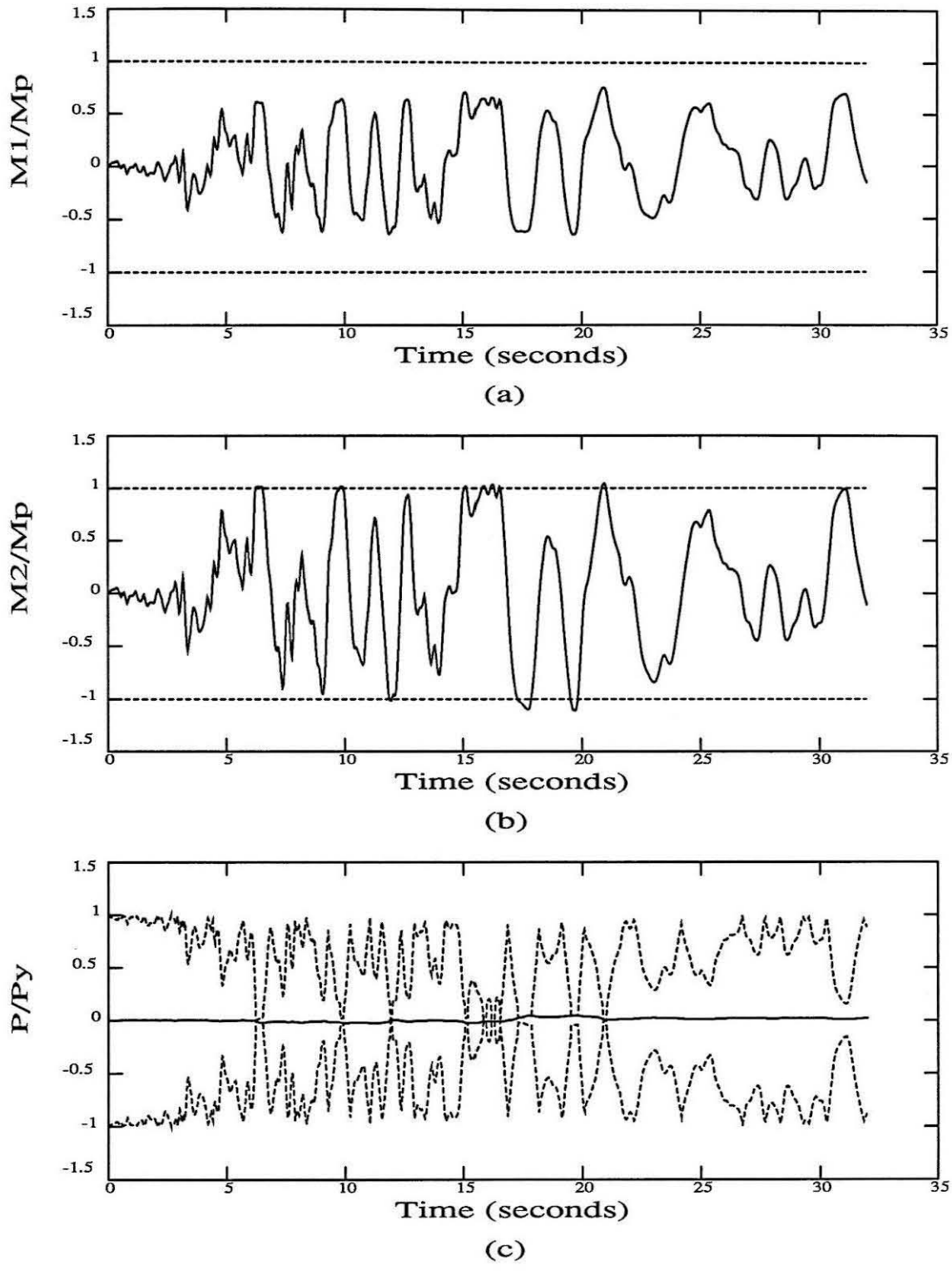

Figure 7.7 : Response time histories of the second floor exterior beam of MRF1 from response **A5**. The full lines represent the responses, while the dashed lines represent the envelopes.

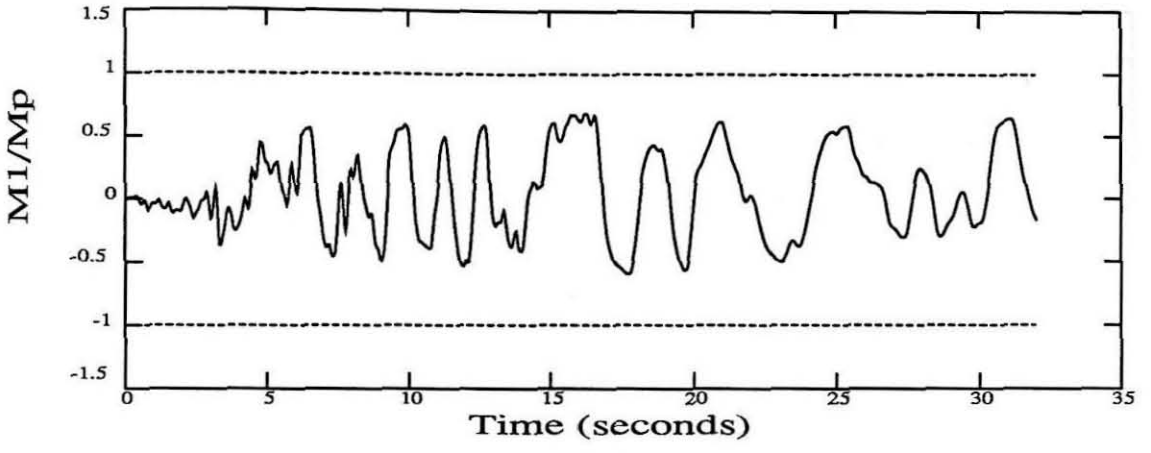

(a)

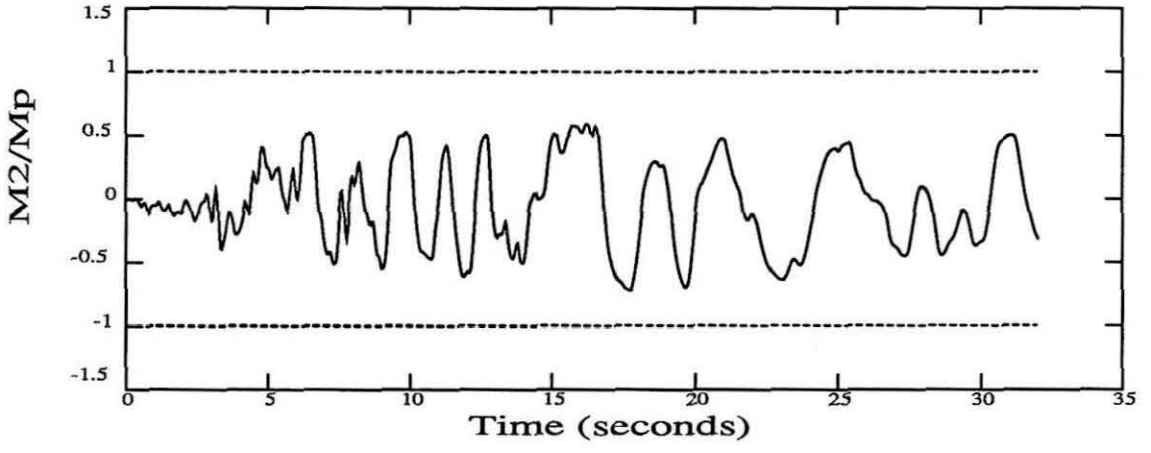

(b)

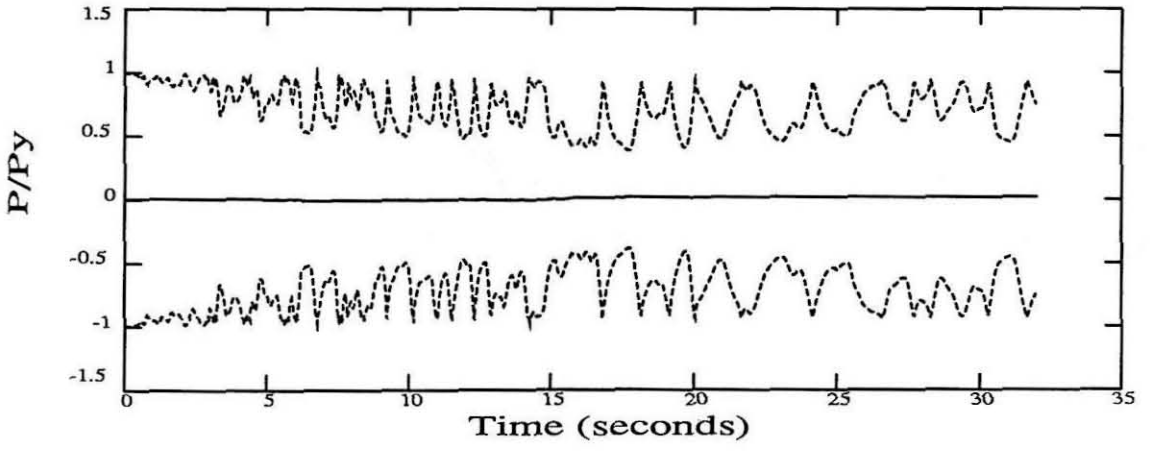

(c)

Figure 7.8 : Response time histories of the second floor interior beam of MRF1 from response **A5**. The full lines represent the responses, while the dashed lines represent the envelopes.

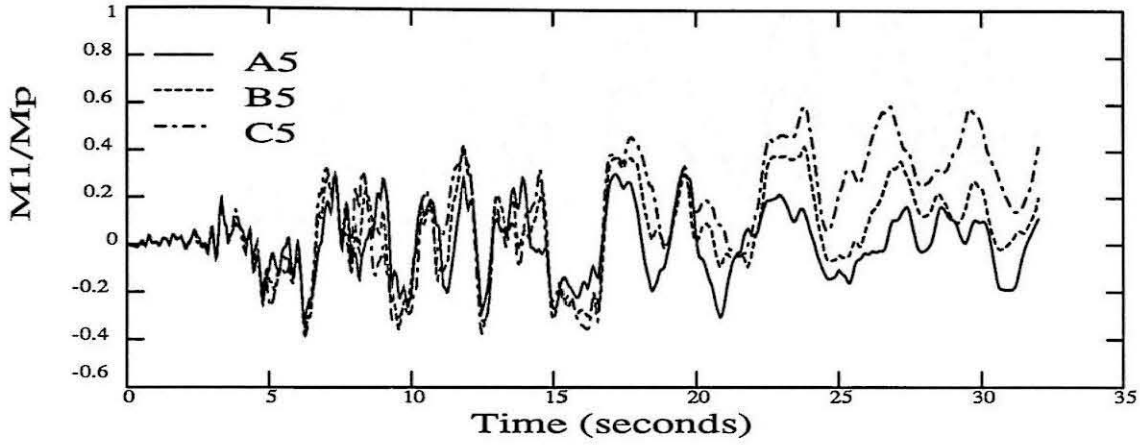

(a)

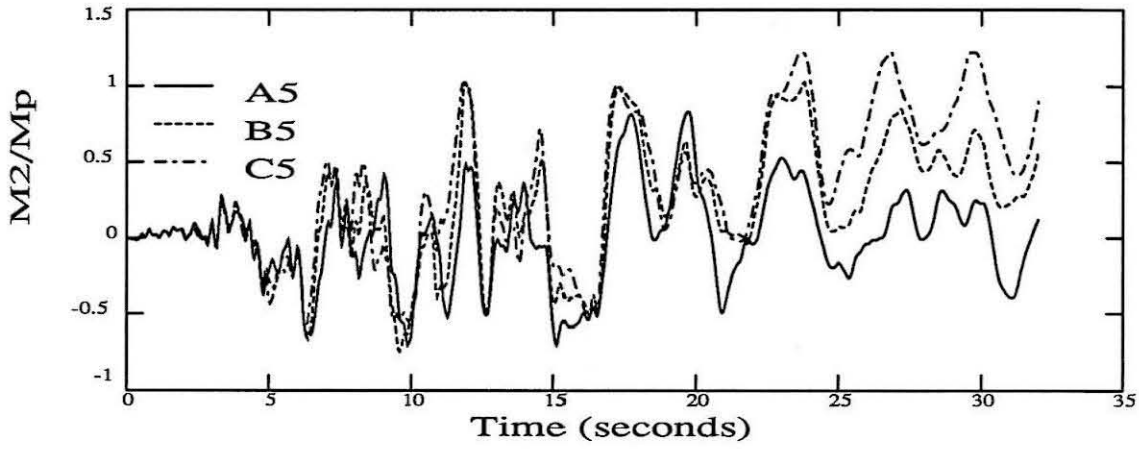

(b)

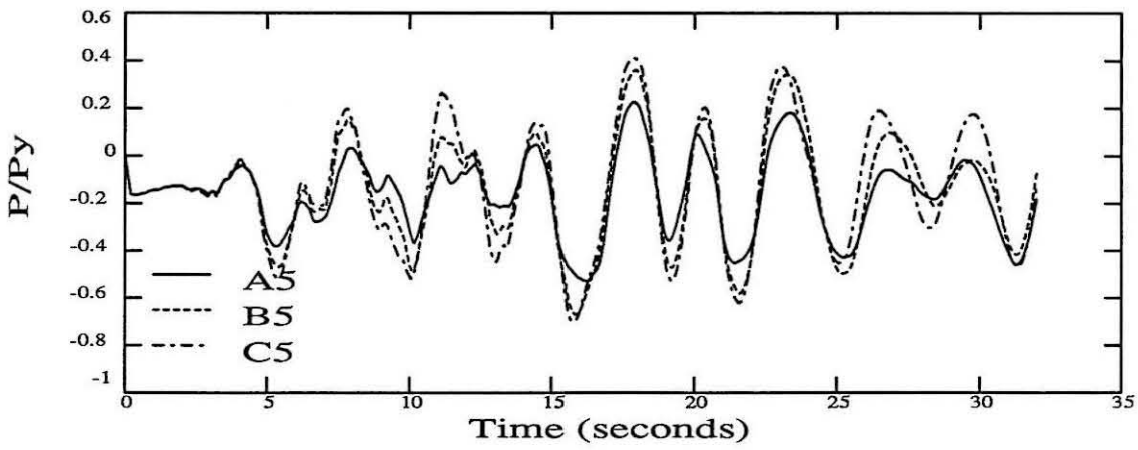

(c)

Figure 7.9 : Comparison of the response time histories of the first storey exterior column of the three MRFs from responses **A5**, **B5** and **C5**.

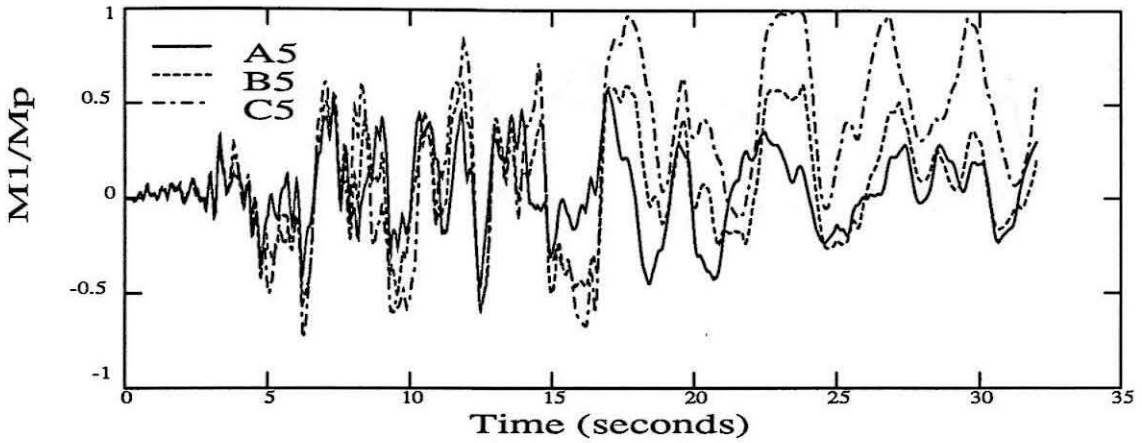

(a)

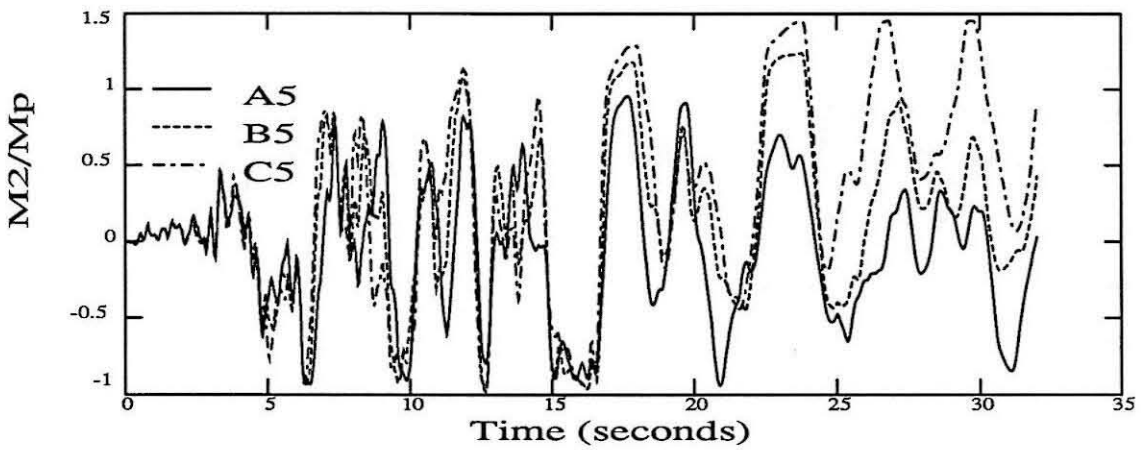

(b)

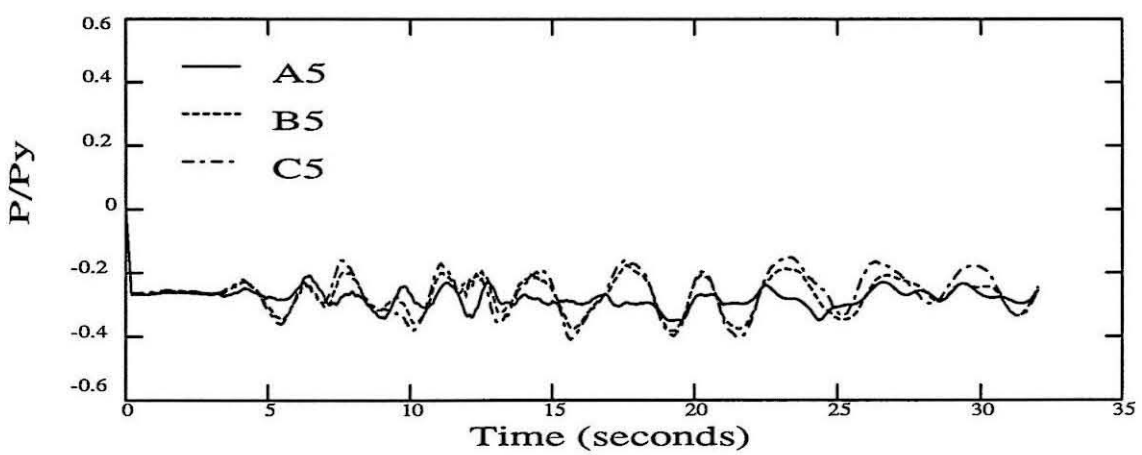

(c)

Figure 7.10 : Comparison of the response time histories of the first storey interior column of the three MRFs from responses **A5**, **B5** and **C5**.

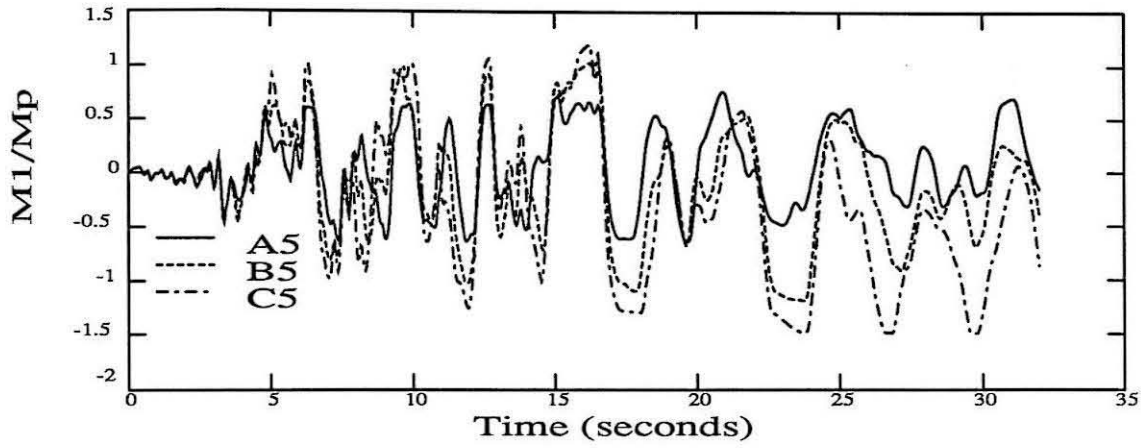

(a)

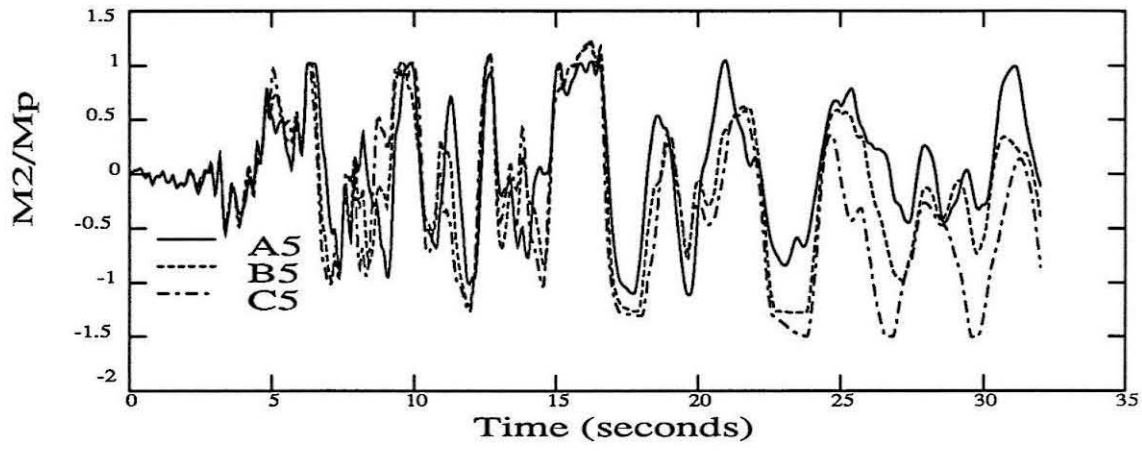

(b)

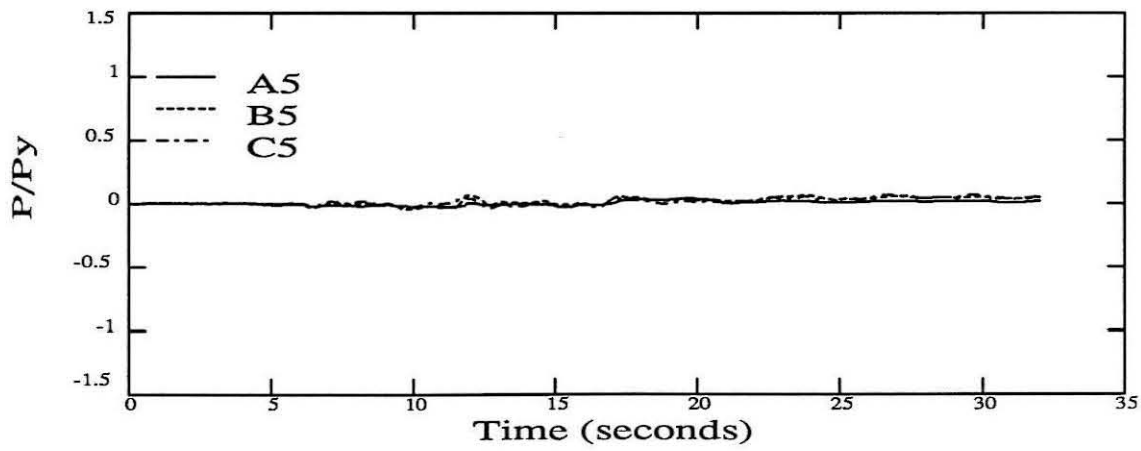

(c)

Figure 7.11 : Comparison of the response time histories of the second floor exterior beam of the three MRFs from responses **A5**, **B5** and **C5**.

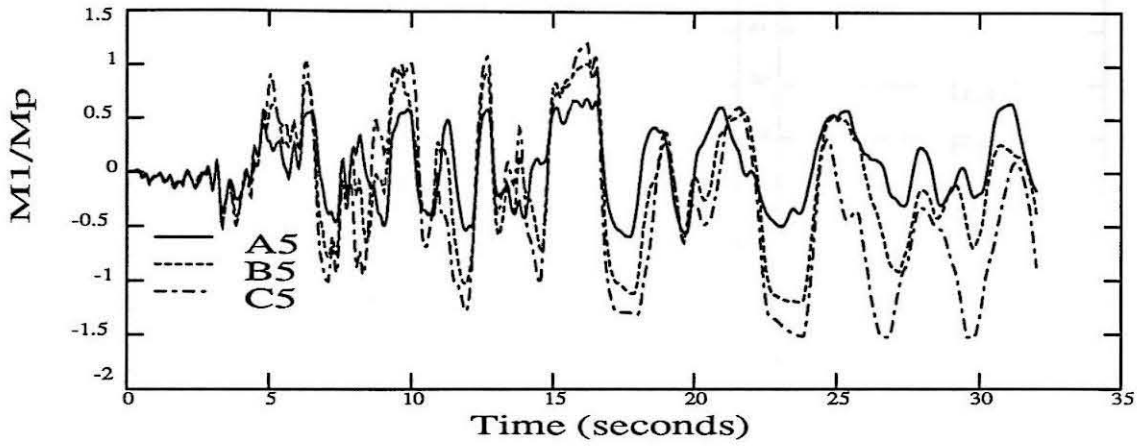

(a)

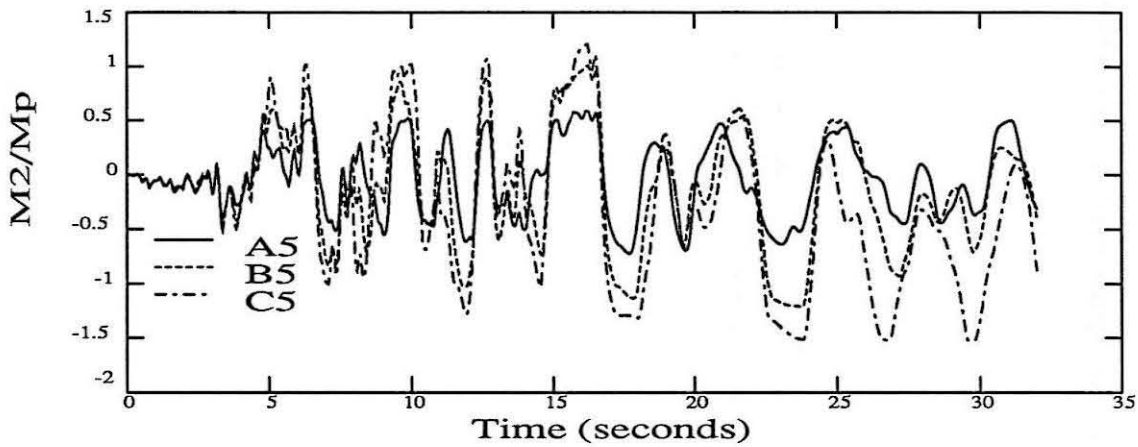

(b)

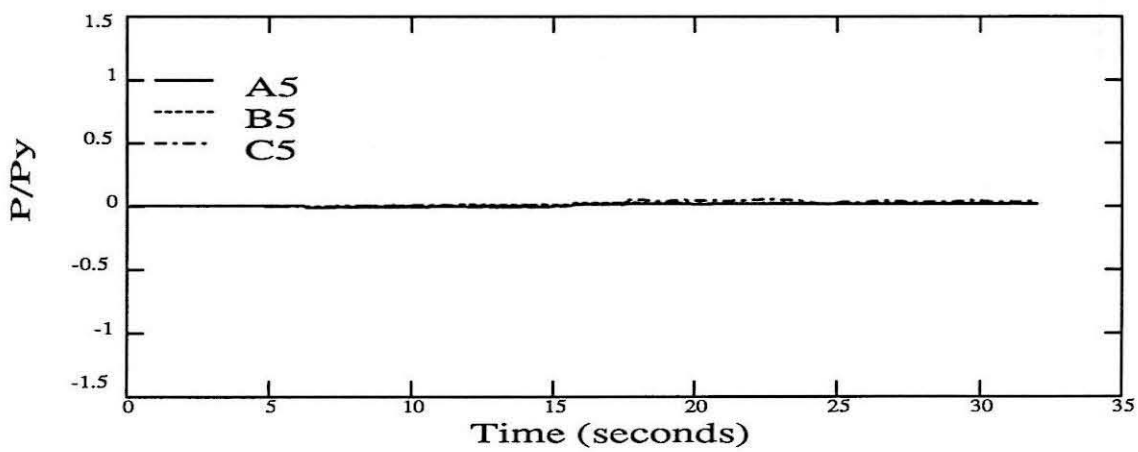

(c)

Figure 7.12 : Comparison of the response time histories of the second floor interior beam of the three MRFs from responses **A5**, **B5** and **C5**.

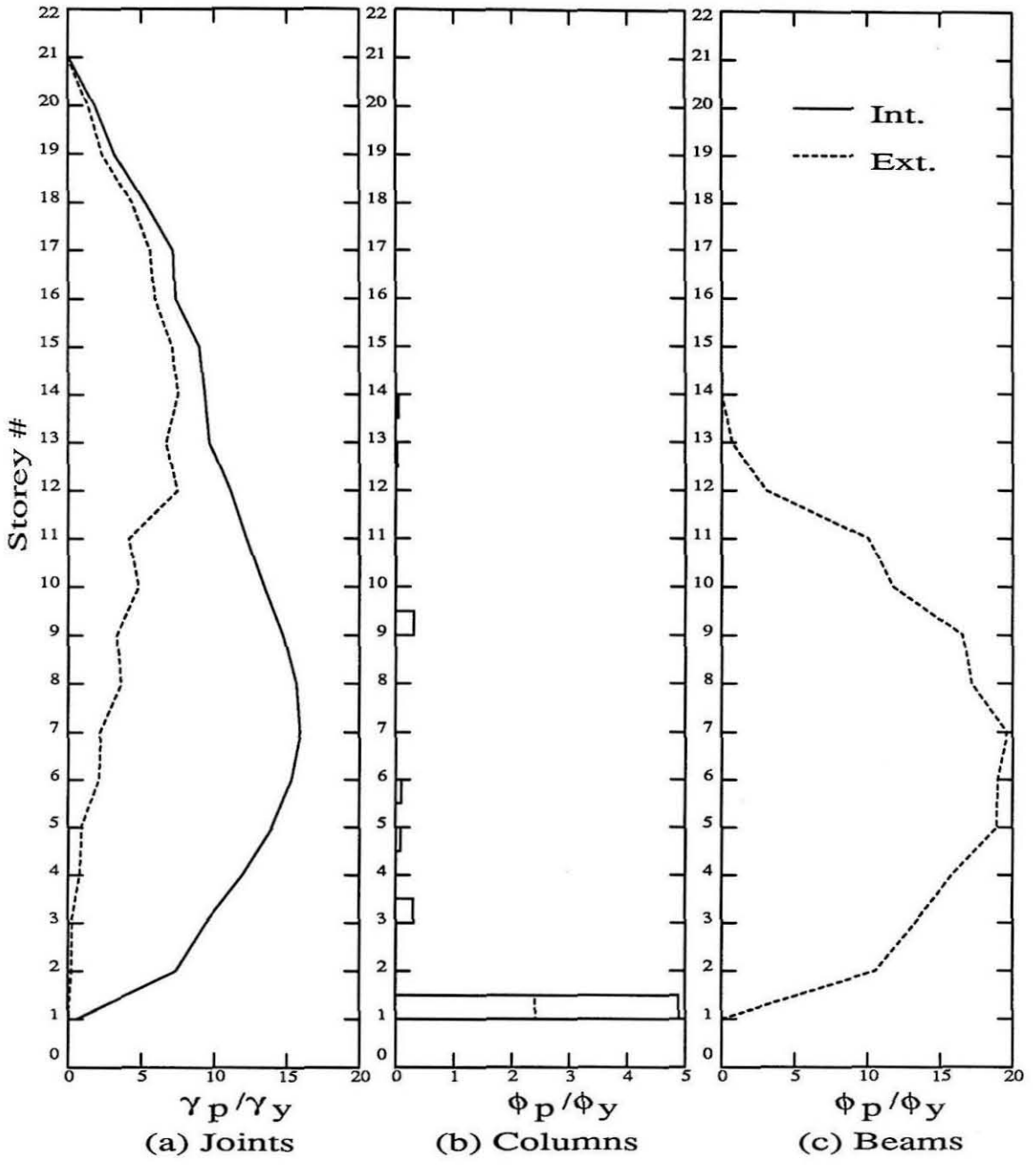

Figure 7.13 : Maximum joint rotation ductilities and maximum member-end curvature ductilities in MRF1 from response **A5**.

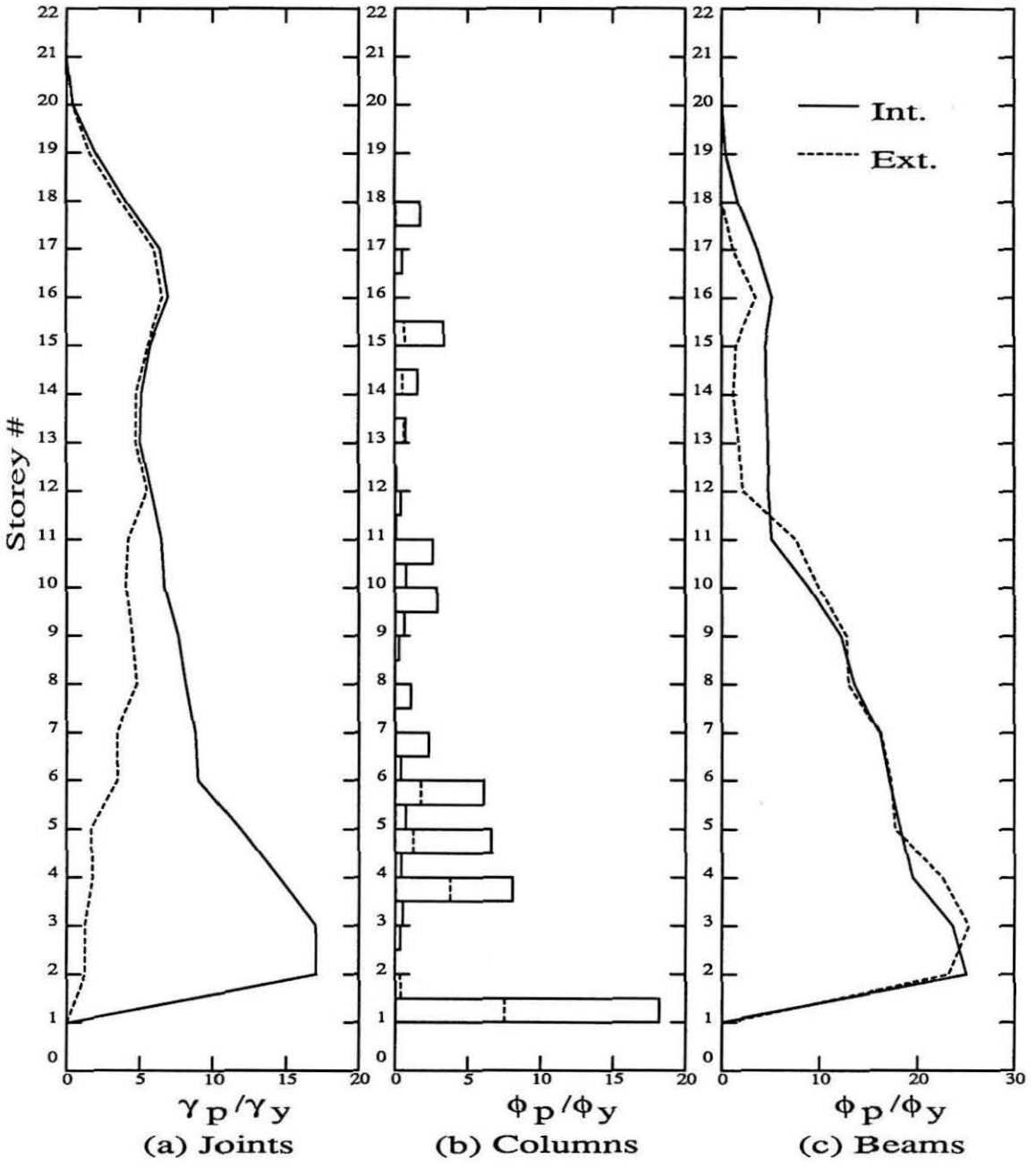

Figure 7.14 : Maximum joint rotation ductilities and maximum member-end curvature ductilities in MRF2 from response **B5**.

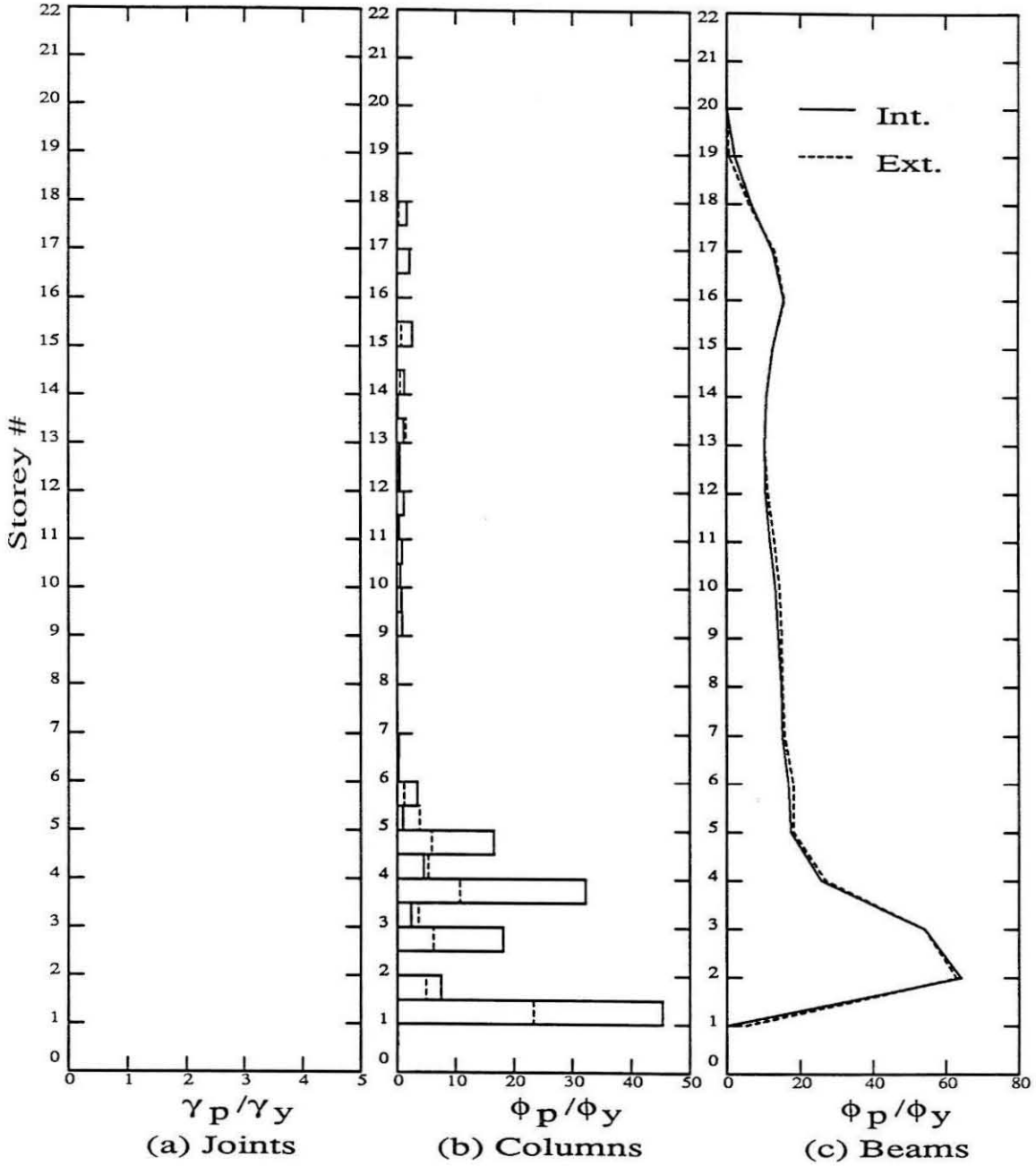

Figure 7.15 : Maximum joint rotation ductilities and maximum member-end curvature ductilities in MRF3 from response **C5**.

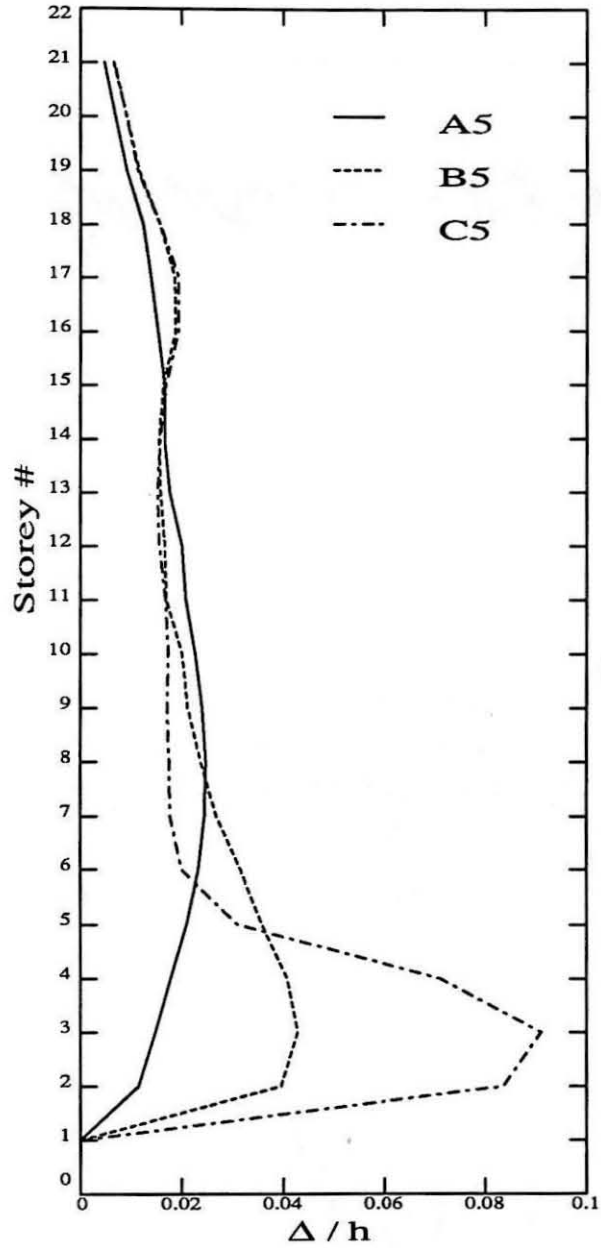

Figure 7.16 : Maximum storey-drifts of the three MRFs from responses **A5**, **B5** and **C5**.

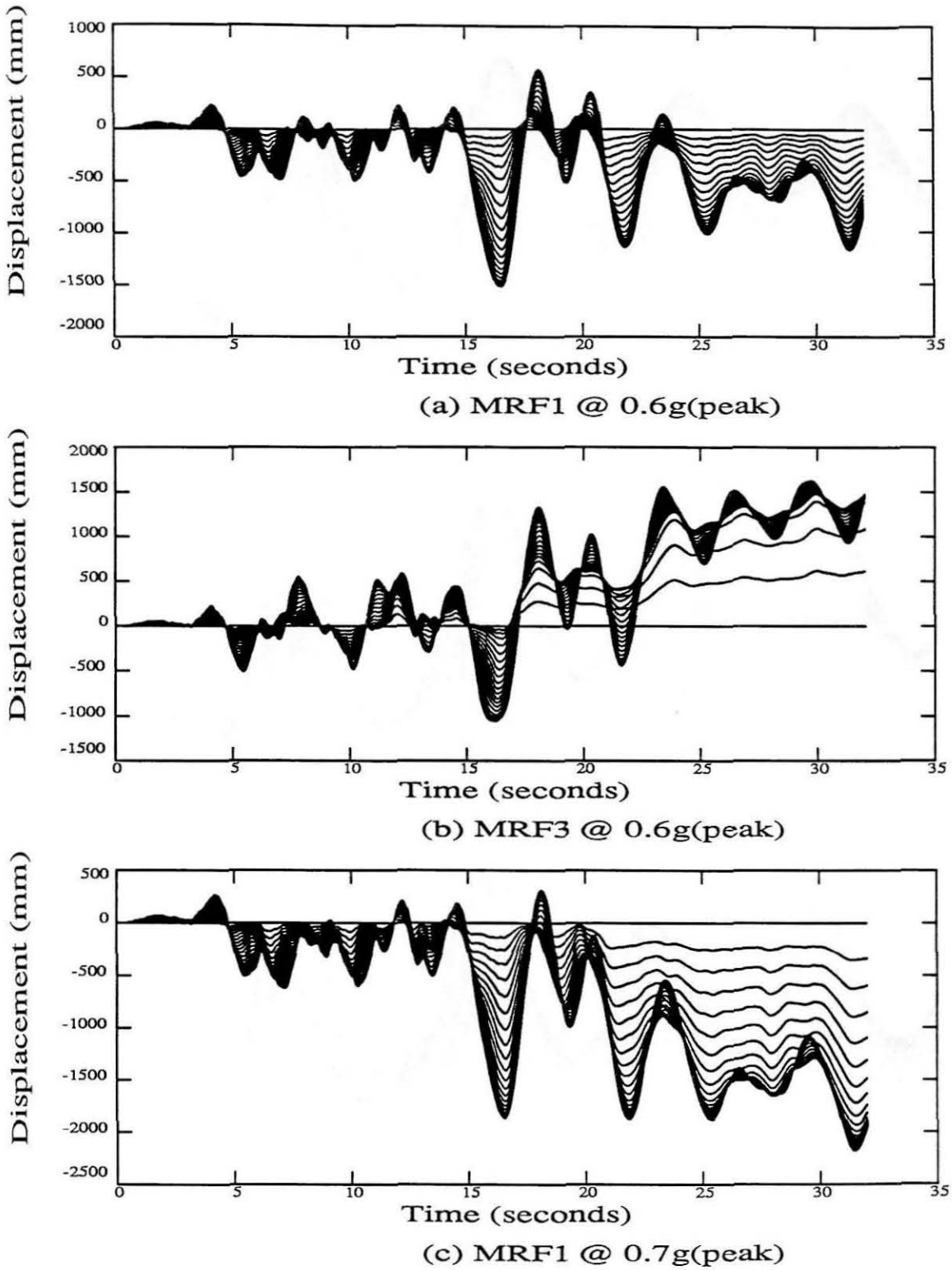

Figure 7.17 : Lateral displacement time histories of all floors of MRF1, MRF3 and MRF1 from responses **A6**, **B6** and **A7**. The outermost curves correspond to the roof, while the innermost curves correspond to the first floor.

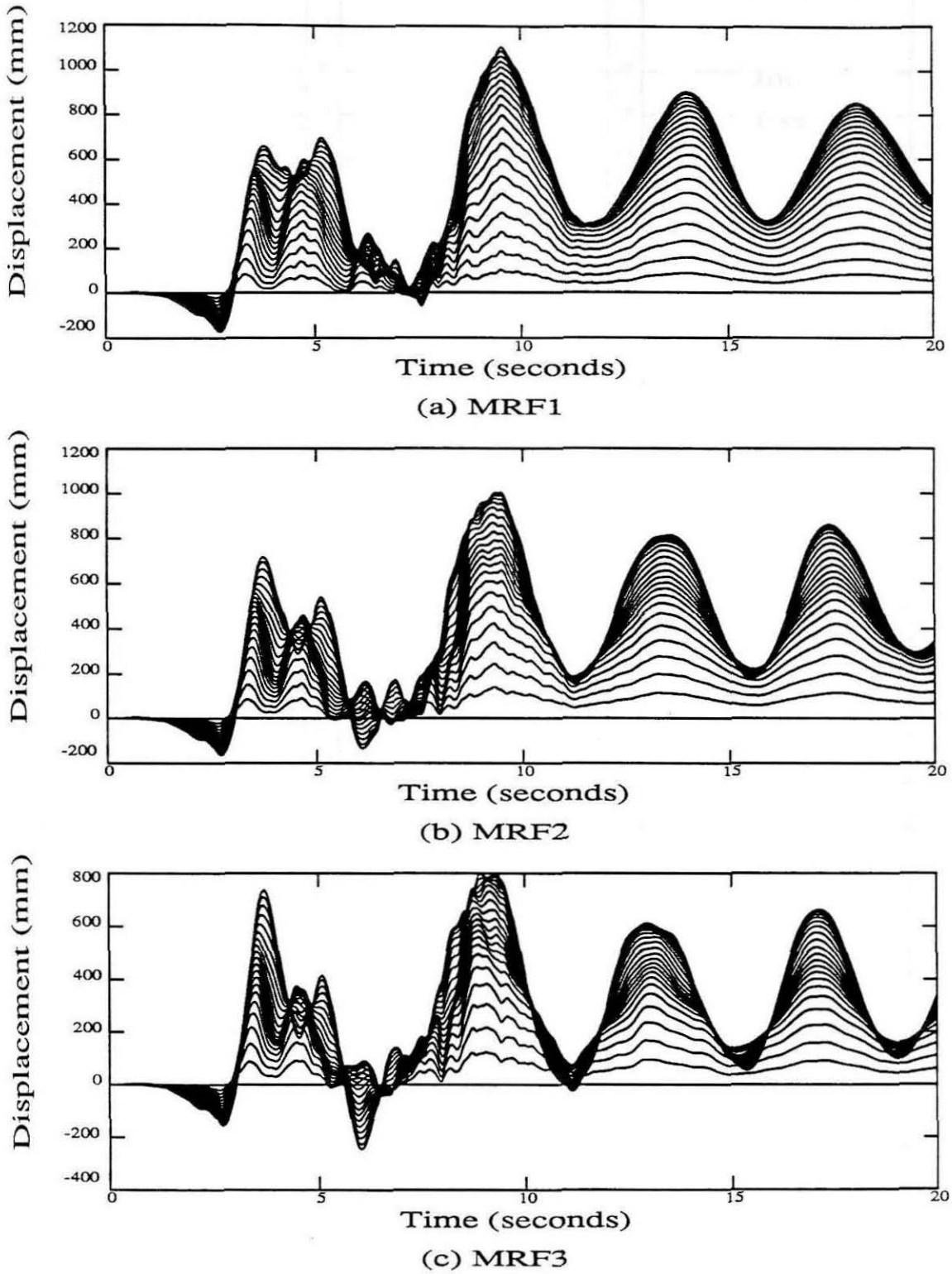

Figure 7.18 : Lateral displacement time histories of all floors of the three MRFs from responses **A0**, **B0** and **C0**. The outermost curves correspond to the roof, while the innermost curves correspond to the first floor.

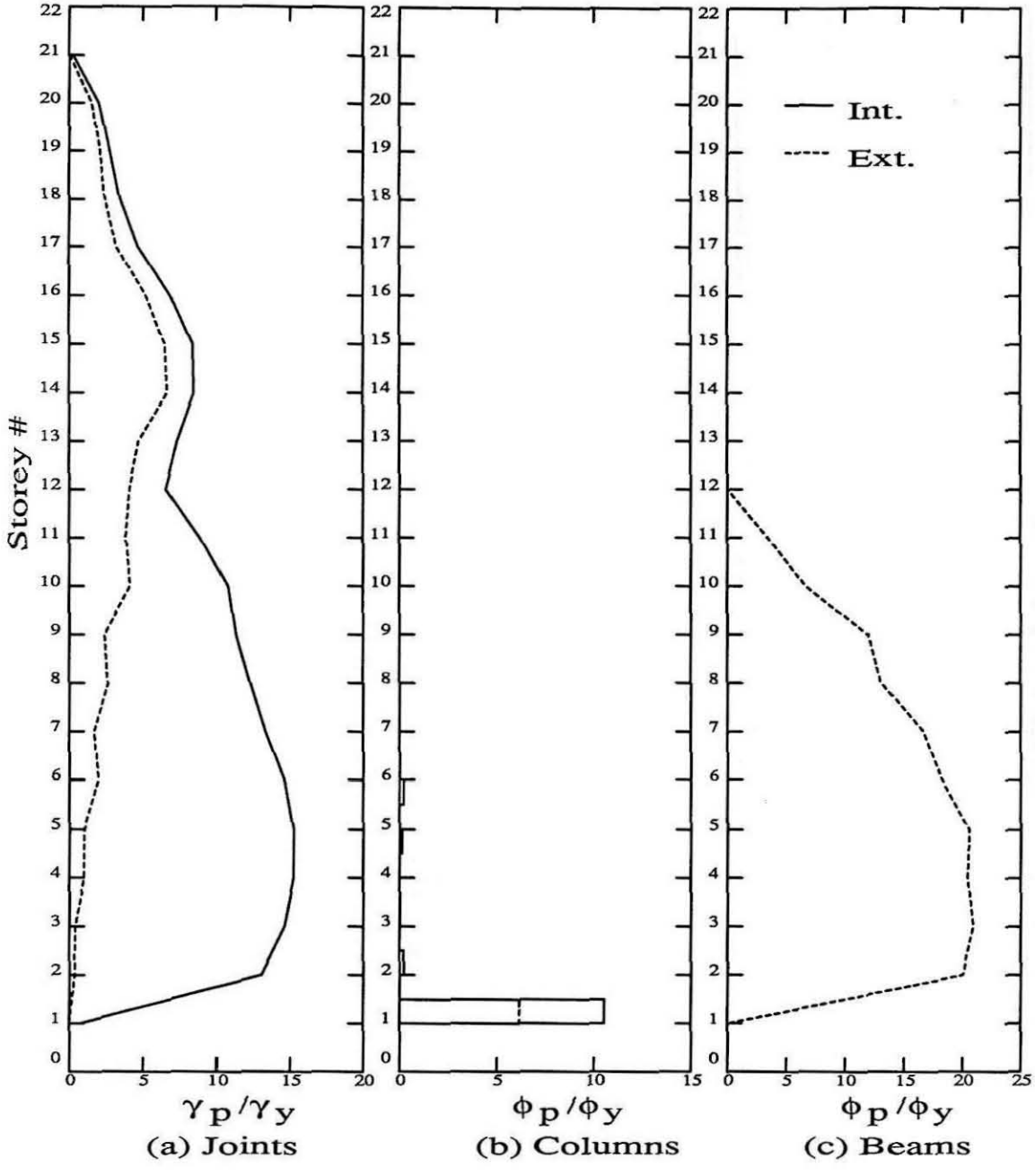

Figure 7.19 : Maximum joint rotation ductilities and maximum member-end curvature ductilities in MRF1 from response **A0**.

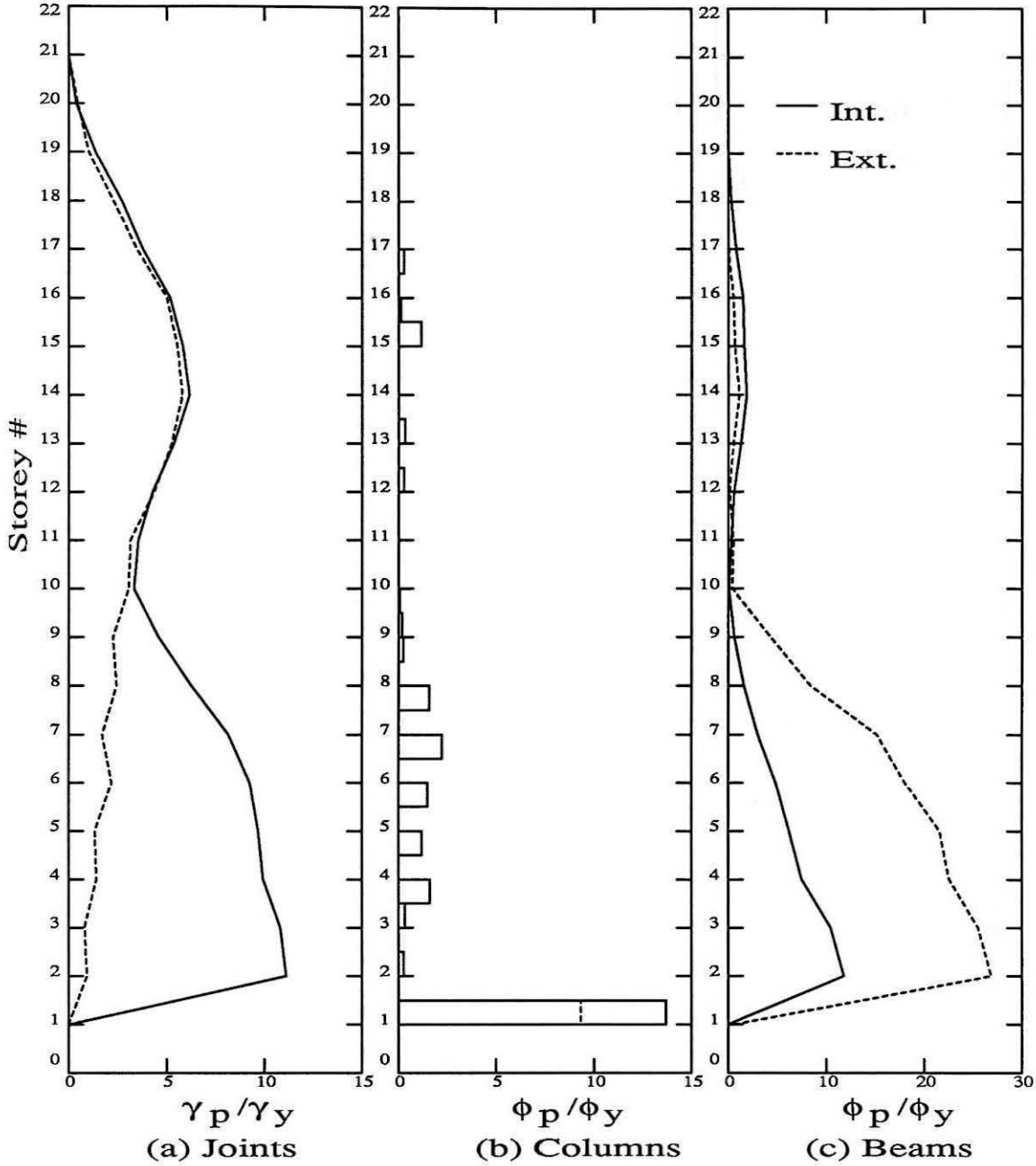

Figure 7.20 : Maximum joint rotation ductilities and maximum member-end curvature ductilities in MRF2 from response **B0**.

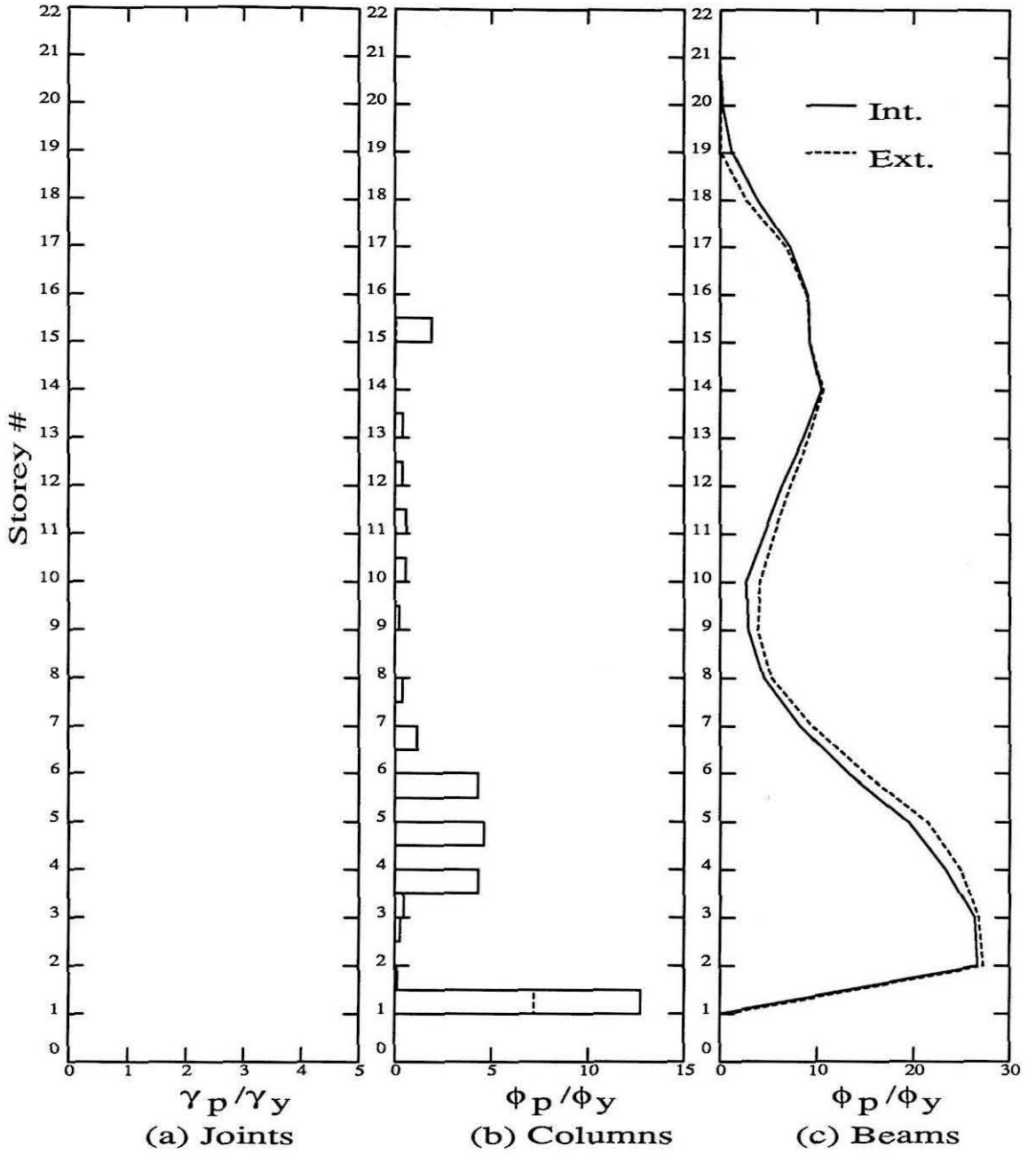

Figure 7.21 : Maximum joint rotation ductilities and maximum member-end curvature ductilities in MRF3 from response **C0**.

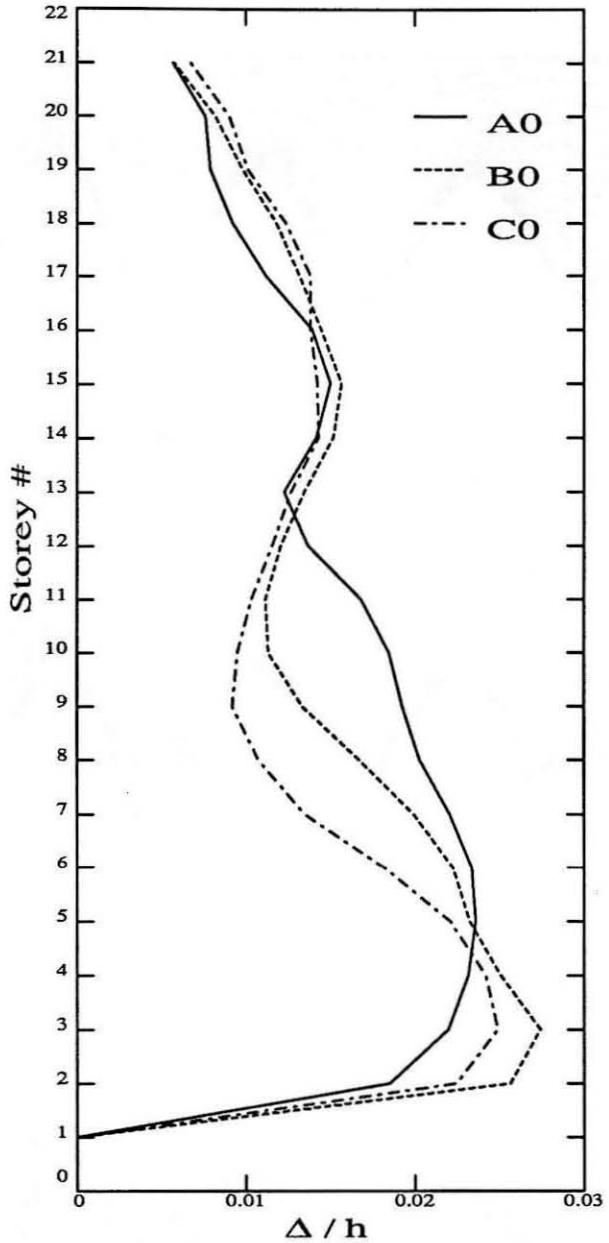

Figure 7.22 : Maximum storey-drifts of the three MRFs from responses **A0**, **B0** and **C0**.

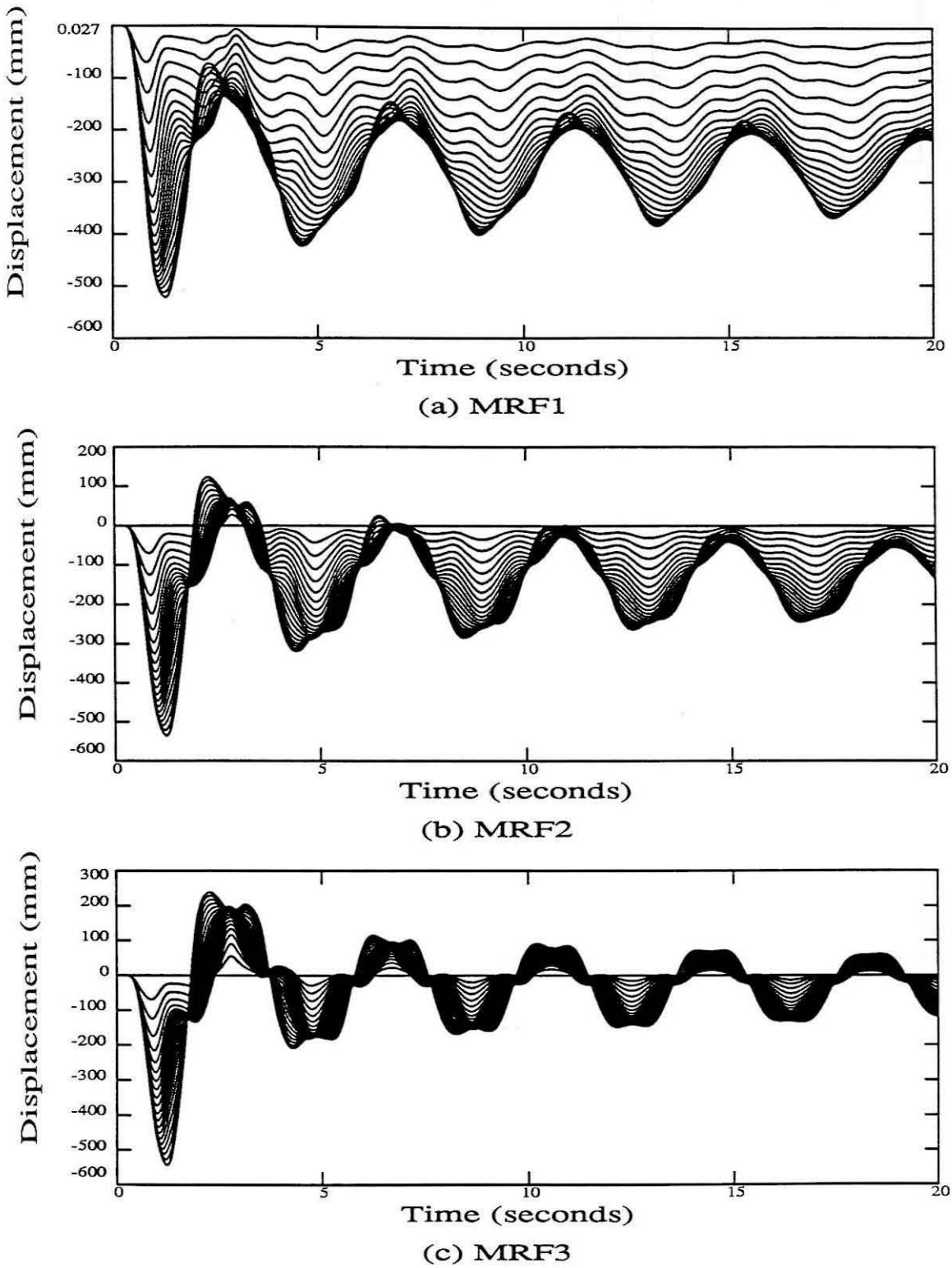

Figure 7.23 : Lateral displacement time histories of all floors of the three MRFs from responses **P1**, **Q1** and **R1**. The outermost curves correspond to the roof, while the innermost curves correspond to the first floor.

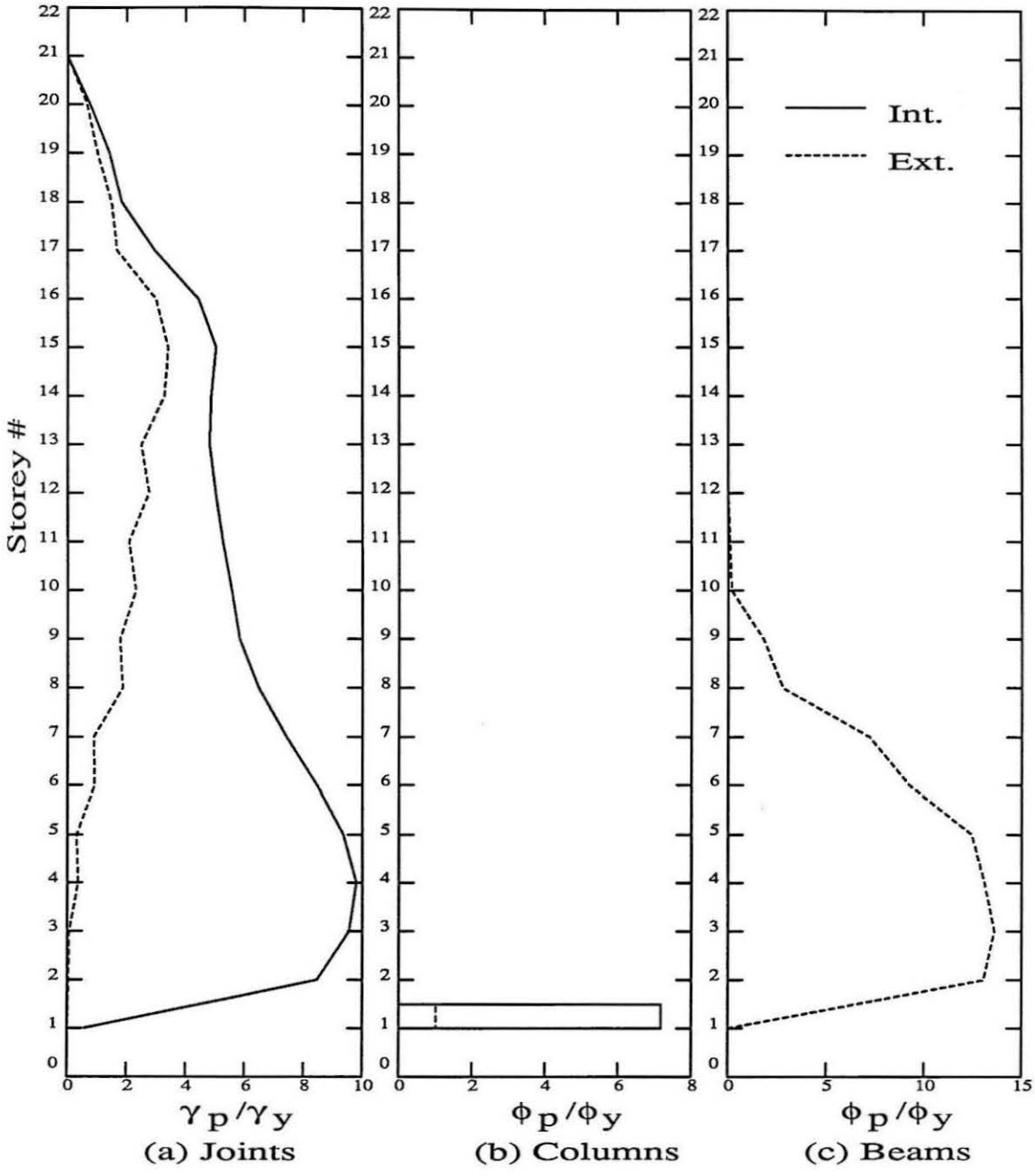

Figure 7.24 : Maximum joint rotation ductilities and maximum member-end curvature ductilities in MRF1 from response **P1**.

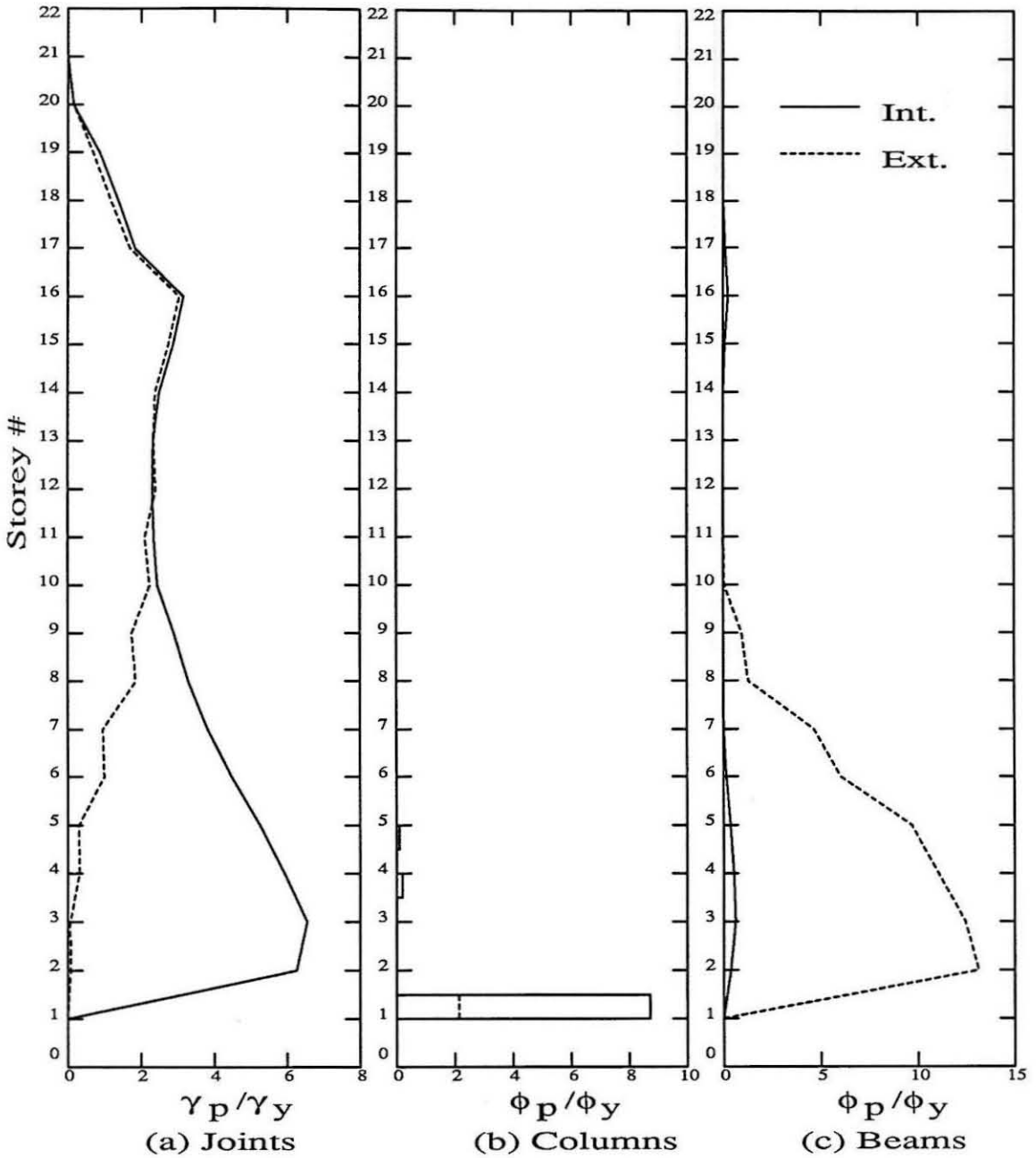

Figure 7.25 : Maximum joint rotation ductilities and maximum member-end curvature ductilities in MRF2 from response **Q1**.

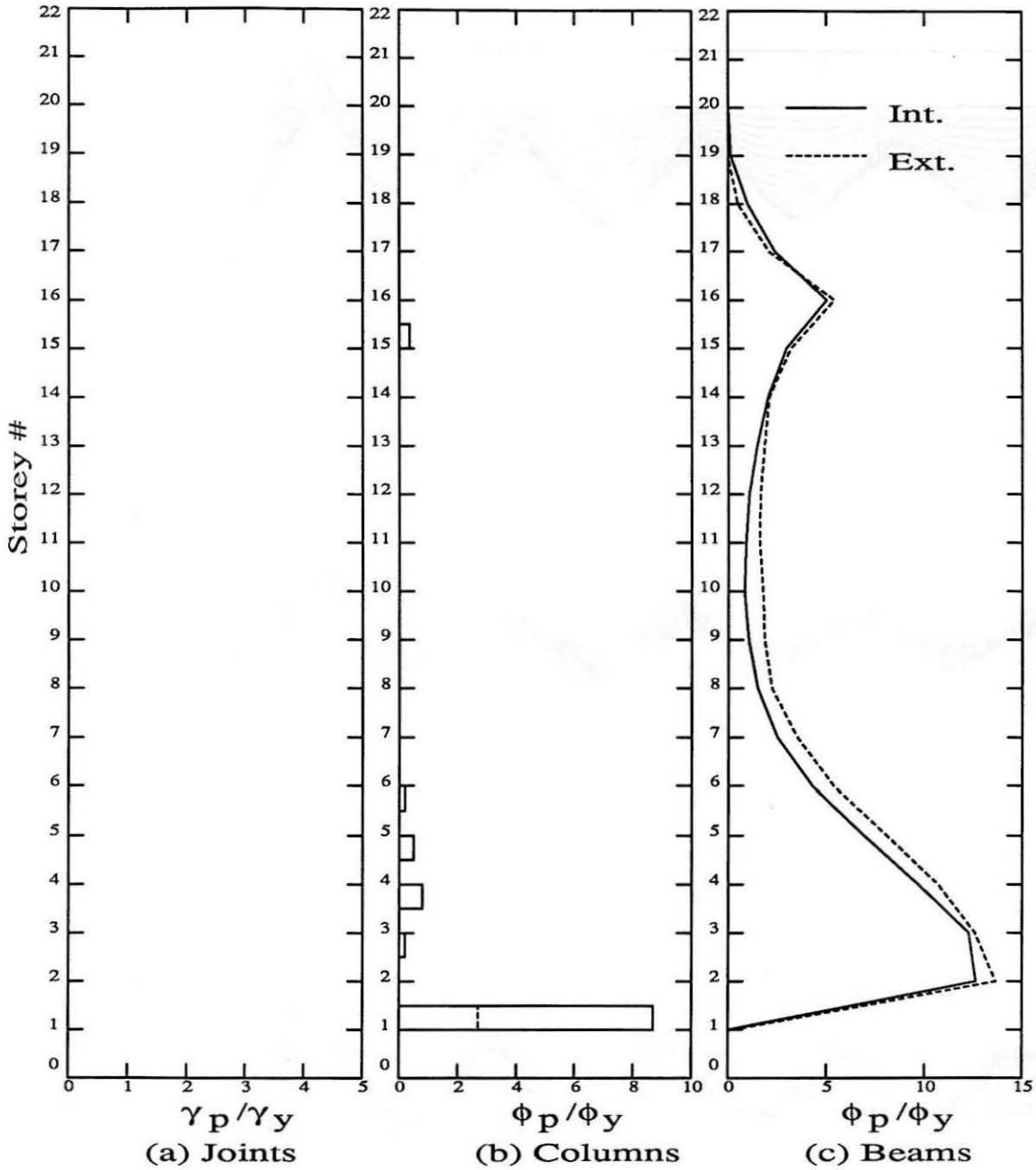

Figure 7.26 : Maximum joint rotation ductilities and maximum member-end curvature ductilities in MRF3 from response **R1**.

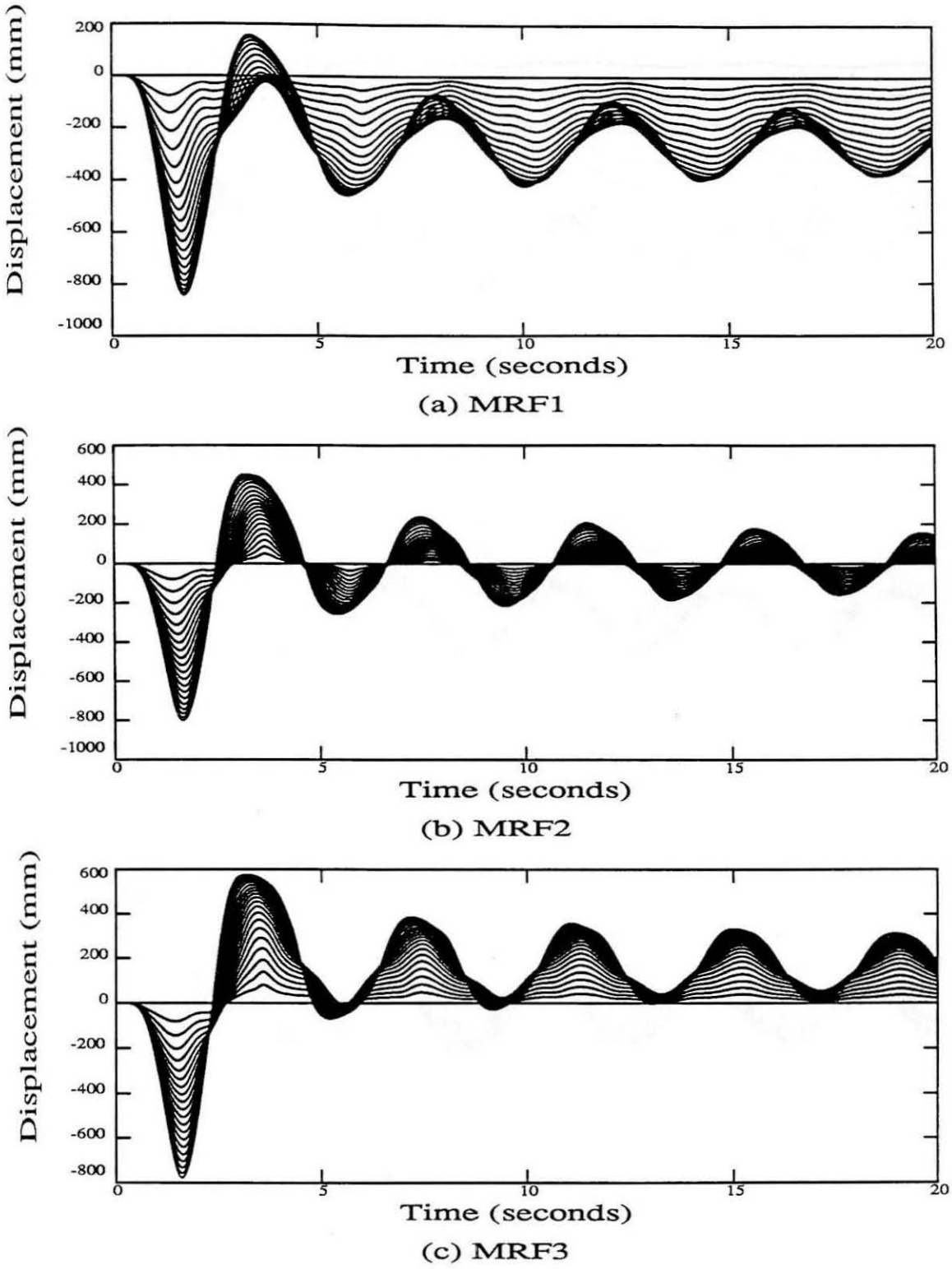

Figure 7.27 : Lateral displacement time histories of all floors of the three MRFs from responses **P2**, **Q2** and **R2**. The outermost curves correspond to the roof, while the innermost curves correspond to the first floor.

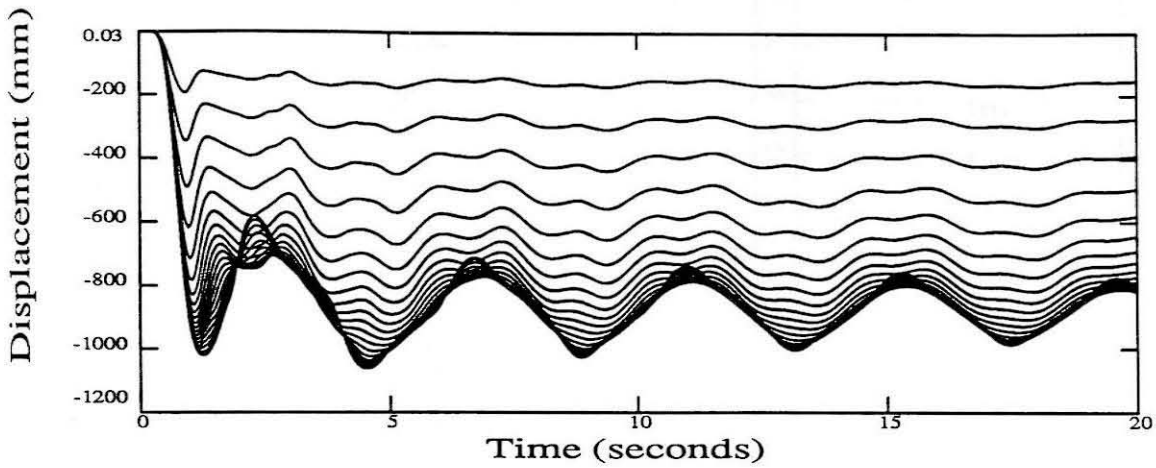

(a) MRF1

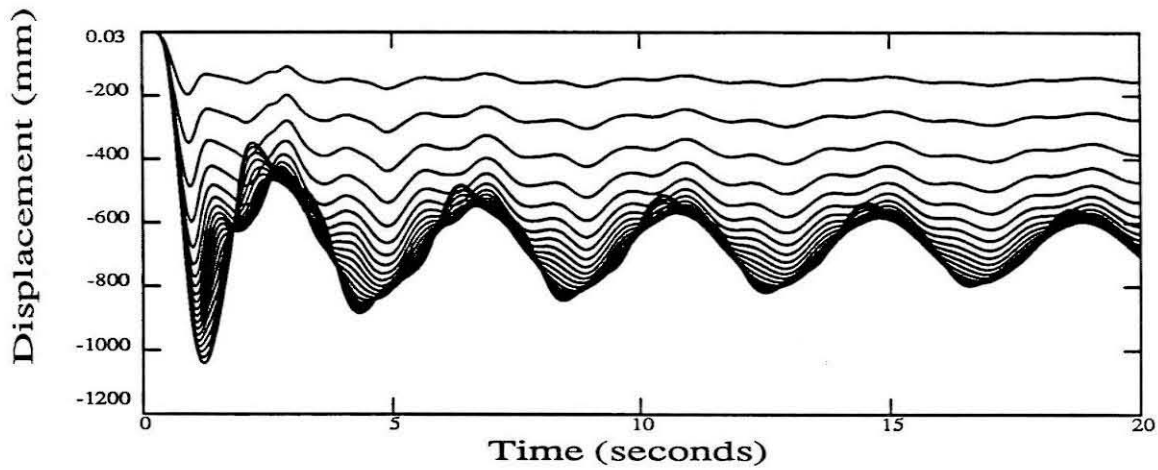

(b) MRF2

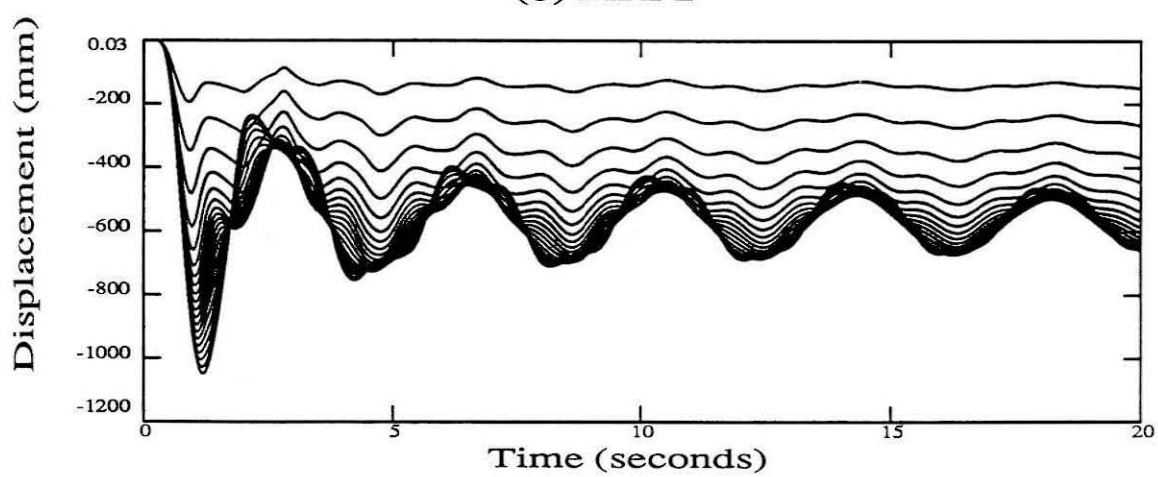

(c) MRF3

Figure 7.28 : Lateral displacement time histories of all floors of the three MRFs from responses **P3**, **Q3** and **R3**. The outermost curves correspond to the roof, while the innermost curves correspond to the first floor.

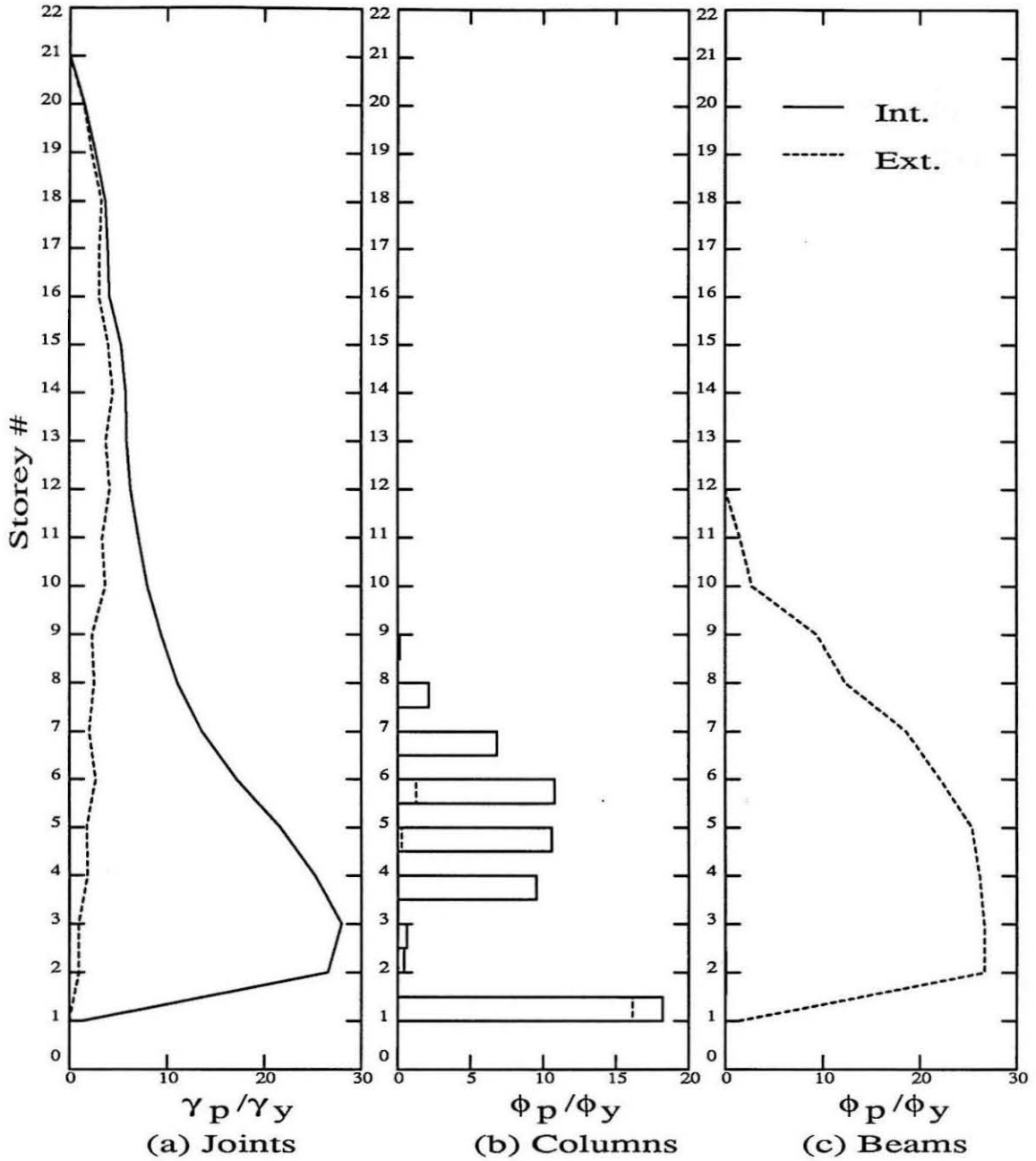

Figure 7.29 : Maximum joint rotation ductilities and maximum member-end curvature ductilities in MRF1 from response **P3**.

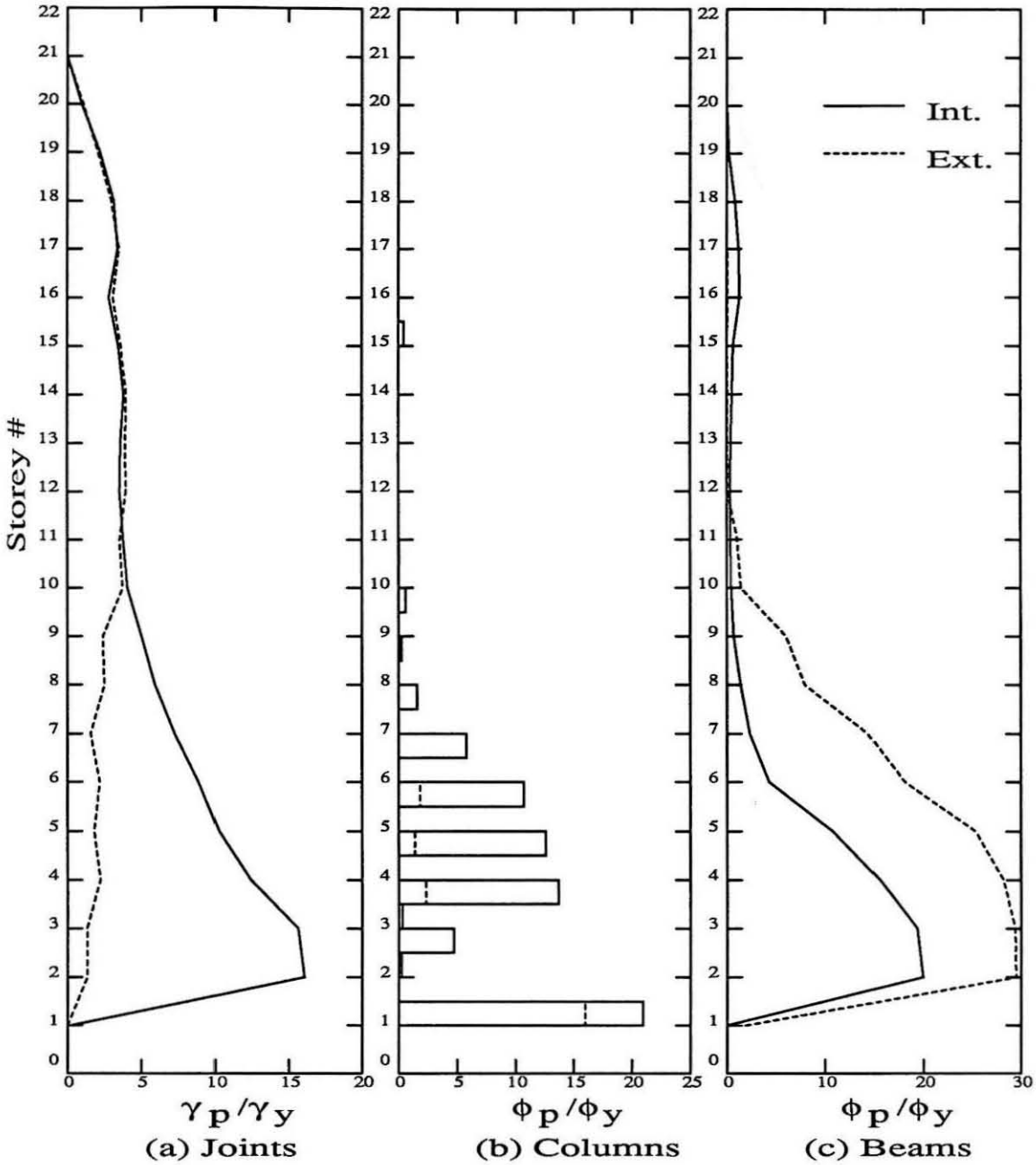

Figure 7.30 : Maximum joint rotation ductilities and maximum member-end curvature ductilities in MRF2 from response **Q3**.

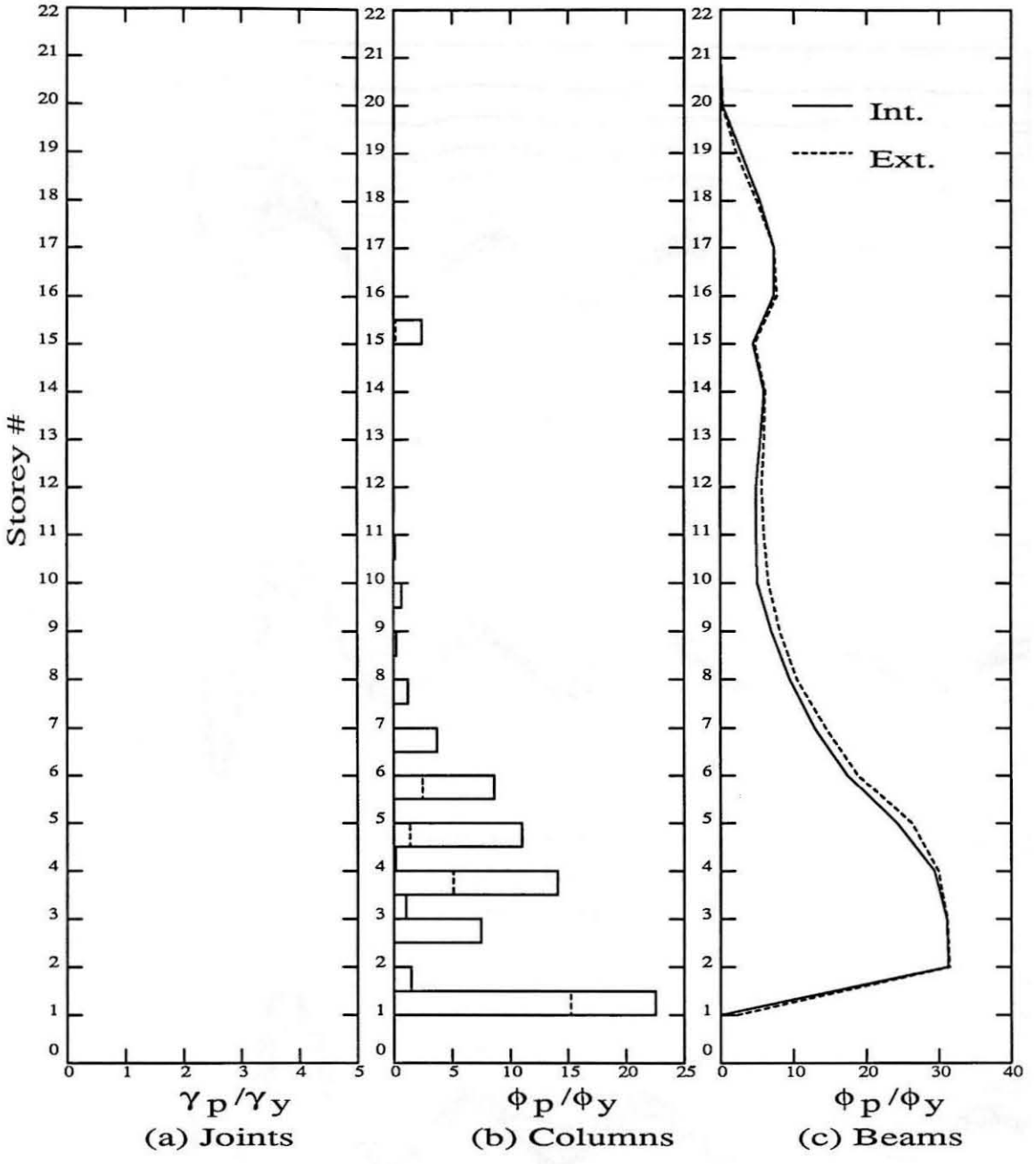

Figure 7.31 : Maximum joint rotation ductilities and maximum member-end curvature ductilities in MRF3 from response **R3**.

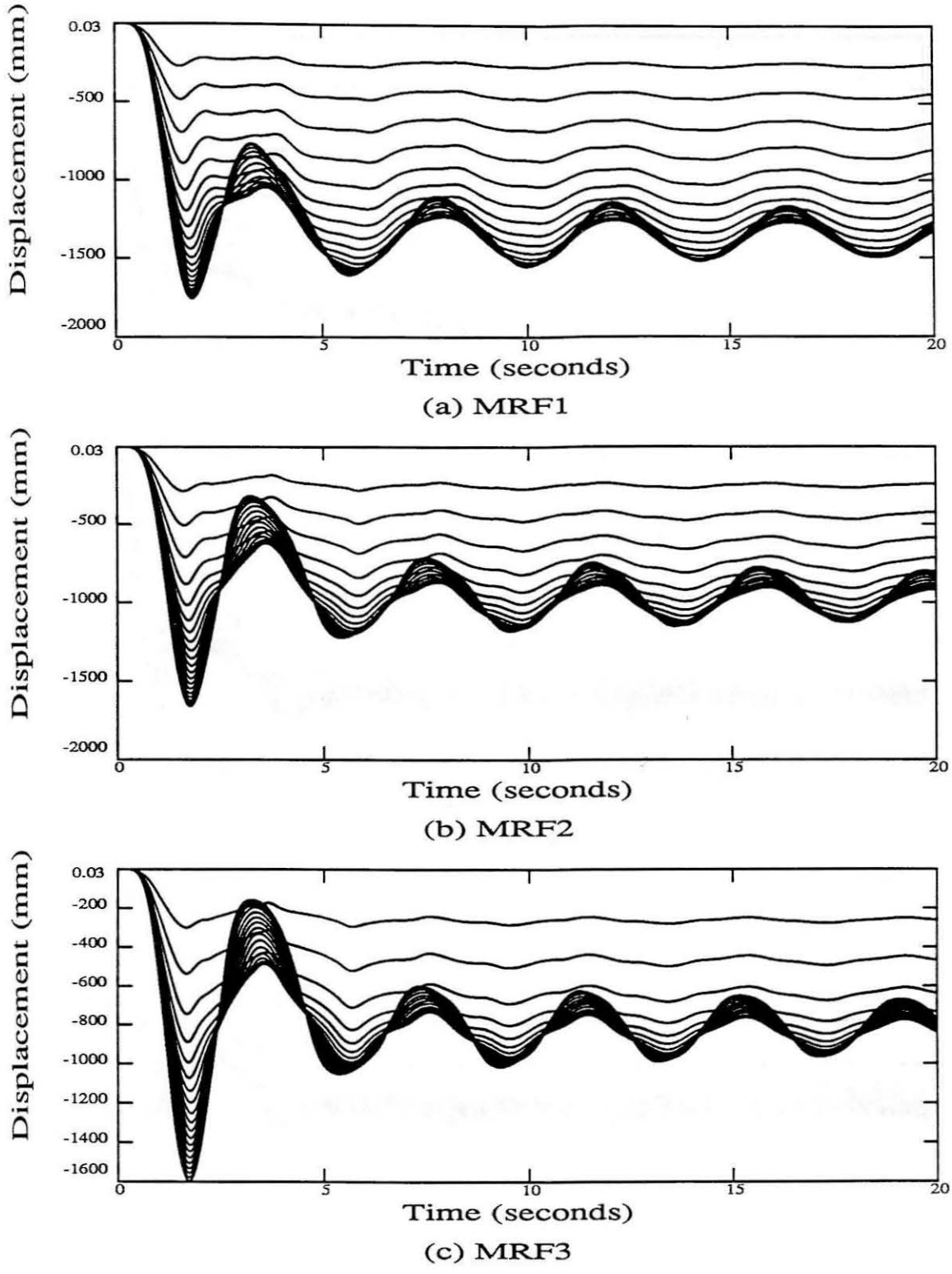

Figure 7.32 : Lateral displacement time histories of all floors of the three MRFs from responses **P4**, **Q4** and **R4**. The outermost curves correspond to the roof, while the innermost curves correspond to the first floor.

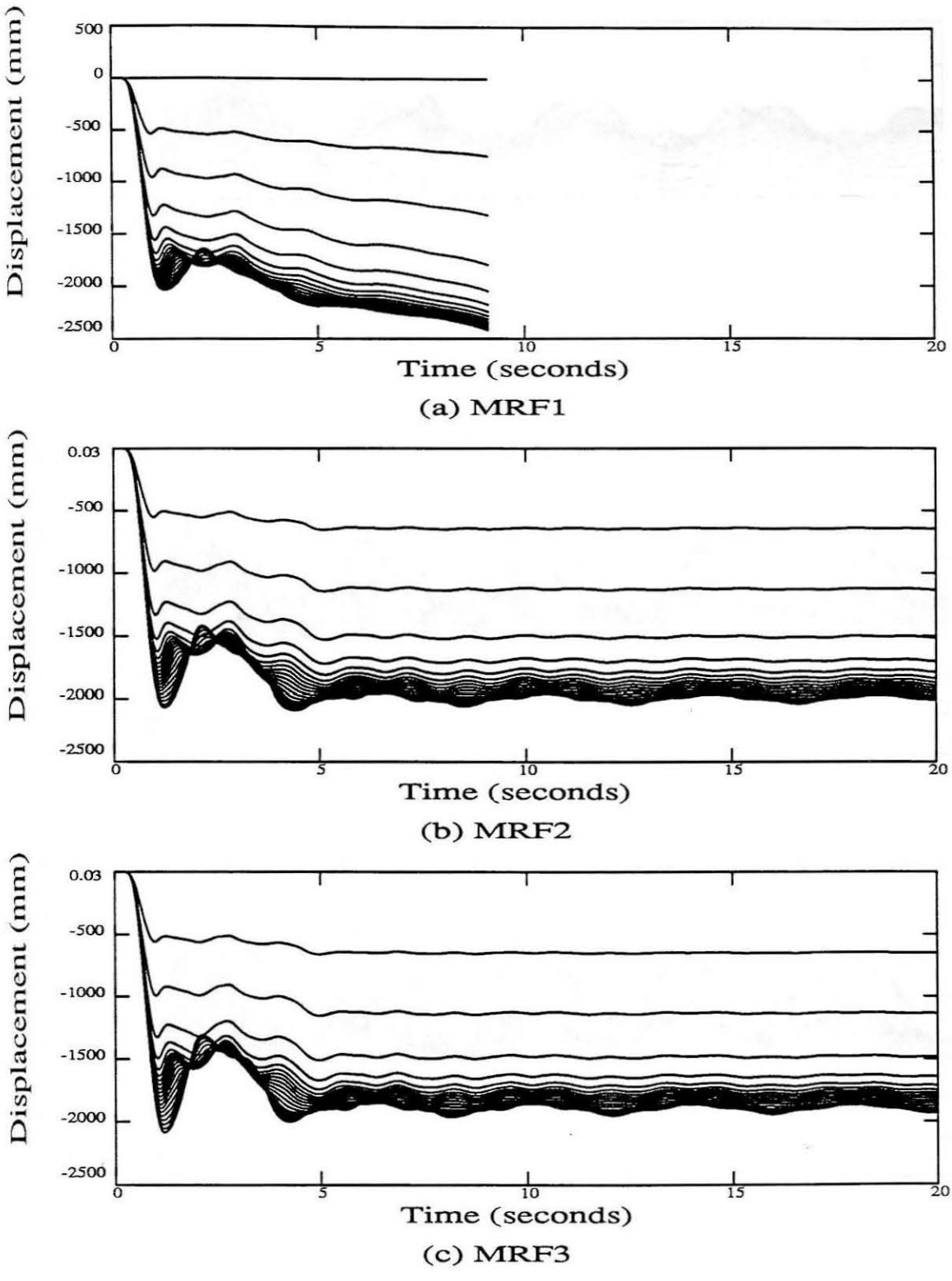

Figure 7.33 : Lateral displacement time histories of all floors of the three MRFs from responses **P5**, **Q5** and **R5**. The outermost curves correspond to the roof, while the innermost curves correspond to the first floor.

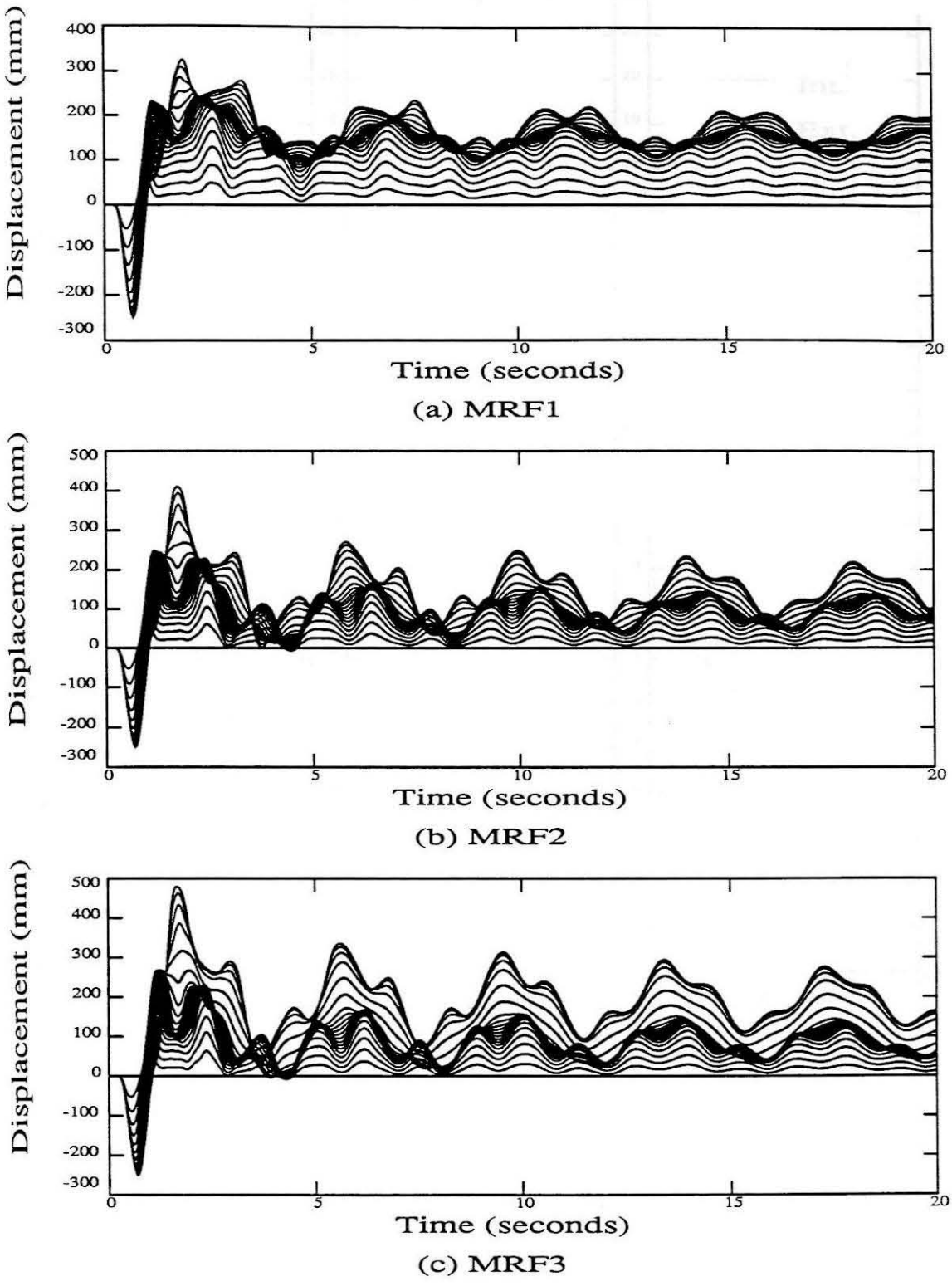

Figure 7.34 : Lateral displacement time histories of all floors of the three MRFs from responses **P6**, **Q6** and **R6**. The outermost curves correspond to the roof, while the innermost curves correspond to the first floor.

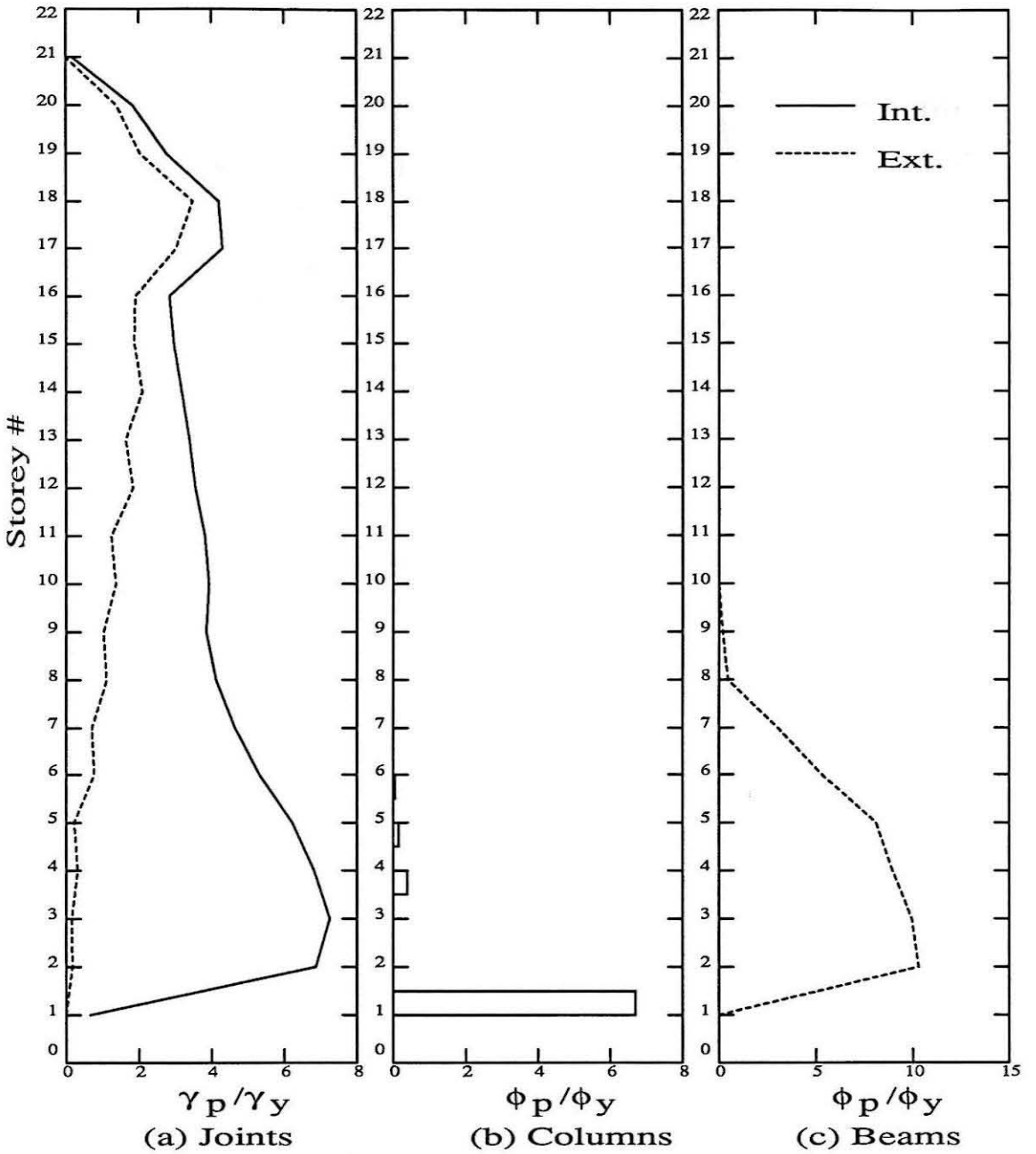

Figure 7.35 : Maximum joint rotation ductilities and maximum member-end curvature ductilities in MRF1 from response **P6**.

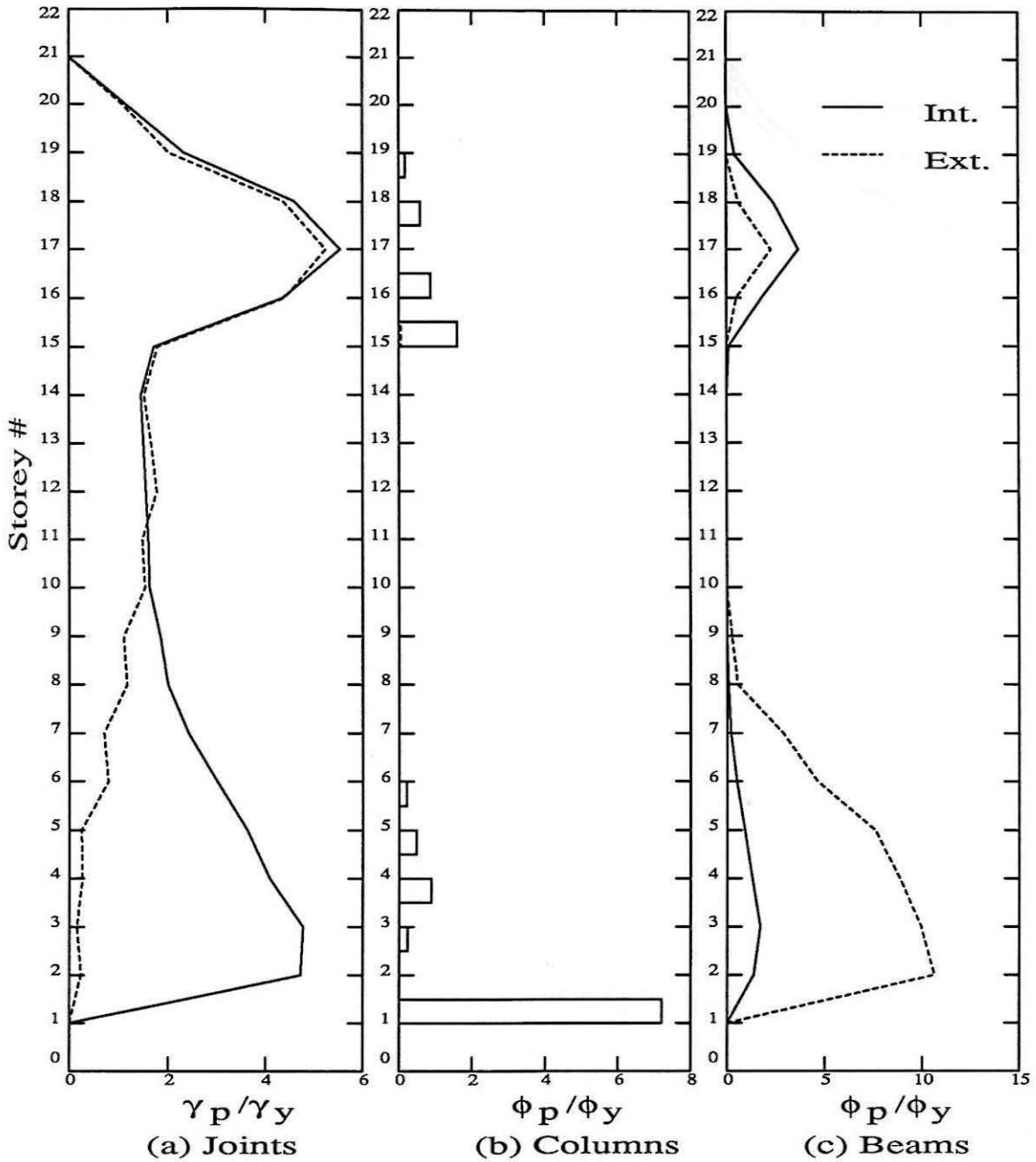

Figure 7.36 : Maximum joint rotation ductilities and maximum member-end curvature ductilities in MRF2 from response **Q6**.

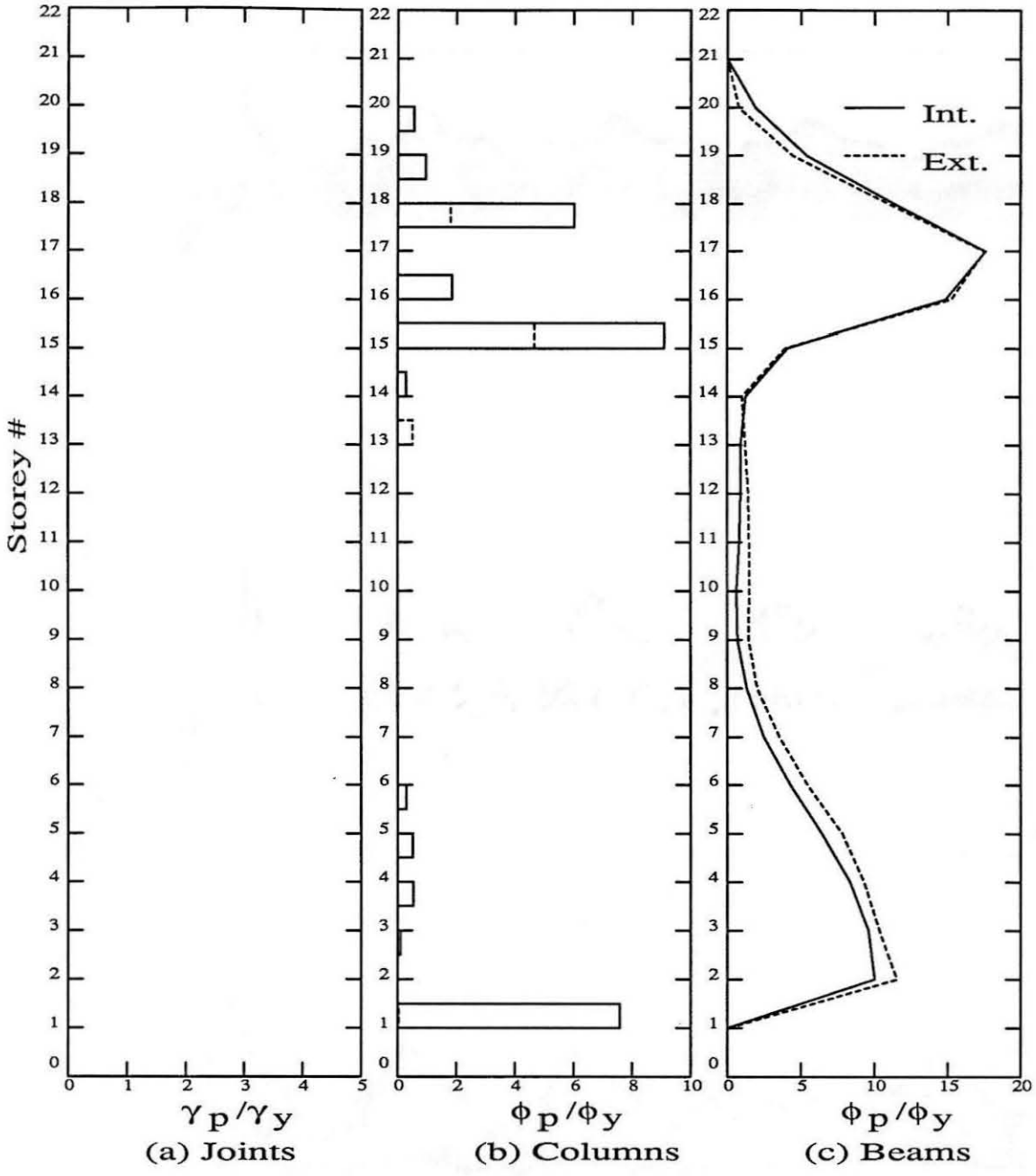

Figure 7.37 : Maximum joint rotation ductilities and maximum member-end curvature ductilities in MRF3 from response **R6**.

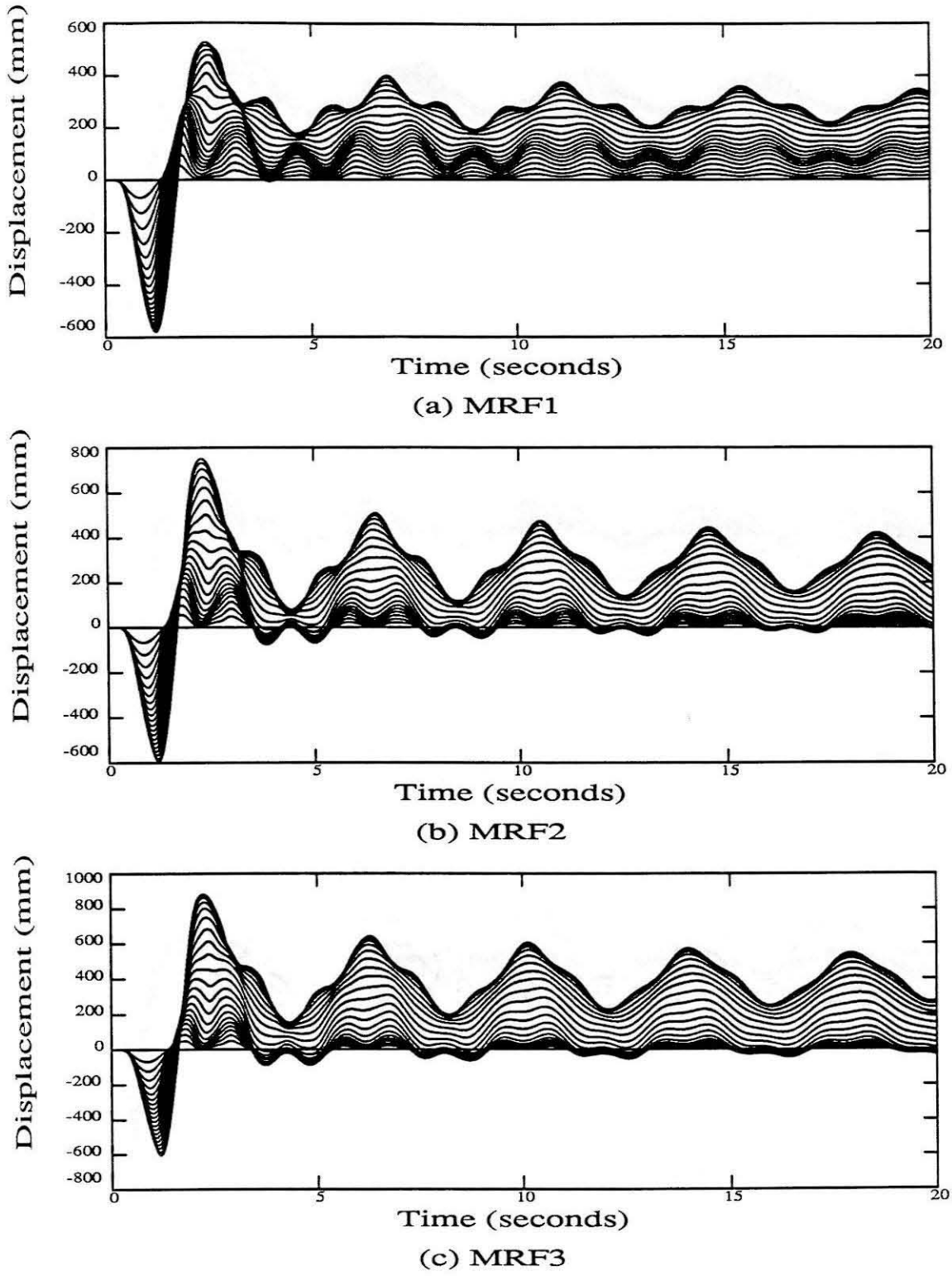

Figure 7.38 : Lateral displacement time histories of all floors of the three MRFs from responses **P7**, **Q7** and **R7**. The outermost curves correspond to the roof, while the innermost curves correspond to the first floor.

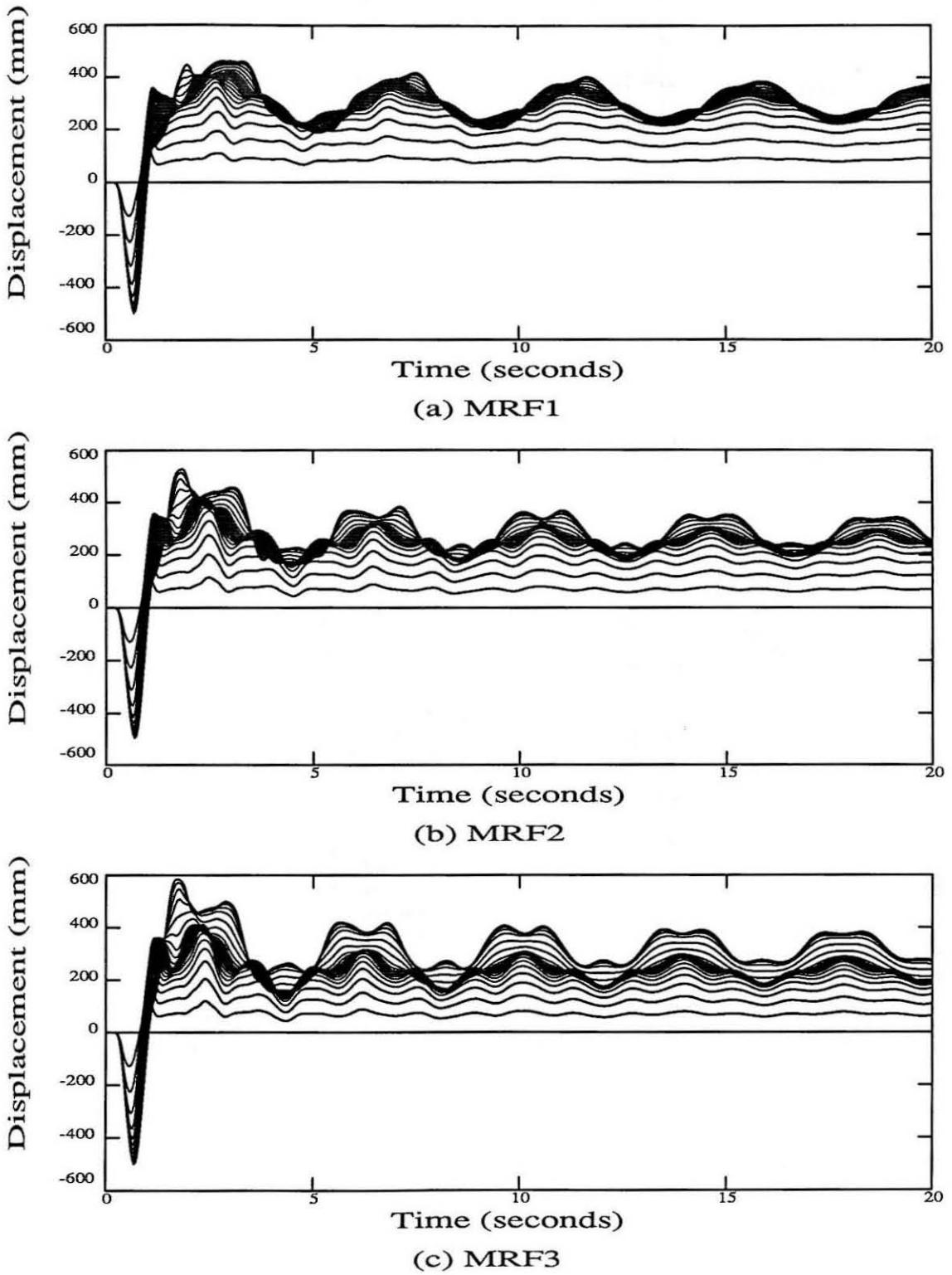

Figure 7.39 : Lateral displacement time histories of all floors of the three MRFs from responses **P8**, **Q8** and **R8**. The outermost curves correspond to the roof, while the innermost curves correspond to the first floor.

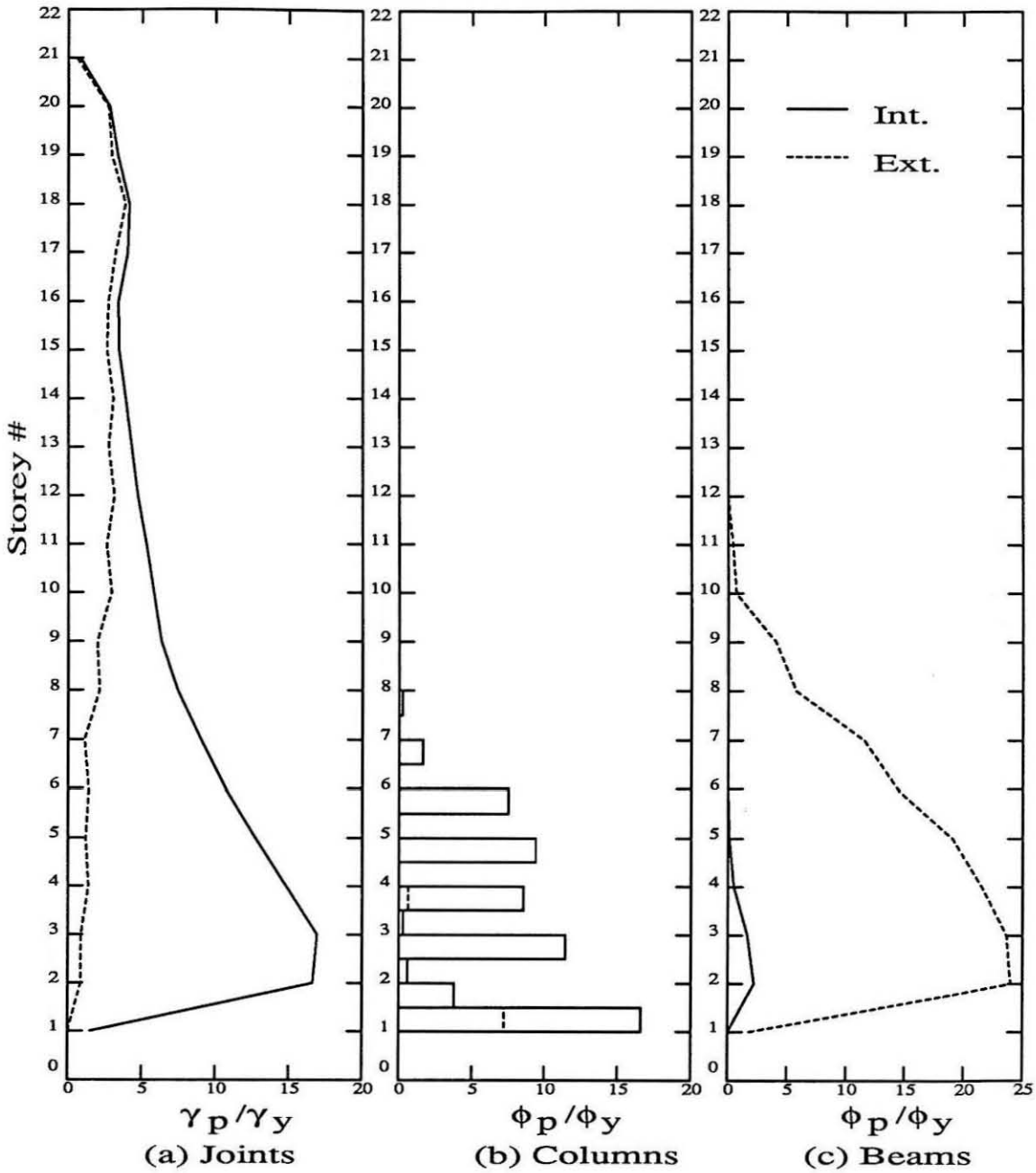

Figure 7.40 : Maximum joint rotation ductilities and maximum member-end curvature ductilities in MRF1 from response **P8**.

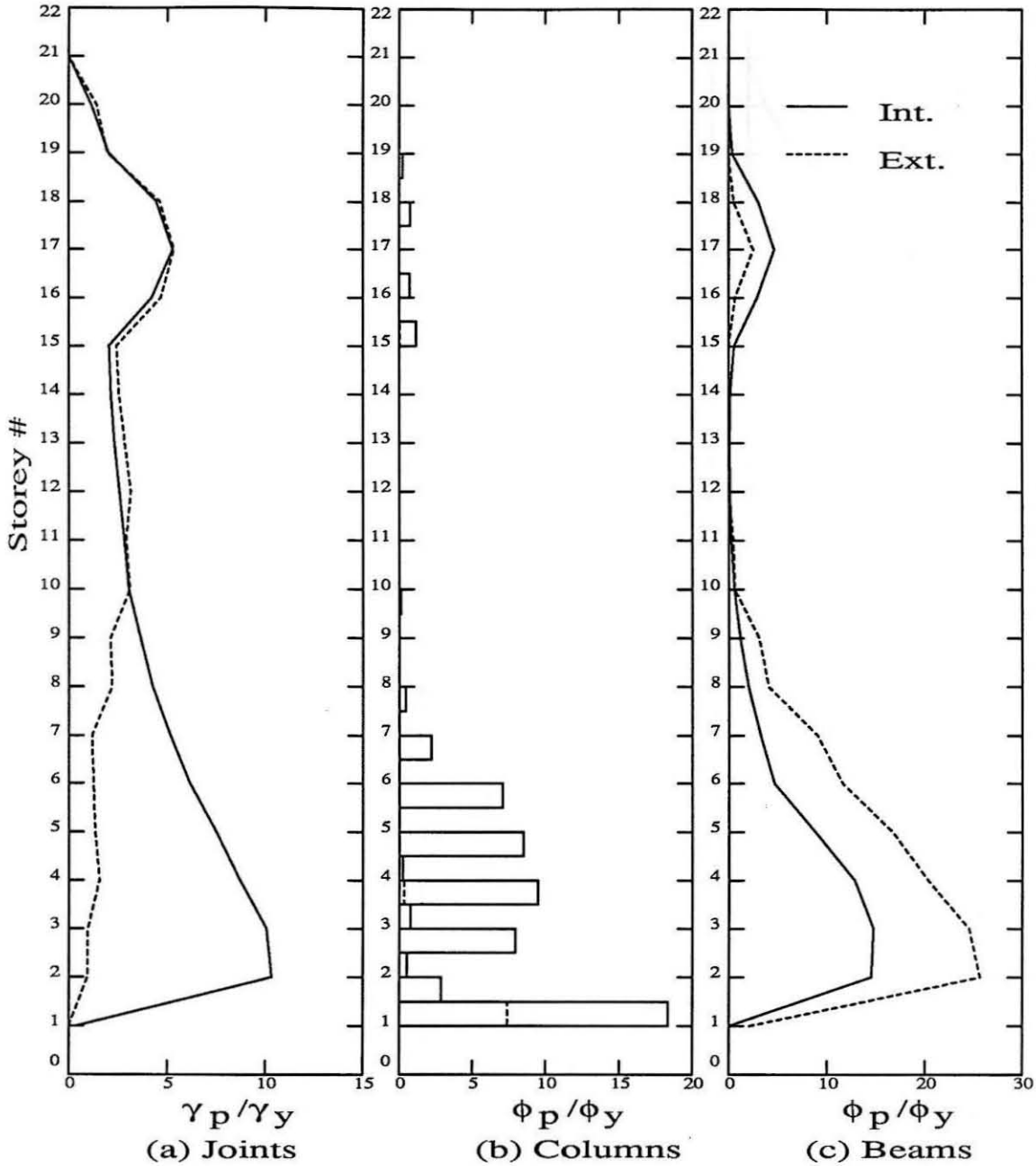

Figure 7.41 : Maximum joint rotation ductilities and maximum member-end curvature ductilities in MRF2 from response **Q8**.

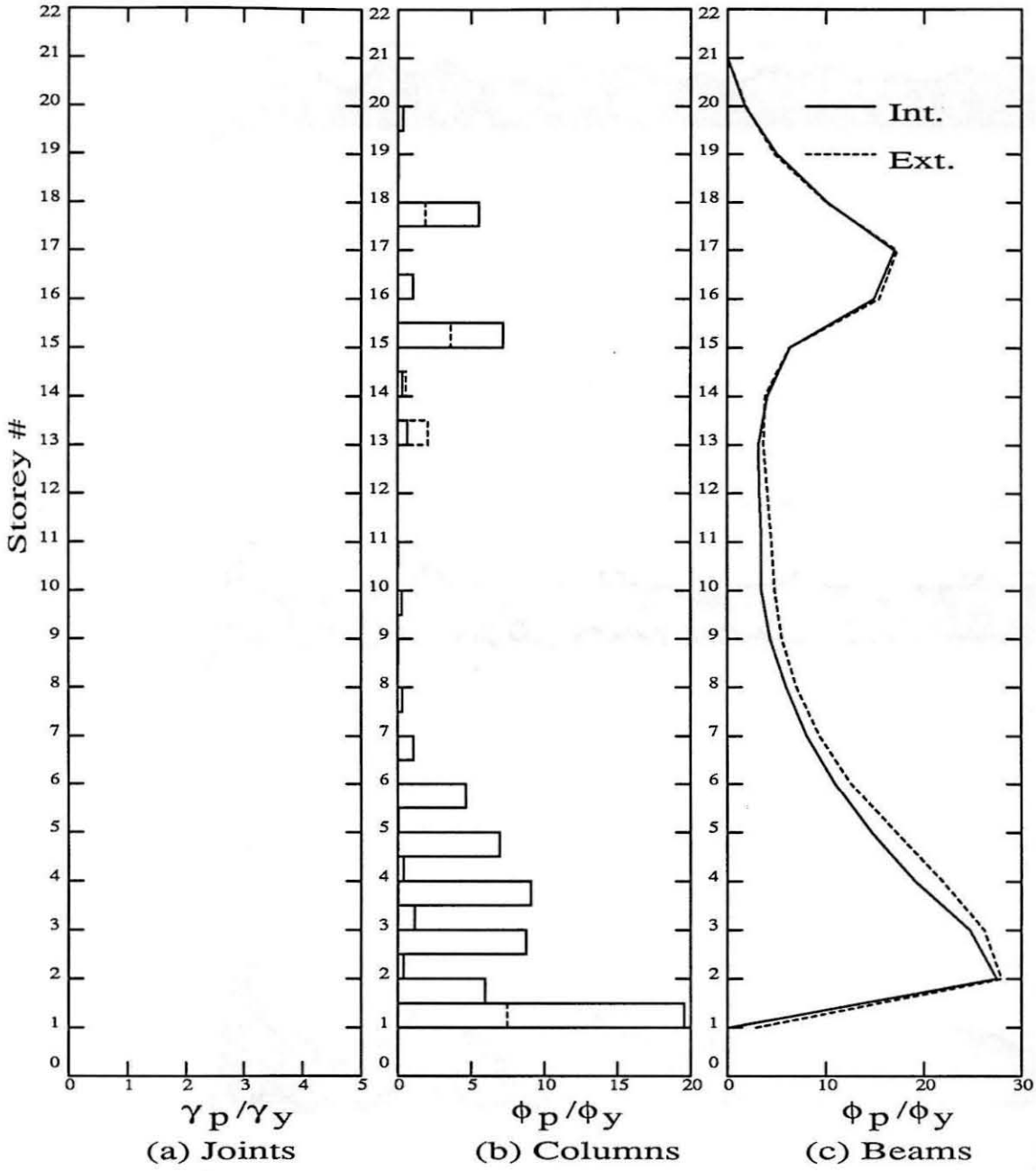

Figure 7.42 : Maximum joint rotation ductilities and maximum member-end curvature ductilities in MRF3 from response **R8**.

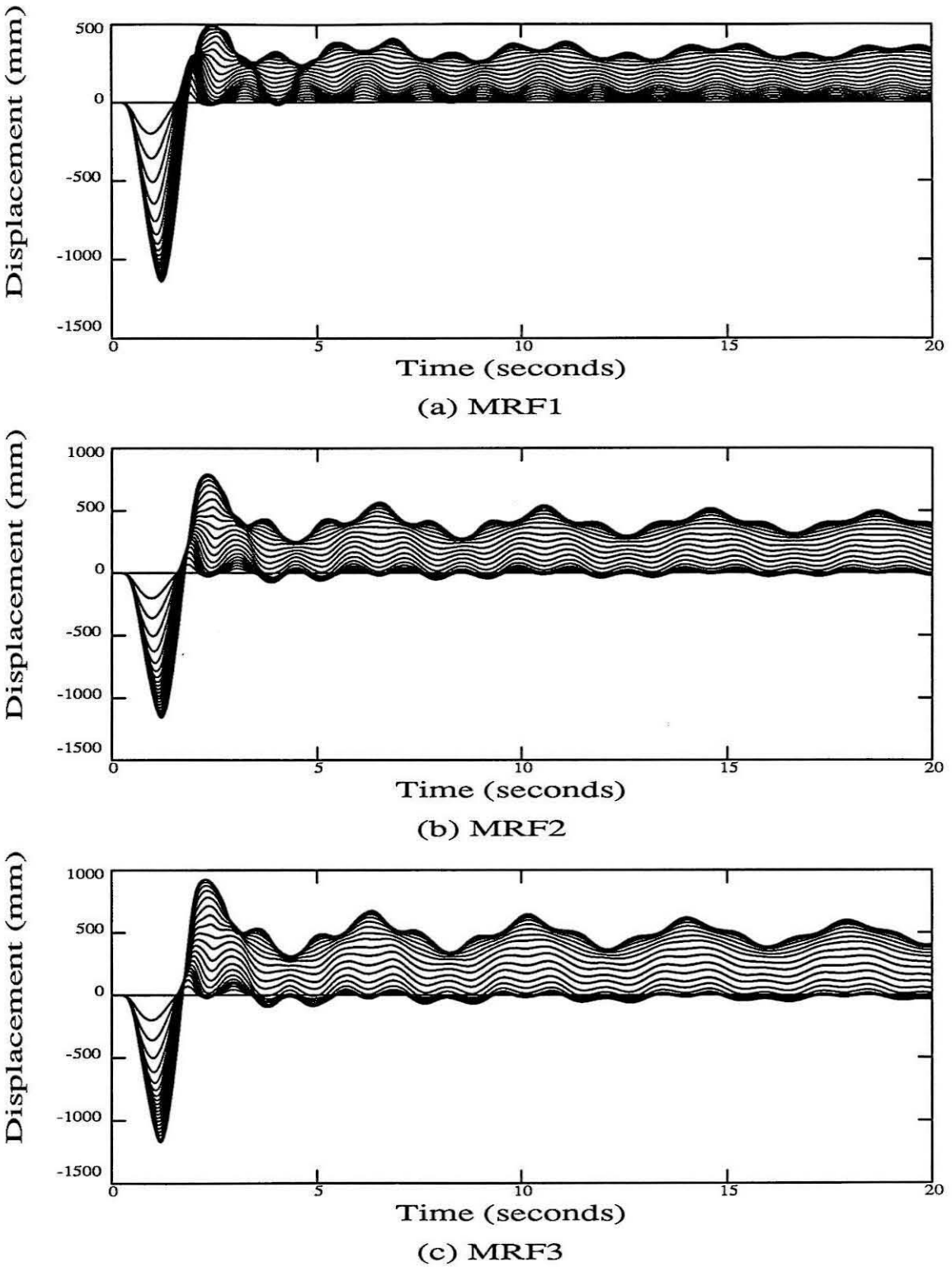

Figure 7.43 : Lateral displacement time histories of all floors of the three MRFs from responses **P9**, **Q9** and **R9**. The outermost curves correspond to the roof, while the innermost curves correspond to the first floor.